CERN – EUROPEAN LABORATORY FOR PARTICLE PHYSICS
NuPECC – NUCLEAR PHYSICS EUROPEAN COLLABORATION COMMITTEE

CERN 99–10
6 December 1999

ELFE AT CERN

**K. Aulenbacher, B. Aune, J. Aysto, J.-L. Baldy, H. Burkhardt (Ed.),
F. Bradamante, E. Cennini, S. Claudet, C. Détraz, E. De Sanctis, H. Fonvieille,
H. Frischholz, S. Galès, M. Garçon, G. Gemme, R. Genand, G. Geschonke,
P. Grafstrom, N. Hilleret, M. Hoffmann, P. Hoyer, K. Hübner, D. Husmann,
J. Inigo-Golfin, M. Jablonka, K.H. Kaiser, E. Keil, G.-E. Körner, S. Kox,
J.-M. Laget, J. Lindroos, J. Martino, Y. Muttoni, R. Parodi, J. Payet,
J. Pedersen, G. Ricco, M. Sassowsky, H. Schmickler, G. Smirnov, G.R. Stevenson,
I. Sick, F. Tazzioli, A. Tkatchenko, R. Van de Vyver and Th. Walcher**

GENEVA
1999

CERN–Service d'information scientifique–RD/995–2000–december 1999

ABSTRACT

The conceptual technical design for a recirculating electron accelerator with a maximum energy of 25 GeV and a continuous beam current of 0.1 mA on target is presented. The machine makes use of the superconducting RF system and other components that will become available after the decommissioning of LEP. The beam will be accelerated in seven passes through a linac with an energy gain of 3.5 GeV per pass.

CONTENTS

1 Introduction and executive summary

An Electron Laboratory For Europe (ELFE) with a continuous 15 to 30 GeV electron beam has been discussed for several years. Workshops on the particle physics with such a machine were held in October 1992 at Mainz, Germany [1], and in September 1996 at Saint Malo, France [2]. Two designs for the ELFE machine were published: The first consisted of a new machine on a 'green site' [3]; the second was an appendix to the linear e^+e^- collider study TESLA at DESY in Hamburg, Germany [4].

With the scheduled shutdown of the large e^+e^- collider LEP at CERN, its superconducting RF system with a total voltage of about 3.5 GV, as well as many other machine components and infrastructure for superconducting RF work, will become available in 2001. This opportunity led NuPECC to ask CERN to engage in a preliminary study of an ELFE machine that would make use of the LEP cavities, as first studied by Geschonke and Keil [5]. In late 1998, CERN and NuPECC set up a joint study of ELFE at CERN with the following mandate:

- Provide a conceptual design of a recirculating electron accelerator of about 25 GeV based on LEP components not required for LHC as indicated in the Geschonke and Keil report.
- The conceptual design report is prepared under the working assumption that this facility could be sited at CERN and integrated into the existing CERN infrastructure.
- Establish the beam specification (average current, longitudinal structure, energy spread and stability) in view of the requirements of hadronic physics.
- A layout and conceptual design of a possible experimental area should be part of the report.
- The conceptual design report should include:
  - a cost estimate of capital investment for construction (including industrial support),
  - an estimate of the manpower required for construction,
  - a rough estimate of the yearly material operations budget,
  - a rough estimate of the man-years required per year for operating this facility.
- A preliminary draft version of this report should be available in June 1999.

In parallel, an internal study group at CERN looked into the accelerator design aspects of ELFE at CERN. In this first report, the physics motivations are summarized, and the conclusions of the study of the technical aspects of the facility are presented.

A brief summary of the conclusions on hadronic physics with ELFE is presented in Chapter 2. The unprecedented luminosity (three orders of magnitude more than facilities already operating in the same energy range) will open up the way to a new generation of exclusive and semi-exclusive experiments at high momentum transfer. ELFE will be a unique facility where quark confinement at work in strongly interacting hadronic systems will be experimentally studied and where the complete spin, flavour and transverse-momentum structure of hadrons will be deciphered. This will take the form of i) the determination of new parton distributions and amplitudes, ii) the use of a variable energy 'secondary beam of quarks' to study the quark hadronization inside and outside the nuclear target, and iii) the accurate determination of hadron structure functions and quark–gluon correlations, especially at large x. Work continues to sharpen the case and will be concluded by a workshop in April 2000. A more detailed report will be issued in spring 2000.

The ELFE beam is transported into two experimental areas: a large high-intensity area housing essentially large mobile spectrometer(s), and a smaller low-intensity area housing a 4π detector. They are discussed in Chapter 3.

Table 1 shows the overall ELFE parameters in our design. Figure 1 shows a schematic view of the ELFE machine. We assume that the electrons are polarized: Their source is discussed

in Chapter 4. An injector accelerates the electrons to 0.8 GeV. Alternatives to the injector — two MAMI-style racetrack microtrons [6, 7] in series and two recirculating linacs with superconducting RF systems in series — are presented in Chapters 5 and 6, respectively. The main accelerator, presented in Chapter 7, has a circumference of about 3924 m, and is of racetrack shape, about 1790 m long and about 300 m wide. It accelerates electrons from 0.8 to 25 GeV in seven passes through the linac, with 3.5 GeV energy gain on each pass. The linac is housed in a long straight section about 1081 m in length. The beam is transported through the opposite long straight section with six vertically stacked beam lines. Spreaders feed the beams into six vertically stacked, roughly half-circular arcs of about 300 m in diameter. Combiners merge the beams from the arcs at the opposite end into the linac. The r.m.s. momentum spread at top energy imposes a lower limit on the bending radius in the arcs, discussed in Section 7.3, and an upper limit on the bunch length, discussed in Chapter 12. The emittance at top energy imposes a limit on the focusing in the arcs, also discussed in Section 7.3. The design achieves the relative energy spread and the emittance at top energy in Table 1. As discussed in Chapter 8, the energy spread also implies a dilution in polarization which starts to be significant ($\sim$ 20% reduction in longitudinal polarization) at the expected energy spread. This may be a reason to aim for a smaller energy spread in future ELFE designs.

Chapters 10 to 16 discuss the accelerator technology, and in particular the superconducting RF system of the linac and the cryogenic system supplying the liquid helium, the magnets for the arcs and the straight sections, the vacuum system, and beam diagnostics. The ELFE cryogenic system will be very similar to the one supplying the LEP cavities. This cryogenics system has recently been successfully upgraded for LEP operation at maximum beam energy. The system will be reused for the LHC. Much experience has been gained in designing and operating large superconducting systems at CERN. We are therefore confident that the system planned for ELFE is well optimized and will be perfectly feasible.

Chapters 17 to 23 discuss the conventional facilities, and in particular distributing approximately 60 MVA of electrical power by extending an existing power station, site and civil engineering, cooling, ventilation, mechanical infrastructure, access control, alarms, safety and radiation protection. Many buildings similar to those described in Chapter 19 have been constructed recently for LEP2 and LHC. ELFE has been put on land already put at disposal of CERN, located in the extension of the SPS external beams in a NE direction, as shown in figures in Chapter 19. This is very advantageous both in terms of the total cost and the time-scale involved in the authorization of the project. The proximity to other CERN installations allows sharing of existing infrastructure and manpower.

Table 2 shows a short breakdown of the estimated capital expenditure for the construction of ELFE at CERN with 1999 prices. The total is about 400 MCHF. Chapter 24 contains more details on the cost and manpower, both for construction and operation.

We believe we have demonstrated that ELFE at CERN is feasible, and that it can be built and operated at about the costs given. We have left many design details to future studies and the ELFE construction team.

Table 1: ELFE performance parameters.

Top energy	25 GeV
Beam current on target	100 μA
Beam power on target	2.5 MW
Injection energy	0.8 GeV
Number of passes	7
Energy gain per pass	3.5 GeV
Relative r.m.s. momentum spread at top energy	$\leq 10^{-3}$
Emittance at top energy	≤ 30 nm
Bunch repetition time on target	2.8 ns

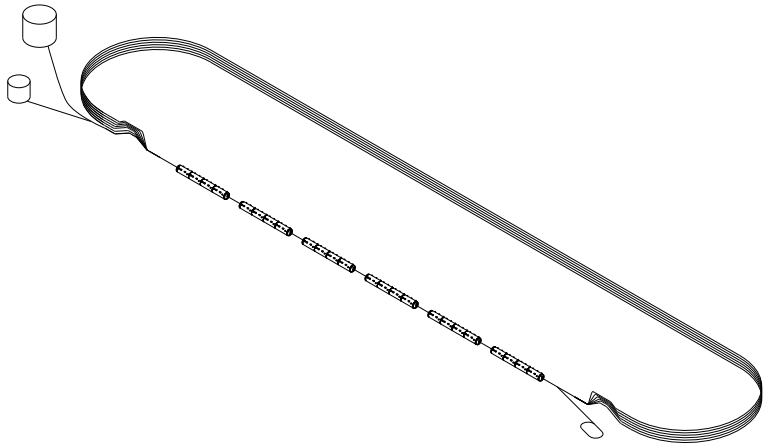

Fig. 1: Schematic view of the ELFE machine.

Table 2: Estimated capital expenditure for the construction of ELFE at CERN (MCHF).

Injection	20.4
RF system	10.9
Cryogenics	63.0
Magnets	55.2
Vacuum	19.4
Beam diagnostics	9.4
Power converters	11.2
Control system	10.0
Sum of accelerator components	199.5
Electrical power distribution	29.0
Civil engineering	109.7
Experimental hall(s)	31.2
Cooling, ventilation, etc.	25.8
Access control, etc.	2.1
Sum of conventional construction	197.8
Total	**397.3**

2 Physics motivation and requirements

Physics Working Group:
M. Anselmino, G. Anton, P. Bertin, S. Boffi, F. Bradamante, M. Düren, E. De Sanctis, H. Fonvieille, S. Forte, M. Garçon, P. Guichon, M. Guidal, D. von Harrach, N. d'Hose, P. Hoyer, K. Rith, K. Königsmann, P. Kroll, J.-M. Laget, J. Martino, P. Mulders, B. Pire, H. Pirner, G. Ricco, I. Sick, G. Smirnov, E. Tomasi, V. Vento, R. van de Vyver, and Th. Walcher.

2.1 Hadronic physics with electromagnetic probes

The scientific goal of hadronic physics is to understand the strong interaction in the region where quarks and gluons are 'confined' into the observed subnuclear particles. The framework for this understanding is the theory of Quantum ChromoDynamics (QCD). While we know how to use it at very short distances and very high energies, its implementation in nucleons and nuclei is still an open issue. At stake is an understanding of the quark structure of matter: How do the basic building blocks of nature interact to form the matter which is responsible for 99.95% of the visible world around us?

Such a quest has several facets:

- The study of the **confinement 'at work'** in ordinary hadronic (i.e. strongly interacting) matter, by selecting the simplest systems made of quarks and gluons and testing them against models or lattice QCD. This is a different path from that taken in ultrarelativistic heavy-ion collisions, which rather study deconfinement in extraordinarily hot and dense hadronic matter.
- The issue of **quark–hadron duality**: It is remarkable that static properties of hadrons are well reproduced by constituent quark models, while a hadronic description of the form factors of few nucleon systems works up to momentum transfers where one would naturally expect to see the onset of quark degrees of freedom. To what extent are the hadronic and the quark descriptions equivalent?
- The study of the various manifestations and the determination of the details of the **gluonic content** of matter. There is strong evidence that a sizeable fraction of the proton is made of glue: What is the structure of this gluonic component? Which states in the hadron spectrum correspond to the excitation of gluonic degrees of freedom?
- The study of the **spin structure** of the nucleon and various hadrons: Where does it come from and what are its various components?
- The study of the **flavour content** of hadrons: Besides light quarks, what are the amounts of strange and charm quarks in their ground state, and what are their distributions?

The electromagnetic interaction provides us with a unique tool to answer these questions. It is well understood and its nature is different from the strong interaction. It provides us with a formidable microscope, with a resolution that can be varied from the size of the largest nuclei down to distances much smaller than the size of a single proton.

An active and lively community of about 400 European scientists is currently performing experiments focused on this goal at existing facilities in Europe, and is leading collaborations in the USA. The realization of QCD at low energy is under study at a number of facilities (MAMI at Mainz, ELSA at Bonn, and GRAAL at Grenoble), while the quark and flavour content of the nucleon is investigated at high-energy facilities (HERMES at Hamburg and, starting from 2001, COMPASS at Geneva). In between, CEBAF at Jefferson Lab, Newport-News (USA), allows more accurate and comprehensive studies of the transition region, where nuclear matter can be understood as being made of constituent quarks. All these studies benefit from the availability of

polarized beams and targets, which make possible a full determination of the relevant response functions.

Still, all the ongoing programmes at these facilities suffer either from too small a luminosity or from too small an energy to address these issues in a comprehensive way. An electron accelerator such as ELFE would operate up to 25 GeV, with an unprecedented luminosity in this energy range. This would make ELFE a unique facility, well suited to the study of hadron structure and of the confinement at work in ordinary matter, by means of

- the determination of new parton distributions and amplitudes through the measurement of exclusive and semi-exclusive reactions at high momentum transfer;
- the production of a variable energy 'secondary beam of quarks', the hadronization of which can be tuned either inside or outside a nuclear target;
- an accurate determination of hadron structure functions and quark–gluon correlations, especially at large x.

The possibility of making use of the LEP accelerating supraconducting cavities opens up a window of opportunity to build a new facility (ELFE at CERN) as soon as 2006.

2.2 Scientific objectives of ELFE

Much of the internal structure of the nucleon has been revealed through *inclusive* scattering of high-energy leptons in the Deep Inelastic Scattering (DIS), or Bjorken, regime (large momentum and energy transfer, Q^2 and ν, but $x = Q^2/2m\nu$ finite). Simple theoretical interpretations of the experimental data have been reached in the framework of QCD, when one sums over all the possible hadronic final states. Accurate tests of QCD have been performed, for instance in the study of the evolution of various response functions. *Unpolarized* DIS brought evidence of the parton (quarks and gluons) substructure of the nucleon, and led to quantitative determination of their distributions. It also showed that quarks carry about half of the nucleon momentum, while *polarized* DIS revealed that only a small fraction of the spin of the nucleon is carried by the valence-quark intrinsic spin.

What is needed now is a new generation of exclusive and semi-exclusive experiments to decipher the complete spin, flavour and transverse-momentum structure of nucleons and hadrons.

A new high-energy, high-luminosity, lepton accelerator combined with large acceptance spectrometers, with an overall energy resolution of about 10^{-3}, makes experimentally accessible a wide variety of *exclusive* processes. Until recently, only a few exclusive channels could be treated in the framework of perturbative QCD. The recently developed formalism [8, 9] of Generalized Parton Distributions (GPD) enlarges such a type of analysis to exclusive electroproduction of mesons and photons.

Such a facility will also enlarge the domain accessible to *semi-exclusive* reactions, by a formidable gain in luminosity (more than three orders of magnitude compared with HERMES or COMPASS), opening access to the transverse distributions of the struck quark, to the transverse spin distribution and to correlation between two or more emitted partons.

Finally, the nucleus will be used as a detector, the size of which is comparable to the formation length of hadrons or to the hadronization length of quarks.

The scientific objectives of ELFE fall into three broad categories.

2.2.1 New parton distributions and distribution amplitudes

- *New parton distributions.* The GPDs have been recently recognized as playing an important role in the description of exclusive reactions [10] in the kinematical domain where

a large energy scale, the virtuality (Q^2) of the virtual photon, coexists with near forward kinematics. These distributions are also called skewed, off-forward, non-forward or non-diagonal parton distributions. They interpolate between the ordinary distributions measured in DIS and the distribution amplitudes which control the hard exclusive reactions.

Factorization theorems have been established in the framework of QCD. They show that in a number of well-identified reactions the amplitude is a convolution of a perturbatively calculable part and a soft matrix element which is parametrized by the GPDs. Renormalization group equations have been derived and it turns out that the Q^2 evolution of the GPD interpolates between the evolution of the parton distributions and the evolution of the distribution amplitudes. So we have a solid theoretical framework to analyse these reactions.

The GPDs can be seen as the interference of the amplitude for a hadron of momentum P_1 to contain a parton having some momentum fraction x_1 with the amplitude for a hadron of momentum P_2 to contain a parton having some momentum fraction x_2. The skewness parameter $(x_1 - x_2)$ measures the non-diagonal character of the process.

The GPDs are non-perturbative quantities which come in different flavour and spin indices. Measuring these soft matrix elements will clarify the understanding of the physics of confinement. Different models, ranging from the constituent quark model to instanton based estimates, lead to quite different predictions. The variety of reactions that can be analysed within this framework will allow a comprehensive study of the GPDs. Different spin–flavour combinations of GPD enter the following processes:

- virtual Compton scattering;
- elastic electroproduction of mesons;
- inelastic electroproduction of mesons with a $\mathrm{p} \to \Delta$ transition;
- electroproduction of a non-resonant pair of mesons; ...

Some pioneering experiments are currently under way at HERA, HERMES and CEBAF. ELFE will be a dedicated facility to determine these GPDs.

- *Light-cone distribution amplitudes for mesons and baryons.* Exclusive reactions induced by highly virtual photons probe small distances in the produced mesons [11]. Therefore one has access to the minimal Fock component (two valence quarks) of the light-cone amplitudes of the produced pseudoscalar and vector mesons. For real-photon induced reactions, the hard scale is set by the momentum transfer t between the photon and the emitted meson, and one has access also to the light-cone distribution amplitudes of the target or emitted baryons. One of the objectives of ELFE is to undertake the study of these large-angle exclusive reactions at the highest energy and momentum transfer available in order to determine the distribution amplitudes of the simplest parton configurations in hadrons.

2.2.2 Quark–gluon correlation, distribution and fragmentation functions

- *Precise determination of inclusive parton distributions at medium to large x.* A substantial improvement of the precision of quark and gluon distributions at large x is required as an input for searches of new physics as well as for the computation of Standard Model processes at present and future colliders. For instance, an adequate knowledge of the gluon distribution is necessary to understand the excesses of large-E_{T} jets observed by CDF (at Fermilab). Similarly, a good knowledge of the valence u-quark distribution is a prerequisite for the analysis of DIS large-Q^2 events seen at HERA. Furthermore, the study of scaling violations of parton distributions at large x provides an important laboratory to test methods of soft-logarithm resummation in QCD. These have been extensively developed

from a theoretical viewpoint but their phenomenology is still largely unknown. Finally, a sufficiently accurate knowledge of large-x parton distribution at moderate Q^2 could give access to higher twist contributions to conventional structure functions, and thus parton correlations.

- *Flavour and valence-sea decomposition of parton distribution.* This study is either very difficult or impossible in inclusive experiments. ELFE will make it possible by the systematic identification of specific hadrons in the final state of a wide class of semi-inclusive experiments. Such a decomposition is necessary for any precision computation of collider processes: for example, computation of the $W^{\pm}$ production cross-section requires an accurate knowledge of the u/d content of the nucleon. Furthermore, detailed knowledge of the parton content is important in testing our understanding of the structure of the nucleon: for example, the $\bar{u}/\bar{d}$ asymmetry is a sensitive probe of the pattern of chiral-symmetry breaking, while the $s/\bar{s}$ asymmetry is sensitive to a possible intrinsic strange-quark component, and thus specifically, in the polarized case, it enables the origin of the suppression of the singlet axial charge (the 'spin crisis') to be understood. Finally, semi-inclusive data may be used to perform an accurate study of fragmentation functions, the time-like counterparts of parton distributions, thereby allowing one to access the parton content of hadrons which are not available as targets.
- *Transverse (spin and momentum) degrees of freedom.* Polarized processes are a rich source of new information on the structure of the nucleon and its fragmentation [12]. Single and double spin asymmetries are sensitive to quark–gluon correlations, which in deep-inelastic inclusive scattering are only accessed by higher twist observables. The following are examples.
  - The transverse spin distribution $h_1(x)$, together with the unpolarized and helicity distributions $f_1(x)$ and $g_1(x)$, completely determines the leading-twist quark–quark light-cone correlator in the nucleon. The measurement of h_1 will be obtained in semi-inclusive leptoproduction, with polarimetry in the final state or specific correlations (two-particle or one-particle azimuthal) in the current fragmentation region.
  - In the current fragmentation region, semi-inclusive leptoproduction will provide a more complete picture of the quark fragmentation process. For instance, in the fragmentation into pions or kaons there is a correlation between the transverse momentum of the produced particle and the transverse polarization of the fragmenting quark [13]. This provides a simple way to probe transverse polarization in the target.
  - The study of single-spin asymmetries in semi-inclusive DIS will provide a cleaner investigation of spin properties than in p–p scattering. The single transverse spin processes observed at Fermilab in $p\uparrow\, p \rightarrow \pi X$ processes at a centre-of-mass energy of about 20 GeV, large x_F and p_T, are much larger than predicted by QCD. Current estimates predict a large value of A_N also in $e\, p\uparrow \rightarrow e'\pi X$ processes. Some of this spin physics is already addressed at HERMES, where preliminary results clearly demonstrate the need for a significant increase in the luminosity.

2.2.3 Quark interactions in nuclei

Exclusive experiments involving nuclear targets offer the unique possibility to use the nucleus as a 'femto-detector' to determine the time-scale evolution of partons or systems of partons propagating inside nuclear matter. But also rare nuclear configurations will be accessible with exclusive reactions induced at high momentum transfer.

- *Colour transparency.* Colour transparency [14] tests a fundamental feature of QCD: that even though quarks and gluons are strongly interacting, a very small quark–antiquark

(meson-like) or three-quark (baryon-like) system will have a small interaction probability. The onset of colour transparency will determine the momentum above which a hard scattering description of exclusive processes makes sense. The experiment consists in transferring all the energy and momentum to a single hadron that subsequently propagates in nuclear matter. A high momentum transfer selects a component in the hadron wave function with a small transverse extension. A difficulty resides in its short lifetime: comparable to the inter-nucleon distance rather than to the size of the nucleus. Two methods appear particularly promising to observe colour transparency.

  - The study of exclusive reactions in few-body systems makes it possible to adjust the distance between two nucleons to the characteristic lifetime, to maximize the rescattering and determine the interaction probability of such a small object.
  - The study of the production of vector mesons makes it possible to vary independently the time in which the photon fluctuates into a pair of quarks and the formation time of the outgoing vector meson. A recent experiment at HERMES (ρ production on nuclei) has demonstrated the relevance of such a picture, but a substantial increase in luminosity, as well as an improvement in the resolution, is needed for a comprehensive study of this phenomenon at the higher Q^2 needed for a sizeable effect.

- *Quark propagation and hadronization.* At the other extreme, all the energy and momentum of the virtual photon can be transferred to a single quark, which propagates and hadronizes after a formation time τ_{F}. This process of hadron formation in DIS cannot be calculated from first principles, as it occurs at energy momentum scales where perturbative QCD is not applicable. An experimental determination of the formation time τ_{F} is necessary to disentangle and constrain various models of hadronization. By embedding the hadron formation process in the nuclear medium, one obtains an experimental tool to adjust τ_{F} to the size of the target nucleus. If τ_{F} is smaller than or of the order of the nuclear radius, one accesses its experimental determination. If τ_{F} is larger than the nuclear radius, one accesses the interaction of a single quark with nuclear medium. Such a secondary beam of quarks will be used as a probe to investigate other hadrons located within the target nucleus.
  The formation time τ_{F} amounts to roughly 1 fm/GeV: An energy transfer above 10 GeV results in the hadronization of a quark outside the nucleus. A continuous electron beam of 20–30 GeV must be achieved to reach, without being swamped by radiative losses, energy transfer varying from a few GeV to 15 GeV. A pioneering experiment at SLAC and a recent experiment at HERMES clearly demonstrate the need of a gain of two orders of magnitude in luminosity in order to achieve a precise binning against the relevant kinematical variables: energy, transverse momentum, rapidity.
- *Rare configurations.* Reactions forbidden by kinematics on free nucleons can be accessed in nuclei. This opens the way to study unusual configurations of nucleons: compact six-quark states, and hot spots, for instance. They manifest themselves by an excess in the nuclear response at $x > 1$, or by an enhancement of the production of particles below threshold for free nucleon targets (cumulative processes, etc.). Hidden colour configurations, in which quarks group into coloured clusters, may also be revealed by processes which involve the exchange of several gluons, like the photoproduction of heavy vector mesons.
- *Charm production near threshold.* The large mass of the charmed quark sets the scale of hard interactions, and perturbative techniques can be used even at low momentum transfer, contrary to the light-quark sector. ELFE will explore charm physics in a relatively low momentum range, where little data exists. Of particular importance will be the study of charmonium (J/Ψ, χ, etc.) formation, which is at present poorly understood. The relatively low binding energy of the charmonium, coupled with the detailed quantum state

of the charm-quark pair, makes these states exquisite probes of the environment created in hard collisions.
Near threshold, or even below threshold in nuclei, the kinematical constraints open up the possibility of studying compact Fock states, via the coherent scattering of all partons: This provides new opportunities of studying exotic states and correlation effects in the nuclear wave function. Also, implanting charm quarks and charmonia in nuclei may provide a new realm of strong interaction studies, through the spectroscopy of their possible bound states.

Such a nuclear programme will be a specificity of ELFE.

2.3 Key experiments

A few key experiments have been selected. Feasibility studies have been reported in the proceedings of the Saint-Malo workshop (Sept. 96) [2] and the Mainz workshop (Oct. 92) [1], or have been worked out since.

2.3.1 Exclusive Compton scattering

- *Large-angle Compton scattering* ([2], page 367). In the p(e, e$'\gamma$)p reaction, a dedicated detector is needed for a clean identification of the γ. When two well-shielded magnetic spectrometers are used for the detection of the scattered electron and the recoiling proton, a luminosity of 10^{38} cm^{-2} s^{-1} will allow the entire angular distribution of the emitted real photon to be determined up to $s = 6$ GeV^2 and $Q^2 = 10$ GeV^2. In the large-acceptance option, the separation of photons from background is less problematic since the luminosity is smaller: 10^{35} cm^{-2} s^{-1}. Moreover it allows non-coplanar kinematics to be accessed, taking advantage of the different behaviour of the azimuthal angular distribution of the virtual Compton scattering and the Bethe–Heitler processes. Finally, the beam asymmetry provides us with an additional way to constrain the Compton amplitude through its interference with the Bethe–Heitler amplitude. Simulation shows that Compton scattering cross-section and beam asymmetry can be accurately determined around $\theta_{\gamma\gamma} = 90°$ up to $s = 10$ GeV^2 (momentum transfer $t \approx -8$ GeV^2). In the case of a real-photon beam, the extraction of the quark distribution amplitude has been proven to be possible ([2], page 144).
- *Deeply virtual Compton scattering.* This corresponds to the production of photons at forward angles in the deep-inelastic regime, through the reaction p(e, e$'\gamma$)p. ELFE will allow the Compton cross-section to be determined and GPDs to be studied at large enough virtuality Q^2 (up to 8 GeV^2) in a domain of x ranging from 0.05 to 0.5. As before, the detection of the three outgoing particles and the use of a polarized electron beam are mandatory to disentangle the Compton and the Bethe–Heitler amplitudes.

2.3.2 Exclusive meson production

- *Deeply virtual production of mesons.* In order to use the factorization scheme for determining GPDs, one must disentangle the transverse and the Coulomb parts of the cross-section. For vector mesons, this will be achieved by the analysis of their decay angular distributions: This requires a large-acceptance detector. For pseudoscalar mesons, a Rosenbluth separation is necessary: This requires the beam energy to be varied between 12 and 24 GeV. A recent estimate shows that ELFE will allow a precise binning of the cross-section, in x, Q^2 and t, up to $Q^2 = 20$ GeV^2 for vector mesons and up to $Q^2 = 10$ GeV^2 for pseudoscalar mesons.

- *Large-angle meson production.* ([2], page 368). The reaction $\mathrm{p(e,e'}\phi)\mathrm{p}$ is the most demanding, as its cross-section is one of the smallest, and a high luminosity is therefore mandatory. Since the ϕ meson is identified by the detection of its $\mathrm{K^+K^-}$ decay, and since the detection of the recoiling proton is useful to overdetermine the kinematics, a large-acceptance detector is also necessary. Assuming a luminosity of 10^{35} cm^{-2} s^{-1}, the differential cross-section will be determined up to $-t = 15$ GeV^2, at $Q^2 = 3$ GeV^2 and below. Counting rates for ρ meson production are higher by about one order of magnitude.

2.3.3 Spin and semi-exclusive hadron production

- *Determination of the transverse structure function* h_1 ([1], page 401). Counting rates have been evaluated for the reaction $\mathrm{p(e,e'}\Lambda)\mathrm{X}$. The experiment consists in determining the spin transfer between the transversally polarized target proton and the Λ emitted at large transverse momentum p_T. A month of running time, with a luminosity of 10^{34} cm^{-2} s^{-1}, is sufficient to accumulate one million Λ with $p_\mathrm{T} > 1$ GeV/c.
- *Azimuthal distribution of emitted partons.* Pioneering experiments ongoing at HERMES have recorded pions, at low Q^2. A significant spin asymmetry of the azimuthal distribution of positive pions has been measured. On the contrary, the asymmetry for negative pions is consistent with zero, in agreement with its predicted suppression by a factor of five. Its accurate determination, at higher Q^2, requires a much higher statistics. ELFE will perform these experiments with an unprecedented luminosity and will extend them to other hadrons: This will open the way for a precise binning against the relevant kinematical variables, which will allow different moments to be measured for transversally and longitudinally polarized targets. Eventually, various chiral-odd distributions and chiral- or time reversal-odd fragmentation functions will be determined [15, 16].

2.3.4 Nuclear targets

- *Colour transparency in few-body systems* ([2], page 377). The simplest reaction $\mathrm{D(e,e'p)n}$ has been simulated in kinematics which maximize np rescattering, where one can determine the interaction of the compact minimal three-quark state, selected in the ejected proton, with the recoiling neutron. If two spectrometers are used, at a luminosity of 10^{38} cm^{-2} s^{-1} , counting rates of several 10 per hour make this experiment feasible up to a virtuality of the photon as large as $Q^2 = 16$ GeV^2. If a large-acceptance detector is used at a lower luminosity (10^{35} cm^{-2} s^{-1}), the experiment is still practicable as far as the counting rates are concerned. However, special care needs to be taken in the design of the detector in order to achieve the resolution of 10^{-3} necessary to guarantee elastic scattering (i.e. absence of particle production). The case of pseudoscalar or vector meson production and rescattering has also been found feasible.
- *Hadronization in nuclei* ([1], page 333). The gain in luminosity (three orders of magnitude compared with HERMES) will allow the production rate of different fast hadrons (rapidity $z_h > 0.7$) to be mapped out with adequate resolution of the relevant variables. For instance, at a luminosity of 10^{35} cm^{-2} s^{-1}, to allow a statistical accuracy of 1% in bins of energy $\Delta\nu = 1$ GeV and virtuality $\Delta Q^2 = 1$ GeV^2 (for $Q^2 \leq 14$ GeV^2), 120 and 500 h for kaon and pion production, respectively, are required.
- *Large x response of nuclei* ([1], page 475). This is one of the few experiments which require two magnetic spectrometers. Counting rates have been estimated for the simplest reaction $\mathrm{D(e,e'p)n}$. One hundred days, at a luminosity of 10^{38} cm^{-2} s^{-1}, will be sufficient to accumulate 500 events at $x = 2$ and $Q^2 = 15$ GeV^2, and more at smaller Q^2.

2.4 Possible detection set-up

Three possible detection scenarios have been originally worked out:

- **MEMUS** (Multiparticle Electroproduction Modular Upgradable Spectrometer; [2], page 157). This is a large-acceptance spectrometer based on a superconducting solenoidal magnet providing a field of 3 T. Such a configuration strongly suppresses the background due to Moller electrons. It covers an angular range from 3° to 165°. It has an asymmetric structure, with large integral field at forward angles, allowing the detection of fast particles, and shorter path length in the backward direction where slow particles are detected. The maximum luminosity will be in the range $10^{35} - 10^{36}$ cm^{-2} s^{-1}. Its moderate momentum resolution (10^{-2}), especially at forward angles, is compensated for by a reconstruction of the final state which allows exclusive channels to be identified by overdetermining the kinematics.
- **FAST** (Forward Angle SpecTrometer; [1], page 511). This is a large-acceptance spectrometer based on a dipole field of 2 T. It covers the forward angular range ($< 35°$), with a resolution of a few 10^{-3}. The maximum luminosity will be in the range $10^{35} - 10^{36}$ cm^{-2} s^{-1}.
- **A pair of magnetic spectrometers** ([1], page 503). These are straightforward extensions of CEBAF high-resolution spectrometers. A combination of magnetic dipoles and quadrupoles, their length is approximately 35 m. Their momentum resolution varies from 5×10^{-4} at 10 GeV/c to 10^{-3} at 20 GeV/c. They allow the detection of two charged particles in coincidence, at the largest luminosity (10^{38} cm^{-2} s^{-1}), at the expense of the solid angle (7 msr).

Pre-conceptual designs have been proposed and issues have been identified. No insurmountable problems are foreseen. However, special attention should be paid to optimize the design of the large-acceptance set-up in order to reach the goal of a momentum resolution of 10^{-3}. To address this issue, a fourth scenario is at present being studied.

- **Dipole + recoil spectrometer.** This set-up combines a forward dipole spectrometer with a field integral of about 5 Tm, covering about ±30° in bending angle, and a recoil detector, covering 30°–120° in polar angle and full azimuthal range. The high magnetic field confines the electromagnetic shower to a limited dead area. The high rates require fast and radiation-resistant detector technologies, while the high resolution requires extremely thin detectors (< 0.01 radiation length) with some in vacuum. Scintillating fibres and hodoscopes, Gas Electron Multiplier (GEM) detectors, fast crystal ElectroMagnetic (EM) calorimetry and Ring Imaging CHerenkov detectors (RICH) with PM readout are promising and sufficiently fast techniques. There should be room for additional specialized detectors which would provide some flexibility in the future.

2.5 Beam requirements

- **Luminosity.** Depending on the detector acceptance, a luminosity in the range $10^{35} - 10^{38}$ cm^{-2} s^{-1} (corresponding to a beam intensity in the range 0.1–100 μA) will be used. For *exclusive reactions*, this will allow a virtuality Q^2 of the photon up to about 20 GeV^2 to be reached or a momentum transfer t up to about 20 GeV^2, well inside the hard scattering regime. For *semi-exclusive reactions*, such a luminosity will open unprecedented opportunities in our understanding of the response of nucleons and nuclei.
- **Energy.** A beam energy of about 25 GeV will allow this momentum transfer and/or virtuality to be reached, in exclusive reactions, at a reasonable scattering angle of the electron. A higher energy will not significantly increase the momentum-transfer range, since the exclusive cross-sections are decreasing too fast. Also, this energy is in the adequate range

to produce, without serious radiative losses, a 'secondary beam of quarks', of variable energy, that can hadronize inside or outside a nuclear target. Finally, beam energy down to about 8 GeV should be achievable, in order to provide a large dynamics in the energy and momentum transfer, and to overlap other facilities.

- **Energy spread.** An energy spread of $\sigma_{\rm E}/E < 10^{-3}$ is necessary to achieve the identification of exclusive channels.
- **Duty factor.** A high duty factor, well above 50%, is mandatory for reducing the accidental background in coincidence experiments and for extracting the tiny relevant signals.
- **Polarization.** A highly longitudinally polarized beam ($P_{\rm e} > 60\%$), at all energies, will allow the spin structure of the various amplitudes to be accessed.

These characteristics will make ELFE a unique, unmatched facility to determine the structure of hadrons and study the confinement at work in an original way.

3 Experimental areas

To get an idea of the type of experimental areas that would be needed we have considered two main classes of possible experiments. In both cases we have asked ourselves if it would be possible to use facilities already existing at CERN.

The first class of experiment considered was a scattering experiment requiring a large two-arm spectrometer with the possibility to rotate independently each arm over a wide angular range. In general this kind of scattering experiment uses high-resolution spectrometers with a corresponding small angular acceptance. Thus there is a need for a high-intensity beam. We have assumed a beam of the order of 100 μA. None of the existing experimental halls at CERN has the space needed and at the same time an adequate shielding for intensities of this magnitude. Thus it is necessary to construct a new hall to house such a spectrometer. The dimensions of the hall are determined by the considered minimum space to house the two rotating spectrometer arms consisting of a combination of magnetic dipoles and quadrupoles. The height of the roof above the beam height and the hook height above the floor are determined by the need for a vertical bending plane of the spectrometer. The chosen shape is circular (see Fig. 86 in Chapter 19) with an internal diameter of 55 m and a height of 24 m. The circular shape has been chosen for cost reasons. The thickness of the concrete walls and the dome-shaped concrete roof have been chosen in order to be consistent with radiation safety requirements also taking into account the outer earth shield. The crane will be polar type with a capacity of 40 t. The beam is dumped in a special beam-dump cavity with sufficient shielding around in all directions. There will be heavy-equipment access to the tunnel by a 10% ramp. Further details and drawings can be found in Chapter 19 on civil engineering.

The second type of experiment would use a large-acceptance detector (close to 4π) in a low-intensity beam. The MEMUS detector mentioned in the previous section is a good example. Typical intensities considered here are of the order of 1 μA. In this case both the shielding and the space requirements are less severe. The present high-intensity underground area ECN3 has certainly the necessary shielding. However the lateral space and the height are limiting factors. The width of this underground area is 16 m with a hook being 8 m above the floor. A reasonably sized 4π detector would have a diameter of the order of 5 m. Allowing for support and access to electronics, it is difficult to imagine a beam height much below 4 m, leaving another 4 m above the beam axis before reaching the height of the hook. The lateral space is not very ample, taking into account the need to be able to roll out different detectors into garage positions. However, supposing that the ECN3 area will be free and no longer used for the fixed target programme of the SPS, we are not excluding the ECN3 area as an option for the large-angle detector.

In order to be complete and to be able to compare different options we have also looked at the possibility to instead construct a new hall also for the 4π detector. In this case one would of course construct a hall with less space limitation than the existing one. Here we have again opted for a circular hall with a diameter of 30 m and a height of 12 m. An option for a tagged photon beam has also been included in this hall. The access to the hall would be similar to the high-intensity hall and there would also be a similar arrangement for the dump. For a drawing see Fig. 86 in Chapter 19 on civil engineering.

4 Polarized electron source

The polarized electron source has to achieve the full current of ELFE with the best possible polarization. Photosources with GaAs-type photocathodes offer polarizations of 80% with c.w. beam currents of more than 100 μA. This Chapter discusses the potential of the photosource to obtain a beam availability for the accelerator close to 100% with the given parameters.

4.1 Physics background

4.1.1 Electron polarization in semiconductors

Photoabsorption of circular polarized light with an energy near the band edge of a semiconductor generates spin polarized electron ensembles in the conduction band of GaAs-type semiconductors. For a GaAs crystal the polarization is limited to $\leq 50\%$ because of the remaining degeneracy of valence band states, which is due to the symmetry of the GaAs crystal. For several years this limit has been circumvented by the use of deformed GaAs-crystal lattices with reduced (tetragonal) symmetry, the so-called 'strained-layer' photocathodes [17]. The polarization in this case is about 80%. Deviations in the band structure from the ideal situation and depolarization processes during electron diffusion in the semiconductor may explain the incomplete polarization of the free electrons.

4.1.2 Electron extraction from the semiconductor

After photoexcitation the electrons will diffuse to the surface where they could possibly escape into vacuum. This phenomenon is characterized by the quantum efficiency (Q_e) which is defined as the number of escaping electrons per incident photon. In general the polarized electrons in the conduction band of the semiconductor cannot escape from it because of the positive energy difference with respect to the vacuum potential.

The desired negative energy difference can be achieved (negative electron affinity, NEA) if strongly p-doped crystals in conjunction with caesium-oxide (CsO) layers on the surface are used. The CsO layers are structures of sub-monolayer thickness.

It is the fundamental task of the polarized source construction to maintain the CsO layer — and with it the Q_e — during operation of the polarized source.

Q_e in 'bulk' crystals with thicknesses of several light absorption lengths (several μm) may be as large as 30%, whereas strained layers can only be produced with thicknesses of approximately 150 nm. For this reason, and since the optimum polarization is only achieved at the extreme absorption edge where the absorption length is larger, the quantum efficiency of high-P photocathodes is limited to about $0.3\% - 0.5\%$ [18].

4.1.3 Electron optics with photosources

In addition to polarization, a photosource offers the following advantages over a thermionic source:

- The emitting area, and therefore the beam emittance, can be controlled by the laser-spot size.
- Any desired time structure of the beam may be generated by modulating the light source.

4.2 The polarized source at MAMI

The polarized source at MAMI in its present state is already able to fulfil most of the requirements of ELFE, especially because it is matched to the racetrack microtron (RTM) operation, one of the schemes which are proposed for injection into the ELFE recirculator.

Figure 2 shows the main building blocks of the Mainz polarized photosource. It is located about 1.5 m above the MAMI pre-injector linac axis.

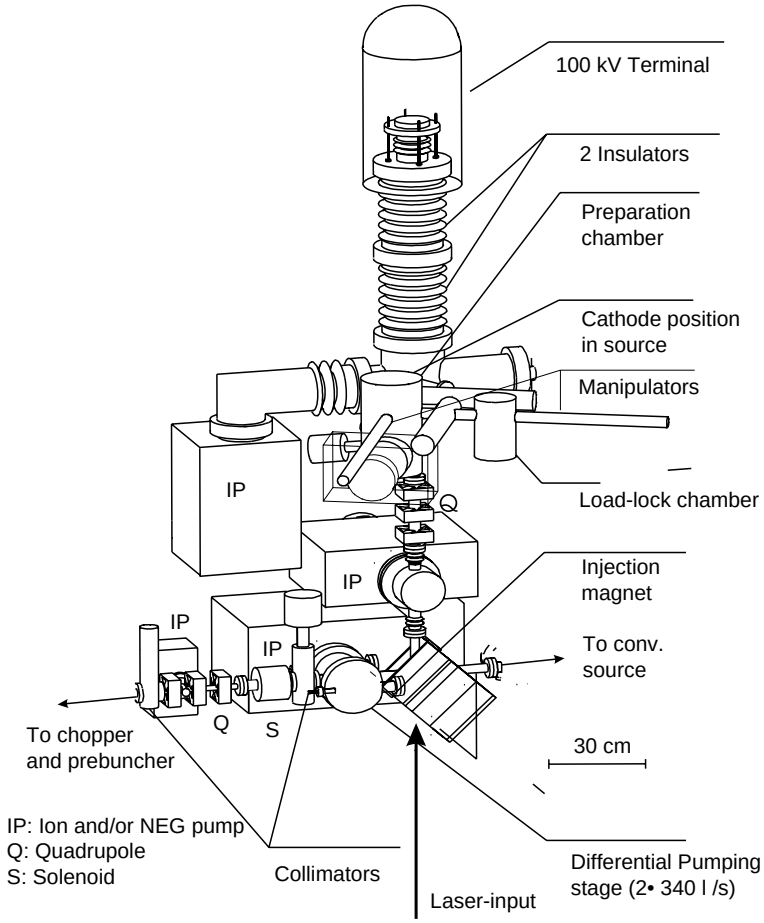

Fig. 2: Artist's view of polarized-source installation at MAMI.

The source is designed for UHV vacuum conditions in the low or sub 10^{-11} mbar range. This is achieved by a bakeable construction together with a high specific pumping speed (400 l/s NEG pump + 110 l/s Triode Ion pump). Differential pumping is employed to avoid backstreaming from the several 10^{-7} accelerator vacuum.

A load-lock system is attached to the source in order to replace photocathodes without breaking the vacuum system. Cathode activation is done in a separate activation chamber in order to minimize accelerator downtime (see below).

The right side of Fig. 3 demonstrates the mechanism of cathode exchange and the left side shows the electron optical arrangement in working position. The arrangement is essentially a diode geometry (potential: -100 kV) with an intermediate electrode held at 50 kV that is used to adjust the field gradient at the cathode surface.

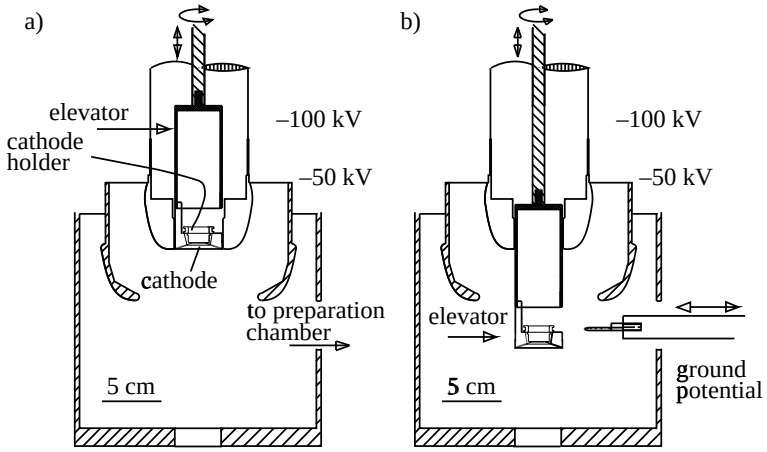

Fig. 3: Section of accelerating stage: a) operational condition, b) cathode exchange.

The HV design is such that field emission and the probability of micro-discharges[1] are minimized. Field emission levels above 100 nA will increase the partial pressure of dangerous gases and therefore limit cathode lifetime. Typical field emission levels at 100 kV are well below 10 nA.

The beam is produced by tightly focused (0.25 mm diameter) laser illumination. After extraction at the cathode surface with a gradient of 0.9 MV/m the beam is accelerated to 100 kV. After a drift space the beam is focused by a quadrupole triplet and then deflected onto the linac axis by an alpha magnet. An advantage of this deflection is that it prevents 'direct view' of backstreaming gases or ions from the injector towards the source.

The polarized electron source delivers a beam of low emittance (see Table 3) because of the small emitting area. Matching to the accelerator acceptance is achieved by solenoids and quadrupoles.

Table 3: Parameters of the Mainz polarized source.

Parameter	Value
Cathode type	Strained layer GaAs
Typical quantum efficiency	0.2% (1.6 μA/mW)
Optimum laser wavelength	826 nm
Polarization at 826 nm	78%
Emitted bunch length	50 ps
Bunch repetition rate	2.449 GHz
Beam energy	100 kV
Normalized r.m.s. emittance	0.048 π mm mrad
Beam transmission to target	95%

Beam set-up time is about one hour and operation without operator intervention is achieved for periods of several days.

Because of the lifetime problem (see below) the emitted charge has to be used effectively. This is achieved by using RF-synchronized photoemission in conjunction with an optimized pre-buncher system. 99% of the emitted Gaussian electron bunches of 50 ps FWHM are transmitted

[1]Micro-discharges lead to immediate irreversible damage to the crystal.

through the 180° acceptance of the buncher system [19]. 2–4% of the beam current is lost on the transverse collimators in front of the chopper system.

The limited lifetime of the source is circumvented by the load-lock system: One cathode is operating in the source while another one is being regenerated in the preparation chamber ('tandem operation'). Because cathodes may be regenerated many times this principle offers long ($> 1500\,\mathrm{h}$) operation with high availability [20].

New cathodes may be introduced from the air side within 24 hours without impact on the vacuum system.

4.2.1 Photocathodes

It is necessary to stress that the performance of ELFE in operation with a polarized source will depend critically on the availability of the photocathode with the highest polarization. Because the beam quality factor goes with P^2 the running costs of ELFE will decrease by 20% for the same 'physics output' if the polarization can be increased to 90% from the currently available 80% with an optimized photocathode structure.

Figure 4 shows the crystal structure of the standard photocathode at MAMI. The cathode band structure is matched to the wavelength of commercially available high-power semiconductor lasers (e.g. SDL 5430). The active layer thickness is $0.15\,\mu$m. Considerable effort (Mg-doping, quantum-well sublayer) has been necessary to achieve thermal stability of the structure.

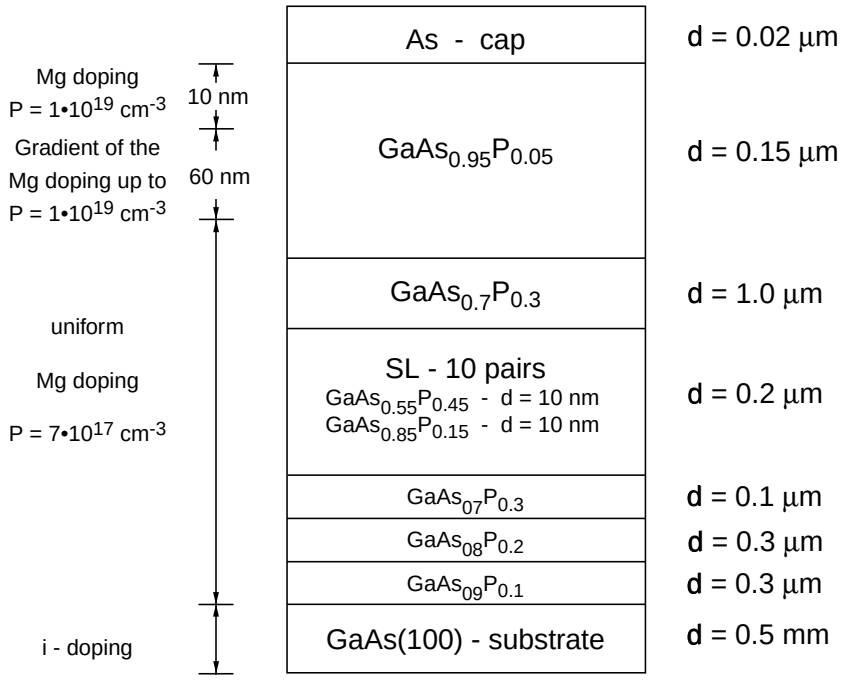

Fig. 4: Structure of strained-layer photocathode.

The quantum efficiency of up to 0.5% in the polarization maximum is one of the highest ever reported for a cathode with $P > 0.75$ [21].

It is expected that the collaborations of present accelerator centres with semiconductor scientists — mainly in Japan and Russia — will lead to a further improvement of photocathode performance in the next few years.

The polarization which is available at the experiment is, however, also dependent on other parameters:

- Spin tuning (see Section 4.5).
- Avoiding energy spreads which lead to depolarization due to different spin precession angles for the individual particles in the recirculating arcs. This is to some extent unavoidable because of synchrotron-radiation emission (see Chapter 7).

4.2.2 Higher bunch charges for ELFE

An experiment was done recently to demonstrate the feasibility of injecting the bunch charges that are required for the operation of ELFE at maximum current: ELFE, operating at 352 MHz and 100 μA average current will require a bunch charge of 0.28 pC.

This charge has to be emitted within the acceptance (of 180°) of the ELFE injector which operates at the seventh harmonic. A d.c. injection will therefore require an average current of 1.4 mA, a value that is at present not achievable in long-term operation. However, this can be avoided by an RF synchronized photosource:

We used an RF synchronized laser system operating at the 32nd subharmonic of MAMI (76 MHz) producing an average current of 10 μA (0.13 pC charge per bunch). The Gaussian laser pulse length was adjusted to 110 ps FWHM. Under these conditions more than 95% of the intensity was accepted by the accelerator. The source was operating at a peak current of 1.1 mA and a peak current density of more than 1.6 A/cm^2.

This current was produced without significant change in the beam parameters and resulted in the usual MAMI beam of very high quality at 855 MeV.

At 0.26 pC/bunch an increase in transverse emittance was observed which is due to the initial restriction of the gun to operative current levels of 1 mA or 1.5 A/cm^2 [22].

Even though the machine was still operational at this bunch charge we observed a nonlinear increase of radiation, which should be avoided for permanent operation.

Transverse emittance can be conserved by a slight increase in the extraction field at the source. Operation at SLAC has demonstrated that GaAs photocathodes tolerate twice the extraction field (1.8 MV/m) than in our gun without problems [23]. This will also reduce the longitudinal bunch growth during the acceleration and the 100 keV drift.

4.3 Cathode lifetime considerations

4.3.1 Principal advantages of load-lock systems

A load-lock system allows accelerator downtime in case of failure of the photocathodes to be reduced.

Photocathode failure is possible due to many effects, e.g.

- catastrophic damage due to HV discharge,
- insufficient polarization of the cathode,
- insufficient quantum efficiency after first activation.

In a system without load-lock option this situation enforces breaking of the vacuum system. This results in a serious downtime of the facility.

There are other advantages of this system, like the possibility of tandem operation, or the longer operation time under vacuum. However, these advantages are not so important if a high value of the C_τ parameter (see below) can be achieved. The possibility of quick repair of unforeseen situations is the main advantage.

4.3.2 Lifetime limiting effects

The CsO surface layer at the photocathode surface is easily deteriorated in operational conditions. Beam losses lead to electron stimulated desorption (ESD). The ESD gas species are more poisonous than the normal residual gas. This is proven by the fact that a photocathode is stable for several months if no beam is produced. The beam losses are large especially in the first part of the beam line where there is no suppression of the ESD-produced molecules by differential pumping. Losses behind the differential pumping stages (like on the collimators of the MAMI system) are not so severe.

Another lifetime limiting effect is the production of ions due to ionization of residual gas in the accelerating region in front of the cathode.

In practice these effects will lead to an exponential decrease of quantum efficiency (Q_e) with a time constant (1/e-time) which is called 'lifetime'. In operation the loss of Q_e is compensated for by increasing the laser power, but this is only possible for a limited amount of time.

Because the size of these effects is always proportional to the average beam current, it is found that for given conditions (beam loss and base pressure) there is a certain limit for the photocathode lifetime. The product of beam current and lifetime $C_\tau = I \cdot \tau$ (C_τ has units of Coulomb) is characteristic for the possible continuous operation time.

The time interval T_op (in seconds) for which a given current (under the conditions of exponential decay) can be delivered continuously is given by

$$T_\mathrm{op} = \ln\left(\frac{Q_\mathrm{e}(t=0)\cdot P_\mathrm{l}}{I}\right)\cdot\frac{C_\tau}{I}\ , \tag{1}$$

where I is the current in amperes, Q_e is given in A/W and P_l is the available laser power on the crystal surface in watts.

Typical parameters for currently available photocathodes and synchro lasers are $Q_\mathrm{e} = 1.6\times10^{-3}\,\mathrm{A/W}$ and $P_\mathrm{l} = 0.2\,\mathrm{W}$.

If the case $P_\mathrm{l}\cdot Q_\mathrm{e} \gg I$ (for the Q_e of highly polarized photocathodes true up to $100\,\mu\mathrm{A}$) is achieved, the only effective way to get to high continuous operation time is to increase C_τ.

The availability of the source is given by

$$A = \frac{T_\mathrm{op}}{T_\mathrm{op}+T_\mathrm{exc}}\ , \tag{2}$$

where T_exc is the time that is required to regain the initial quantum efficiency, e.g. by a new activation of the photocathode.

In our present case at MAMI C_τ is limited to 7 C [24], which would lead to a reduction of availability to 90% at $100\,\mu\mathrm{A}$ average current (see Table 4).

It should be mentioned that long runs have been performed only with currents of $20\,\mu\mathrm{A}$ at Mainz because of the absence of experiments which would have tolerated higher currents. Short-term tests with up to $150\,\mu\mathrm{A}$ at the source have demonstrated that the cathodes behave as expected, so the extrapolation to $100\,\mu\mathrm{A}$ seems reasonable. All tests have been performed with strained-layer photocathodes operating at the laser wavelength resulting in maximum polarization.

It is evident that better vacuum conditions — either achieved by higher specific pumping speed, lower desorption or lower beam losses — will increase C_τ and with it the availability.

As a consequence of this reasoning the CEBAF group has increased the pumping speed at its source to 4000 l/s.

Further improvement can be achieved by suppressing the beam halo that is generated by the scattering of the laser light on the crystal surface [25]. These two measures have recently improved the C_τ of the CEBAF source to 100 C.

Another gain can be expected by covering the beam pipes with low-desorption NEG material. This technology is available at CERN [26].

4.3.3 Conclusion for the ELFE design

Both relevant parameters for availability — the lifetime–beam-current product C_τ and the cathode exchange time T_{exc} — should be optimized. However, the improvement of C_τ is more important because a cathode exchange means an undesired interruption of operation, which might even require some additional machine optimization.

It is clear that a new design at ELFE will use the best possible vacuum technology so that a value of $C_\tau > 100$ C can be regarded as realistic. The necessary improvements can be made without compromising the possibility of a load-lock system.

T_{exc} can in principle be reduced to 15 minutes if the cathode activation (deposition of caesium and oxygen) are controlled remotely.

Table 4 summarizes the values possible at MAMI and those which can be expected by further optimization of the construction at ELFE.

Table 4: Lifetime relevant parameters for MAMI and ELFE (projected).

Parameter	Value (MAMI)	Improved value (ELFE)
Base pressure	$< 2 \times 10^{-11}$ mbar	$< 1 \times 10^{-11}$ mbar
Pumping speed	500 l/s	4000 l/s
Transmission loss	$< 10^{-3}$	10^{-4}
Field emission	< 5 nA	< 5 nA
Lifetime–beam-current product (C_τ)	7 C	100 C
Cathode exchange time	< 2 hours	< 15 min
Availability at 20 μA	99.2%	> 99.9%
Availability at 100 μA	90% (extrapolated)	99.9%

4.4 Laser system

The desired availability at maximum current can be achieved with the currently available RF-synchronized laser systems [27]. Such a laser is a master oscillator power amplifier system (MOPA) (see Fig. 5) which has only semiconductor lasers as active elements.

Laser operation in the MAMI regime is not typical for ELFE injection, because the new machine will require operation at the seventh subharmonic.

However the CEBAF laser system operates at 499 MHz and offers nearly the same transmission [27]. Therefore no new technology is required for the ELFE laser system.

A disadvantage of such a synchro laser system lies in the relatively high d.c. background between the pulses which may be as high as 1%. This portion of the beam current would be lost in the main accelerator. Therefore the construction of a 352 MHz chopper is advantageous.

It is expected that a physicist with experience in laser science could set up the laser system dedicated for ELFE within one year.

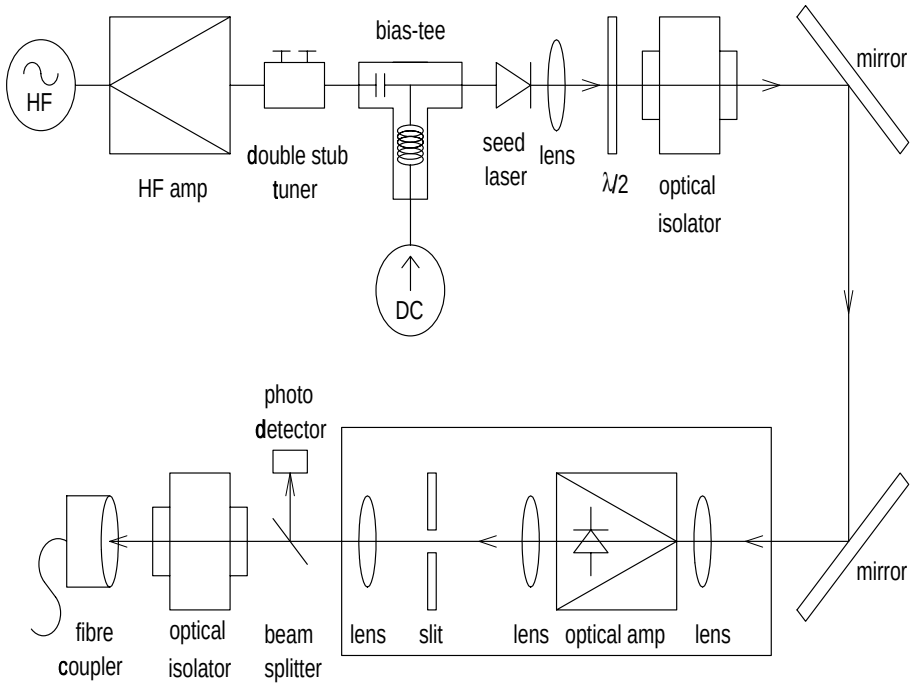

Fig. 5: RF-synchronized semiconductor laser system (MOPA) at MAMI [28].

4.5 Polarimetry and spin tuning

Polarimetry has to be regarded as an important part of beam diagnostics. It is desirable to have a low-energy polarimeter in the vicinity of the source. This allows possible problems with photocathodes or with spin transport to be located, and measurement of polarization at the experiment.

This task is most conveniently achieved by Mott polarimeters. These devices can exclusively measure transverse polarization components. Because the source produces a longitudinally polarized beam it is necessary to have a spin rotation device (e.g. Wien filter) in front of the polarimeter.

Mott polarimeters are devices with good reproducibility (better than 1%). The achievable accuracy is about 3% in $\Delta P/P$.

The Wien filter can also be used to do spin tuning of the machine. This option depends on the compensation of the optical changes introduced by the settings of the filter for different spin-tuning angles.

On the other hand, for the MAMI complex efficient spin tuning is achieved by energy variation of the last microtron stage [29]. Therefore integration of the Wien filter in the interface between source and preaccelerator is not an essential task for ELFE operation. It may be more convenient to use it exclusively as a diagnostic device in a separate arm. This would allow the 100 keV drift space in front of the injector to be minimized.

4.6 Back-up system

In case of a major failure of the polarized gun system (e.g. vacuum leak) the unscheduled downtime of the facility can extend for weeks. Therefore a back-up system (a second source) is desirable.

The second gun can be coupled conveniently to the accelerator by switching off the alpha magnet shown in Fig. 2. A conventional (thermionic) gun has the advantage of producing a 'reference' beam without any change in beam parameters, maintenance-free for years.

Another photosource would be a true back-up system. The reference quality of the beam would have to be ensured by good position and distribution control of the laser system, and preferably by the use of a simple and reproducible cathode material (e.g. bulk GaAs).

5 Microtron injector

The goal of an 800 MeV CW beam has already been attained by the three-staged normal conducting RTM cascade MAMI B (MAinz MIcrotron, extension B) of the Johannes Gutenberg University in Mainz. This machine was designed and built from 1976 to 1990 under the guidance of H. Herminghaus [6, 7]. The floor plan of the machine is shown in Fig. 6. Since 1991 MAMI B has been running routinely and very successfully for nuclear-physics experiments and for the production of coherent X-rays. Owing to its high reliability more than 7000 operational hours per year have been reached and nearly all experiments have been served on schedule. With the exception of some minor modifications a copy of this machine could be used directly as an injector for the ELFE recirculator. Therefore, in the first part of this report the fundamental properties of MAMI B are summarized and the design of its main components is briefly described.

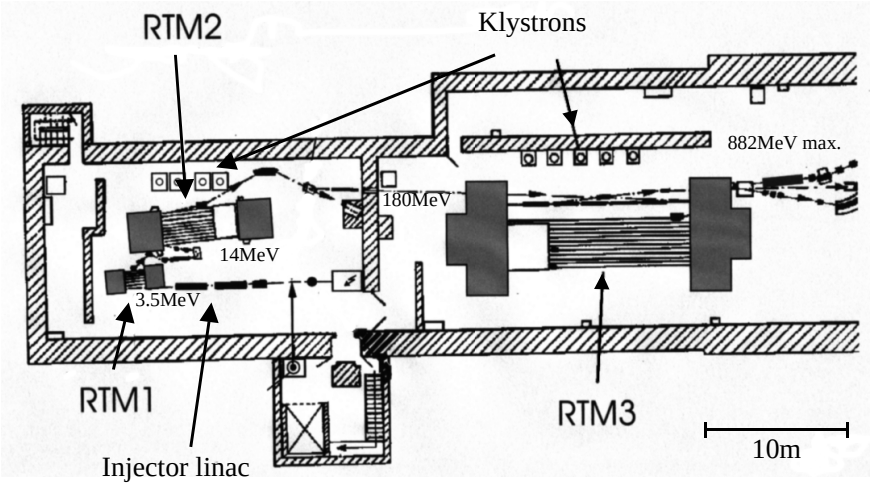

Fig. 6: Floor plan of MAMI B.

Since the choice of the energy steps of MAMI B was influenced by the availability of inexpensive used components at the time of its construction, it may now be worthwhile thinking about a somewhat simplified arrangement. As a first approximation, a preliminary concept of a machine with only two stages is presented at the end of this report. From the point of view of operational complexity, however, there is no strong argument to reduce the number of stages.

The microtron injector of ELFE would have to produce electron bunches with a repetition frequency of 352 MHz. By coincidence, the accelerator sections of MAMI are operating at very close to seven times this frequency (2.45 GHz), so that klystrons and accelerator structures would need only small modifications. The bunches could be produced by a pulsed laser gun with the correct repetition frequency. In a short test 0.14 pC bunches produced by a 76 MHz laser have been accelerated successfully and with good beam quality through MAMI. To reach the goal of 100 μA CW beam current at 352 MHz, however, the bunch charge must be doubled. In order to achieve optimum beam emittance the optics of the electron gun should be adapted to the higher space charge.

5.1 Fundamental properties and design criteria

5.1.1 Coherence condition and longitudinal motion

A schematic view of an RTM is shown in Fig. 7.

From the condition for coherent acceleration of relativistic electrons in an RTM the following relation can easily be deduced

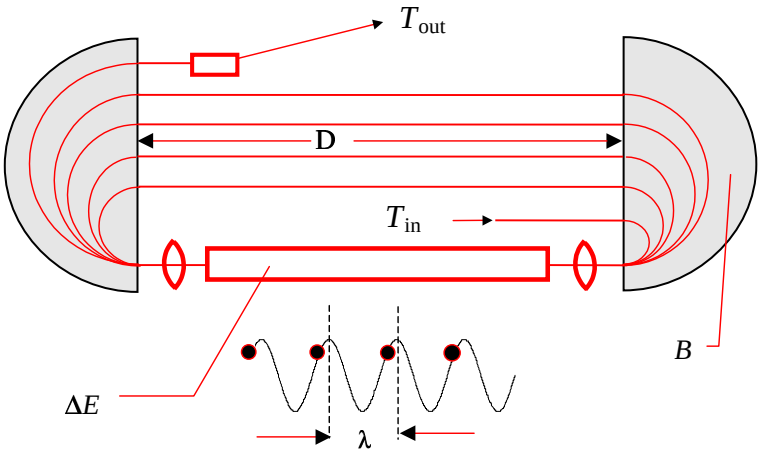

Fig. 7: Scheme of the racetrack microtron (RTM).

$$\Delta E = \frac{ec}{2\pi} B\, n\, \lambda \ , \tag{3}$$

where ΔE is the energy gain per turn; e and c are the electron charge and velocity of light, respectively; B is the flux density in the homogeneous 180° dipoles; and n is the path length increase per turn in units of the RF wavelength λ. In order to achieve maximum longitudinal stability, n must be equal to 1. In this case stable longitudinal motion is possible between the crest of the acceleration wave (0°) and −32.3°, with the exception of the region around −25.5°, where a strong 1/3 resonance would be excited by the non-linearity of the cosine wave. A synchronous phase angle $\varphi_s \approx -16°$ is a good compromise between the size of the acceptance area and the efficient use of the RF power. If the injection energy is not fully relativistic or if the magnet field distribution is significantly different from the ideal shape, the coherence condition is automatically met by an appropriate shift of φ_s from turn to turn if input phase and energy are correct.

As an example the phase oscillations in the third microtron (RTM3) of MAMI are shown in Fig. 8. At normal operation the central phase angle is −16°, which corresponds to $Q_1 \approx 0.23$. In this case the amplitude ΔE_b of the energy oscillations in the middle of the acceleration section is given by

$$\Delta E_b \approx \frac{\Delta\varphi_b}{2\pi} \Delta E \ , \tag{4}$$

where $\Delta\varphi_b$ is the amplitude of the phase oscillations. Intrinsic phase deviations and fluctuations by imperfections of the RF control system are in the order of 1° only.

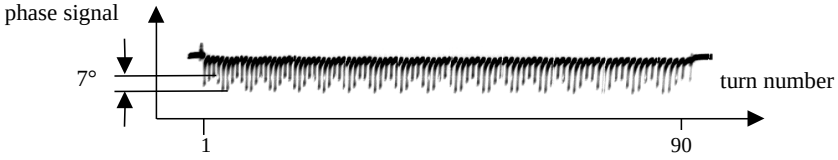

Fig. 8: Measured oscillation of the bunch phase in RTM3 of MAMI, deliberately excited by a 3° phase displacement of the acceleration section at a central phase angle of –11.8° (standard: −16°).

5.1.2 Transverse motion

Basic properties
As long as the bending radius R is large compared with the gap distance, the transformation by two homogeneous 180° dipoles separated by the distance D is equivalent to simple drift spaces equal to $2D$ and $2\pi\, R + 2D$ for the horizontal and vertical phase planes, respectively. In order to avoid unwanted couplings between the transverse and the longitudinal phase space the focusing lenses must not be placed on the return paths. Equal horizontal and vertical focusing on the common accelerator axis of the RTM, however, results in a relatively strong decay of the focal strength with the beam energy:

$$F^{-1} \approx F_{\mathrm{in}}^{-1} \left(\frac{E_{\mathrm{in}}}{E} \right)^2 \ . \tag{5}$$

Owing to this equation the energy in an RTM designed for simple operation should not be raised by more than a factor of about 10.

Under the realistic assumption that the horizontal tune is equal to 0.25 at the beginning of the acceleration, the energy-dependent horizontal beta function is roughly given by

$$\beta_{\mathrm{hor}} \approx \frac{D}{\sqrt{2}} \frac{E}{E_{\mathrm{in}}} \ . \tag{6}$$

Since the transverse emittance shrinks by adiabatic damping, the size of the eigen ellipse x_{ell} is practically constant during acceleration:

$$x_{\mathrm{ell}} = \sqrt{\epsilon\, \beta} = \sqrt{\epsilon_{\mathrm{in}} \frac{E_{\mathrm{in}}}{E} \frac{D}{\sqrt{2}} \frac{E}{E_{\mathrm{in}}}} = \sqrt{\epsilon_{\mathrm{in}} \frac{D}{\sqrt{2}}} \ . \tag{7}$$

In the vertical plane the behaviour is virtually the same. The larger effective drift space of the bending system leads to a somewhat faster increase in the beta function only. By way of demonstration the measured horizontal and vertical betatron oscillations excited by a beam displacement at the microtron input are shown in Fig. 9. While the tunes become smaller with increasing turn number the amplitudes of the oscillations stay nearly constant according to Eq. (7).

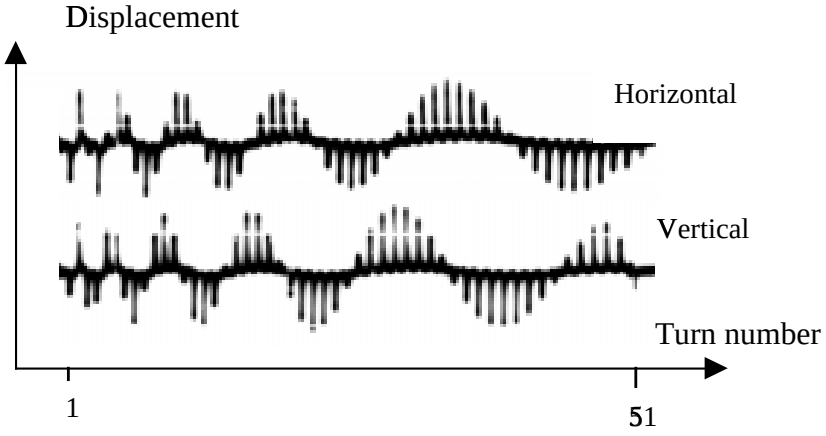

Fig. 9: Horizontal and vertical betatron oscillations in RTM2 of MAMI.

At low bending radii the defocusing effect of the fringe field has to be compensated for locally. Therefore, a reversed field stripe [30] has been installed along the front edge of each 180° bending magnet. At the RTM2 the reversed field pole had to be positioned as close as possible to the main field in order to compensate for the defocusing down to $R = 0.089$ m, which is the smallest bending radius in the MAMI RTMs.

The drop of focusing at high energies can be reduced by choosing a small field gradient decaying with respect to the z coordinate, pointing normal to the pole edge of the inner part of the bending magnets.

According to Ref. [31] this focusing acts only vertically and the inverse focal length is approximately given by

$$F_{\mathrm{cs}}^{-1} = 2\,\frac{\Delta B}{\Delta z}\,\frac{1}{B}\ . \tag{8}$$

Of course, the slope of the field is limited by the condition that the resulting bunch phase migration ends before the $Q = 1/3$ resonance at $-25.5°$. During the design phase of MAMI such a gradient had been calculated for RTM2 [32], but was not realized because in those days not enough practical experience existed with the longitudinal behaviour of CW RTMs. We now propose it for the second stage of the two-stage microtron injector for ELFE (see below).

Synchrotron-radiation effects
Because of the stochastical behaviour of the emission of synchrotron radiation in the bending magnets, the horizontal emittance increases significantly at higher energies. This effect is further exacerbated by the decay of the focusing force in the RTM. Therefore, the input energy of RTM3 has been chosen as high as possible by pushing the end energy of RTM2 to 180 MeV. In Fig. 16 the emittance measured by imaging the synchrotron radiation at the entrance of the right-side dipole of RTM3 (Figs. 6 and 13) is shown. This would be acceptable for the acceleration by the ELFE recirculator.

Ion trapping
At an intensity of about 500 μA the electrical potential of the beam in a tube of 20 mm diameter is large enough to trap ions produced from the residual gas. Since all recirculations add up at the accelerator axis, a maximum intensity of 90 times 100 μA can be reached in RTM3 of MAMI.

The presence of positive ions perturbs the balance between defocusing space–charge forces and the focusing effect of the magnetic field produced by the beam itself. As a consequence some additional transverse focusing is produced. In Fig. 10 the measured increase of transverse focusing is shown as a function of the beam current. From this a maximum increase of focal strength of 3% at 100 μA can be extrapolated. Although the effect fluctuates and depends strongly on the position of the different beams at the accelerator axis, the experience has shown that the long-term operation of MAMI at high currents (more than 80 μA until now) needs no countermeasures. In Table 5 the measured beam parameters of MAMI B are summarized.

Beam halo
In combination with diaphragms of different beam-hole radii r, radiation detectors were used to measure the beam halo. The results given in Fig. 11 show that, at an intensity around 10^{-5}, the Gaussian beam profile is replaced by a much more slowly decaying curve. This distribution can be explained by small angle scattering from the residual gas atoms, leading to a $1/r^2$ dependence.

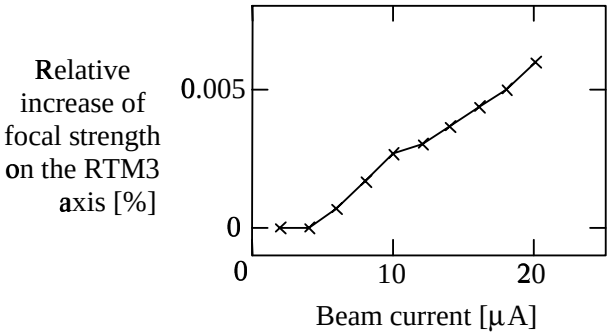

Fig. 10: Measured relative increase of horizontal focusing as a function of transmitted beam current in RTM3. The threshold corresponds to a beam potential of about 0.035 eV.

Table 5: Measured beam parameters of MAMI B.

Transverse beam properties	
Emittance hor./vert. @ 855 MeV (1σ)	$8 \times 10^{-9}/0.5 \times 10^{-9}$ π·m
Relative intensity in the halo	$10^{-4} - 10^{-5}$
Energy	
Standard range	180–882 MeV in steps of 15
Absolute definition	$\pm$ 160 keV
Intrinsic spread (1σ)	13 keV
Long-term stability (1 h, 1σ)	3 keV
Short-term stability (1 min, 1σ)	1 keV
Resolution of measurement	1 keV
Current	
Max. (thermionic gun @ 855 MeV)	107 μA
Max. (polarized gun @ 80% pol.)	20 μA
Resolution of absolute measurement	30 nA @ 855 MeV
Long-term stability	10^{-3}
Ripple unpolarized/polarized	$2 \times 10^{-3}/10^{-2}$
Spin	
Polarization	80%
Hor. spin rotation/RTM3-energy change @ 855 MeV	4.4°/100 keV

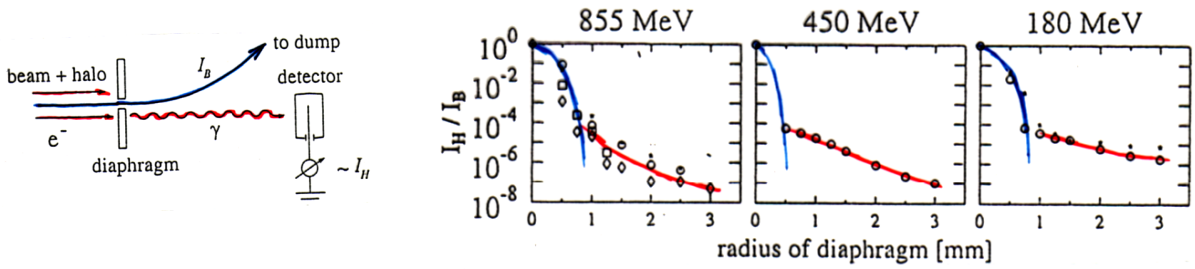

Fig. 11: Scheme and results of the halo measurement.

5.2 Subsystems and main components

5.2.1 Magnets

The flux density B of the reversing magnets of an RTM depends on the energy gain by Eq. (3). At low fields, where the cross-section of the yoke is significantly smaller than the pole area, the magnet can be constructed in a C-configuration for simplicity. At higher fields (above 1.3 T) a combination of a C- and an H-configuration must be chosen in order to minimize the total weight. At MAMI the maximum flux density has been limited to 1.3 T in order to avoid the risk of too large field deviations owing to saturation effects. Modern three-dimensional codes like TOSCA would perhaps make it possible to design an RTM magnet with higher flux density. This report, however, is based on the conservative value for the flux density.

In order to avoid non-linearities of the transverse motion and to achieve the correct longitudinal behaviour of the beam, the magnet field has to be homogenized to 10^{-4} by surface coils. In addition, small correction magnets are needed on both ends of each return path to centre each beam exactly at the accelerator axis (see Fig. 13).

Owing to the relatively weak transverse focusing, the beam position at the RTM output is very sensitive to small changes of the magnet positions. Therefore, the floor has to be stable against temperature changes and the supports must be very stiff to avoid movements of the magnets excited by building vibrations.

5.2.2 Accelerator structure and RF system

The accelerator sections are designed as resonators consisting of biperiodic $\pi/2$ structures [33]. A cross-section of the first accelerator section of the injector linac is shown in Fig. 12 The coupling between the accelerating and coupling cavities is achieved by pairs of slots in the cavity walls. A coupling factor of 4% to 5% between two accelerator cells serves for a stable and sufficiently flat distribution of the RF power. The structure is cooled by axial holes in the outer wall. This is far enough away to remove the dissipated power of typically 12 kW/m (corresponding to an energy gain of 0.86 MeV/m) without significant distortions to the cavities. The global thermal shift of the resonance frequency is stabilized by means of tuning plungers.

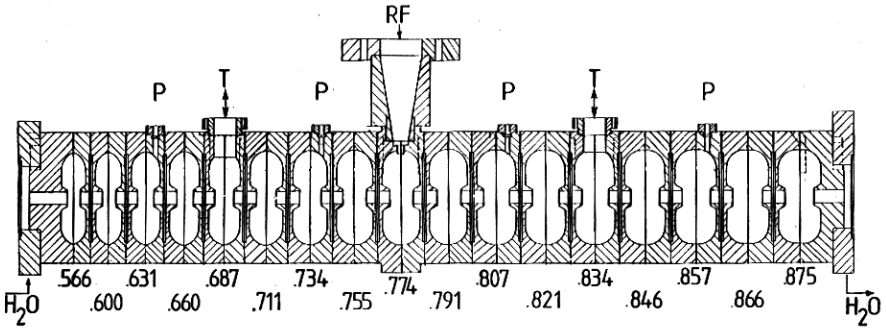

Fig. 12: Cross-section of the first accelerator section of the injector linac of MAMI (graded beta-section). RF is the RF input, P the probe channel, and T the hole for tuning the piston. The numbers give the phase velocity of the corresponding cavity in units of the velocity of light.

The RF amplitude in the sections is controlled to less than 10^{-3} by a feedback loop to the klystron input. In order to get enough loop gain, the working point of the klystron is displaced from the saturation (efficiency there 60%) to the steep region in the output power versus input power curve. At the same time the RF phase is stabilized to a few tenths of a degree by a second loop from the klystron output to a fast phase shifter at the input. The high bandwidth of these

loops enables a fast (10 μs) switch-on of the full beam current without considerable losses in the whole RTM cascade.

5.2.3 Monitor system

An efficient beam-monitor configuration for an RTM is schematically shown in Fig. 13. It consists of position, phase and intensity cavities at the accelerator axis, and of synchrotron monitors for imaging the beam profile from turn to turn. In RTM1, where synchrotron radiation is not yet visible, a movable fluorescent screen is used for this purpose. The installation of a highly sensitive d.c. transformer at the microtron axis proved to be very useful for the measurement of the absolute beam current. The sensitivity of this monitor makes use of the fact that the beam intensity is enhanced by the number of turns at the axis and that the losses are below 10^{-4}. By measuring the AC component of the magnetic field produced by the CW beam, the current ripple can be detected with a resolution of about 20 mV/μA in the RTM3 of MAMI.

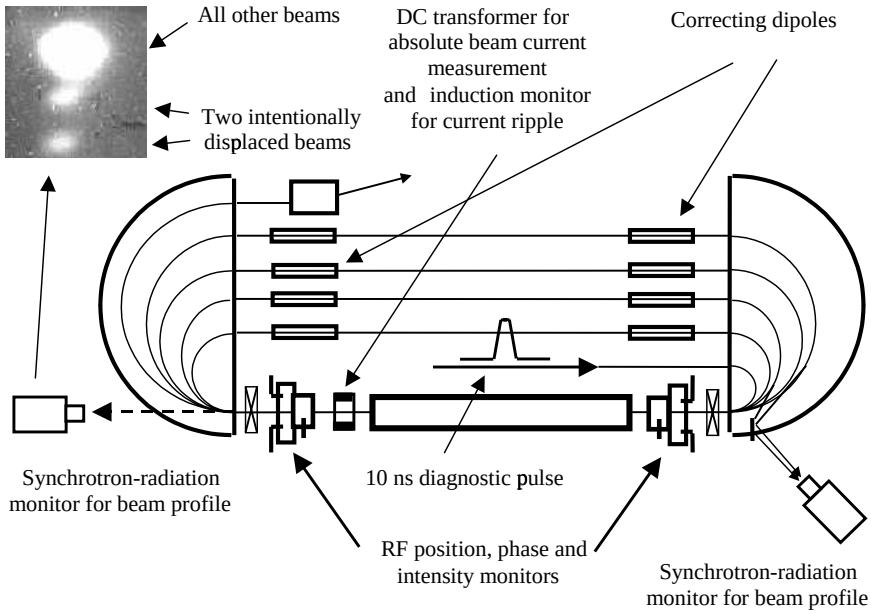

Fig. 13: Scheme of the RTM beam-monitor system.

In order to determine the coordinates of the recirculating beams on the accelerator axis separately, short beam pulses are injected into the RTM during set-up and retuning. The oscillogram of a position-monitor signal (see Fig. 9) shows that the different turns can easily be distinguished by their arrival time. By operator request all these data are evaluated by the control system and the beam positions are automatically corrected by means of the correcting dipoles on the return paths.

As the magnet fields are homogenized to 10^{-4} and measured by NMR probes, the absolute beam energy can be determined with the same precision by reconstructing the bending radii precisely by means of position monitors at the accelerator axis and at the higher return straights. In addition, a time-of-flight measurement by means of two 9.8 GHz cavities in front of and behind the last 180° deflection can be used to measure energy fluctuations with a resolution of 10^{-6} [34].

In the transport systems between the different stages the beam can be observed and controlled by a dense system of wire scanners, RF monitors, view screens and synchrotron-radiation monitors [35]. The whole accelerator complex is protected against damage from beam losses by

means of ionization chambers distributed around the RTMs and along the beam transport lines. Because of the high dynamic range of four orders of magnitude, the system is also routinely used for a more global but very sensitive control of the beam quality.

5.3 A two-stage RTM cascade for ELFE

The proposed arrangement consists essentially of the following sections: the pulsed sources for polarized and unpolarized electrons; the chopper–buncher system for 50% d.c. beam transmission; the 10 MeV linear accelerator and two cascaded RTMs (R1 and R2) for 120 MeV and 800 MeV, respectively. By increasing the end energy of the injector linac by a factor of three compared with MAMI and by lowering the injection energy for the last stage, the number of microtrons could be reduced from three to two. However, one more klystron is needed in this configuration. On the other hand, the longitudinal acceptance is increased by about a factor of four because of the higher energy gain of the first stage. This makes it easier to operate the machine with a high capture efficiency. A scaled scheme of the accelerator is shown in Fig. 14, and its main parameters are given in Table 6. Because of their importance and complexity, the polarized electron source, the systems for beam diagnostics and polarization measurement, and the matching to the injector linac are described separately.

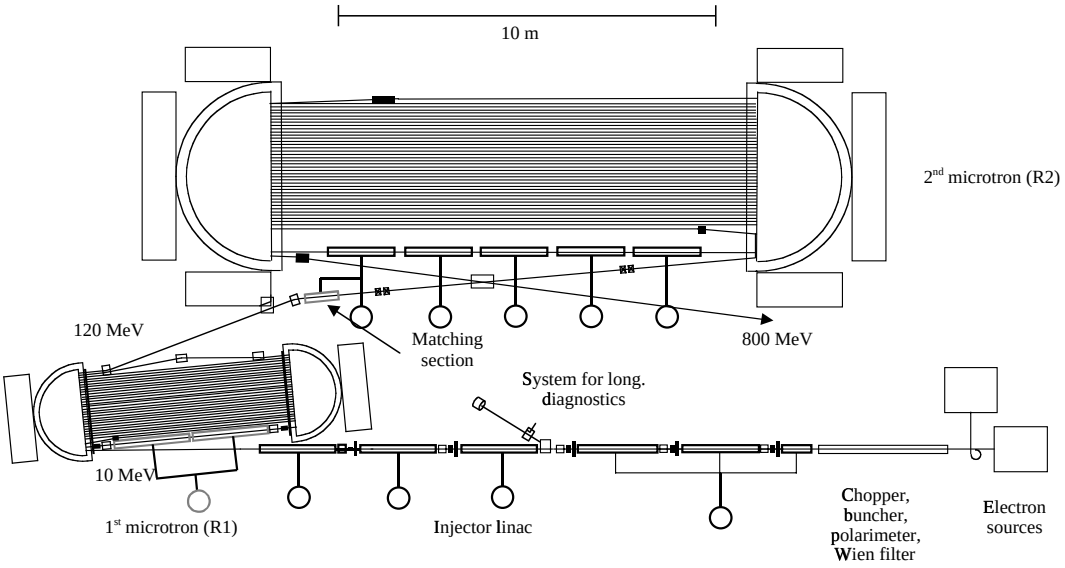

Fig. 14: Scaled scheme of the microtron injector for ELFE.

5.3.1 Injector linac

In its first and most complicated part the injector linac is a copy of the 3.5 MeV preaccelerator of MAMI. The three sections behind are standard accelerator structures with a phase velocity equal to the velocity of light. At 3.5 MeV a device for the measurement of the longitudinal phase space is installed. This system, which can also be copied from MAMI, is necessary to optimize the RF parameters in respect of maximum capture efficiency and correct matching to the acceptance of the first microtron (R1). Figure 15 shows the measured phase space at 3.5 MeV obtained with harmonic bunching of 50% of the d.c. current from the 100 kV thermionic gun. This phase space is transformed to 10 MeV and compared with the eigen ellipse of R1, which represents only a fraction of the R1 acceptance.

Table 6: Main parameters of the 800 MeV microtron injector.

		Injector linac	R1	R2 (+matching)
General				
Kinetic input/maximum energy	[MeV]	0.1 / 10	10 / 120.4	120.4 / 800
Number of turns		–	48	90
Total power requirement	[kW]	362	115	650
RF system				
Energy gain/turn	[MeV]	10	2.3	$7.55 + 0.65$
Synchronous phase angle	[deg.]		–16	–16
Frequency	[GHz]	2.464	2.464	2.464
Linac length (electrical)	[m]	10.93	3.53	$8.82 + 0.913$
Number of sections/klystrons		6 / 4	2 / 1	$5 + 1$ / 5
Diss. RF power/beam power	[kW]	138.2/0.50	23.3 / 5.5	$104.4 + 6.9$ 34
Power requirement	[kW]	360	90	450
Magnet system				
Field strength in the air gap	[T]	–	0.394	1.30
Gap distance	[cm]	–	7	10
Min./max. beam radius	[m]	–	0.089 / 1.024	0.309 / 2.052
Spacing between return paths	[cm]		3.873	3.873
Fe/Cu weight of the magnets	[t]	–	57 / 1	710 / 8.2
Number of correcting dipoles		54	192	360
Number of quads & solenoids		26	4	4
Power requirement	[kW]	2	25	200
*Beam parameters**				
Emittance hor./vert. (1σ, norm.)	[$\pi \cdot \mu$m]	0.2 / 0.2	1.5 / 0.37	6.3 / 0.78
Longitudinal emittance (1σ)	[keV$\cdot$ deg.]	18	26	32

*) For short bunches (10% of d.c. current from the 100 keV gun)

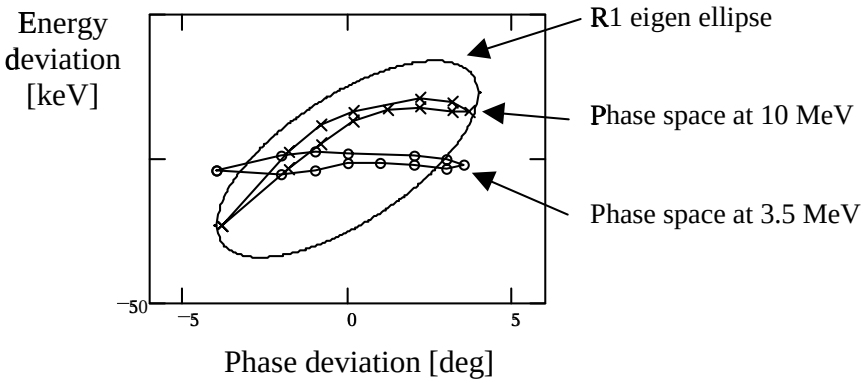

Fig. 15: Measured longitudinal phase space for 50% transmission of a d.c. beam in comparison with the eigen ellipse at R1 entrance.

5.3.2 First microtron (R1)

As a consequence of the relatively large energy gain in R1, the focusing in the higher turns is rather weak. As the experience with MAMI has shown, the beam quality can be maintained if the bending magnets are homogenized by surface coils and if their position is stable and not influenced by building vibrations and temperature changes.

5.3.3 Transfer and matching to R2

At the last turn of R1, the beam path is lengthened by a flat chicane in order to obtain a phase displacement from $-16°$ to $-25°$ in the accelerator section. In combination with the longitudinal dispersion of the magnet system between R1 and R2 and a slight longitudinal focusing by a short accelerator section this serves for longitudinal matching to R2. The short section is also used to tune the input energy of R2. Transverse matching can be done by appropriate bending radii of the transfer magnets and quadrupoles on the long dispersion-free line to R2.

5.3.4 Second microtron (R2)

In order to counteract emittance growth due to synchrotron-radiation effects, the horizontal focusing has to be as strong as possible. By introducing a small 'clamshell-like' field gradient of 3%/m in the 180° magnets the beam gets additional vertical focusing. This allows the vertical focusing strength of the quadrupoles at the accelerator axis to be reduced, leading automatically to higher horizontal focusing. As a consequence of the field decay, a shift of the central phase from $-11°$ to $-25°$ occurs during the acceleration process. Numerical simulations showed that the emittance achieved in this configuration is still smaller than that of the RTM3 of MAMI with its higher injection energy (see Fig. 16).

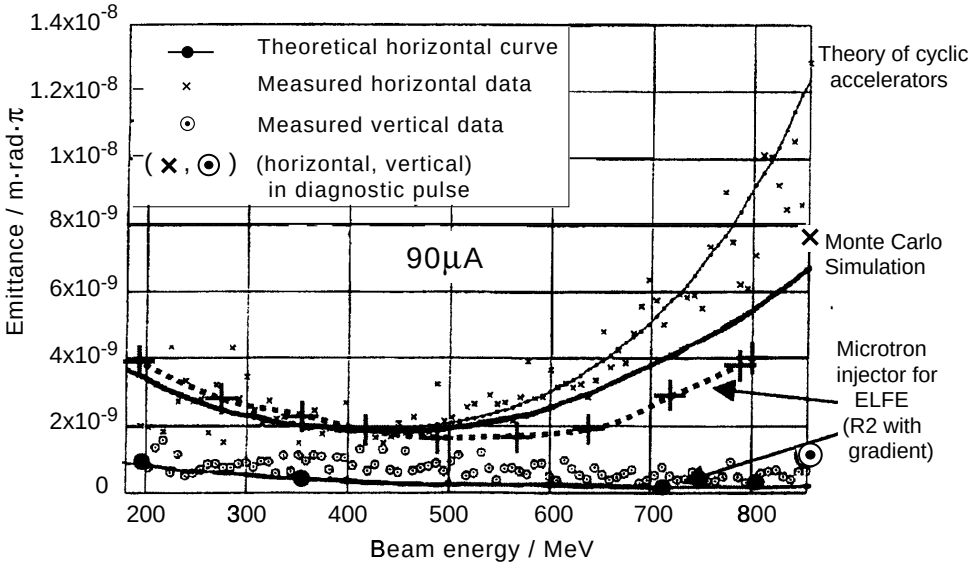

Fig. 16: Calculated and measured transverse emittances in RTM3 and simulated emittances in R2.

5.3.5 Spin dynamics

Owing to the anomalous magnetic moment of the electron, the spin of relativistic electrons rotates faster than the momentum. This makes it possible to tune the horizontal spin direction by means of the R2 end energy. An energy change of 2.7% at 800 MeV produces a spin rotation of 90°. In combination with a 180° spin flip at the source this is sufficient to reach all horizontal spin orientations. The R2 end energy can easily be tuned within this small range by changing all fields as well as the input energy accordingly. By increasing its maximum amplitude to 0.65 MeV, the accelerator section between R1 and R2 can be used for both the longitudinal matching and the variation of the R2 input energy.

6 Superconducting injector

The production of an 800 MeV CW beam is well suited to a superconducting (SC) linac using modern technology, associated with a small number of recirculations to reduce the costs of construction and operation. The technology developed for the TESLA Test Facility (TTF) at DESY can be used with minor changes for this purpose by designing a linac working at 1.408 GHz (i.e. the fourth harmonic of the LEP cavities) which is not far from the RF frequency of the TTF linac (1.3 GHz).

The machine would be composed of a 12 MeV SC preinjector, a 115 MeV linac and three passes in a 230 MeV linac, giving a final energy in excess of the design value of 800 MeV (817 MeV in this example). This is obtained by assuming an accelerating gradient of about 15 MeV/m, well below the average value obtained at TTF on a large number of cavities fabricated by European companies [36].

6.1 The SC linac

The linac is composed of cryomodules, each containing eight accelerating cavities. A complete description of the system can be found in Ref. [37]. The existing design for cryostats, helium tanks, tuners and couplers can be used with only minor changes. The difference in frequency makes the cavities shorter, which would be compensated for by using longer beam tubes between cavities.

6.1.1 Cavities and cryomodules

The design of the cavities for TTF led to an optimized geometry in terms of surface fields, higher-order mode (HOM) damping and coupling. A scaling of this design for the ELFE injector does not change these properties, and the fabrication techniques would not be very different, the frequencies being quite close.

Eight nine-cell cavities are installed in a cryomodule, giving a total accelerating length of 7.66 m. The length of the cryomodule is 12.2 m, including SC quadrupoles and a beam position monitor. Keeping exactly the TTF design for the cryostat leads to a lower filling factor, which is not important for this injector. The energy gain per module is 115 MeV with a gradient of 15 MeV/m. The linac is composed of three modules, two of them being in the recirculator. Table 7 shows the main characteristics of the cavities.

Table 7: Main RF characteristics of the cavity.

Parameter	Value
Fundamental π mode frequency	1408.8 MHz
Number of cells	9
Accelerating gradient	15 MeV/m
Q_0	10^{10}
Coupling cell to cell	1.87%
$E_{\mathrm{peak}}/E_{\mathrm{acc}}$	2
$H_{\mathrm{peak}}/E_{\mathrm{acc}}$	42 Oe/MV/m
(R/Q) per cavity	1035 Ω
Effective length	0.958 m
Total length	1.385 m
Aperture diameter	64.6 mm

The only modifications to make to the TTF cryomodule would be the length of the individual helium tanks and of the beam tubes between cavities. The tuning system, the input coupler and HOM couplers do not need any change.

6.1.2 The RF system

For the design current of 100 μA, the beam power per cavity is 1.44 kW in the 115 MeV linac and 4.31 kW in the recirculator. However the RF power needed per cavity must be higher because a perfect matching for this low current would lead to unreasonable coupling ($Q_{\rm ex} = 1.4 \times 10^8$ for the linac and three times less for the recirculator). A value of $Q_{\rm ex} = 1 \times 10^7$, i.e. a bandwidth of 140 Hz, seems possible; CEBAF is even proposing to use $Q_{\rm ex} = 2 \times 10^7$ for the energy upgrade [38]. The RF power needed per cavity in both cases is given in Table 8 together with the beam power (in kW).

Table 8: RF power per cavity (kW).

	P beam	$Q_{\rm ex} = 10^7$	$Q_{\rm ex} = 2 \times 10^7$
115 MeV linac	1.44	5.7	3.3
Recirculator	4.31	7.4	5.1

Two solutions can be used for the RF system: one klystron per cavity or one klystron per module. In the first scenario a klystron delivering 8 to 10 kW has to be developed. It would not be too different from the CEBAF klystrons which give 6 kW at 1.5 GHz. One HV power supply per module (8 klystrons) would be a good economic compromise. In the second scenario a more powerful klystron has to be developed (60 to 80 kW).

In both cases, an energy stability of a few 10^{-4} can be obtained using an RF feedback system for phase and amplitude of the accelerating field as demonstrated by the experience gained at TTF and CEBAF.

6.1.3 Cryogenic load

It is assumed that the cavities are running at a field level of 15 MeV/m (14.37 MeV energy gain) with a Q_0 of 10^{10} at a temperature of 2 K. In these conditions the power dissipation at 2 K is 20 W per cavity. The RF load from the lower part of the input coupler represents a negligible fraction of this amount (less than 1%). The total RF load at 2 K is then 500 W (three modules plus the preinjector, i.e. 25 cavities). The static load at 2 K, measured on the first cryomodule of TTF, is 6 W [39]. The total static load would then be of the order of 30 W for three modules and the capture cavity cryostat.

At 4.5 K, the RF load comes mainly from the input couplers. It would be of the order of 0.5 W per cavity. The static load per module is 23 W. The total load at 4.5 K would then be of the order of 100 W.

At 70 K, the RF load from the couplers would be less than 10 W per cavity. The static load is 90 W per module. The total load at 70 K would then be of the order of 500 W.

6.2 The Preinjector

The preinjector will deliver a 12 MeV, 100 μA beam of polarized and unpolarized electrons in the form of a 352 MHz, 0.28 pC bunch train. The capture and the acceleration of the electrons is performed by a nine-cell, $\beta = 1$, 1408 MHz SC cavity identical to those used in the SC linac. It is housed in a separate cryostat and powered by a separate klystron. This proposal closely follows

the scheme of the TTF low-charge per bunch injector that has been built and commissioned quite satisfactorily by a Saclay–Orsay group [40], at the RF frequency of 1300 MHz.

6.2.1 Proposed scheme

To be captured by a $\beta = 1$ cavity, electrons need to have a higher initial energy than is required with a lower or graded β cavity. This somewhat complicates the electron source but avoids the design and fabrication of a special cavity. For an accelerating gradient of 15 MV/m simulations show that 250 keV electrons are efficiently captured, bunched and accelerated. The bunch formation of the unpolarized electrons is made by modulating the gun current with a 352 MHz signal applied to the cathode-grid space rather than by using an RF chopper in the beam line. For polarized electrons, a photocathode will be illuminated by an RF synchronized laser. In both cases, bunches are then compressed by velocity modulation along a 2.5 m drift with a 352 MHz subharmonic buncher (SHB) cavity. The transverse focusing is ensured along that drift space by two solenoidal short magnetic lenses. After the capture cavity, triplets are used.

6.2.2 Beam dynamics

The TTF injector had been extensively simulated using several computer codes, in particular PARMELA. The first requirement for using such codes is to have a calculated map of the capture cavity gradients in the axis region. Here, we just have scaled by a factor of 1300/1408 the length of the field map on the axis of the TTF nine-cell cavity by keeping the same coefficients for the Fourier series that was used. Besides, due to the very low charge per bunch, space charge is not expected to play a role and a single particle tracking can be used (Fig. 17). By starting with a bunch extension of 60° (of the SHB wave), i.e. a 470 ps bunch length, and applying a 32 kV peak field across the SHB gap, we obtain at the capture cavity output the bunch parameters summarized in Table 9:

The beam envelope has also been plotted (Fig. 18) assuming an emittance of 2 mm mrad. One can see the strong focusing effect of the capture cavity.

6.2.3 Electron source

As in the TTF injector, the electron source is a 250 kV thermionic electron gun. A 0.5 cm^2, Y845 Eimac dispenser cathode, for example, can deliver a few mA. Such a cathode is mounted with a densely meshed control grid placed very close (about 100 μm). A d.c. bias voltage is applied to cut off the gun current. To that voltage is superposed a 352 MHz signal adjusted in such a way that the emission takes place only for 30° of phase each side of the maximum. That corresponds to 240° of phase extension for the 1408 MHz (or 470 ps). Several laboratories have used such a method [40, 41, 42].

Table 9: Beam parameters at the capture cavity exit.

Energy	12.6 MeV
Bunch length (r.m.s.)	0.5 mm (0.3° of 1408 MHz wave)
Energy spread (r.m.s.)	123 keV

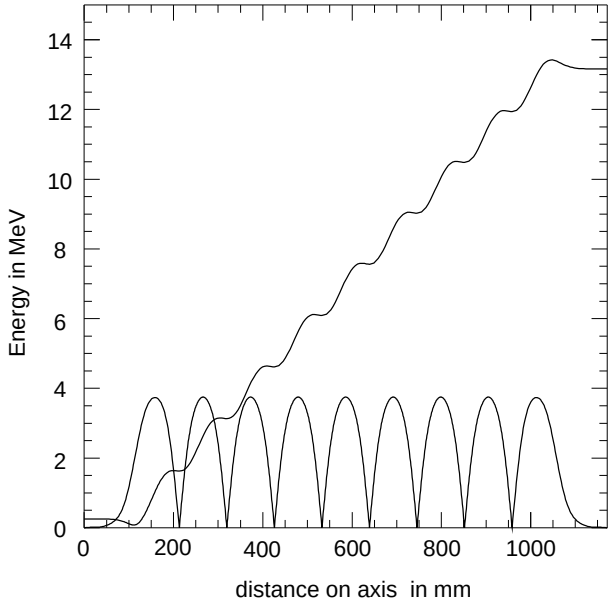

Fig. 17: Energy gain of a 250 keV injected electron into a 1408 MHz nine-cell SC cavity. Superposed is the plot of the maximum accelerating field along the axis (in a.u.).

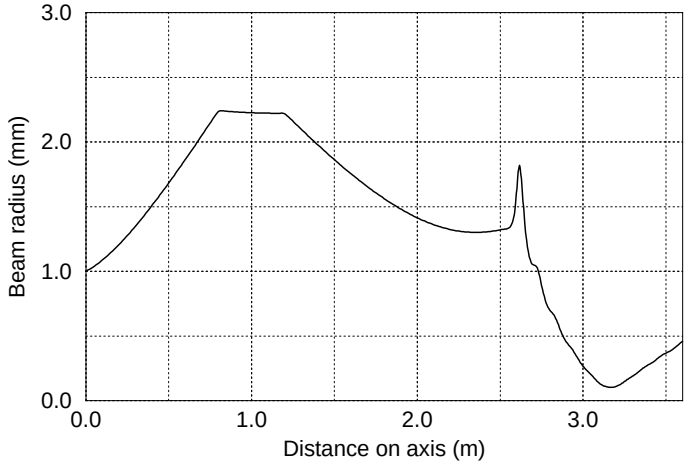

Fig. 18: Beam envelope through the prebunching drift space and the capture cavity. Two magnetic lenses are used in the drift space. The capture cavity has a strong focusing effect.

6.2.4 Polarized source

The description of the polarized source and the considerations that are given in this report by MAMI experts in their proposal (see also Refs. [43] and [44]) can also apply here. If the laser pulse is shorter than 470 ps, there will not be losses in the capture cavity, i.e. a 100% transmission between the cathode and the linac.

It may be, however, that building such a source at 250 kV causes difficulties. In that case, a 100 kV source could be used, followed by a short 1408 MHz normal-conducting accelerating structure, increasing electrons energy to at least 250 keV. This will neither cause transmission problems nor reduce the photocathode lifetime.

6.2.5 Subharmonic buncher cavity

The subharmonic buncher is a TM010 cavity with a reduced gap to increase the shunt impedance. In the TTF 216 MHz model, it was made of stainless steel, copper plated inside. The shunt impedance was 2.7 MΩ. At 352 MHz, one would get

$$R_s = 3.4\,\mathrm{M}\Omega$$

and could produce a 32 kV peak field with

$$P = \frac{E^2}{R_s} = 300\,\mathrm{W}\ .$$

As this is a CW power, better cooling is required and a bulk copper design is justified.

6.3 Recirculation scheme

We envisage an independent orbit recirculating accelerator as an injector [45]. A schematic view is shown in Fig. 19.

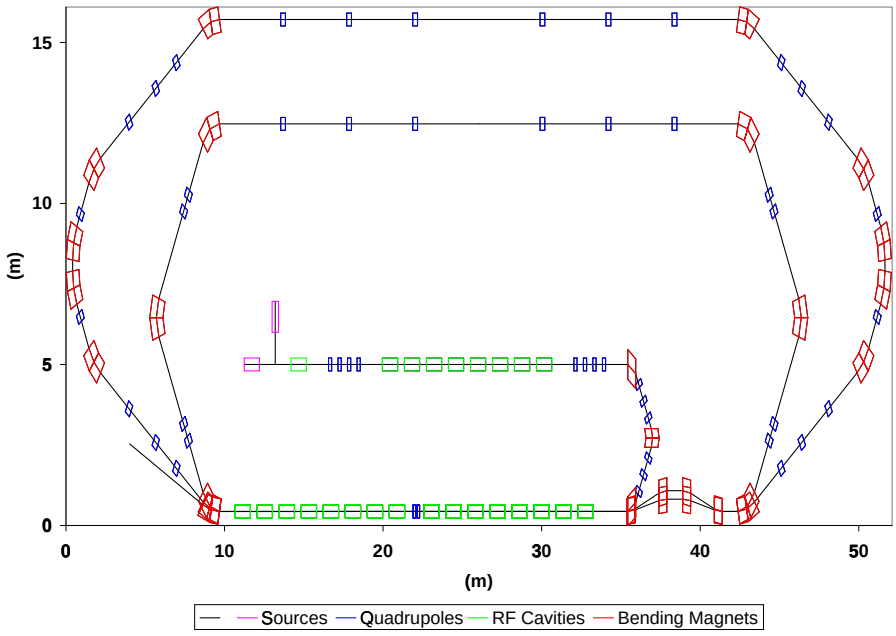

Fig. 19: SC injector layout.

After a first 115 MeV linear accelerator the beam energy increases from 12 MeV to 127 MeV. The final energy, 817 MeV, is obtained with three passes through a 230 MeV main superconducting linear accelerator. The 127 MeV beam is deflected to the main linac through the last dipole of an achromatic chicane which is introduced at the entry of the main linac. At the extremities of the main linac are horizontal bending magnets to merge the beams of different energies (357 MeV, 587 MeV) before going through the linac, and to direct them to their respective transport beam lines or to the ELFE injection beam line.

6.3.1 127 MeV beam line

The beam is injected at 127 MeV via a 180° deviation which is isochronous ($R_{56} = 0$) and achromatic (D_x and its derivative D'_x vanish at the end of the deviation). Three 60° bending magnets and six quadrupoles, to be organized in three families, are used (they are listed in

Table 10). The focusing by quadrupoles is designed such that the isochronous and achromatic conditions are obtained and such that the phase advance, in the horizontal and vertical planes, is equal to 2π. Four additional quadrupoles are needed to obtain the matching of the optical functions β and α at the entrance of the deviation. With the matched initial values, the optical functions β do not exceed 80 m along the transfer line (Fig. 20).

Table 10: 127 MeV transfer line elements [$(B\rho) = 0.425417$ T m].

Bending magnets						
Family	Number	Angle (rad)	Length (m)	Field (T)	Radius (m)	Edge angle (rad)
P0DIP	3	$\pi/3$	0.5	0.73684	0.57735	0
Quadrupoles						
Family		Number	Normalized strength (m^{-2})			Length (m)
P0QP1		2	15.687			0.2
P0QP2		2	−6.871			0.2
P0QP3		2	6.678			0.2

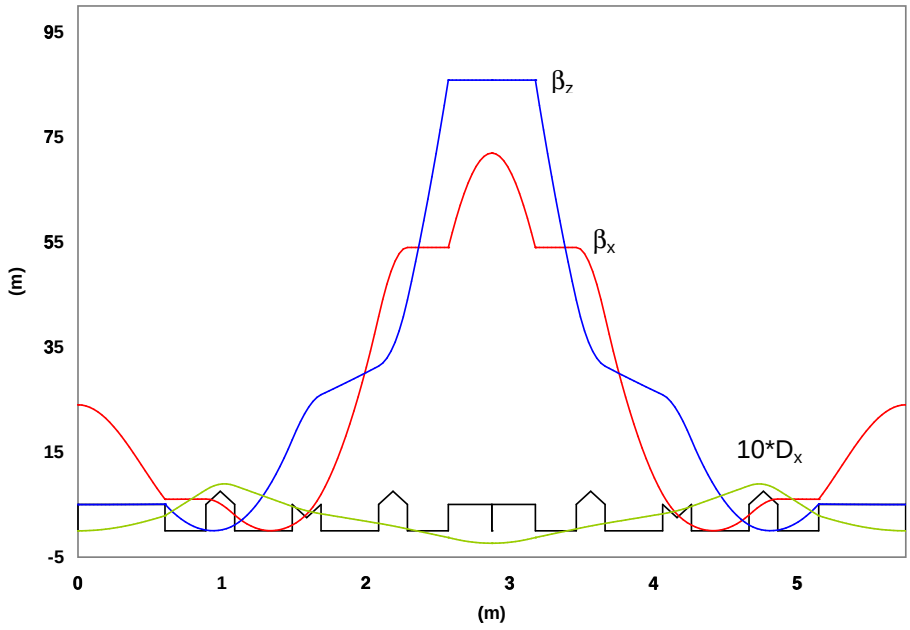

Fig. 20: 127 MeV beam line optical functions β_x, β_z, and D_x.

6.3.2 Recirculation beam lines

The two orbits are each designed with two achromatic 180° deviations, a return line with two quadrupole triplets and a pass through the common achromatic chicane.

For each orbit, the path length is a multiple of the RF wavelength ($\lambda = 0.212919$ m). The chicanes for the fine adjustments of the path lengths are included in the return lines, in the 7.72 m long straight sections located between the triplets.

The quadrupole-triplet focusing of the return lines is arranged to obtain a negative unitary transfer matrix in both transverse planes.

The anisochronism in the arcs compensates for the contribution of the passage through the chicane.

For each orbit, the focusing of the arcs quadrupoles ensures the isochronous condition at the end of the chicane.

The modifications induced by the chicane on the beam optics, for both passes, are not taken into account in this report.

357 MeV beam line

Each 180° deviation is achieved with three bending magnets.

For each arc the focusing of the two families of two quadrupoles is arranged such that the phase advances, in the horizontal and vertical planes, are respectively equal to 2π and 1.5π, in addition to the achromatic and isochronous conditions. The elements are listed in Table 11.

With these conditions, the optical function β, in the two planes, never exceeds 80 m along the transfer line for initial β values ranging from 5 m up to 20 m (Fig. 21). The path length is equal to 72.8183 m ($\approx 342\,\lambda$).

Table 11: 357 MeV transfer line elements [$(B\rho) = 1.192529$ T m].

Bending magnets						
Family	Number	Angle (rad)	Length (m)	Field (T)	Radius (m)	Edge angle (rad)
P1DIP	6	$\pi/3$	1.0327	1.0	1.192529	0.26
Quadrupoles						
Family	Number	Normalized strength (m^{-2})				Length (m)
P1QP1	4	2.98381				0.3
P1QP2	4	−0.910936				0.3
RP1QP1	2	0.797113				0.3
RP1QP2	4	−0.459542				0.3

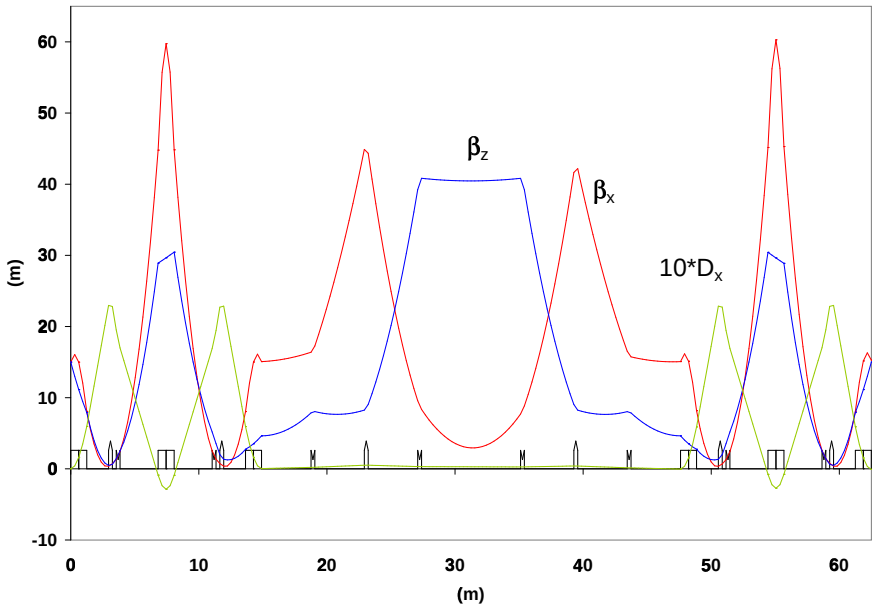

Fig. 21: 357 MeV beam line optical functions β_x, β_z, and D_x, for initial values of $\beta = 15$ m, and $\alpha = 0$.

587 MeV beam line

The 180° deviation is achieved with six bending magnets. To limit the transverse extension of the injector, four dipoles are grouped in the middle of the arc.

Four families of two quadrupoles are used to adjust the phase advances in the horizontal plane to 2.5π and in the vertical plane to 0.5π, in addition to the achromatic and isochronous conditions. The list of elements is given in Table 12. The optical function β, in the two planes, never exceeds 100 m for initial β values ranging from 10 m up to 100 m (Fig. 22). The path length is equal to 93.2585 m ($\approx 438\,\lambda$).

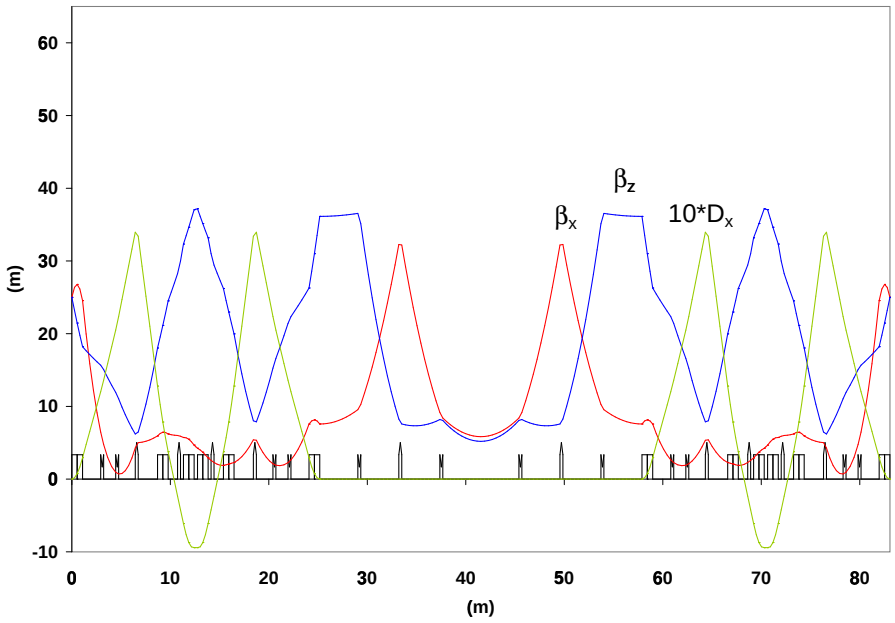

Fig. 22: 587 MeV beam line optical functions β_x, β_z, and D_x, for initial values of $\beta = 25$ m and $\alpha = 0$.

Table 12: 587 MeV transfer line elements [$(B\rho) = 1.959728$ T m].

Bending magnets						
Family	Number	Angle (rad)	Length (m)	Field (T)	Radius (m)	Edge angle (rad)
P1DIP	2	0.555056	1.0327	1.0	1.959728	0.26
P2DIP	6	0.507869	0.95305	1.0	1.959728	0.12
Quadrupoles						
Family	Number	Normalized strength (m^{-2})				Length (m)
P2QP1	4	1.69797				0.3
P2QP2	4	−0.179271				0.3
P2QP3	4	0.18842				0.3
P2QP4	4	−0.195656				0.3
RP2QP1	2	0.797113				0.3
RP2QP2	4	−0.459542				0.3

6.3.3 Emittance and energy spread

A particle beam of energy $E = \gamma\, m_e c^2$ which passes a bending magnet of length L and radius ρ gains an additional r.m.s. energy spread of:

$$\sigma_e = \sqrt{\frac{110\sqrt{3}e^2\hbar c}{24^2\pi\varepsilon_0}}\sqrt{\frac{\gamma^7 L}{\rho^3}} \approx 1.94\times10^{-14}\,\mathrm{MeV\,m}\sqrt{\frac{\gamma^7 L}{\rho^3}}\ .$$

The transverse emittance also increases when the dispersion is non-zero:

$$\Delta(\gamma\varepsilon) \approx 4.04\times10^{-8}\,\frac{\mathrm{m}^2}{\mathrm{GeV}^6}\,E^6\frac{L}{\rho^3}H\ ,$$

where

$$H = \frac{1}{L}\int_0^L \frac{1}{\beta(s)}\left(D(s)^2 + \{\beta(s)D'(s) + \alpha(s)D(s)\}^2\right)\,ds\ .$$

At 800 MeV, the transverse emittance blow-up and the energy spread due to the SC injector arcs and chicane are then:

$$\Delta\varepsilon < 10^{-11}\,\mathrm{m\,rad}$$
$$\frac{\sigma_e}{E} < 2\times10^{-6}\ .$$

These values show that the synchrotron radiation effects are negligible in the SC injector bending magnets.

7 Main ring

We envisage that ELFE will be in the shape of a racetrack. A schematic view is shown in Fig. 1. One of the long straight sections contains the accelerating RF system. Injection at 800 MeV occurs at the upstream end, and ejection at the downstream end of this long straight section. The energy gain in a pass is 3.5 GeV. Six arcs at either end join the two straight sections. The beam passes through the arcs at energies of 4.3, 7.8, 11.3, 14.8, 18.3 and 21.8 GeV. Adjacent to the straight sections there are spreaders and combiners to feed the beams of different energies into their respective arcs and to merge them before going through the linac again. There are six beam channels in the long straight section opposite the RF system. The beam lines of the arcs and the return lines are stacked vertically (Fig. 1).

Our work is based on this reference layout. In a future design study, the choice between this layout and the alternatives listed below will also be based on a comparison of their costs:

a. The linac could be split into two halves, and they could be put into the two opposite straight sections. This would shorten the total tunnel length, but would need twice the number of spreaders and combiners, approximately double the vertical emittance, and make an energy upgrade at a later time more difficult. One arc and one spreader and combiner set would need a seventh channel at higher energy which would increase energy spread and emittance further. A first cost estimate is given in Chapter 24.3.
b. The spreaders, arcs and combiners could be arranged side-by-side instead of the vertical arrangement proposed here.

Table 1 shows the overall ELFE parameters in our design. In this chapter, we discuss how the specified values of emittance at top energy and the relative r.m.s. momentum spread are achieved by our choice of beam-optical parameters.

7.1 Optical modules

ELFE consists optically of five modules: the linac, the spreader, the arc, the return beam lines and the combiner modules, which are discussed below. The chicane for injecting the beam is included in the combiner module. The extraction of the highest energy beam is included in the spreader module. Extraction at lower energies is not foreseen. The chicanes for fine adjustments of the path lengths are included in the return lines.

The parameters of the components in this section are internally consistent. The total length of the tunnel is about 200 m shorter than that assumed elsewhere, in particular in Chapter 19 (on civil engineering). We shall leave the necessary adaptations to a future detailed design study.

7.1.1 Linac

Table 13 shows the parameters of the linac module which houses 72 superconducting RF cavity modules. Figure 23 shows the layout of two neighbouring half-cells. A half-cell contains the RF module, a sector valve, a pumping port, a LEP arc quadrupole MQ, a beam position monitor, an orbit corrector, a sector valve, and three bellows.

The focusing in the linac module is adjusted such that the betatron wavelength is constant during the first pass. The phase advance in a cell is $\mu/2\pi \approx 0.3904$. This is achieved by choosing the gradients of the quadrupoles in proportion to the beam energy during the first pass. During the second and later passes the betatron wavelength decreases along the linac module. The values of the optical functions at the entrance of the second and later passes are adjusted in order to facilitate the matching of the spreaders. Figures 24 to 30 show the optical functions β_x and β_y in the linac module for all seven passes.

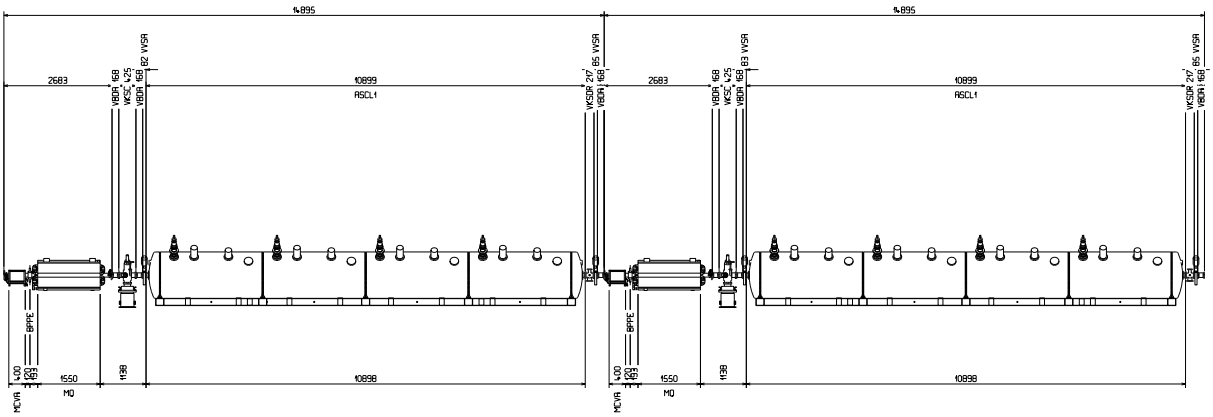

Fig. 23: Layout of two linac half-cells.

Table 13: Parameters of the linac module.

Frequency of RF system	352.209 MHz
Wavelength of RF system	0.851178 m
Number of RF modules	72
Total accelerating RF voltage	3.5 GeV
Length of half-cell	$17.5\lambda_{\mathrm{RF}} = 14.895615$ m

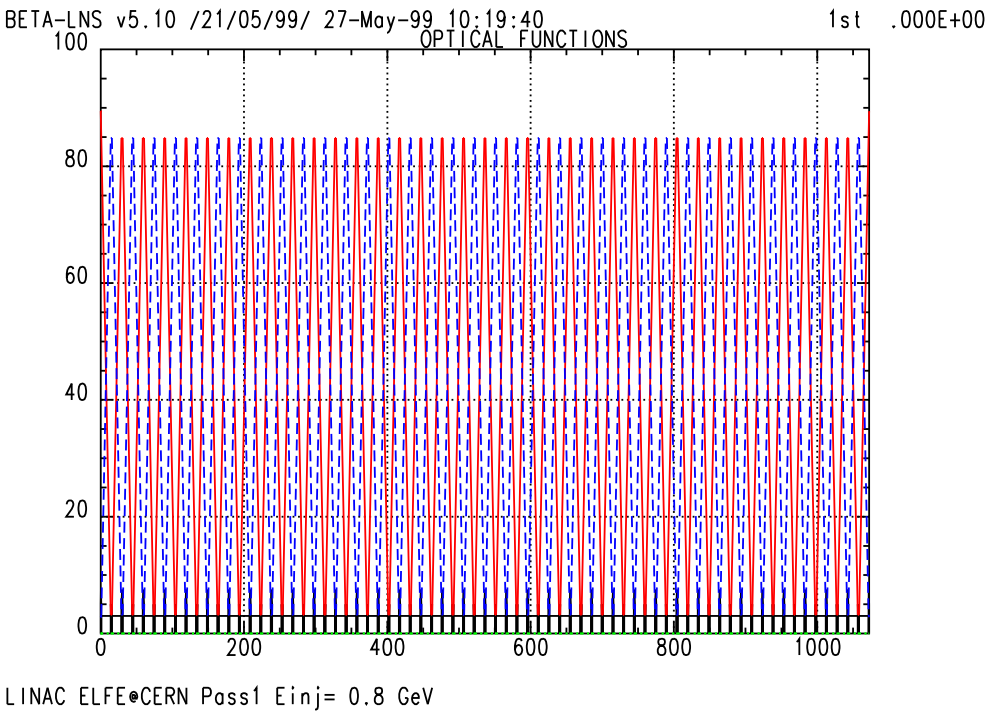

Fig. 24: Optical functions β_x in red and β_y in blue during Pass 1 through the linac.

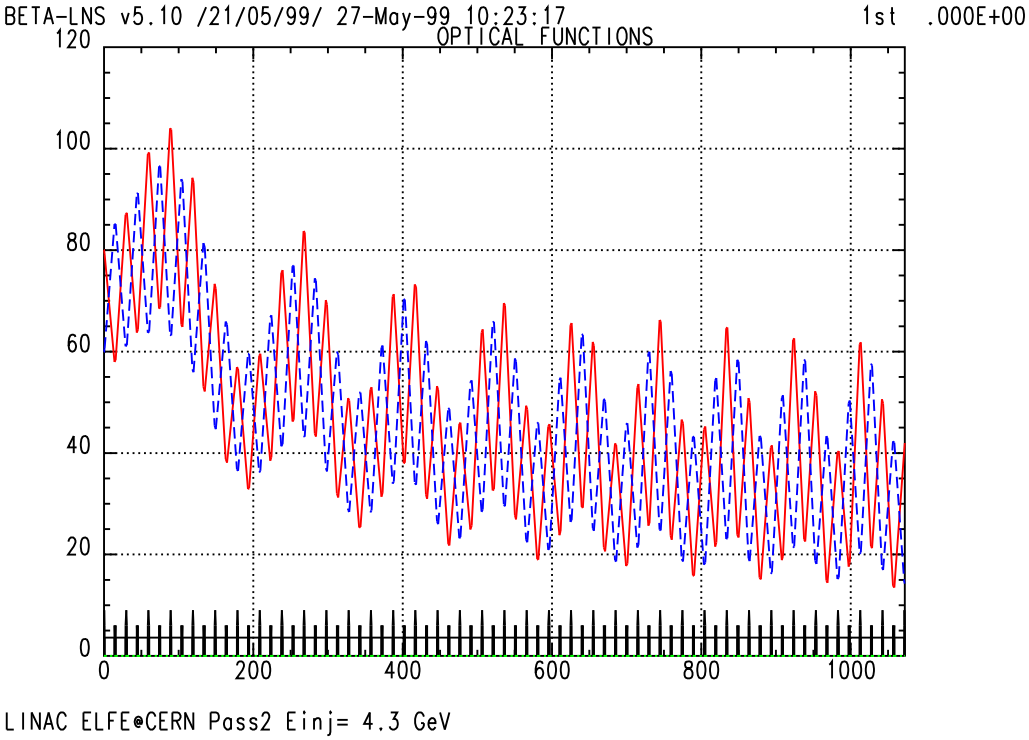

Fig. 25: Optical functions β_x in red and β_y in blue during Pass 2 through the linac.

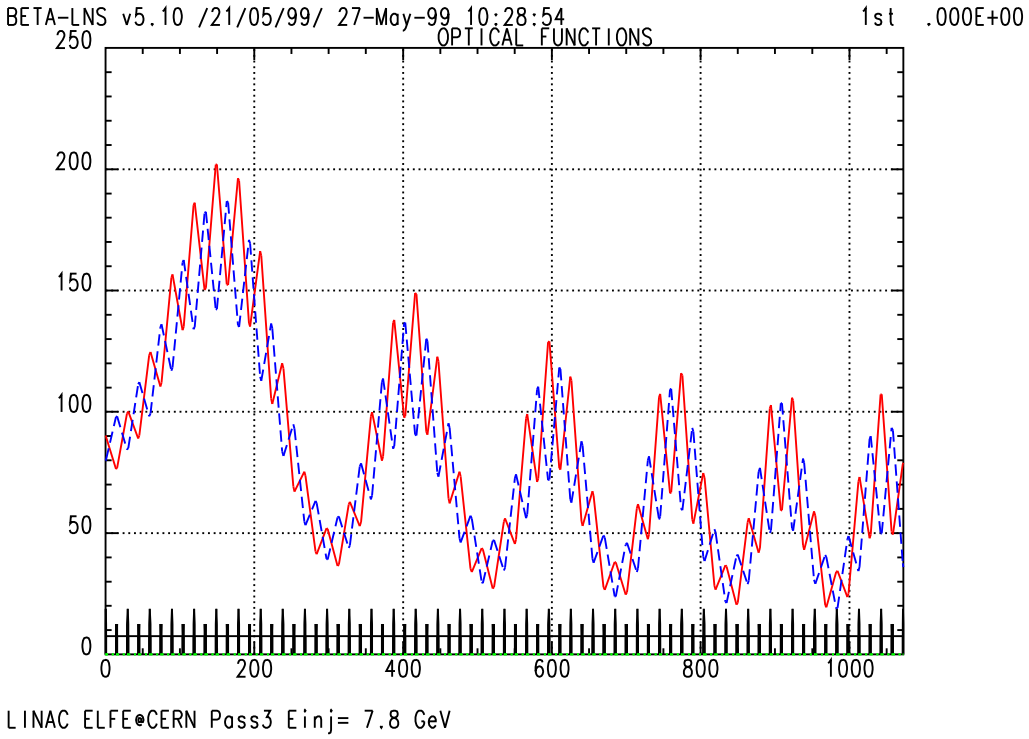

Fig. 26: Optical functions β_x in red and β_y in blue during Pass 3 through the linac.

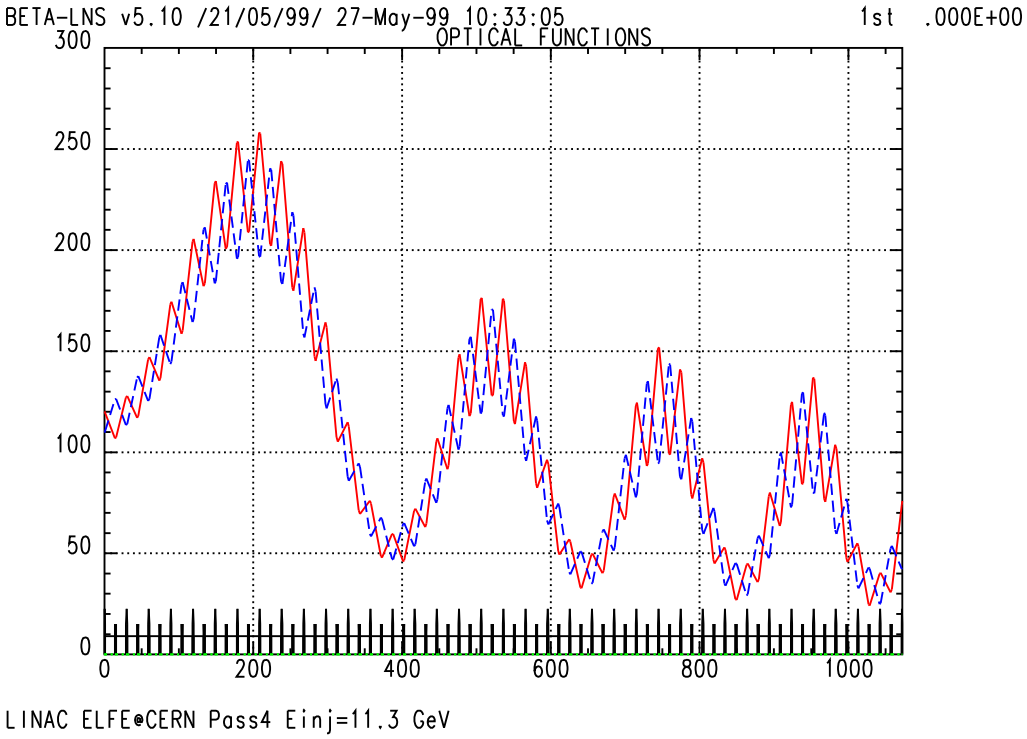

Fig. 27: Optical functions β_x in red and β_y in blue during Pass 4 through the linac.

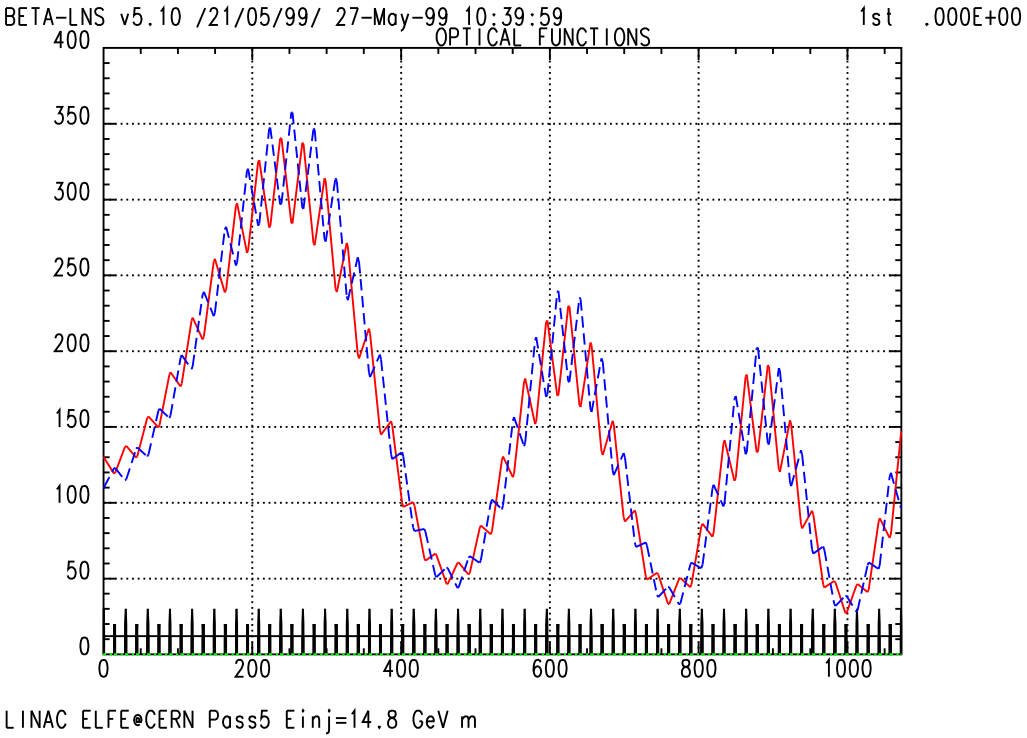

Fig. 28: Optical functions β_x in red and β_y in blue during Pass 5 through the linac.

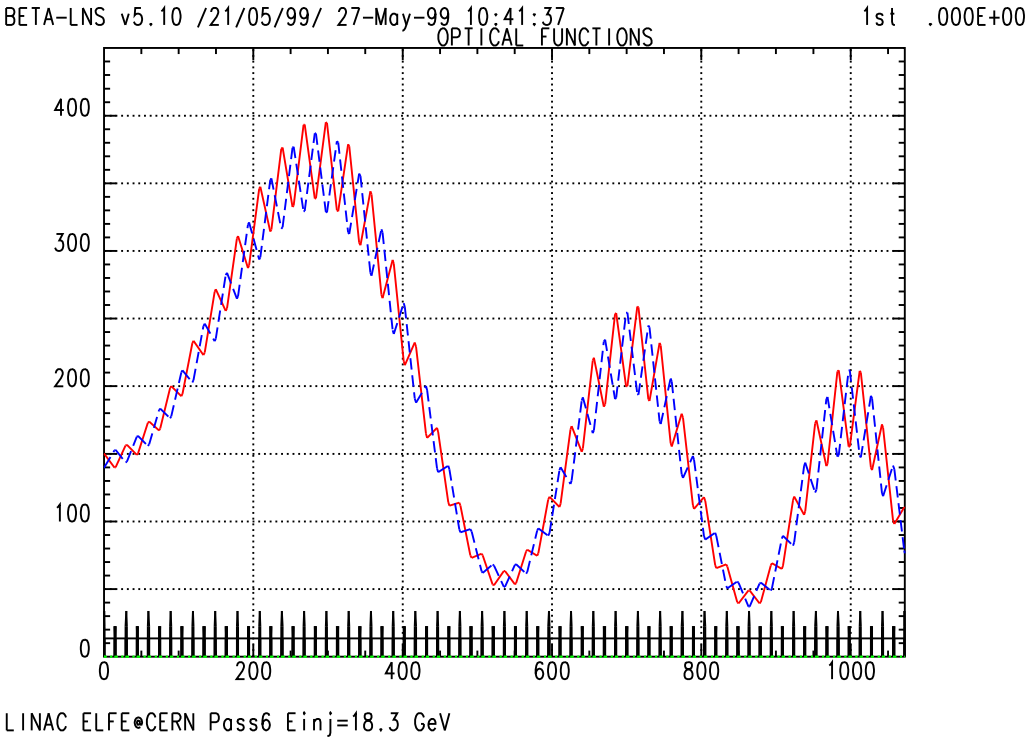

Fig. 29: Optical functions β_x in red and β_y in blue during Pass 6 through the linac.

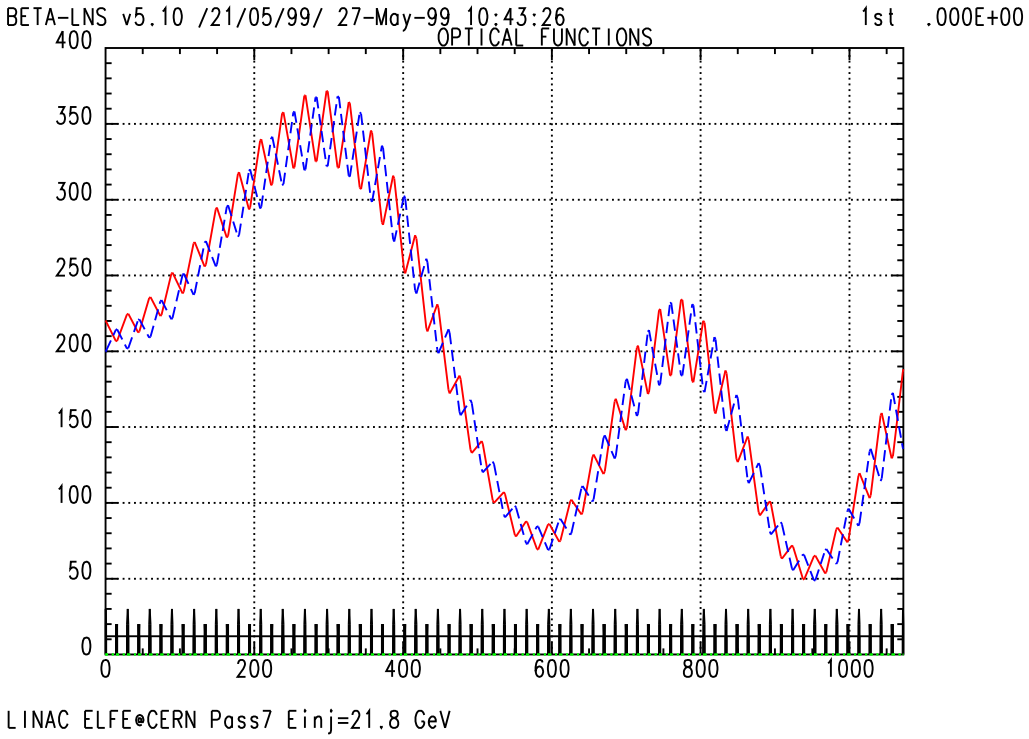

Fig. 30: Optical functions β_x in red and β_y in blue during Pass 7 through the linac.

7.1.2 Spreader

The spreader distributes the beams from the linear accelerator into the beam line for the extracted beam and into the six recirculating arcs. Figure 31 shows the geometrical layout. A large vertical dipole magnet initiates the separation. Figure 32 shows the trajectories inside this magnet. The deflection angles are inversely proportional to the beam momenta. The vertical separations and the positions of the second and third series of dipoles are adjusted such that there is practically no overlap between the dipoles. The fourth series of dipoles bends the beam back into the horizontal direction at the vertical spacing in the arcs. The extracted beam is 0.6 m below the level of the linear accelerator beam. The beams in the arc are between 0 and 3 m above the level of the linear accelerator beam. The focusing by quadrupoles is arranged such that the vertical dispersion D_y and its derivative D'_y vanish at either end of the spreader, and such that the optical functions α and β are matched to those in the linear accelerator and the arcs, respectively, in both planes. Table 14 shows the normalized quadrupole strengths and Table 15 the lengths and bending angles for the seven passes through the spreader. Figures 33 to 39 show schematic layouts and the optical functions for the seven passes through the spreader. The leftmost half quadrupole belongs to the linac module, the rightmost one to the arc module.

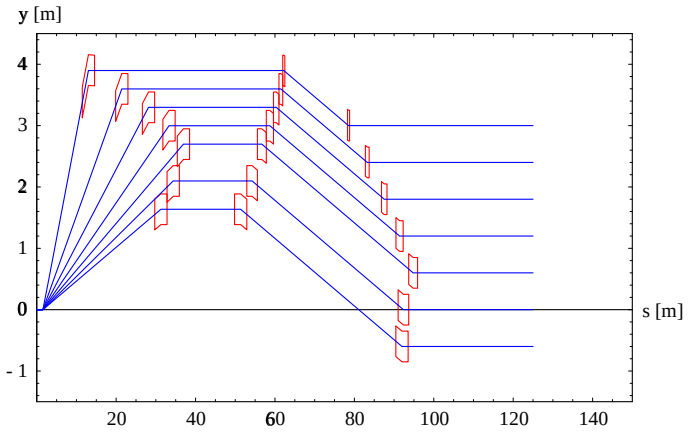

Fig. 31: Geometry of the spreader.

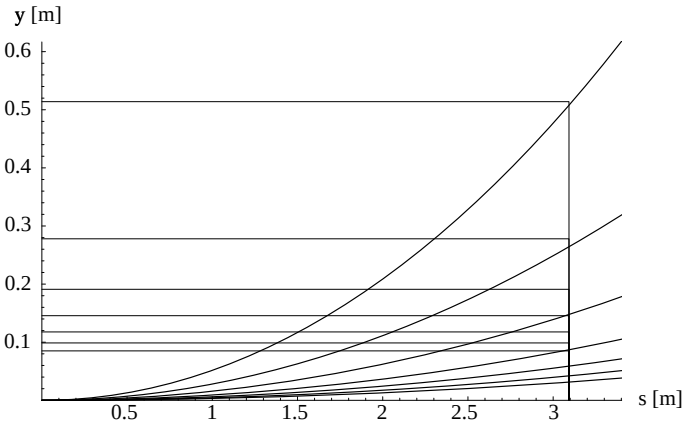

Fig. 32: Trajectories in the first dipole magnet.

Our choice of seven passes through the linac makes the design of the spreader — and the combiner — difficult. The height is determined by the requirement that the vertical separation between the passes must be large enough to install all the magnets. It fixes the product of the lengths of the sloping beam lines in Fig. 31 and the bending angle in the dipoles, as well as the values of the vertical dispersion D_y in the second and third series of dipoles. Increasing these lengths makes matching the spreader to the linac and the arcs more difficult, but would reduce the bending angles, and hence the synchrotron radiation losses and the quantum excitation of the vertical emittance which will be discussed in Section 7.3.

Table 14: Normalized quadrupole strength K1 in m^{-2} in the spreader. Horizontally-focusing quadrupoles have positive K1. The quadrupole QPLEP1 belongs to the linac module. Its normalized strength is inversely proportional to the beam energy. The quadrupoles QF1 belong to the arcs. Their strengths agree with those shown in Table 16.

Pass	1	2	3	4	5	6	7
QPLEP1	–0.082000	–0.045207	–0.031205	–0.023826	–0.019269	–0.01617	–0.013938
QK2	0.190000	0.104749	0.072306	0.055207	0.044648	0.03740	0.032295
QK3	–0.110000	–0.060644	–0.041861	–0.031962	–0.025849	–0.02169	–0.018697
QP1	–0.062740	–0.077932	–0.082356	–0.042263	0.042400	–0.00017	0.059267
QP3	0.296795	0.239228	0.182729	0.070384	0.054347	0.00019	–0.043634
QP4	–0.418006	–0.414629	–0.273664	–0.106482	–0.077013	0.26913	–0.118062
QP5	0.547077	0.572523	0.563988	0.049191	0.212697	–0.28745	0.237287
QP6	–0.382038	–0.207854	–0.256199	0.186648	–0.210355	0.03765	–0.107239
QP7	0.507910	0.100418	0.044317	– 0.203807	0.156826	0.04690	0.033314
QF1	0.695039	0.501899	0.491800	0.251899	0.252557	0.254651	0.252521

Table 15: Lengths L and bending angles Φ of the dipoles in the spreader. The magnet SP1DIP is one magnet and used for all passes. Figure 32 shows the trajectories inside this magnet. All other magnets are separate for each pass. Practical adjustments of their lengths still need to be carried out.

Pass	Dipole	L/m	Φ/r	Pass	Dipole	L/m	Φ/r
1	SP1DIP	3.14949	–0.329331	5	SP1DIP	3.09586	–0.760728
1	DDIP2	3.14949	0.329331	5	DDIP2	3.09586	0.760728
1	DDIP3	0.52598	0.055000	5	DDIP3	2.23828	0.055000
1	DDIP4	0.52598	–0.055000	5	DDIP4	2.23828	–0.055000
2	SP1DIP	3.10950	–0.179258	6	SP1DIP	3.09497	–0.638413
2	DDIP2	3.10950	0.179258	6	DDIP2	3.09497	0.638413
2	DDIP3	0.95405	0.055000	6	DDIP3	2.66636	0.055000
2	DDIP4	0.95405	–0.055000	6	DDIP4	2.66636	–0.055000
3	SP1DIP	3.10072	–0.123389	7	SP1DIP	3.09443	–0.055000
3	DDIP2	3.10072	0.123389	7	DDIP2	3.09443	0.055000
3	DDIP3	1.38213	0.055000	7	DDIP3	3.09443	0.055000
3	DDIP4	1.38213	–0.055000	7	DDIP4	3.09443	–0.055000
4	SP1DIP	3.09744	–0.094110				
4	DDIP2	3.09744	0.094110				
4	DDIP3	1.81021	0.055000				
4	DDIP4	1.81021	–0.055000				

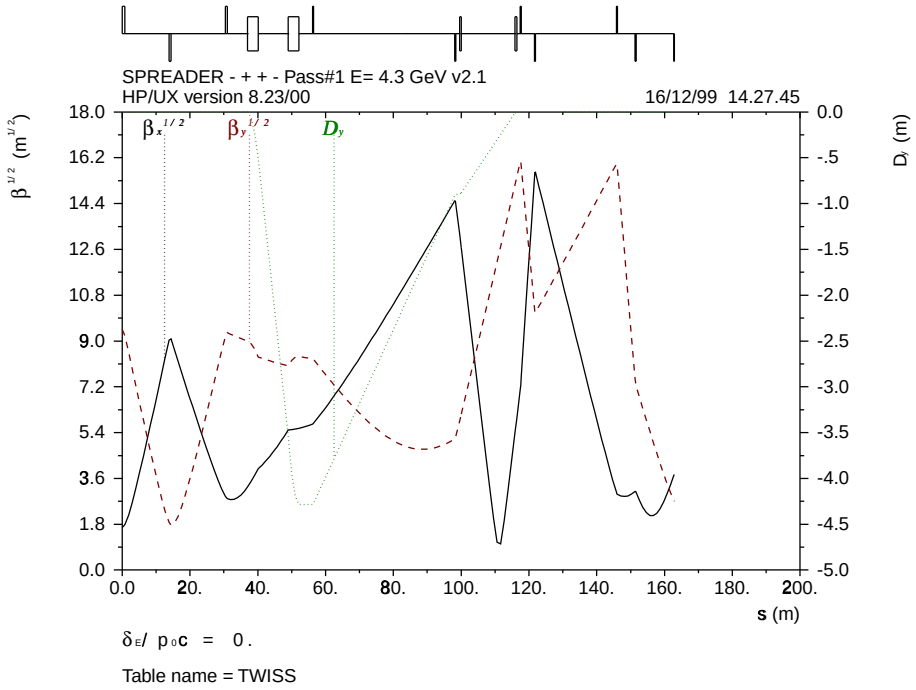

Fig. 33: Optical functions $\sqrt{\beta_x}$, $\sqrt{\beta_y}$ and D_y for Pass 1 through the spreader. In the schematic layout in Figs. 33 to 39 dipoles are marked by rectangles centred on the horizontal line, and horizontally (vertically) focusing quadrupoles by rectangles below (above) it.

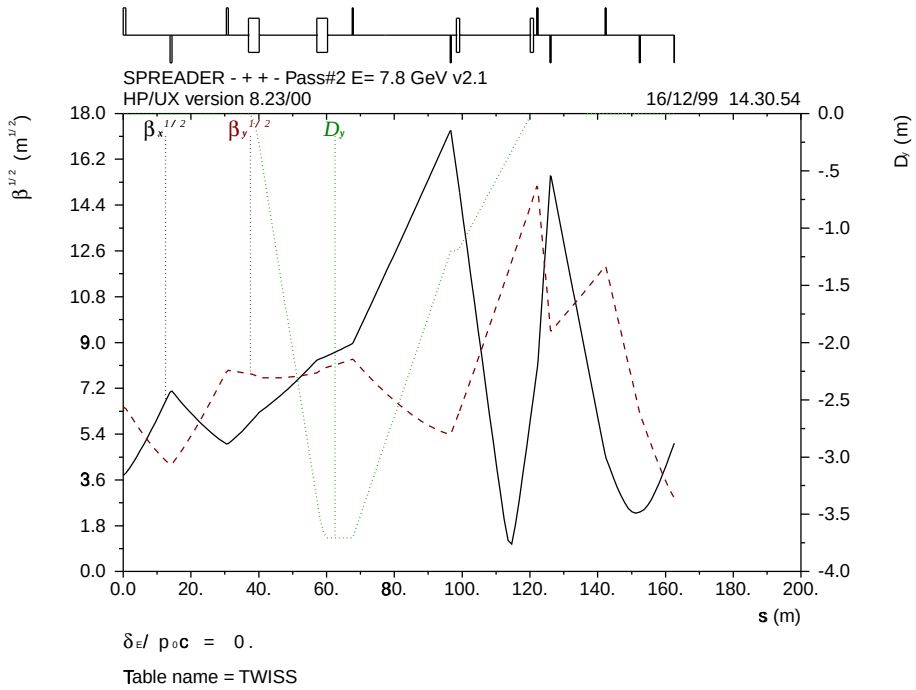

Fig. 34: Schematic layout and optical functions for Pass 2 through the spreader.

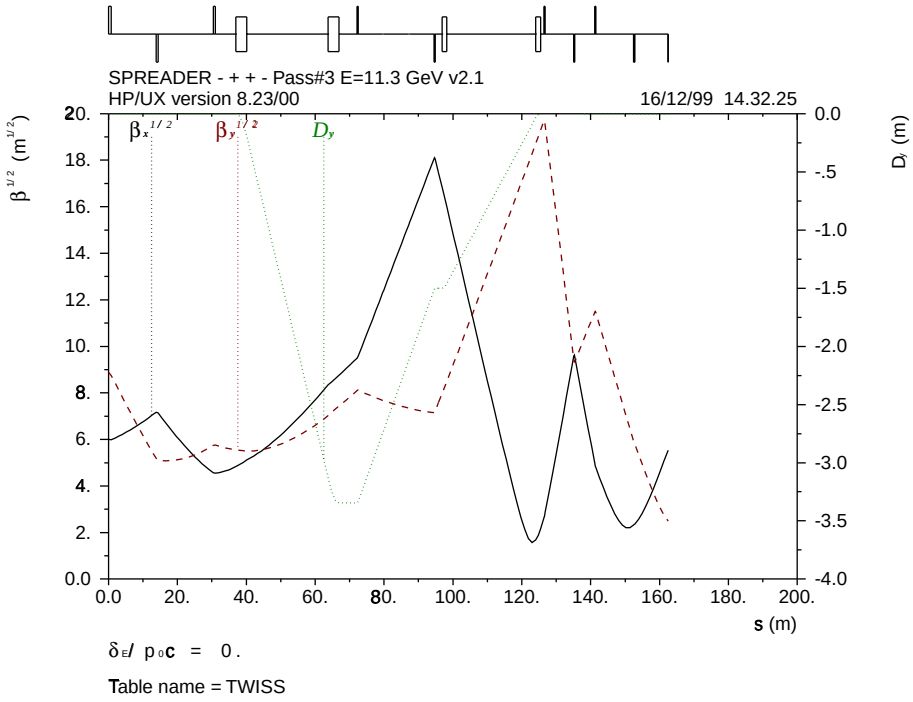

Fig. 35: Schematic layout and optical functions for Pass 3 through the spreader.

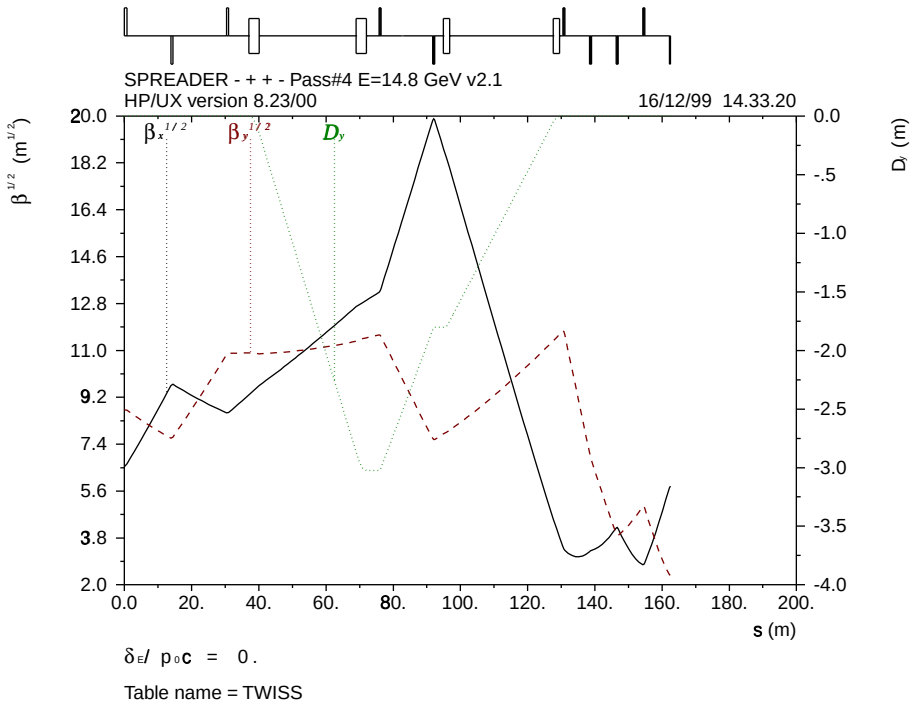

Fig. 36: Schematic layout and optical functions for Pass 4 through the spreader.

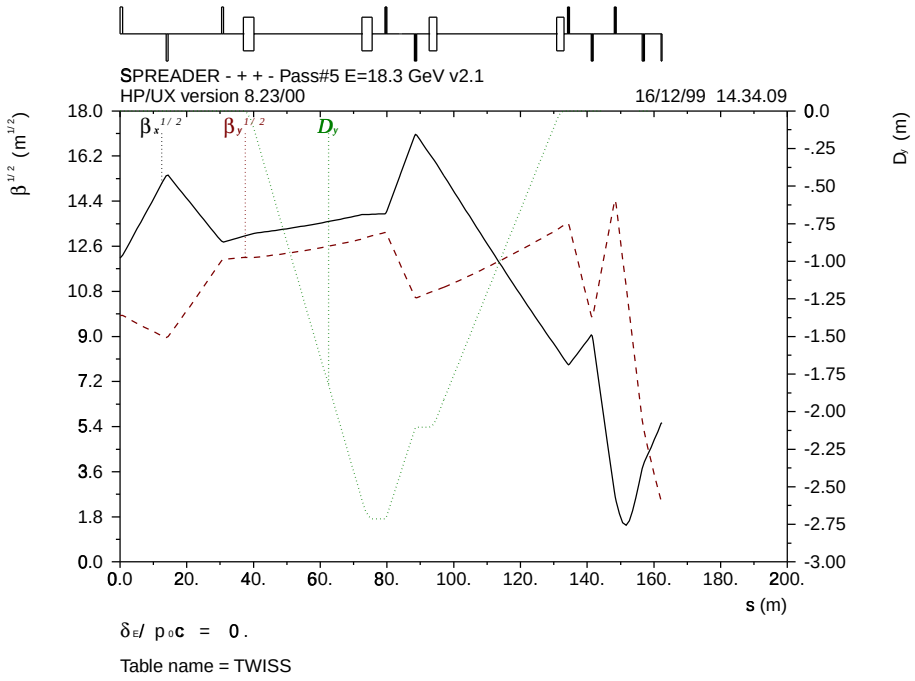

Fig. 37: Schematic layout and optical functions for Pass 5 through the spreader.

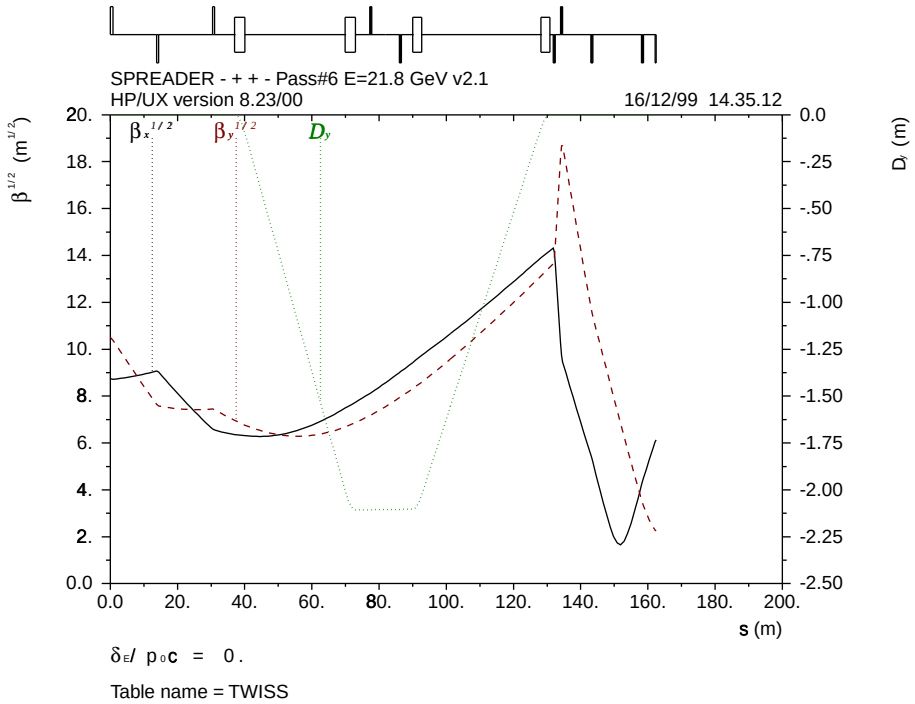

Fig. 38: Schematic layout and optical functions for Pass 6 through the spreader.

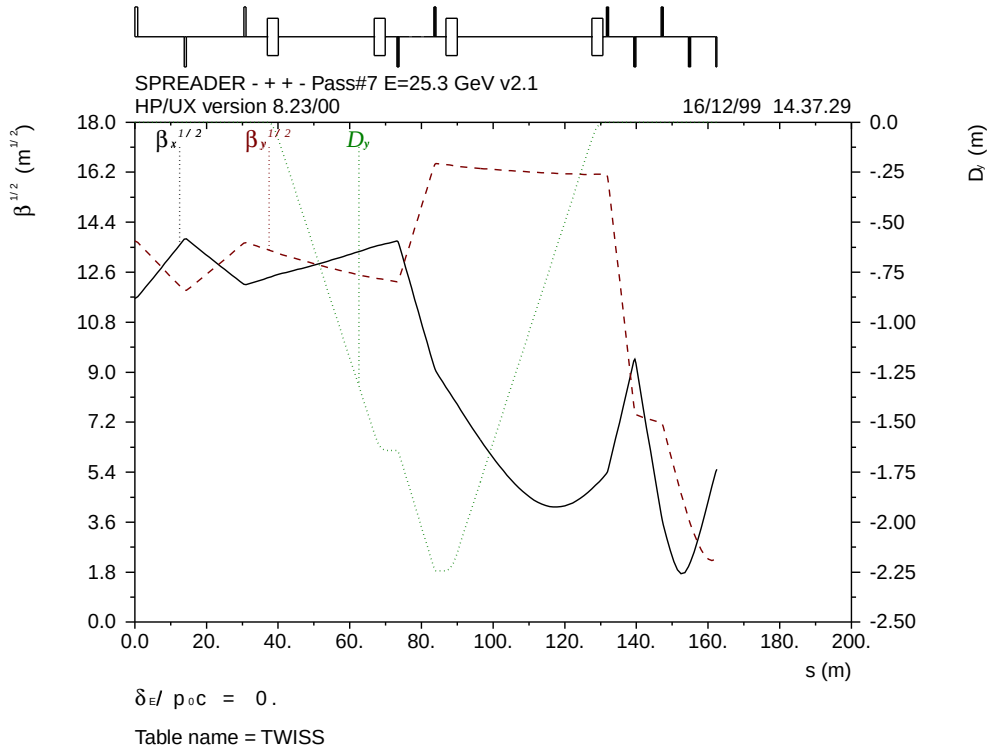

Fig. 39: Schematic layout and optical functions for Pass 7 through the spreader.

7.1.3 Arc

The recirculating arcs consist of six cells each. The cells consist of four FODO periods. The dipoles are installed close to the minima of the horizontal dispersion D_x in order to limit the emittance increase caused by synchrotron radiation, and are arranged such that the cells are almost isochronous achromats. Figures 40 to 45 show a schematic layout and the optical functions. Both D_x and its derivative D'_x vanish at both ends of the cells. The anisochronism in the arcs compensates the negative contribution of the passage through the spreader. This is achieved by choosing the values of D_x near the centre of the cells. Close inspection of Figs. 40 to 45 shows how D_x at the centre of the arc cells becomes smaller and eventually negative for the higher passes whilst the contribution of the spreaders to the anisochronism decreases. The bending radius in the dipoles is chosen such that the increase of the momentum spread in the beams caused by synchrotron radiation is small enough. Emittance and energy spread are discussed further in Section 7.3. Tables 16 and 17, respectively, show the normalized quadrupole and sextupole strengths in the arcs. The sextupoles compensate the chromaticity of the arcs, and at the same time minimize the increase in the bunch length, caused by the orbit lengthening due to betatron oscillations [46].

Table 16: Normalized quadrupole strengths K1 in m^{-2} in the arcs.

Pass	1	2	3	4	5	6
QF1	0.695039	0.501899	0.491800	0.251899	0.252557	0.254651
QD1	–0.402431	–0.416579	–0.442870	–0.228329	–0.230575	–0.232128
QF2	0.490084	0.511496	0.519267	0.264009	0.265063	0.266330
QD2	–0.473013	–0.445048	–0.420267	–0.208569	–0.206635	–0.205202
QF3	0.511999	0.560499	0.553324	0.273259	0.270935	0.266842

Table 17: Normalized sextupole strengths K2 in m^{-3} in the arcs.

Pass	1	2	3	4	5	6
SXF	0.405631	0.563160	0.625337	0.662188	0.688961	0.728458
SXD	–1.472095	–1.760587	–1.744193	–1.799944	–1.850517	–1.930582

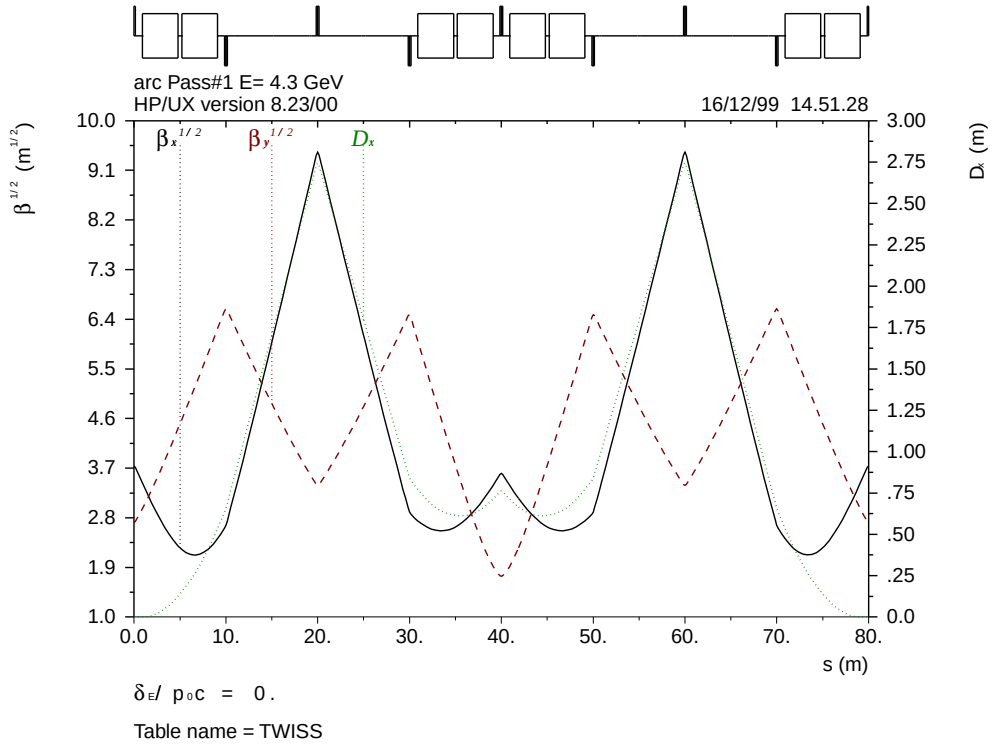

Fig. 40: Optical functions $\sqrt{\beta_x}$, $\sqrt{\beta_y}$ and D_y of the arc cells at 4.3 GeV. In the schematic layout in Figs. 40 to 52 dipoles are marked by rectangles centred on the horizontal line, and horizontally (vertically) focusing quadrupoles by rectangles above (below) it.

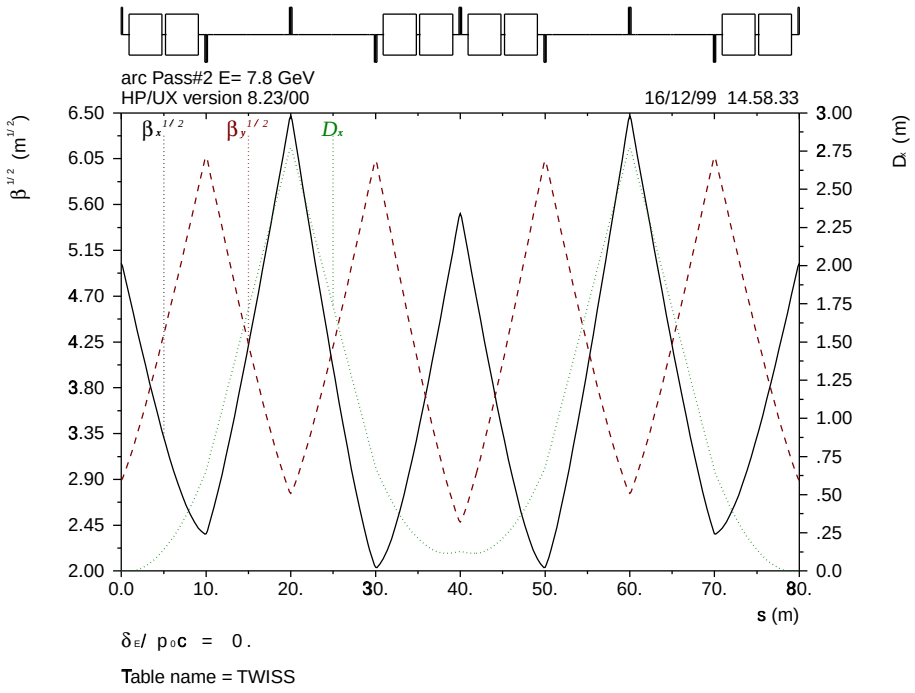

Fig. 41: Schematic layout and optical functions of the arc cells at 7.8 GeV.

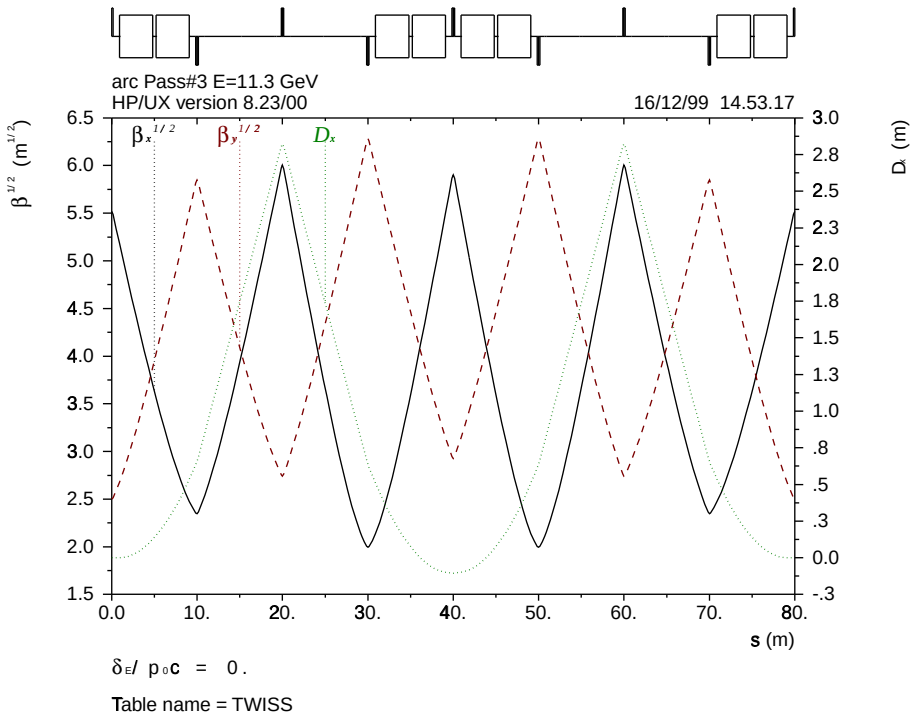

Fig. 42: Schematic layout and optical functions of the arc cells at 11.3 GeV.

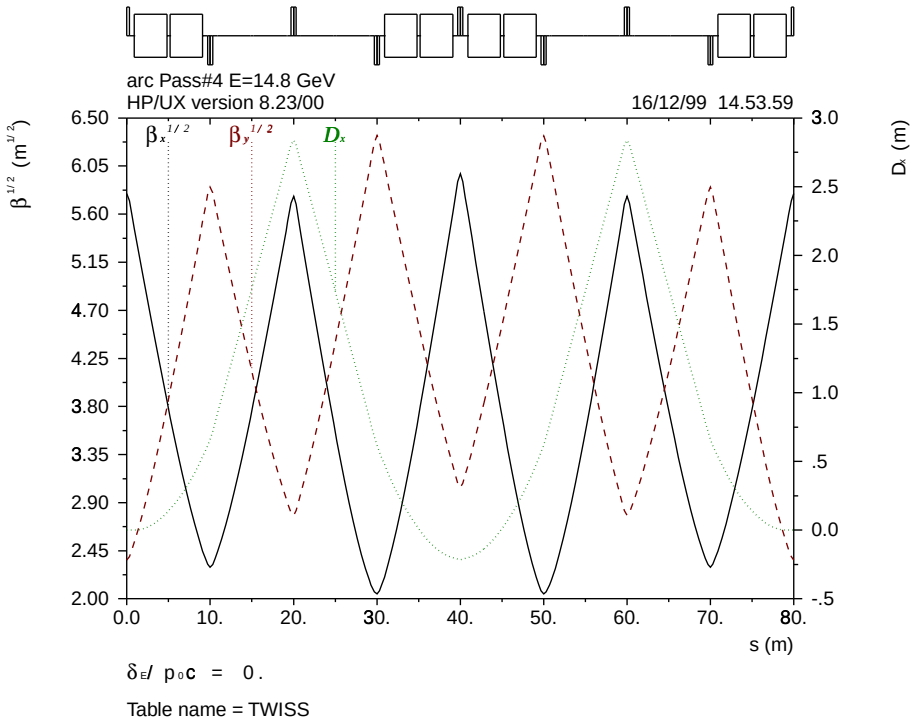

Fig. 43: Schematic layout and optical functions of the arc cells at 14.8 GeV.

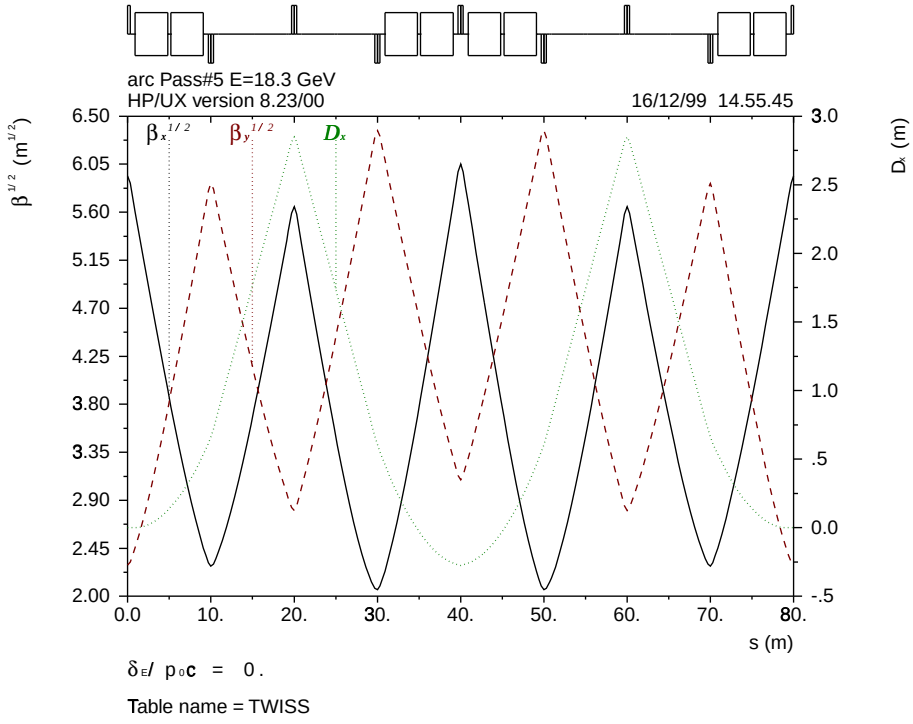

Fig. 44: Schematic layout and optical functions of the arc cells at 18.3 GeV.

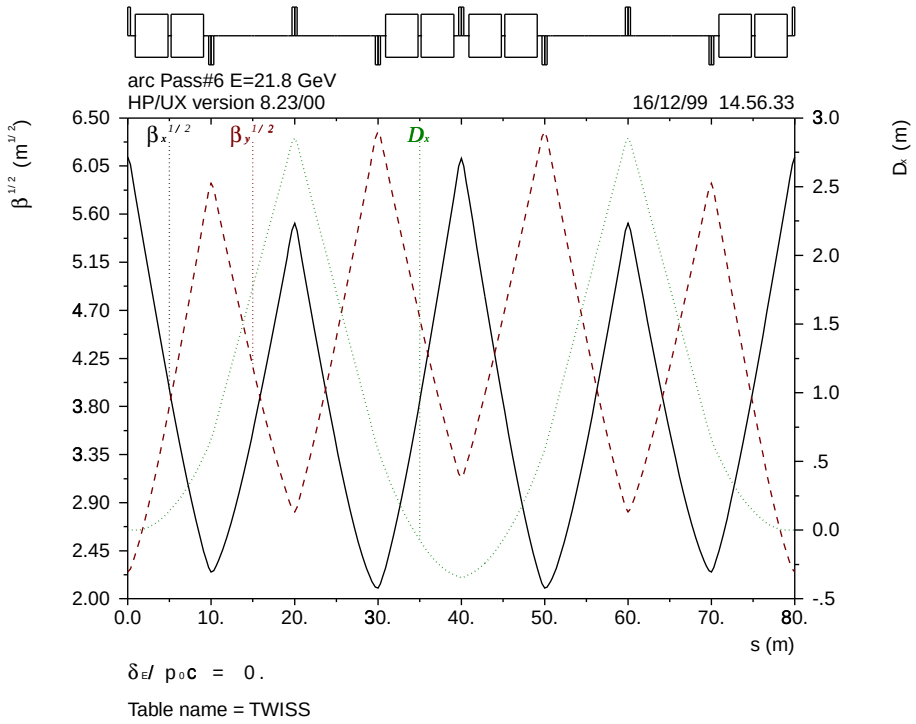

Fig. 45: Schematic layout and optical functions of the arc cells at 21.8 GeV.

7.1.4 Return beam lines

The beams are transported from one arc to the next by six super-imposed 1200 m long transport lines. They consist of 80 m long simple FODO cells with matching sections at both ends. Table 18 shows the normalized quadrupole gradients of the quadrupoles there. Figure 46 shows the schematic layout and optical functions in the return lines. The alternative of having a single return line with combiner and spreader at the ends is less attractive, because it would approximately double the vertical emittance (Section 7.3). Figures 47 to 52 show the schematic layout and optical functions in the six matching sections from the return lines into the six arcs.

Table 18: Normalized quadrupole strength K1 in m^{-2} in the return lines and adaptors. The quadrupoles QPLEP belong to the return line. The horizontally-focusing quadrupoles there have the opposite strengths. The quadrupoles QF1 belong to the arcs. Their strengths are the same as those shown in Table 16.

Pass	1	2	3	4	5	6
QPLEP	–0.022398	–0.022398	–0.022398	–0.022398	–0.022398	–0.022398
QP1	0.023060	0.028924	0.030180	0.030724	0.031047	0.031489
QP2	–0.034409	–0.035019	–0.036254	–0.036455	–0.036553	–0.036755
QP3	0.052509	0.052529	0.054324	0.056034	0.056892	0.058341
QP4	–0.071544	–0.064293	–0.070998	–0.073349	–0.074459	–0.075250
QF1	0.695039	0.501899	0.491800	0.251899	0.252557	0.254651

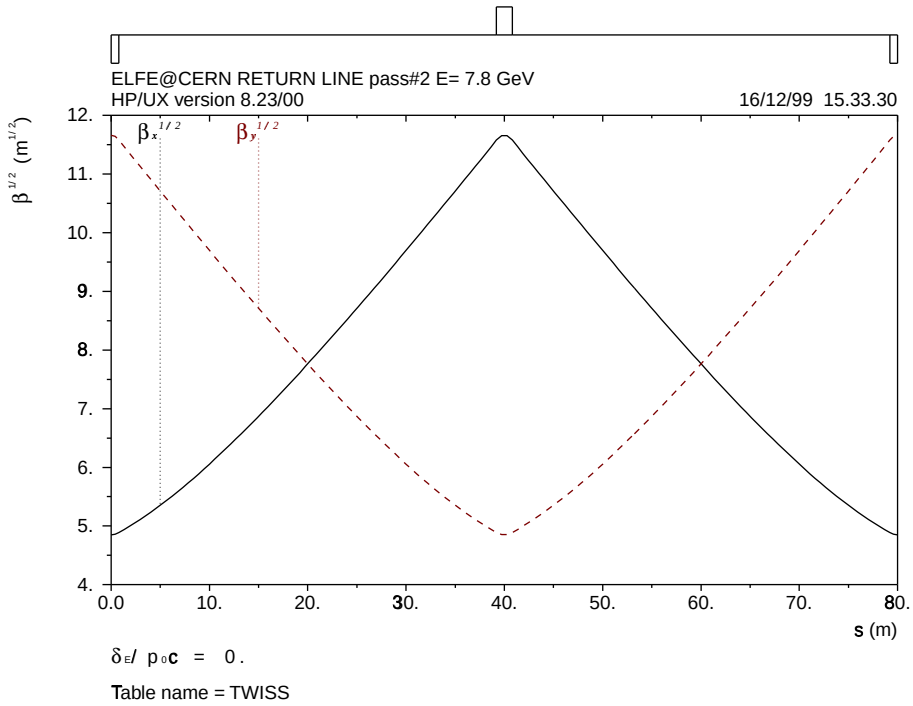

Fig. 46: Schematic layout and optical functions of the FODO cells in the return lines.

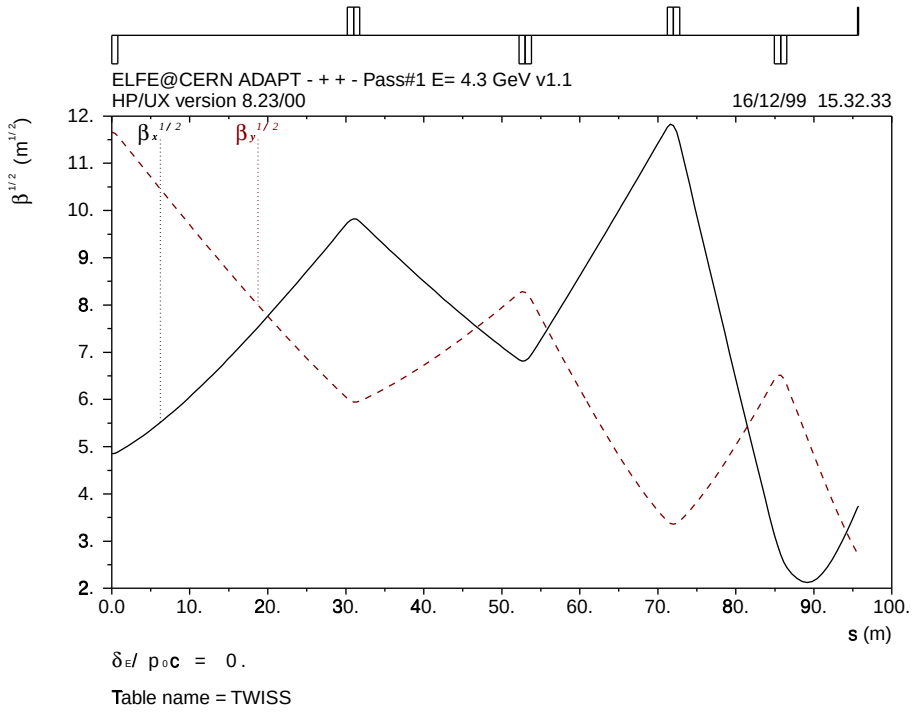

Fig. 47: Schematic layout and optical functions of the matching section into the first arc.

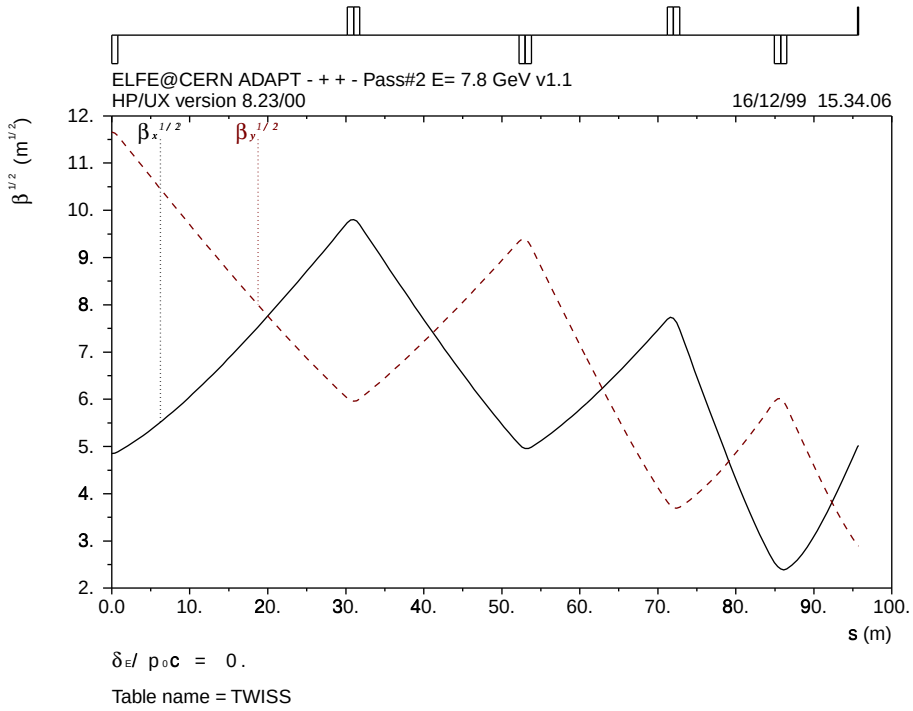

Fig. 48: Schematic layout and optical functions of the matching section into the second arc.

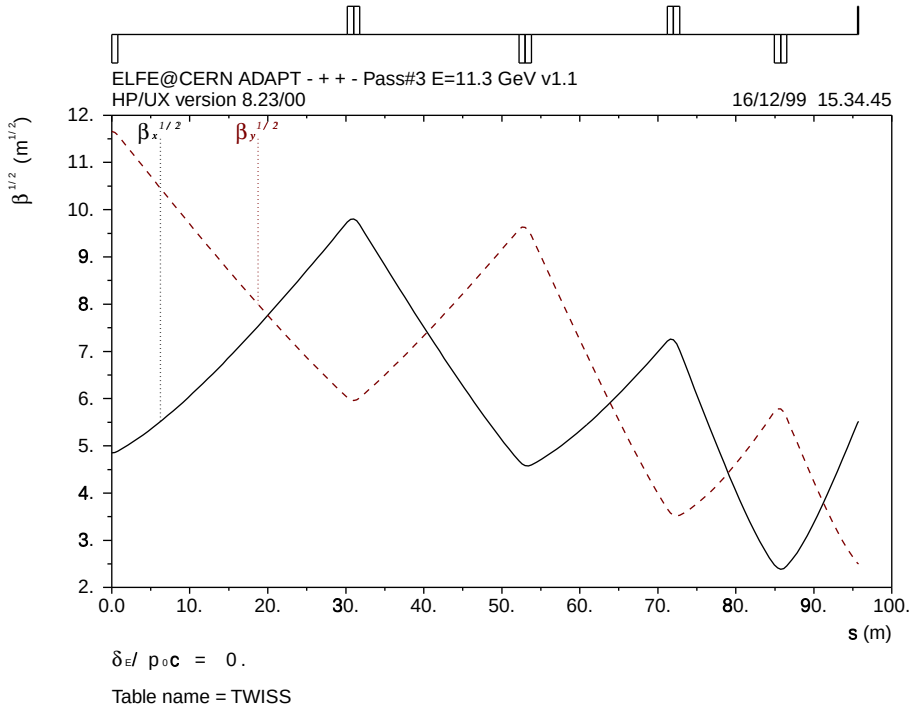

Fig. 49: Schematic layout and optical functions of the matching section into the third arc.

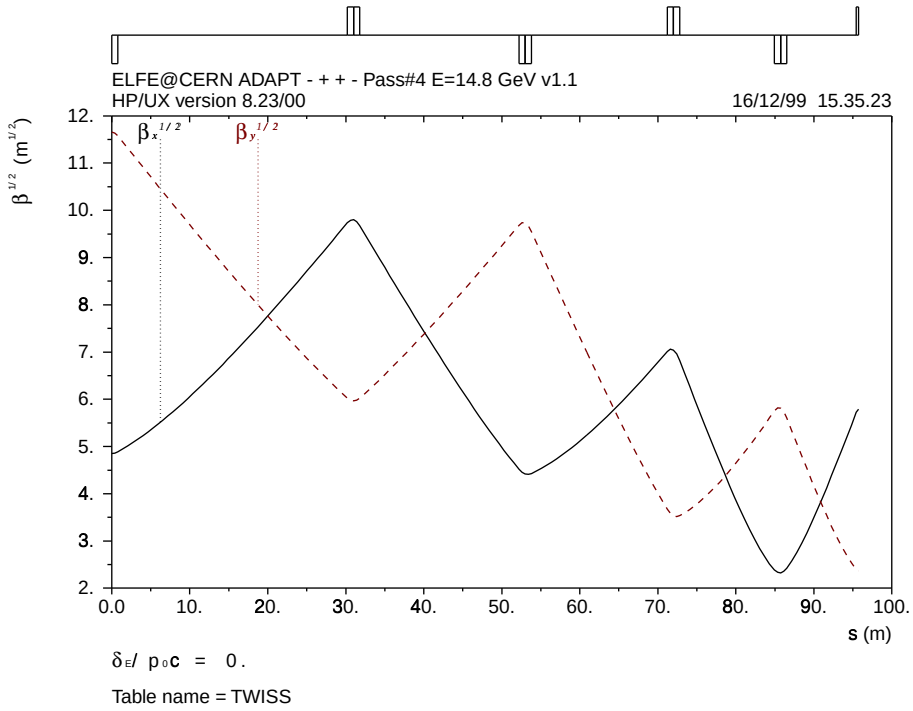

Fig. 50: Schematic layout and optical functions of the matching section into the fourth arc.

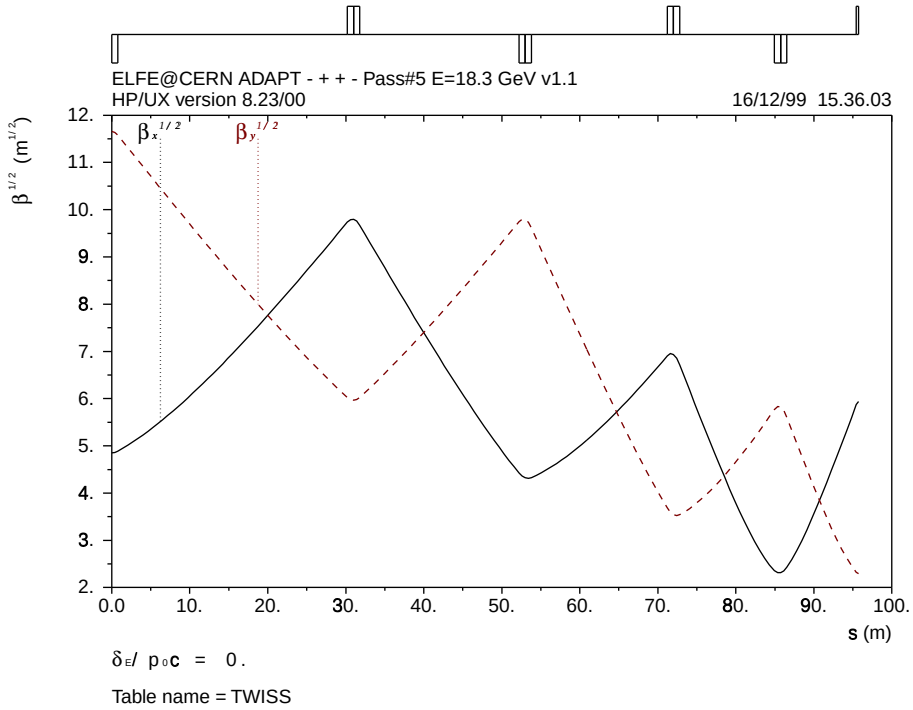

Fig. 51: Schematic layout and optical functions of the matching section into the fifth arc.

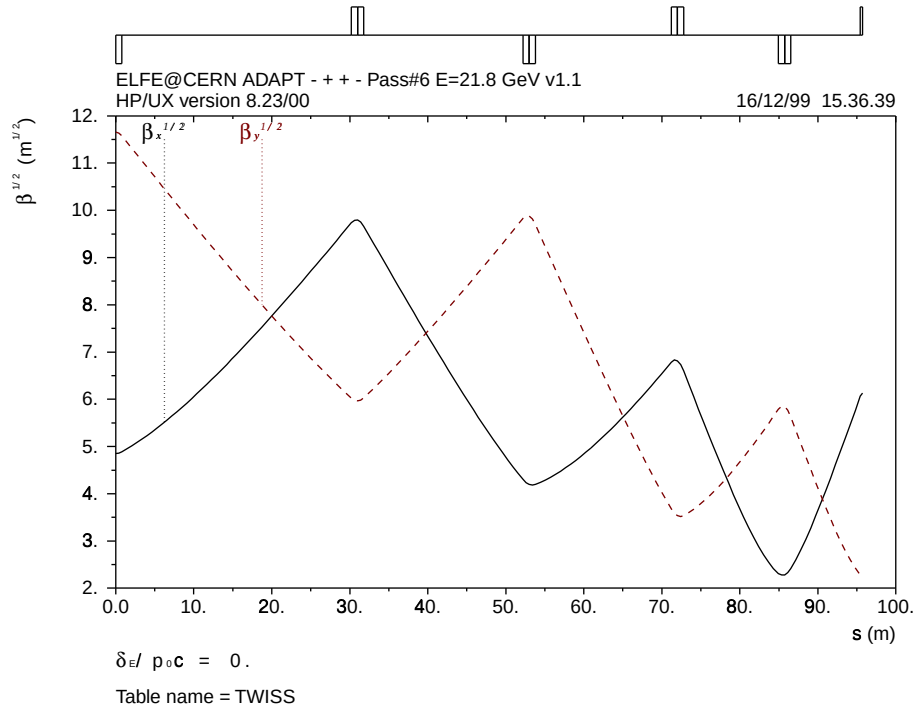

Fig. 52: Schematic layout and optical functions of the matching section into the sixth arc.

7.1.5 Combiner

The combiner merges the beams from the arcs into the single beam line of the linac, i.e. it has the opposite function to the spreader. Its geometrical layout is the mirror image of the spreader layout shown in Fig. 31. However, the optical matching is different since the optical functions at the entrance and the exit of the linac are different. Table 19 shows the normalized quadrupole strengths, and Figs. 53 to 58 show the schematic layout and the optical functions for the six passes through the combiner.

Table 19: Normalized quadrupole strength K1 in m^{-2} in the combiner. The quadrupole QPLEP1 belongs to the linac module. Its normalized strength decreases with the beam energy. The quadrupoles QF1 belong to the arcs. Their strengths agree with those shown in Table 16.

Pass	1	2	3	4	5	6
QPLEP1	–0.015263	–0.008415	–0.005808	–0.004435	–0.003586	–0.003011
QK2	0.021034	0.011596	0.008004	0.006111	0.004942	0.004149
QK3	–0.000000	–0.000000	–0.000000	–0.000000	–0.000000	–0.000000
QP1	–0.062740	–0.077932	–0.082356	–0.042263	–0.042400	–0.000179
QP3	0.296795	0.239228	0.182729	0.070384	0.054347	0.000179
QP4	–0.333679	–0.315015	–0.250489	–0.114527	–0.088751	–0.188019
QP5	0.372724	0.358211	0.350566	0.113874	0.143509	0.213449
QP6	0.180477	0.094097	0.031790	0.130952	–0.063727	–0.041581
QP7	–0.296390	–0.248210	–0.249772	–0.235942	–0.075726	–0.277032
QF1	0.695039	0.501899	0.491800	0.251899	0.252557	0.254651

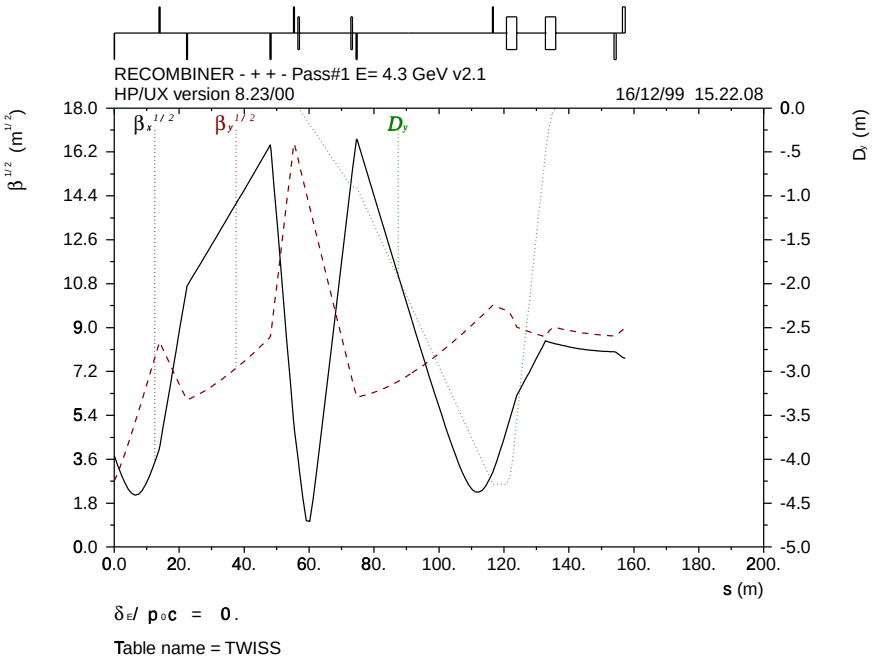

Fig. 53: Optical functions $\sqrt{\beta_x}$, $\sqrt{\beta_y}$ and D_y of the combiner at 4.3 GeV. In the schematic layout in Figs. 53 to 58 dipoles are marked by rectangles centred on the horizontal line, and horizontally (vertically) focusing quadrupoles by rectangles below (above) it.

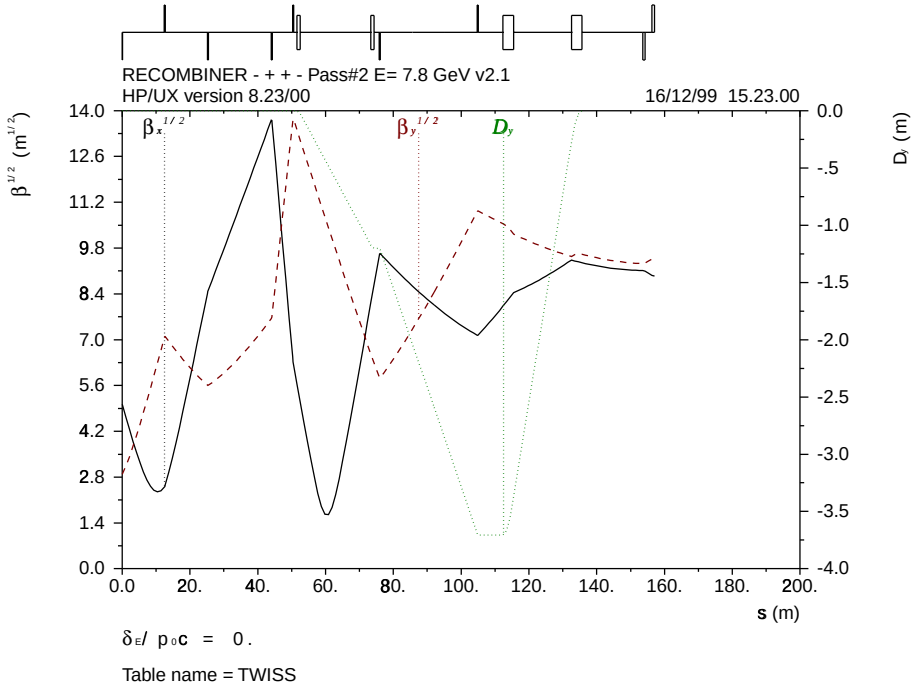

Fig. 54: Schematic layout and optical functions of the combiner at 7.8 GeV.

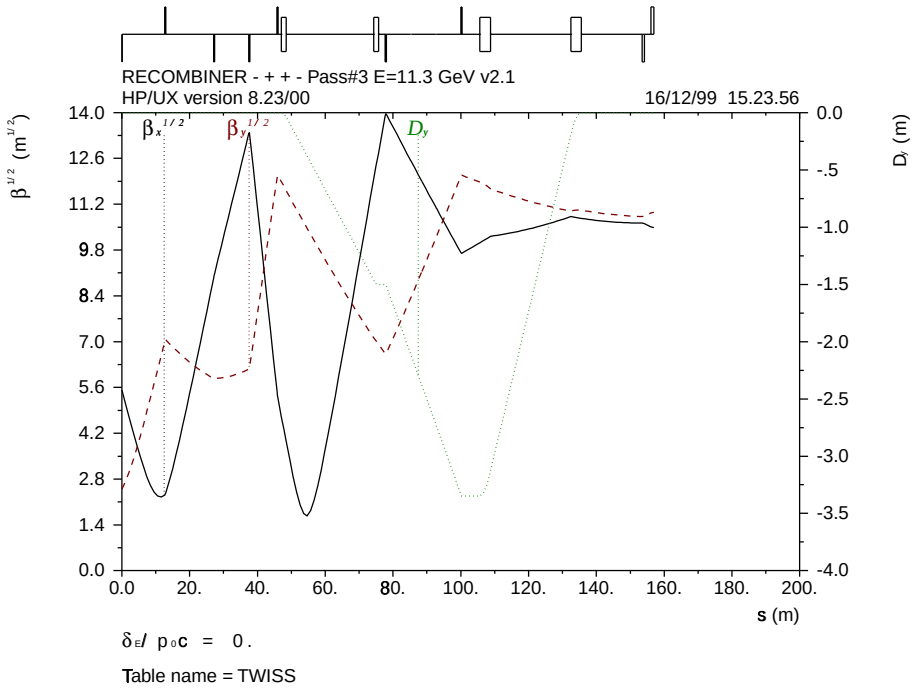

Fig. 55: Schematic layout and optical functions of the combiner at 11.3 GeV.

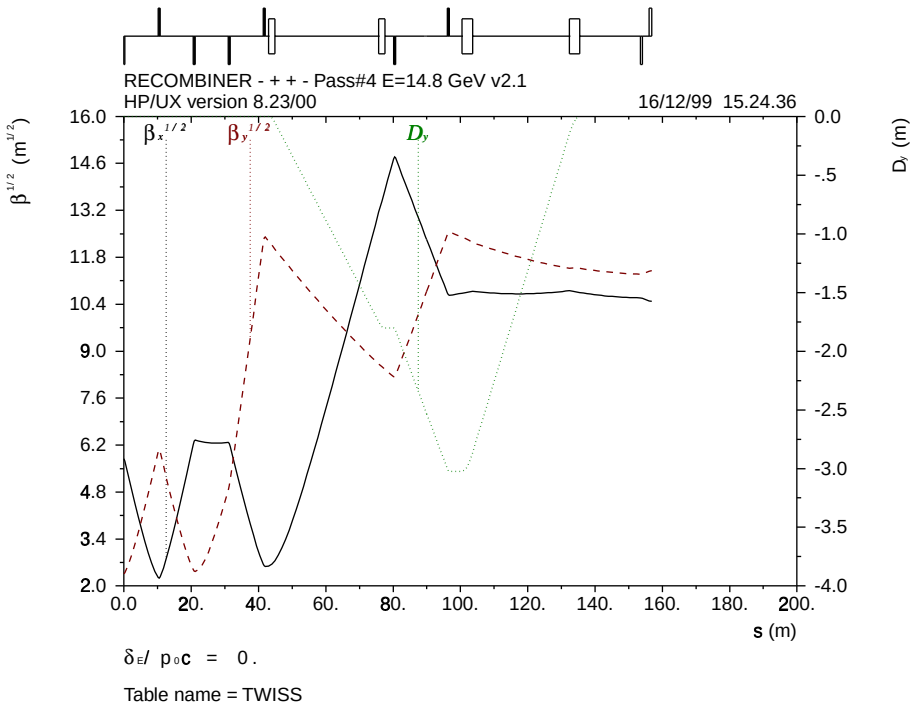

Fig. 56: Schematic layout and optical functions of the combiner at 14.8 GeV.

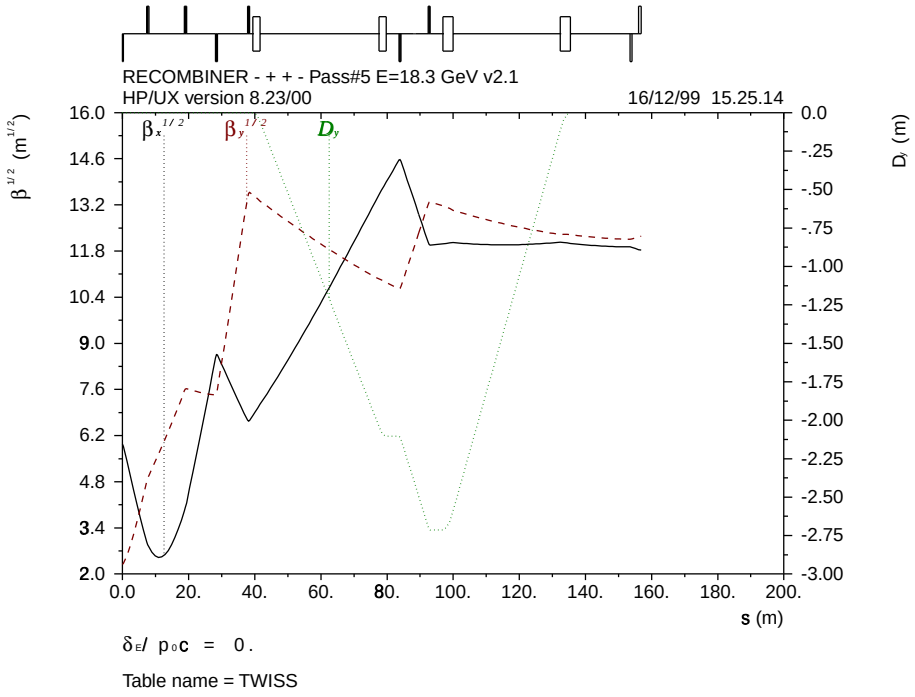

Fig. 57: Schematic layout and optical functions of the combiner at 18.3 GeV.

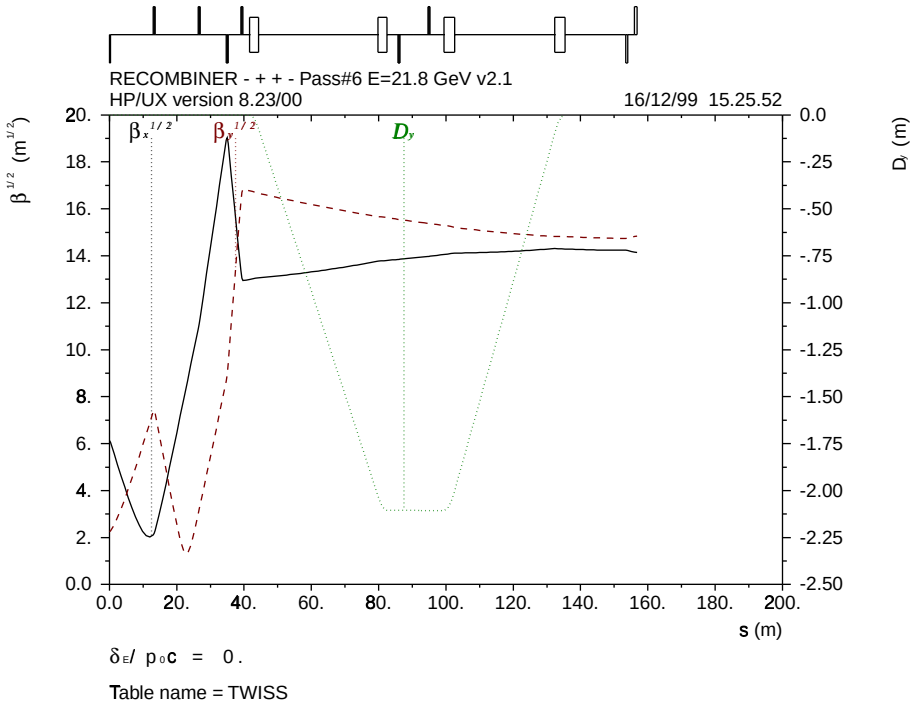

Fig. 58: Schematic layout and optical functions of the combiner at 21.8 GeV.

7.2 Module integration

The vertical deflections in the spreaders and combiners cause an increase in the path length which is largest for the first pass. Table 20 shows by how much the arc lengths differ between the passes, although the lengths of their projections on the horizontal plane are practically identical. The first pass through the spreader and combiner is about 1 m longer than the sixth pass. This is longer than an RF wavelength $\lambda = 0.851178$ m. Hence, the first pass will be made an RF wavelength longer than the others. The remaining differences between the path lengths, about 0.44 m, will be compensated by making the lengths of the spreader, combiner, and matching modules different by up to 0.11 m each. The fine adjustments needed for the compensation of ELFE length variations according to seasonal or tunnel temperatures will be made with chicanes in the return lines. The design of these chicanes remains to be carried out.

Table 20: Comparison of the lengths of the vertical projections for the spreader z_s and the combiner z_c with the arc length in the spreader l_s and in the combiner l_c for all passes. The path length difference is $\Delta a = l_s + l_c - z_s - z_c$.

Pass	z_s/m	l_s/m	z_c/m	l_c/m	Δa/m
1	162.300011	162.913396	156.700021	157.313406	1.226770
2	162.300116	162.639128	156.700156	157.039168	0.678024
3	162.299961	162.536290	156.699961	156.936290	0.472658
4	162.300066	162.485200	156.700066	156.885200	0.370268
5	162.300041	162.456300	156.700061	156.856320	0.312518
6	162.299971	162.421220	156.700051	156.821300	0.242498
7	162.300027	162.403440			

7.3 Emittance and energy spread

The design of the arcs is dominated by the requirements on the emittance and energy spread of the ejected beam, shown in Table 1. The energy spread essentially imposes a lower limit on the bending radius in the arcs [5], and an upper limit on the bunch length, as discussed in Chapter 12. The desired emittance also imposes an upper limit on the length of the arc modules.

Table 21 summarizes the results for the synchrotron radiation losses U_s and the contribution of the synchrotron radiation losses to the relative r.m.s. momentum spread σ_e^{SR}/E for each of the seven passes. Table 21 also shows the accumulated mean momentum offset $\Delta p/p$, the relative r.m.s. momentum spread σ_e/E, and transverse emittances ϵ_x and ϵ_y, which can be deduced from the particle coordinates in the six-dimensional phase space, for all seven passes. Both $\Delta p/p$ and σ_e/E include the contribution of the bunch length $\sigma_z = 3$ mm discussed in Chapter 12. Figure 59 shows the distribution of the relative momentum error, and Fig. 60 the distribution of the horizontal particle positions at the exit of the seventh pass at 25.3 GeV. The perspicaceous reader will notice that the relative momentum spread σ_e/E in Fig. 59 agrees very well with that in Table 21, whilst the relative momentum offset $\Delta p/p$ only includes the contribution of the seventh pass.

The total synchrotron radiation loss $U_s \approx 693$ MeV is sufficiently high for ELFE to not quite reach the design energy $0.8 + 7 \cdot 3.5 = 25.3$ GeV. These losses will have to be taken into account in future designs. The total momentum spread $\sigma_e/E \approx 0.735 \times 10^{-3}$ and the horizontal emittance $\epsilon_x \approx 24$ nm are dominated by the last pass through the spreader, arcs and combiner. However, the vertical emittance growth is caused by the passes through the spreader and combiner which are quite different, and cause the somewhat unexpected contributions from the different passes. Their total becomes $\epsilon_y \approx 19$ nm. On the basis of these results we adopted the ELFE parameters listed in Table 1. The contribution of the seventh pass through the spreader to the vertical emittance shows that violent vertical deflections in the transport lines

to the experimental halls are not advisable. It also makes it unattractive to split the linac into two halves, because this would imply doubling the number of spreaders and combiners, and hence doubling the vertical emittance.

Table 21: Energy and emittance parameters: The first two columns give the pass number and the nominal energy E_n. The next three columns contain the contributions of the individual passes to the energy loss due to synchrotron radiation U_s, the relative momentum spread σ_e^{SR}/E, and the mean momentum offset $\Delta p/p$. The last three columns are the accumulated relative r.m.s. momentum spread σ_e/E and transverse emittances ϵ_x and ϵ_y. Both $\Delta p/p$ and σ_e/E include the contribution of the bunch length $\sigma_z = 3$ mm.

Pass	E_n/GeV	U_s/MeV	σ_e^{SR}/E	$\Delta p/p$	σ_e/E	ϵ_x/nm	ϵ_y/nm
1	4.3	1.28	3.365E-5	–4.916E-04	2.780E-04	0.0032	0.723
2	7.8	8.29	7.605E-5	–1.171E-03	3.161E-04	0.0891	2.965
3	11.3	30.59	1.484E-4	–2.783E-03	3.555E-04	0.722	4.337
4	14.8	82.92	2.571E-4	–5.660E-03	4.292E-04	3.247	6.806
5	18.3	185.14	4.144E-4	–1.016E-02	5.733E-04	10.58	10.33
6	21.8	362.46	6.194E-4	–1.666E-02	8.035E-04	27.84	14.44
7	25.3	22.51	1.717E-4	–9.233E-04	7.354E-04	23.96	18.83

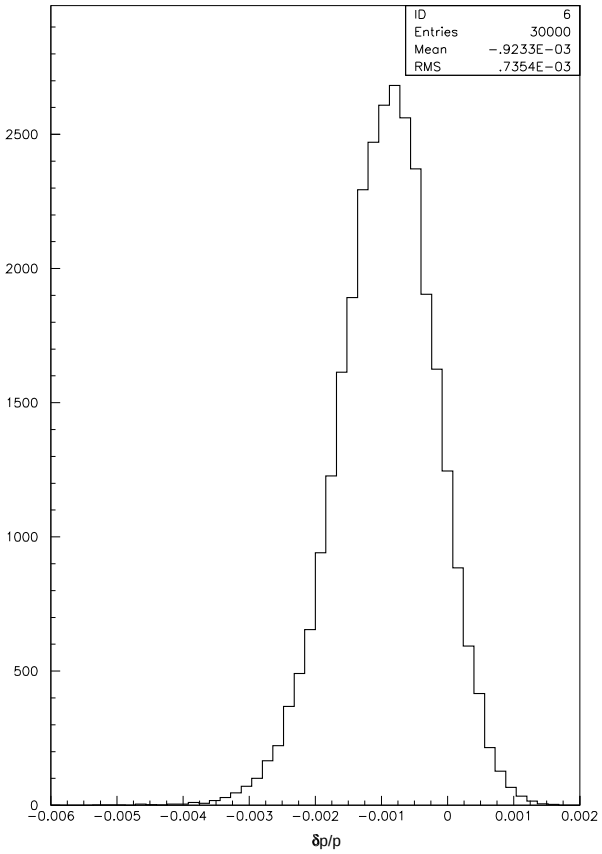

Fig. 59: Distribution of the relative momentum error $\delta p/p$ at the exit of the seventh pass at 25.3 GeV.

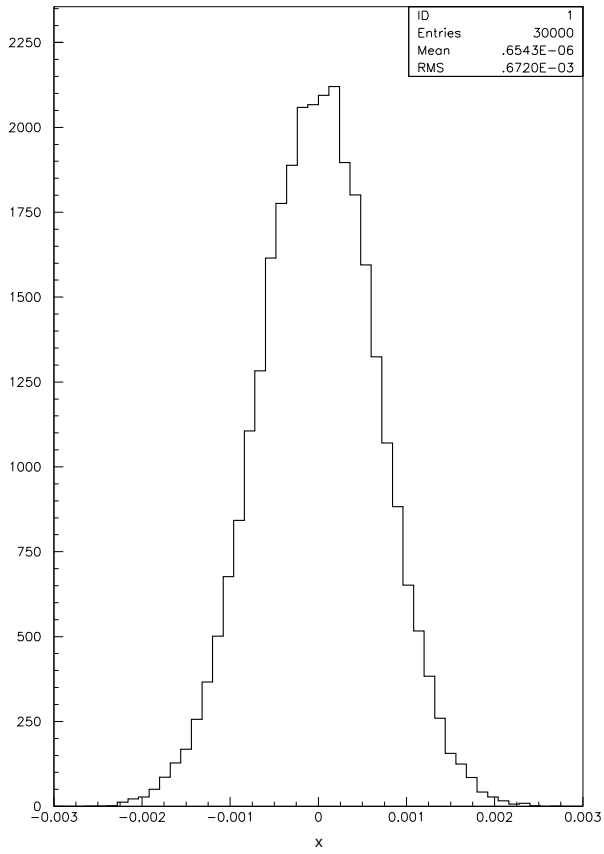

Fig. 60: Distribution of the horizontal particle position x in m at the exit of the seventh pass at 25.3 GeV.

7.4 Beam size and aperture

The data assembled in Section 7.3 may be used to determine the beam size, and hence the aperture needed. Figure 61 shows an example of the results for the sixth pass through the spreader, arc, adaptor, return line, adaptor, arc and combiner and the seventh pass through the linac. The assumptions are described in the caption. It turns out that the aperture radii, ± 28 mm, adopted at the meeting of the CERN internal working group on 12 February 1999 well before the optics of ELFE was frozen, are larger than the values needed.

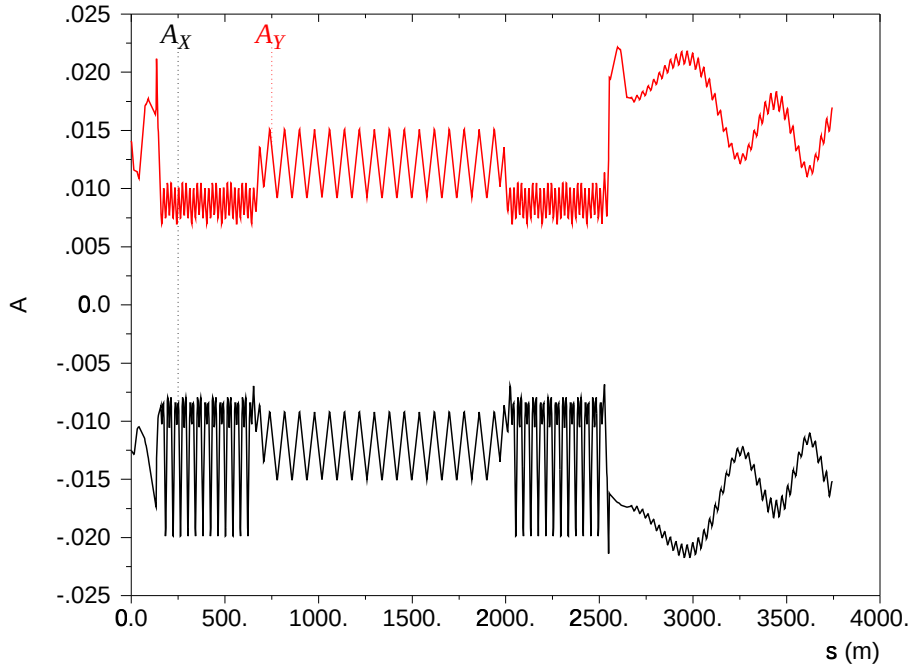

Fig. 61: Vertical A_y and negative horizontal aperture radius $-A_x$ in m for the sixth pass through spreader, arc, adaptor, return line, adaptor, arc and combiner and the seventh pass through the linac. The apertures allow for five r.m.s. beam radii and an extra 5 mm for orbit distortions. The emittances are $\epsilon_x = \epsilon_y = 30$ nm. The relative momentum spread is $\sigma_e/E = 10^{-3}$.

8 Polarization

The polarization at the experiment depends on the polarization of the electron gun, polarization losses in the beam lines and injector, the energy spread in the main accelerator, depolarizing effects due to the magnet lattice, and spin adjustment.

This chapter gives an estimate of the effect caused by the energy spread which is one of the major sources of depolarization in circular accelerators at high energies. It is especially important for ELFE, where the polarization vector of the injected beam is perpendicular to the direction of the magnetic guide field such that polarization can be lost completely.

There will also be depolarizing effects from the magnet lattice. With only six full turns for the beam in ELFE, we expect these effects to be negligible compared with the depolarization caused by the energy spread. For a full study of depolarization, a complete spin tracking through the lattice would be necessary.

8.1 Spin dynamics and depolarization due to energy spread

The discussion here proceeds in three steps. We start with a discussion of spin precession as a function of energy, and the effect of a fixed energy offset ΔE. In the second step, we discuss and illustrate the depolarization caused by a Gaussian energy distribution with a fixed energy spread in all passes. In a third step, this is generalized to allow for different spreads in individual passes. The spin of the electrons precesses under the influence of magnets in a circular accelerator (see Fig. 62). Since the strongest magnets are the bending magnets in the arcs, the main precession axis is vertical. Therefore, unless the beam is injected with all spins already pointing in the vertical direction, the spins precess with a frequency $\Omega_{\rm sp}$ in the particle's rest frame, given by

$$\Omega_{\rm sp} = \gamma a \cdot \omega_0 \quad ,$$

where ω_0 is the revolution frequency, and $a = \frac{g-2}{2} = 1.159652 \times 10^{-3}$, the gyromagnetic anomaly of the electron. The product γa is also called the spin tune, which is directly proportional to the particle energy. For ELFE this means that with each revolution of the electron in the ring the spin vector precesses γa times. After six full revolutions the total spin precession angle[2] is

$$\Phi_{\rm sp} = 2\pi \cdot a \cdot \sum_{n=1}^{6} \gamma_n = 2\pi \cdot 177.7 = 1116.4 \quad .$$

This is valid for the reference particle and defines the polarization design direction which could be adjusted to the direction of the extracted beam by proper choice of the extraction energy. Since the precession depends on energy, a particle with an energy offset will precess faster or slower than the design particle and consequently its spin will not point exactly in the design direction. Only the average of the projections of the individual polarizations with respect to the design direction is useful for the experiment. For instance, particles with an average energy deviation of $\Delta E/E = 10^{-3} = \Delta\gamma/\gamma = \Delta\Phi_{\rm sp}/\Phi_{\rm sp}$ have only a polarization $P = \cos(\Delta\Phi_{\rm sp}) = \cos(\Phi_{\rm sp} \cdot 10^{-3}) = 44\%$.

Now, as a second step we discuss the effect of a Gaussian energy distribution with a constant relative energy spread σ_e/E. With the normalized Gaussian energy distribution of the beam

$$I(E) = \frac{1}{\sqrt{2\pi}\,\sigma_e} e^{-\frac{(E-E_0)^2}{2\,\sigma_e^2}} \quad ,$$

[2]The beam passes through the arcs at energies 4.3, 7.8, 11.3, 14.8, 18.3 and 21.8 GeV. This leads to $\gamma_1 = 8414$, $\gamma_2 = 15264$, $\gamma_3 = 22113$, $\gamma_4 = 28962$, $\gamma_5 = 35812$, $\gamma_6 = 42661$. $\sum_{n=1}^{6} \gamma_n = 153226$.

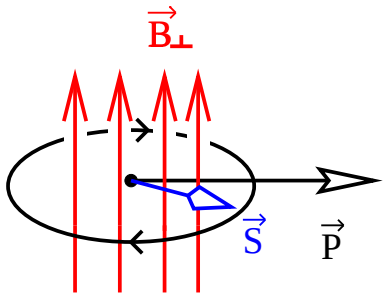

Fig. 62: Thomas precession: In this constellation the precession axis (given by the vertical bending magnetic field $\vec{B}_\perp$) is perpendicular to the particle's momentum $\vec{P}$. In the current ELFE design the spin $\vec{S}$ does more than 177 full turns in the horizontal plane.

we find that the average observed polarization is

$$P = \int_0^\infty I(E) \cdot \cos\left[\Phi_{\rm sp}\left(\frac{E}{E_0} - 1\right)\right] dE \quad .$$

The integral in the expression above can be solved analytically [47]. We introduce the turn number $T = \Phi_{\rm sp}/2\pi$ and $x = E/E_0 - 1$ and obtain

$$I(x) = \frac{1}{\sqrt{2\pi}\,\sigma_e} e^{-\frac{E_0^2 x^2}{2\,\sigma_e^2}} \quad ,$$

and for the polarization

$$(P_L + iP_x) = E_0 \cdot \int_{-\infty}^{\infty} I(x) \cdot e^{2\pi i T x} dx \quad .$$

We see that the absolute value of the polarization P is the Fourier transform of the energy distribution

$$P = E_0 \cdot \tilde{I}(T) = e^{-\frac{1}{2}\left(\frac{2\pi T \sigma_e}{E_0}\right)^2} = e^{-\frac{1}{2}\left(\Phi_{\rm sp}\frac{\sigma_e}{E}\right)^2} \quad . \tag{9}$$

This expression has been used in Fig. 63 to illustrate the degree of polarization as a function of a constant Gaussian energy spread. For a constant energy spread of $\sigma_e/E = 10^{-3}$ we obtain 53% average polarization in ELFE (or $P = 86\%$ for a spread of $\sigma_e/E = 5 \times 10^{-4}$).

Now in the third step, we generalize Eq. (9) to different energy spreads for individual passes and find

$$P_{\rm final} = \exp\left\{-\frac{1}{2}\left[2\pi\, a \sum_{n=1}^{6} \gamma_n \left(\frac{\sigma_e}{E}\right)_n\right]^2\right\} \quad . \tag{10}$$

There is still a variation of σ_e/E within each pass, and the estimate based on this expression will be slightly conservative if we take the energy spread at the end of each pass, as listed in Table 21 in Chapter 7.

8.2 Energy spread

The energy spread in a recirculation linac is determined by the energy spread of the injector, the bunch length, instabilities of acceleration in the linac, and by quantum excitation due to synchrotron radiation in the spreader, recombiner, and the arcs of the main ring.

The energy spread of the injector is small compared to the other effects (of order 10 keV or $\sigma_e/E = 1.2 \times 10^{-5}$, see Chapters 5–6). Moreover, the relative energy spread decreases during the acceleration and can therefore be neglected in this discussion.

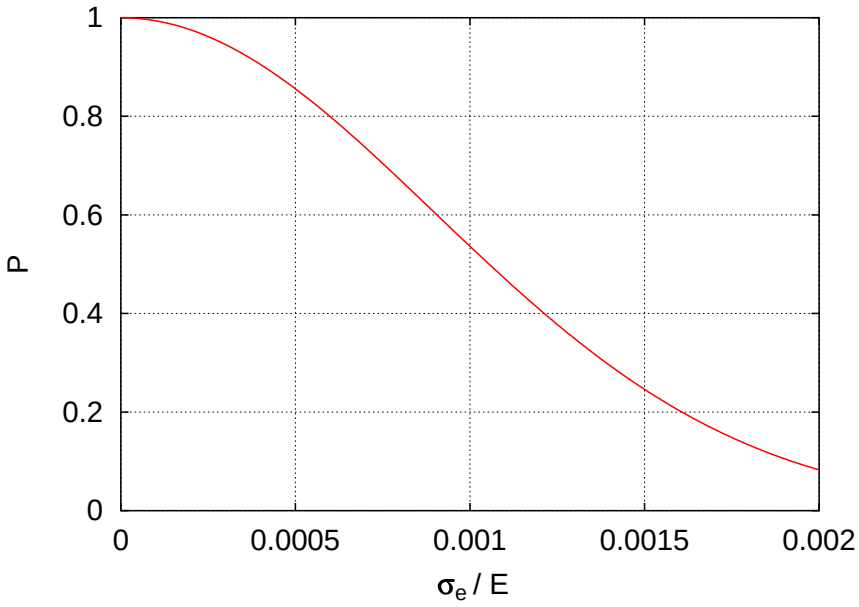

Fig. 63: Polarization in ELFE versus energy spread, assuming the same constant relative energy spread in all passes.

It is thus sufficient to consider only the energy spread in the main ring. This was done in Chapter 7.3 and the results, including both the spread from synchrotron radiation and the bunch length, have been summarized in Table 21. The resulting depolarization levels are listed below in Table 22.

Table 22: Depolarization in ELFE caused by energy spread, taking into account the contributions of individual passes.

Turn No.	Electron energy [GeV]	Energy spread σ_e/E	Polarization %
1	4.3	2.78×10^{-4}	99.99
2	7.8	3.16×10^{-4}	99.86
3	11.3	3.55×10^{-4}	99.40
4	14.8	4.29×10^{-4}	98.02
5	18.3	5.73×10^{-4}	94.07
6	21.8	8.04×10^{-4}	83.56

There is, in addition, a contribution from RF phase and amplitude instabilities in the linac. The energy spread from this source is 2.6×10^{-4}, as described in Section 12.3. This reduces the polarization by 95.87%. Combined with the contributions from quantum excitation and bunch length, we obtain an energy spread of 7.80×10^{-4} for the extracted beam and an overall polarization of 80.1%.

8.3 Conclusion

The loss of longitudinal polarization at ELFE is a much more serious problem than with the low-energy machines like MAMI or CEBAF. The depolarization strongly depends on the energy spread of the electron beam. It has to be kept as small as possible, but there is a lower limit given by synchrotron radiation. When the spread due to the non-zero bunch length is included,

it amounts to $\sigma_e/E = 8 \times 10^{-4}$ at the end of the last full pass at 21.8 GeV energy. In its passage through the main ring, the polarization level of the extracted beam is reduced to 80% of its level at injection.

If it turns out that the loss of polarization due to energy spread is too large, the beam could be accelerated with vertical polarization as is customary for the acceleration of polarized particle beams in a synchrotron. This can be achieved by spin rotation to the vertical direction at the source and rotation back to the longitudinal direction in front of the experimental target. The vertical component would then be conserved in the main ring and only the residual horizontal component be subject to depolarization by the energy spread. A small deviation from the vertical orientation will be caused, for instance, by the horizontal magnetic fields in quadrupoles. The spreader and recombiner will also cause a small deviation from the vertical orientation: the deviations caused by the vertical bends do not cancel exactly, since the energy changes slightly in the passage through the spreader and recombiner by synchrotron radiation. The exact amount of these effects could be determined by spin-tracking studies.

9 Collective effects, beam break-up

In a recirculated linac with low charge per bunch and low current per beamlet, multipass regenerative beam break-up is the dominating collective phenomenon. An off-axis bunch passing several times through the linac cavities interacts with deflecting higher order modes (HOMs). It induces voltages proportional to the bunch charge and displacement and receives transverse kicks from the previously induced voltages. These voltages are attenuated, from one pass to the next, by the HOM absorbers. The bunch kicked by a cavity can return with a larger displacement and therefore induce a larger voltage. Above a certain threshold the power induced in the HOMs is larger than that which is dissipated through the damping couplers and the beam displacement diverges in time.

For a first rough check of the instability current threshold we will use a worst-case formula, simplified with the following assumptions. The linac is represented by a single localized cavity with a single deflecting HOM having a shunt impedance obtained from the sum over all the cavities. For a two-pass configuration one obtains a simple formula for the current threshold [48]:

$$I_{\rm th} = -\frac{2p_{z2}}{k\,R_0\,R_{12}\sin(\omega_s T)} \tag{11}$$

where ω_s is the radian frequency of transverse oscillation of the unstable beam, T is the time delay along the recirculation orbit, k is the mode wave number, p_{z2} is the particle momentum at the exit of the linac after the first pass, R_{12} is the term of the TRANSPORT matrix [49] relating the displacement of the beam after recirculation to the kick received by the deflecting mode in the cavity, and R_0 is the transverse impedance of the cavity HOM defined as $R_0 = Q(R/Q)_T$, with

$$\left(\frac{R}{Q}\right)_T = \frac{1}{2}\left(\frac{1}{k\,a}\right)^2\left(\frac{V_{\rm acc}^2}{\omega\,U}\right)$$

where U is the stored energy, $V_{\rm acc}$ is the longitudinal voltage seen by a particle passing at a distance a from the axis, and Q is the HOM external quality factor.

It is to be noted that in Eq. (11) the injection momentum is included in p_{z2} and the momentum imparted by the linac prevails. The sensitivity to injection energy is therefore rather low. This is not too unrealistic, because in our case the injection momentum is very high (500 to 800 MeV) and the beam is already rigid when it encounters the modes of the initial linac cavities.

For N passes, making the further assumption that the phase shifts around all the orbits at the frequency of the deflecting mode are $2\pi j - \pi/2$, where j is an integer, the current threshold is given by [50]

$$I_{\rm th} = \frac{2p_{z2}}{k\,m\,R_0\,\sum_{s=2}^{N}\sum_{r=1}^{s-1}\;R_{12}^{rs}\left[\frac{p_{z2}}{p_{z2}+(r-1)\Delta p}\right]} \tag{12}$$

where m is the number of cavities and Δp is the momentum increment per pass. Eq. (12) can be simplified without too large a loss of accuracy by neglecting the terms due to interactions of the beams in the higher order recirculations among themselves ($r > 1$), because the weight of those terms decreases with energy. The various terms R_{12} figuring in the sum can be evaluated only through detailed knowledge of the magnetic focusing structure of the whole machine. However, a further pessimistic assumption, consisting in assuming all the terms of the sum equal in magnitude and sign, allows a simplification of the formula which does not require such knowledge. Moreover, R_{12} can be assumed to be of the order of the maximum Twiss beta function in the linac.

The final simplified formula used in the following evaluations is

$$I_{\rm th} = \frac{2p_{z2}}{k\,m\,R_0\,R_{12}\,(N-1)} \quad . \tag{13}$$

Assuming the following values for the parameters and the HOM characteristics of the LEP SC cavities [51], one obtains the threshold values reported in Table 23, $R_{12} = 100\,\mathrm{m}$, $p_{z2} = 4\,\mathrm{GeV}/c$, $N = 7$ passes.

Table 23: LEP SC cavity dipole modes and corresponding break-up thresholds.

Mode	Freq. (MHz)	$R/Q(\cdot)$	$Q_{\rm ex}$	$I_{\rm th}$ (mA)
TE111	461	18	15 300	18
TE111	476	15	12 400	26
TM110	506	20	13 100	17
TM110	513	13	34 200	10
TM111	688	25	5 000	26.5

Several computing codes have been elaborated in recent years at Saclay (BBU-EIGEN), Mainz (HBBU) and TJNAF (TDBBU) to simulate multipass instabilities in recirculating linacs and racetrack microtrons. In the first two codes the bunch structure is ignored. TDBBU considers the wakefieds induced by each bunch in the cavities and tracks the evolution of the beam through the machine focusing lattice, represented with matrices. We have checked our results, for mode TM110 around 513 MHz, with the code TDBBU [52, 53] by simulating the worst-case assumptions illustrated above. We have assumed all identical recirculation matrices and a recirculation delay time $T = 6.6\ \mu$s. Figure 64 shows a scatter graph of current threshold versus HOM frequency. The points lie approximately on a periodic curve with a period equal to the inverse of the delay time T. In the real case, with recirculation paths differing from one another and with corresponding mixing of phase shifts at the frequency of the HOM, we expect the periodicity to disappear and the minimum threshold to rise. In any case, even with all the pessimistic assumptions, the thresholds exceed by more than one order of magnitude the machine working current. Even without detailed calculations we are therefore justified in asserting that there is a large margin of safety against this kind of instability.

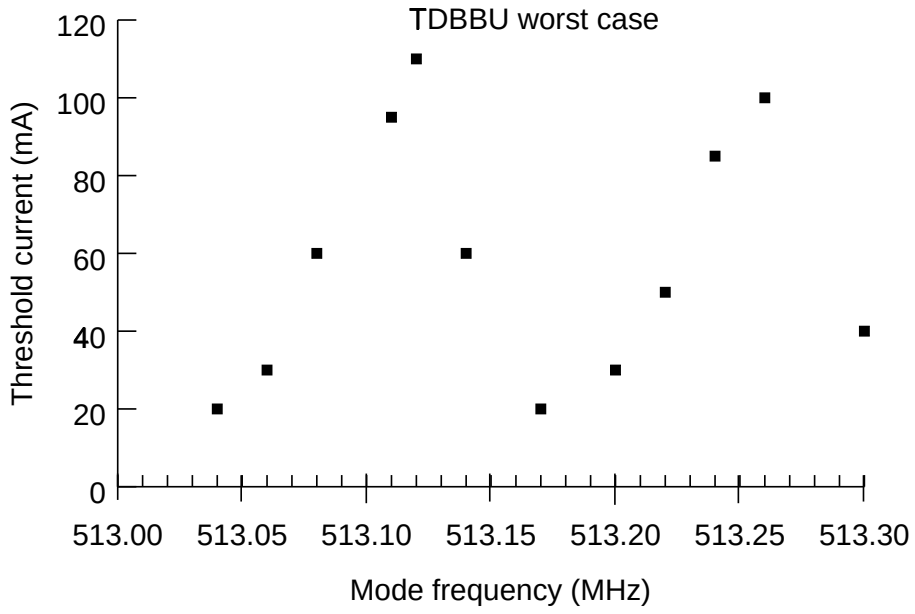

Fig. 64: Threshold current versus HOM frequency in the worst case.

A question has been raised regarding the effect of unshielded 'pill box cavity-like' bellows which could be recovered from LEP and used to connect the beam pipes in the arcs. These cavities do not enter directly into the above illustrated instability mechanism because the beam passes through them only once. Their role is more appropriate for cumulative single-pass beam break-up, but the impedance level of deflecting HOMs is so low and the beamlet current so small that the beam blow-up effect is insignificant. We have computed the characteristics of these transverse HOMs and found that the R/Q is always below 10 and the Q factor is about 1000, the material being stainless steel. The parameter which characterizes this kind of instability is the steady-state e-folding factor [54]. With such a magnitude of the impedance, even with a large number of bellows (about 400 are foreseen) and without focusing, this factor does not have significant values.

10 Overview of the LEP RF system

In this chapter only the major features of the LEP RF system are described; other equipment, such as low power controls, RF reference generation and distribution, is described in Ref. [55].

The LEP RF system is the biggest SC accelerating system built so far. The cavity technology was developed at CERN especially for this project. In total 288 cavities were produced and are currently working well above their design specifications.

The majority of them are made of copper (Cu), sputter coated with a thin layer of niobium (Nb). The specification requires an operating gradient of 6 MV/m at an unloaded Q value of $Q_0 = 3.2 \times 10^9$. In order to achieve the maximum possible beam energy in LEP, to be reached during the year 2000, a programme was launched to raise the useful gradient above the design value, to near 7 MV/m, making use of pulse power processing, helium (He) processing, equalization of cavity fields, etc. [56]. During commissioning of the RF system in 1999 very promising results have been achieved. The Cu/Nb cavities were conditioned *in situ* to an average gradient of 7.2 MV/m. A total voltage of the SC RF system of about 3430 MV has been achieved with beam. During the 1999/2000 winter shutdown and during operation in 2000 efforts will continue to improve the performance further. All these procedures have to be done under the constraints of *in situ* processing in the LEP tunnel.

Sixteen of the 288 cavities are prototypes made of solid Nb, with an operational gradient of about 5 MV/m.

After demounting from LEP, some cavities which degraded or otherwise limited performance can be treated offline. High-pressure rinsing with ultra-pure water can be applied or the cavities can be recoated with a new film of Nb. Improved techniques will possibly be available, allowing the performance to be improved further. A total accelerating voltage of 3500 MV looks feasible.

The normal-conducting RF system of LEP will not be considered in this report.

The LEP2 RF power plant [57, 58] consists of 44 klystrons with a continuous rated output power of 1.3 MW. 22 power converters with a rated power of 4 MW supply the 100 kV d.c. voltage. Each klystron has its own tetrode modulator and the two klystrons, powered by the same HV power converter, are protected by a common thyratron crowbar circuit.

At present the total maximum circulating beam current is about 6.5 mA in two beams of four bunches each.

The RF power distribution is done with a symmetric system of WR2300 aluminium waveguides using magic Tees as power dividers.

During exploitation in LEP many features were implemented in order to improve the reliability of the system. Efforts are continuing to achieve better performance, both towards higher beam current and higher accelerating gradients. The gradients are limited by field emission in the cavities and other sources of high He consumption, such as for example Q degradation. The maximum cooling power per cavity is given by the cryostat design and is about 160 W. A major operational difficulty in LEP is caused by ponderomotive oscillations [59], when the cavities are driven off their resonant frequency. This detuning is caused by beam loading effects, and leads to vibrations of the cavities at their mechanical resonant frequency of around 100 Hz at high fields. Two methods are at present applied to avoid these oscillations: One is to introduce tuning offsets in order to reduce the beam-induced detuning, the other is an active damping system added to the existing cavity tuning equipment.

11 ELFE RF system

In order to leave room for future developments, a beam current of 150 μA on target has been assumed in this section. The design presented in this report makes maximum use of existing equipment. ELFE will use all accelerating cavities from LEP. With refurbishment of some cavities and offline conditioning the total available gradient will be 3500 MV. A chain of 16 cavities will be fed in parallel from the available klystrons. The general layout follows very closely the LEP design. The klystrons and all electronic equipment are outside the accelerator tunnel, in separate buildings above the tunnel, separated by 4 m of shielding.

11.1 Cavities and cryostats

The accelerating cavities consist of four cells of ellipsoidal shape, coupled to each other electrically via the beam hole. 16 of the cavities consist of solid sheet niobium (Nb); the other 272 are made out of copper (Cu), sputter coated with a thin layer of a few μm of Nb. The cavities are made of OFHC Cu, by spinning and electron-beam welding. All vacuum connections are made with stainless-steel knife-edge flanges. Any exposure of the inner surface to air, after cleaning and sputtering, has to be done under clean-room conditions of better than class 100. The cavities are cooled by immersion in a bath of liquid helium (He) at a temperature of 4.5 K; the stainless-steel He container is directly welded onto the cavity structure.

The cavity and its He vessel are flexible; therefore the dynamic frequency tuning during operation can be done by slightly changing the overall length. For this purpose the cavities are enclosed in a cage formed by three nickel (Ni) bars connected to the beam pipes. The length of these bars can be varied by electric heating and simultaneous cooling with cold He gas and via magnetostriction of the Ni by applying a magnetic field. The thermal tuner has a range of 40 kHz; the magnetostrictive one is used for fast variation, within a range of about 1.6 kHz.

Four cavities are grouped together in one common cryostat of about 12 m length, called a 'module'. One cavity section of a module is shown in Fig. 65.

Liquid He is fed into the first cavity and the gas is evacuated from the last one. Thermal insulation is done only via multiple layers of superinsulation foils. Additional static heat load is caused by mechanical cavity suspensions and several connections for each individual cavity: Coaxial RF and control cables, rigid coaxial links between Higher Order Mode (HOM) couplers and RF absorbers, RF power couplers and end cones bridge the full temperature difference between 4.5 K and room temperature. The heat influx through the large cross-section links (RF power couplers and transition cones) is minimized by cooling them with cold He gas. The total static heat losses amount to 20 W per cavity. This has to be compared to the dynamic RF losses of 70 W at 6 MV/m. The cryostat design allows a total cooling power of 160 W to be supplied to each cavity.

The main parameters of LEP cavities in ELFE are given in Table 24.

The operation of the cavities in ELFE is far easier than in LEP for a number of reasons:

- The maximum d.c. beam current in the linac is only 1.05 mA (7×150 μA) as compared to over 6 mA in LEP.
- The low beam current and the high bunch repetition frequency leads to bunch populations of only 1.6×10^7 particles in the linac, compared to 4×10^{11} in LEP at 6 mA total circulating current. This substantially reduces problems related to HOMs.
- Beam-induced detuning will not occur, because the beam passes the cavities at the crest of the RF sine wave. Ponderomotive oscillations are therefore not expected to pose any problem.

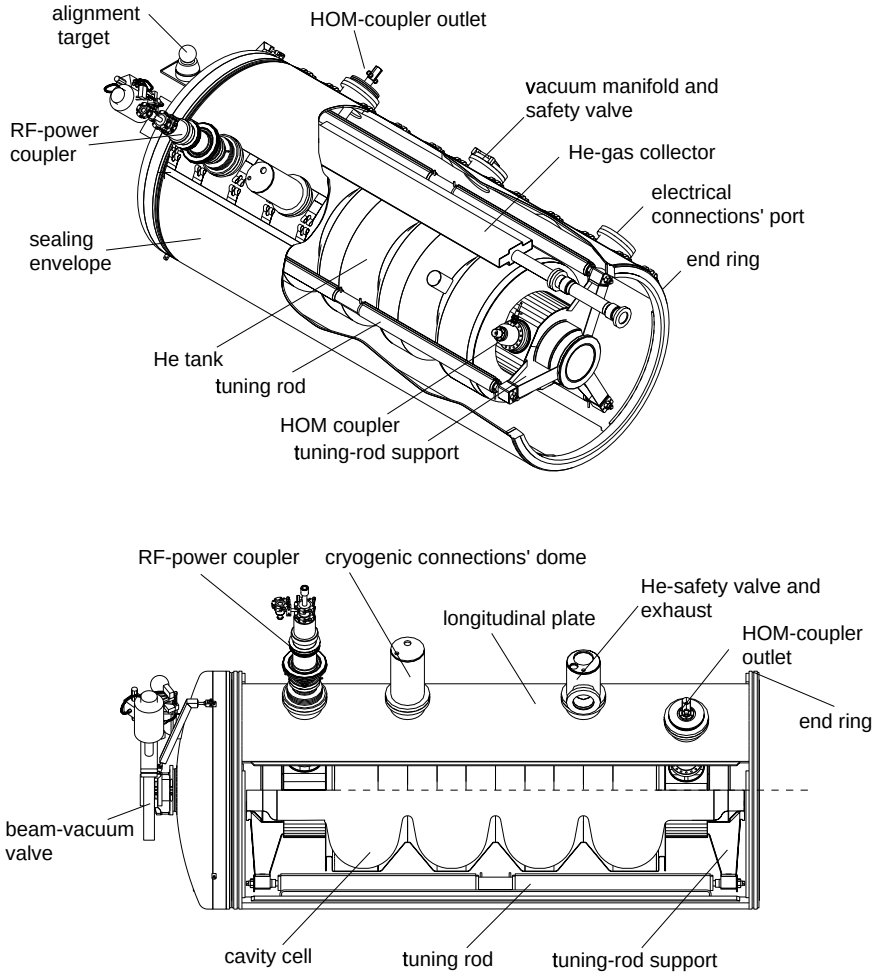

Fig. 65: Superconducting cavity with cryostat section.

Table 24: Parameters of superconducting cavities.

Frequency	352.209 MHz
Operating field	7.3 MV/m for Nb/Cu, 5 MV/m for solid Nb
Number of cavities	272 Nb/Cu, 16 Nb
Number of cells per cavity	4
Effective length (four cells)	1.702 m
$R/Q(R = V^2/P)$	464 Ω
Tuning sensitivity	$\pm$40 kHz/mm
He pressure sensitivity	<10 Hz/mbar
Tuning range:	50 kHz thermal, 1.6 kHz magnetostricive tuner
Q_0 specified at 6 MV/m (4.5K)	$> 3.2 \times 10^9$
Q_0 at low field (4.5K)	$> 6.4 \times 10^9$
Q_0 expected at 7.3 MV/m	$> 2.7 \times 10^9$
RF losses at 7.3 MV/m and 4.5K/cavity	104 W

- Operation is stable at constant field. In LEP, conditions permanently change due to different machine conditions like injection and accumulation of beam at low accelerating fields, energy ramping, and physics coasts.

11.2 Power couplers and higher order mode couplers

The power couplers have a double task: They transfer RF power up to 125 kW into the cavities by coupling to the electric field of the acceleration mode, and at the same time they have to provide an RF transparent seal between the cavity vacuum and the atmospheric pressure in the waveguides. They consist of an all-metallic gas-cooled coaxial line, bridging the temperature difference between 4.5 K at the cavities and ambient temperature through the insulating vacuum. The connection to the waveguides is done via a doorknob transformer, matching the waveguide to the coaxial coupler line. The RF window is a ceramic cylinder, brazed onto the outer conductor in the doorknob transformer. A drawing of the coupler design is shown in Fig. 66.

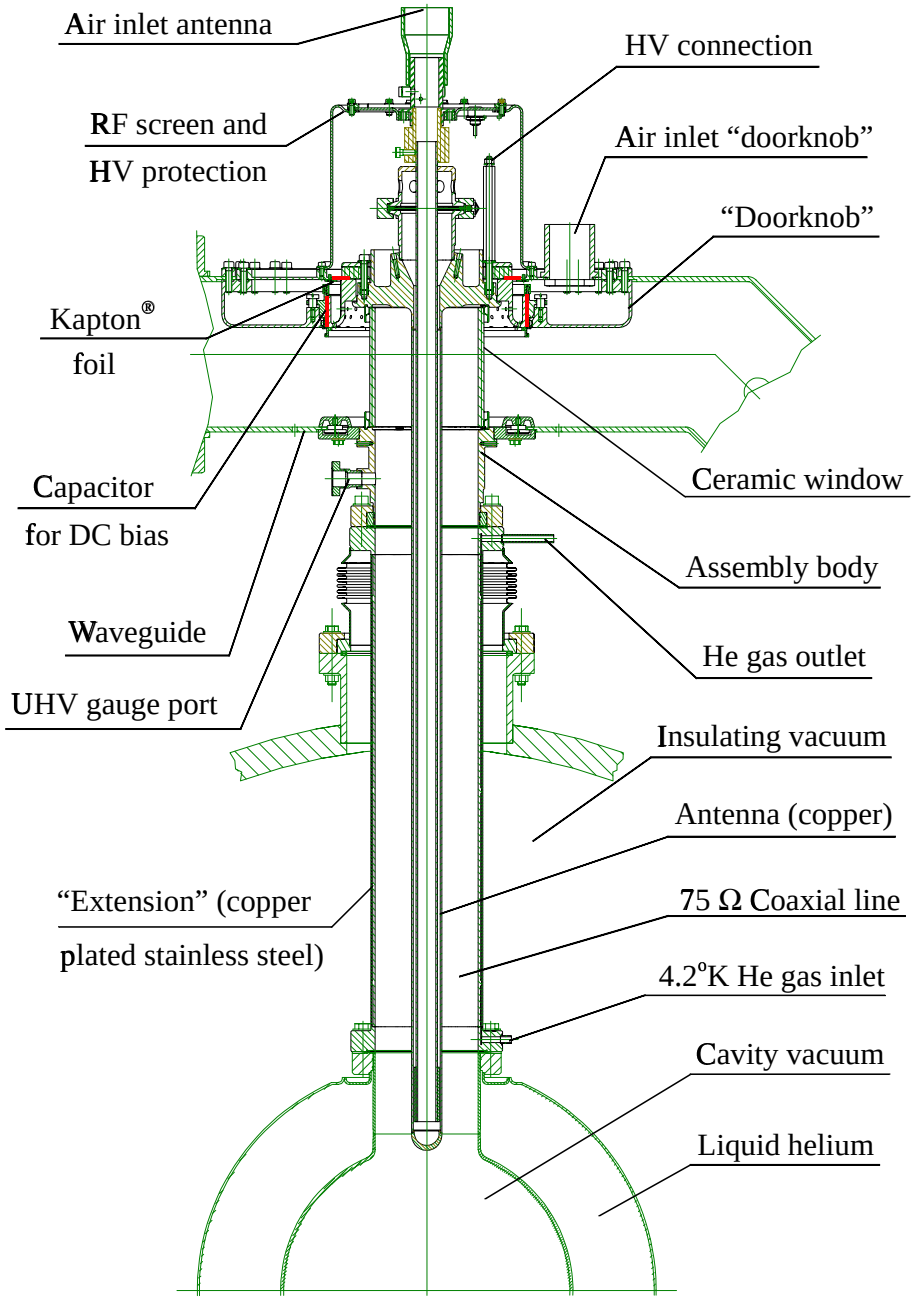

Fig. 66: Power coupler.

Initial problems with multipacting in the coaxial line have been solved by applying a bias voltage of +2.5 kV to the inner conductor and by an *in situ* bake out of the window before cooling. In tests on a dedicated cavity fitted with two couplers, 500 kW of RF power have been transmitted through the cavity, in long-term tests of several days.

At present the power couplers are adjusted to give a loaded Q value of $Q_{\mathrm{L}} = 2.2 \times 10^6$. For ELFE beam currents of up to 1.05 mA in the cavities the coupling factor of the power coupler for optimum power transfer to the beam requires an external Q factor $Q_{\mathrm{L}} = 2.2 \times 10^7$ at 7 MV/m. This results in a cavity bandwidth of only 15 Hz, which makes tuning of the cavities very difficult. A bandwidth of 70 Hz (compared to the present 176 Hz) seems possible, which gives $Q_{\mathrm{L}} = 5 \times 10^6$. The RF power per cavity at 7 MV/m and 1.05 mA is then 22.1 kW, out of which 10.7 kW are transferred to the beam, while 11.4 kW are reflected back to the klystron. This is far below the power handling capability of the couplers and should allow very safe operating conditions.

The cavities are equipped with two HOM couplers mounted on the beam pipes, one at each side of the cavities. They couple to the electromagnetic fields via a loop with an integrated rejection filter for the fundamental accelerating mode. Previous problems were solved by geometry changes and increased cooling. The power they extract from the cavities is transported to RF absorbers outside the cryostats through rigid coaxial lines. The whole system was tested up to 850 W CW RF power per coupler at 630 MHz and beam currents up to 8 mA.

For LEP conditions this bunch length of 3 mm would be unacceptably short, because of problems with HOM couplers, and RF pick-up cables in the cryostats. The HOM power P_{HOM} excited by the beam is given by

$$P_{\mathrm{HOM}} = k \, \frac{i^2}{f_{\mathrm{b}}}$$

with k being the loss factor of the structure in question, i the total d.c. current, and f_{b} the bunch repetition frequency. The HOM power generated by a beam of 1.05 mA is only 7.7×10^{-6} of that in LEP with a beam of 6 mA for the same loss factor. The loss factor depends on bunch length and is not more than a factor of 10 higher at 3 mm than at 8 mm. Therefore no problems are expected from HOMs due to the short bunches.

11.3 Modifications to cavities before reuse

The LEP power couplers are adjusted to an external Q value $Q_{\mathrm{L}} = 2.2 \times 10^6$ to match the cavities to the LEP beam current. As shown above, for reasons of RF power consumption the coupling factor of the RF power couplers has to be modified to $Q_{\mathrm{L}} = 5 \times 10^6$. This can be done by withdrawing the inner conductor of the couplers by several cm, an operation which requires opening the beam vacuum and inserting a spacer into the outer conductor. This is a relatively simple operation; however, it must be done in a clean room, as any operation involving the cavity beam vacuum. The relatively small change in Q_{L} could alternatively be achieved with transformer plates in the waveguides in front of the cavities, thereby avoiding opening the cavity vacuum.

Some of the cavities which are limited in performance will have to be refurbished after removal from the tunnel. This will require rinsing with ultra-pure water, and probably new sputter coating of the inner surface and repair or replacement of deteriorated components. Based on present LEP experience, we expect that no more than 5% to 10% of all cavities will need repair. Conditioning to higher gradients, using pulse processing and He processing can be done in dedicated test stands, wherever necessary.

11.4 RF power plant and controls

The proposed coupling factor of the power couplers gives a loaded Q value of $Q_{\mathrm{L}} = 5 \times 10^6$ for a beam current in the linac of 1.05 mA at a gradient of 7.3 MV/m. 22.1 kW are required at the cavity window, out of which 10.7 kW are transferred to the beam, while 11.4 kW are reflected back to the klystron.

The available klystrons have a specified output power of 1.3 MW. One klystron, protected by a circulator, feeds 16 cavities in parallel. The RF power per klystron is about 360 kW, which should guarantee very reliable operation. In total 18 klystrons are required, in LEP 44 klystrons are installed. The efficiency of the klystrons at this power level is about 50%. In LEP 22 klystron power converters, each with a rated output power of 4 MW d.c. at 100 kV, are used. One such power converter supplies two klystrons, therefore nine are required for ELFE. The option to power each cavity individually with it's own klystron has not been studied for cost reasons.

The RF power distribution uses LEP standard WR2300 waveguides in a symmetrical splitting arrangement with magic Tees, like the LEP system. Compared to a linear system with waveguide directional couplers with varying coupling ratios as power splitters, this system has equal electrical lengths between the klystrons and each cavity and is thus in principle not sensitive to changes of electrical lengths due to temperature variations. In order to minimize the number of feedthroughs into the accelerator tunnel all splitting stages are in the accelerator tunnel. Full-height waveguides are used for the first four splitting stages; from then on half-height waveguides are used for the remaining two stages for space and cost reasons. The half-height waveguides have slightly higher RF losses. The power lost in the waveguides is 21 kW per 16 cavities at a klystron power of 350 kW. Since some of the RF power is reflected back to the klystrons, the total power dissipated in the waveguides amounts to about 30 kW per unit of 16 cavities. A schematic view of the layout of the waveguide distribution system is shown in Fig. 67.

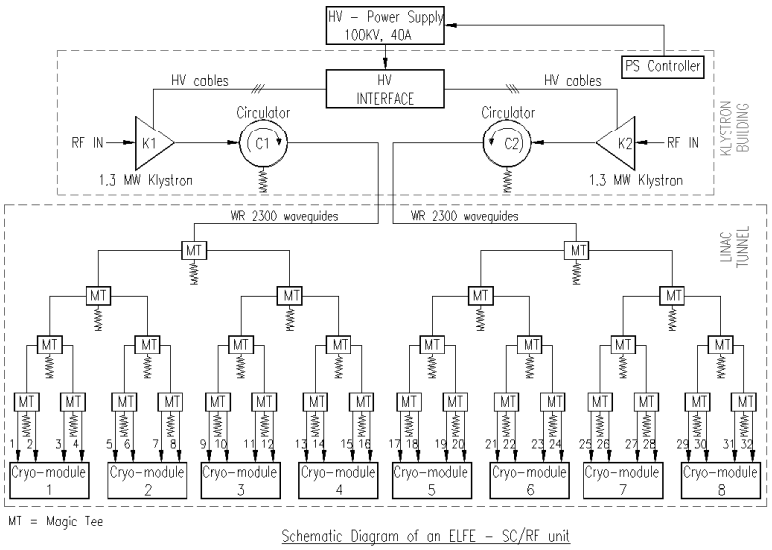

Fig. 67: Schematic layout of the waveguide distribution system.

Two klystrons with circulators as well as the electronic control racks for 32 cavities will be located in individual surface buildings, separated from the accelerator tunnel by a 4 m thick earth/concrete shielding. This is considered to be significantly cheaper than a continuous klystron gallery parallel to the whole linac tunnel. In total nine such buildings will be required. Each surface building provides space for a spare klystron, in order to limit down-time in case of failures. The power converter electronics for the d.c. supply as well as the high-voltage interface with crowbar [57] are also located in this building.

11.5 Low-power controls

It is proposed to use a maximum of the LEP RF low-power equipment. The klystron output power is controlled via the modulating anode (slow, limited to about 10 Hz) and via a fast RF feedback, acting on amplitude and phase of the RF drive into the klystron. The RF feedback is based on the vector sum of the fields in all 16 cavities driven by the same klystron.

11.6 RF reference distribution

The RF reference signal is generated with a synthesizer, synchronized to the GPS system. A frequency stability of 1×10^{-12} is achieved with this system. Additionally a rubidium stabilized synthesizer is available.

The RF reference signal is distributed to the klystrons via optical fibres, equipped with an active phase stabilization system [60]. Over a length of 9.5 km a phase stability of $\pm$ 2 degrees can be obtained with the LEP system.

11.7 Cavity tuning

The cavity tuning system will be taken from LEP. The cavities are tuned by longitudinal deformation with a slow thermal system, giving a range of 40 kHz and a fast (several Hz) system with a tuning range of 1.6 kHz. Additionally an active damping system is available which was developed to work at the frequency of mechanical resonances around 100 Hz. This system acts on the magnetostrictive tuner.

The system uses the phase between the forward-travelling wave towards the cavities and the cavity fields. All RF systems are mixed down to 20 kHz, phase detection is done at 20 kHz.

The residual phase jitter achievable with this system is about $\pm 2.5^\circ$.

12 Momentum spread due to RF

The beam specification requires a relative r.m.s. momentum spread of $\sigma_e/E < 1 \times 10^{-3}$. This is quite demanding for the RF system. Part of the momentum spread is created in the arcs by emission of synchrotron radiation. In this chapter various contributions from the RF system are estimated. All these effects cause both an energy distribution over the bunch described by the relative r.m.s. value σ_e/E and an energy offset of the centre of gravity of the bunches, the relative value of which is δ_e. Both these values are estimated in the following up to second order of bunch length σ_z and tuning angle ψ.

12.1 Bunch length

The bunches are accelerated at the crest of the sine wave. The maximum relative momentum spread over a Gaussian bunch of r.m.s. length σ_z and the relative energy offset are given by

$$\sigma_e/E = \frac{1}{\sqrt{2}} \left(\frac{\omega\, \sigma_z}{c} \right)^2 \qquad\qquad \delta_e = \frac{1}{2} \left(\frac{\omega\, \sigma_z}{c} \right)^2 \ .$$

Here ω is the angular RF frequency, c the speed of light. A bunch length of 3 mm gives $\sigma_e/E = 3.4 \times 10^{-4}$ and $\delta_e = 2.4 \times 10^{-4}$. The energy offset is constant in time.

12.2 Cavity-field oscillations

A change of a cavity's geometry because of mechanical movements of it's walls is associated with a variation of the cavity resonant frequency. Since the cavities are driven with a fixed RF frequency, this leads to a change of the cavity-field amplitude and of the RF phase between the RF generator and the cavity by the tuning angle ψ. The centre of the bunch sees a cavity field of

$$E = E_{\mathrm{res}} \cos^2(\psi)$$

where E_{res} is the field at resonance. This changes the energy gain of the centre of gravity of the bunches as well as the energy distribution over the bunch. This can be expressed in terms of the tuning angle ψ up to second order:

$$\sigma_e/E = \frac{\omega\, \sigma_z\, \psi}{c} \qquad\qquad \delta_e = \psi^2 \ .$$

Three sources of cavity oscillations play a role in LEP:

- Beam-current-dependent ponderomotive oscillations are caused by coupling between stored RF energy and mechanical oscillations of the cavities at a cavity resonance of about 100 Hz. The oscillations occur when the cavities are driven off resonance. This happens at high beam loading, when the tuning system changes the tuning angle in order to keep the cavity impedance real. Since in the linac the bunches are accelerated on the crest of the wave, the detuning angle vanishes and the cavities are always at resonance. Ponderomotive oscillations are therefore not expected to be a problem.
- Thermo-acoustic oscillations. The major source of thermo-acoustic oscillations has been identified and cured by filling up oscillating volumes in the He supply circuit. The residual jitter on some cavities is still 5° peak-to-peak. However, hardware modifications not possible in the LEP tunnel should allow them to be suppressed completely.
- Pressure oscillations, noise and mechanical vibrations. Pressure oscillations are slow and can easily be tuned. Coupling to other sources of oscillations has never been a problem in LEP.

The residual phase jitter is of the order of about 5° peak-to-peak. The above equations have been applied to a bunch of r.m.s. length 3 mm, assuming an even distribution of the phase errors with 2.5° maximum. This gives $\sigma_e/E = 9.6 \times 10^{-4}$ and $\delta_e = 5.7 \times 10^{-4}$. The oscillations are incoherent from cavity to cavity, such that the overall effect on the energy distribution inside bunches reduces to $\sigma_e/E = 5.7 \times 10^{-5}$.

The rather high maximum energy offset can be reduced with the vector sum RF feedback system described above and with the energy feedback proposed below. With the phase precision of the vector sum feedback of one degree one should achieve $\sigma_e/E = 9.1 \times 10^{-5}$ and $\delta_e = 2.2 \times 10^{-5}$.

12.3 RF amplitude and phase control

Amplitude and phase errors of the RF power delivered to the cavities cause energy variations from bunch to bunch.

12.3.1 RF phase

The effect of stability and precision $\Delta\varphi$ of the phase of the RF signal feeding the cavities on σ_e/E and δ_e is given by (for a Gaussian bunch)

$$\sigma_e/E = \frac{\omega\,\sigma_z\,\Delta\varphi}{c} \qquad\qquad \delta_e = \frac{1}{2}\,\Delta\varphi^2 \ .$$

All klystrons are fed by one master oscillator via a phase stable reference distribution. In LEP this is done via optical fibres with an active phase stabilization system, providing a stability of the order of 2°. The phase around the klystrons and the waveguide distribution is kept constant by means of a control loop to within an error of about one degree. Assuming an even distribution of errors with a total maximum of three degrees we get $\sigma_e/E = 1.1 \times 10^{-3}$ and $\delta_e = 4.1 \times 10^{-4}$. For incoherent errors of the 18 RF stations (16 cavities each) we get $\sigma_e/E = 2.6 \times 10^{-4}$. Better performance requires further developments.

12.3.2 Amplitude control of RF power

The stability of the cavity amplitudes is directly proportional to the energy offset for coherent errors. The modulation of klystron power with multiples of the mains frequency will have to be suppressed. Developments are needed to achieve the required precision.

12.4 RF feedback on vector sum of cavity fields

The fast vector-sum feedback, developed for LEP, can control amplitude and phase of the accelerating voltage seen by the beam for a group of 16 cavities fed by one klystron to within about one degree, which is sufficient, assuming that the oscillations are incoherent. The amplitude precision is only about 1%. For better performance more developments are needed.

12.5 Numerical simulations of the energy spread

In addition to the analytical estimates of the different contributions to the energy spread discussed above, numerical simulations were done, in order to verify the results quantitatively. A computer code, originally developed for investigating field emission and RF resonant discharges in TW accelerating structures, has been modified and optimized for this task. Large errors in phase and amplitude were assumed, in order to get significant effects.

- **Influence of phase errors.** An accelerating section consisting of 16 cavities, fed by a single klystron, has been simulated, assuming phase errors of 10 degrees peak-to-peak from cavity to cavity, randomly distributed around the synchronous phase. The energy distribution obtained at the end of the section has $\sigma_e/E = 1.1 \times 10^{-4}$. For the last pass through the whole linac a randomly distributed phase error of $\pm$ 7.5 degrees has been simulated. The result is $\sigma_e/E = 1 \times 10^{-4}$.
- **Influence of amplitude errors.** For an even distribution of RF amplitudes with a relative variation of 10% maximum from cavity to cavity, the simulations give a relative energy distribution at the end of the first accelerating section (16 cavities) of $\sigma_e/E = 1.6 \times 10^{-3}$.
- **Vector sum.** The effect of the vector-sum feedback has been simulated on the whole linac (18 RF stations, 16 cavities each). The required value of the field amplitude of each module is kept fixed, allowing a residual phase error (randomly distributed) of 15 degrees from cavity to cavity. The particles at the end of the first 16 cavities have a relative r.m.s energy distribution of $\sigma_e/E = 1.5 \times 10^{-2}$, whilst at the end of the linac $\sigma_e/E = 6 \times 10^{-4}$. Furthermore the mean energy of the beam is reduced by 1%.

The simulations are in agreement with the analytical results.

12.6 Feedback on beam energy

In view of the contributions to the relative momentum spread of the beam mentioned above, it looks difficult to achieve the target value without feedback. We therefore plan to use a measurement of the beam energy to feed back on the amplitude and phase of some RF stations. This spectrometer should be able to measure both the energy of the centre of gravity of the bunches, as well as the width of the energy distribution inside the bunch. It could either be a dedicated instrument or integrated into the beam lines.

13 Cryogenics

13.1 Introduction

Cryogenics will be mostly involved in the linac for the cooling of the SC cavities. It will have to be built from scratch as the LEP cryogenic infrastructure will be entirely converted for LHC. Besides, a SC injector is envisaged as an alternative to the reference microtron injector. It will require a dedicated standalone system of about 600 W at 2 K to be studied. In case the experiments need cryogenic support, existing cryogenic plants serving the north area facilities at CERN will have to be converted. This chapter covers the cryogenic aspects of the main ring of ELFE. Variants and possible ways of optimization are also proposed.

13.2 Review of heat loads and total cooling power required

The heat loads review given in Table 25 is based on LEP measured data whenever possible or on expressed assumptions. For the time being, the 72 existing modules of four cavities are foreseen along the 1.1 km linac, requiring the total cooling power given in Table 26. As the uncertainties on the various loads are relatively low, the installed capacity has been defined with the minimum margins of 5%. One has nevertheless to keep in mind that there are no contingencies for potential beam-induced losses.

Table 25: Review of heat loads.

	Heat load values	Comments
Static	107 W at 4.5 K (per module)	• 80 W for the module itself (measured during acceptance tests) • 27 W for the helium lines contribution (measured during acceptance tests)
Liquefaction	0.80 g/s of LHe (per module)	Couplers and tuners measured losses
Dynamic	532 W at 4.5 K (per module)	Assuming a Q value of 2.3×10^9 at 7 MV/m [5]
Thermal shield	12 000 W at 75 K (for the linac)	Conservative value based on 10 W/m^2 1200 m helium lines

Table 26: Total cooling power required.

	Installed capacity (including 5% margins)	Comments (Equivalence at 4.5 K)
Refrigeration at 4.5 K	48.3 kW	1 W $\Leftrightarrow$ 1 W
Liquefaction	60.5 g/s	1 g/s $\Leftrightarrow$ 125 W
Thermal shield (50 to 75 K)	12.6 kW	1 kW $\Leftrightarrow$ 70 W
Total equivalent at 4.5 K	57 kW	1 kW $\Leftrightarrow$ 70 W

13.3 Description of the cryogenic system

The proposed cryogenic system illustrated in Fig. 68 is based on proven functional blocks similar to existing units in operation at CERN. The total helium inventory is stored as gas. This will

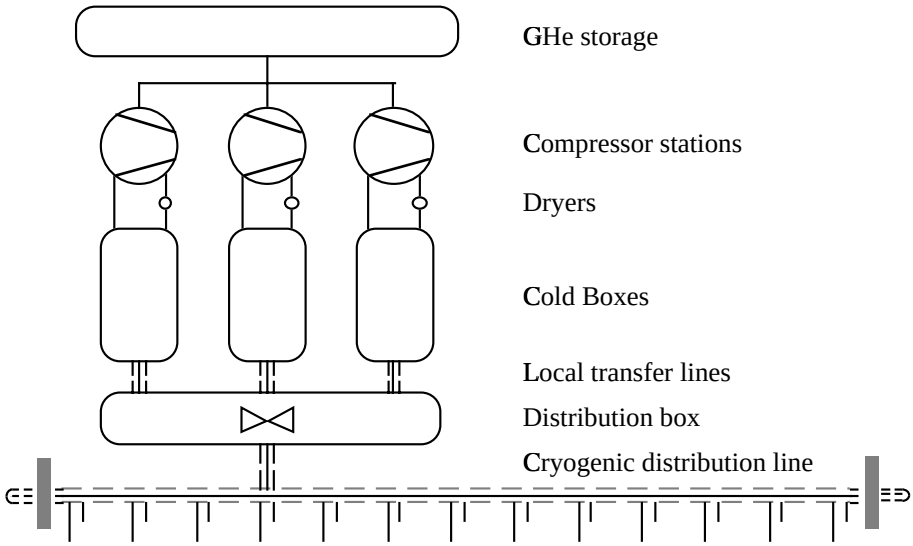

Fig. 68: ELFE cryogenic system principle.

allow the recompression and storage of evaporated helium in case of power supply failures. In view of the large quantity of helium to be liquefied when filling the modules, a helium drier is foreseen. The total refrigeration capacity of 57 kW at 4.5 K could be achieved using three refrigerators of 19 kW at 4.5 K each, similar to the four 18 kW at 4.5 K currently in operation with LEP (original 12 kW recently upgraded to 18 kW). The three refrigerators, grouped in the centre of the linac, are connected via local helium transfer lines to a distribution box. From this interface, the cryogenic distribution line enters the linac and covers the 1100 m of radio-frequency (RF) accelerating zone. The valves and instrumentation for RF couplers and tuners are installed in the linac itself in front of each module. One should keep in mind that the redistribution of cold gaseous helium from the loads back to the three refrigerators could be a delicate point. It might require extra pressure drop in the distribution box to balance the flows properly.

13.3.1 Helium inventory and storage

The helium inventory is given in Table 27. Based on 250 m^3 horizontal storage tanks at 20 bar as done for LHC, a minimum of 14 tanks will be necessary. The delivery of liquid helium with appropriate filtering will reduce the impurities in helium to the minimum possible at the source. Nevertheless, the large helium inventory that could be stored in gaseous form implies that a drier be connected to the inlet of each cold box, each of them including as well adsorbing beds for air components.

Table 27: Helium inventory.

	Helium inventory	Comments
Refrigerators	7 500 Nm^3	2500 Nm^3 each
Helium lines	10 000 Nm^3	LHe=1100 kg, GHe=500 kg
Modules	38 300 Nm^3	700 litres / module
Total	56 000 Nm^3	

13.3.2 Refrigerators and distribution box

The refrigerators are identical and consist of a compressor station and a cold box. Such cooling power could lead to a total helium flow rate of about 1400 g/s per 19 kW at 4.5 K, with a Joule–

Thomson flow of about 900 g/s and a cumulated precooling turbine flow of 450 g/s. An efficiency close to 30% of Carnot could be expected. The compressor station providing gas at about 20 bar is made of five to seven oil-lubricated screw compressors with the dedicated oil removal system. The cold box includes all expansion turbines, heat exchanger blocks, 80 K adsorbers for air-component trapping and valves for process control. Unlike for LEP where cold helium had to be brought back to the surface over about 100 m against its own weight, the ELFE linac is almost at the surface allowing the usual single cold box design. Liquid nitrogen precooling is not included as only relatively small masses have to be cooled down.

13.3.3 Transfer lines

A compound design including supercritical helium delivery, cold gaseous helium return and a thermal shield loop in the same vacuum jacket is envisaged. This will correspond to a maximum outer diameter of the vacuum jacket of about 450 mm. Making use of existing LEP2 helium transfer lines would impose constraints on the system architecture. The centralized cryogenic production place would have to be replaced by two distinct zones, as the maximum length of the lines is 250 m. It would also impose a given arrangement of the modules as there are 'left' and 'right' ones. Therefore, this scenario has not been studied further.

13.3.4 Module hardware

Valves and instrumentation for RF couplers and tuners will be installed in the linac along each module. Proper tests after LEP dismantling will show how much of existing hardware could be re-used.

13.4 Infrastructure requirements

13.4.1 Buildings

For the helium storage tanks, two layers of seven units are proposed, with similar slabs to the existing ones and foreseen for LHC. For the compressors, three standard areas of about $15 \times 40\,\mathrm{m}^2$ are envisaged. There should also be the provision of three times 50 m^2 for the electrical sub-stations, 20 m^2 for the instrumentation air production, 40 m^2 for truck unloading, 300 m^2 for spare parts storage and work place, and 60 m^2 for local control units. In total, this makes 2400 m^2 with 6 m useful height below the crane hook. Standard CERN construction with concrete walls could be envisaged at this stage. For the cold boxes, three standard areas of about $10 \times 25\,\mathrm{m}^2$ should be envisaged, about $30 \times 10\,\mathrm{m}^2$ for the distribution box and local lines, 40 m^2 for unloading, 60 m^2 for local control units and supervision, totalling about 1200 m^2 with 10 m useful height. Standard CERN construction with metallic walls could be envisaged. A $1 \times 1\,\mathrm{m}^2$ duct should connect the storage tanks to the compressor building and a $2 \times 2.5\,\mathrm{m}^2$ gallery should connect the compressor building to the cold box building, the latter being close to the centre of the linac.

13.4.2 Cranes

The typical 20 ton crane for the compressor building allows installation of the machines and later on maintenance or special interventions. As the cold boxes' weight is expected to be above 50 tons, their installation is envisaged with an appropriate rented crane. A 5 ton crane allows maintenance or potential interventions on the cold boxes.

13.4.3 Power supply

With a power factor of 250 W/W, the 57 kW at 4.5 K installed power will result in a nominal power consumption of 14 MW. With 1.2 power rating of the motors, the installed power to be considered will be about 17 MW. At least one compressor ($\approx$ 1 MW) of each refrigerator should be supplied with a back-up to allow for recompression of evaporated helium in case of utility failure.

13.4.4 Cooling water

For the design of the cooling water capacity required, a value equal to the nominal power consumption is considered, i.e. 14 MW. This covers both compressor and cold box needs.

13.4.5 Ventilation

A typical value to be considered for the compressor building is about 4% of the nominal power consumption, i.e. 600 kW. As can be anticipated from estimates on the existing LEP2 system, cooling units will not be necessary.

13.4.6 Instrumentation air

By the time it will be needed, one could anticipate that digital valve positioners with reduced air consumption will be available. Therefore, a typical 300 Nm^3/h unit with –40°C dew point will suit the needs.

13.5 Possible ways of optimization to reduce costs

13.5.1 Operating temperature

One should consider operating the cavities at lower temperature, thus reducing the heat loads to be evacuated. As the cost of cryogenic power will increase when decreasing the operating temperature, a theoretical optimum could be defined. As lower temperature means lower pressure and as the cryogenic hardware of the LEP2 modules was not designed for subatmospheric pressures, technological reasons could prevent reaching the theoretical optimum. Nevertheless, it has been measured that a reduction of 0.3 K of the operating temperature will result in a 16% reduction of the dynamic cryogenic power. One could envisage operating the cavities at 4.2 K (1.0 bar), which corresponds to ambient pressure, and compensate the corresponding 0.3 bar at the refrigerator entrance by cold pumps similar to the one foreseen for LHC or by more warm compressors.

13.5.2 Maximum refrigerator size

One should also investigate if 30 kW at 4.5 K refrigerator units could be built, as this might bring some savings on these units and would suppress the distribution box.

13.5.3 A different way of contracting cryogenic power

When preparing the existing contract concerning operation and maintenance of cryogenic installations at CERN, the idea of subcontracting the entire system has been expressed. This would mean purchasing cooling power at 4.5 K with a given availability. Although such principles are now common in industry for the supply of clean gas (e.g. hydrogen) it is not yet the case for cooling power. One should also investigate how this could be implemented at CERN and how long the original gain in capital costs would remain profitable to CERN.

13.5.4 Improved cavities

As considered for the latest LEP performance maximization scenario [61], the average quality factor of the cavities is slightly lower than the nominal value, thus leading to lower heat losses. An economical trade off between treating the worst cavities to reduce the refrigeration capacity required and keeping them 'as stored' but purchasing somewhat larger refrigeration capacity should be studied.

14 Magnets

This chapter summarizes the design of the magnets needed for the ELFE accelerator. All magnets are of the traditional iron-dominated type. The yokes are laminated using low carbon steel sheets of 1.5 mm thickness stacked between massive low carbon steel end-plates. The coils are built from rectangular OFHC copper conductor with a circular cooling hole. The conductor dimensions are chosen from standard sizes readily available from manufacturers. The inter-turn and mass insulation is made from half-lapped glass-fibre tape. The coils are vacuum impregnated in a radiation-resistant epoxy resin.

To align the magnets, standard Taylor Hobbson spheres are used. To save space in the vertical direction, they are mounted on the side of the magnets. Reference surfaces on top of the magnets serve to adjust the magnet tilt.

To ease reference to the individual magnet types, the following naming scheme is introduced:

First letter	Equipment category **M** = Magnets
Second/third letters	Function **B** = Bending **Q** = Quadrupole **S** = Sextupole **CB** = Corrector Bending
Third/fourth letters	Location **A** = Arc **L** = Linac **S** = Spreader **R** = Return lines **M** = Matching section
Fourth/fifth letters	Further characterization of types as necessary

The following sections describe the individual magnet types. The characteristics of all magnets are tabulated in the last section.

14.1 Arc dipoles

The arc dipoles have to be vertically as compact as possible in order to keep the distance between the recirculation arcs as small as possible. This favours H-type magnets. However, because of the synchrotron radiation, the coils have to be positioned in such a way that they are not in the mid-plane of the magnet. To increase mechanical stiffness and reduce sag, angular plates are used as tension straps. The pole profile contains shims to obtain a good transverse field homogeneity while keeping the aperture width as small as possible. This is desirable as the thickness of the return yoke is proportional to the aperture width. The poles are tapered to reduce saturation effects in the shim area. On the one hand this reduces losses in the pole area, on the other hand the transverse field homogeneity is less affected by the different field levels needed for the individual arcs.

The coils are racetrack coils, which is the simplest and cheapest coil type. The two coils of each magnet are separated by jacks, they are mechanically insulated from the yoke by means of epoxy/glass-fibre laminate and radiation-resistant rubber. The coils are designed to have only one cooling circuit, which simplifies the hydraulic and electrical connections of the coil tails. A low current density was chosen to minimize the overall cost of the magnets and the electricity consumption.

Two different types of arc dipole are used: one type for the three lower energy arcs (MBAL) and a second type for the three higher energy arcs (MBAH). The basic shape and the length of both types are the same. The magnets differ in the aperture width and height (and therefore by the outer yoke dimensions) as well as the number of turns of the coils and the conductor dimensions.

Figure 69 shows the field line distribution in the high-energy arc dipoles (MBAH) obtained from a 2D finite element calculation. Only one quarter of the magnet is modelled; the symmetry is accounted for by appropriate boundary conditions. The relative transverse field homogeneity is better than 5×10^{-4}.

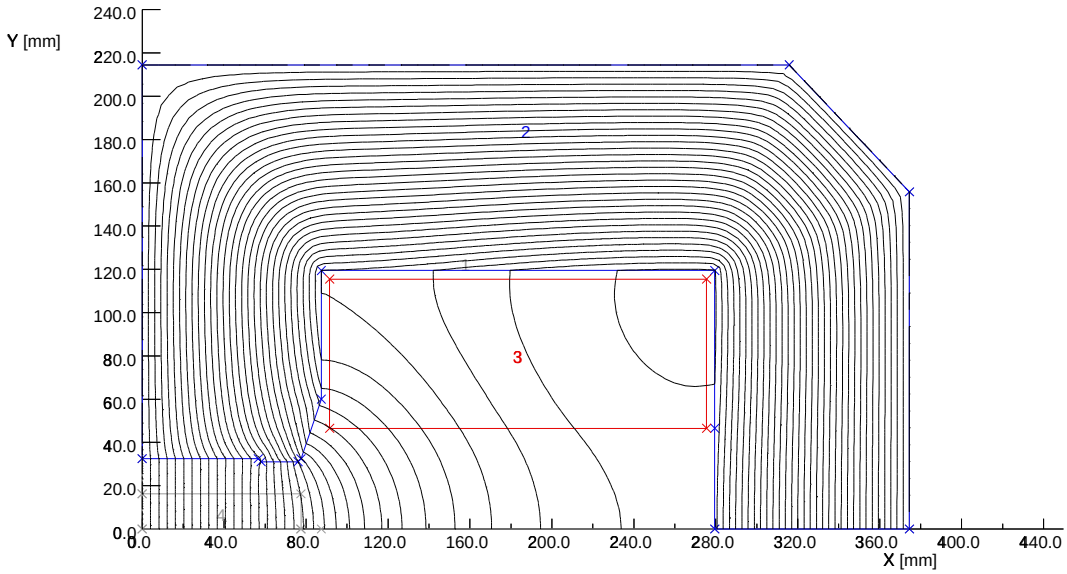

Fig. 69: Field lines in the MBAH dipoles.

14.2 Arc quadrupoles

The pole profile used for the arc quadrupoles has a hyperbolic central part, followed by a straight line which is a tangent to the hyperbola, and a radius as transition to the coil window. The linear part acts as a shim to improve the transverse field homogeneity while limiting the physical aperture of the magnet.

As the required gradients are rather low, the pole-tip field can be chosen so low that the poles can be built non-tapered. This permits the use of simple and cheap racetrack coils. Two types of quadrupole are used: one for the low energy arcs (MQAL) and one for the high energy arcs (MQAH).

Figure 70 shows the field line distribution in the high-energy arc quadrupoles (MQAH) obtained from a 2D finite element calculation. Only one eighth of the magnet is modelled; the symmetry is accounted for by appropriate boundary conditions. The relative transverse gradient homogeneity is better than 1×10^{-3}.

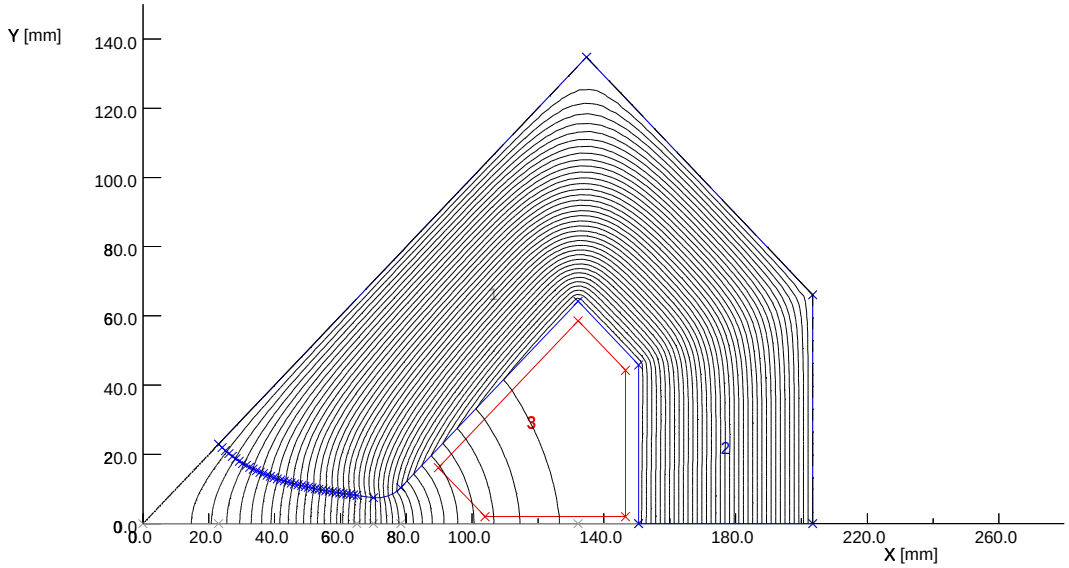

Fig. 70: Field lines in the MQAH quadrupoles.

14.3 Arc sextupoles

The pole profile used for the arc sextupoles is given by a cubic equation, followed by a linear part and a radius similar to the quadrupoles. Becasue of the low field levels, the poles can be built non-tapered and the coils can be built air-cooled. Two types of sextupole are used: one for the low energy arcs (MSAL) and one for the high energy arcs (MSAH).

Figure 71 shows the field line distribution in the high-energy arc sextupoles (MSAH) obtained from a 2D finite element calculation. Only one twelfth of the magnet is modelled; the symmetry is accounted for by appropriate boundary conditions.

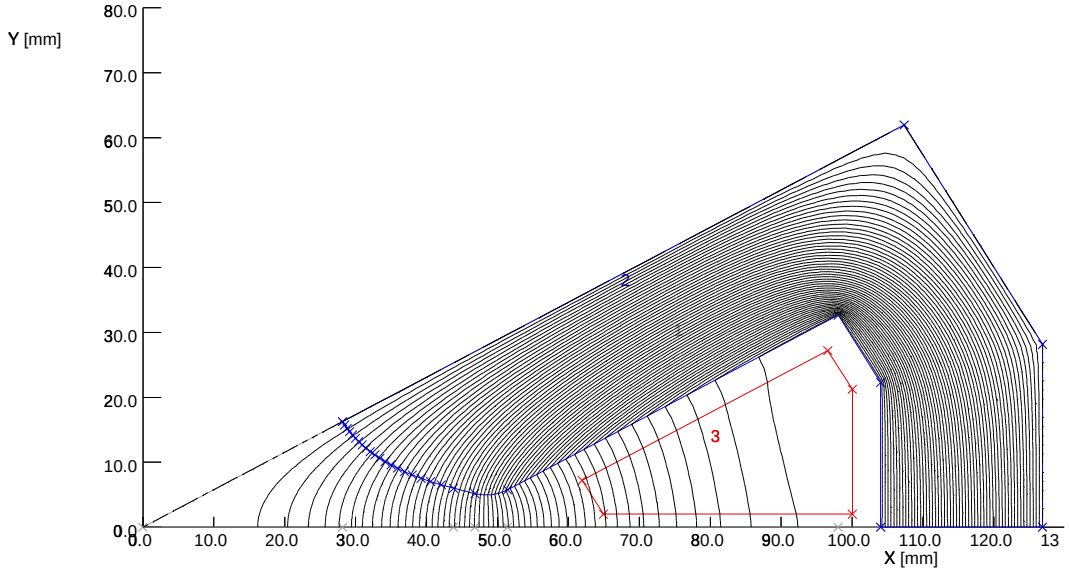

Fig. 71: Field lines in the MSAH sextupoles.

14.4 Arc corrector dipoles

The maximum strength of the arc corrector dipoles is high enough to create an $\int B\mathrm{d}l$ equivalent to the field the beam experiences when mis-steered by 2 mm in an arc quadrupole. The magnets are C-shaped and can be built using air-cooled coils.

14.5 Spreader dipoles

The design of the spreader magnets is determined by the small distance between adjacent beam lines. To increase the space available in the vertical direction, all magnets are longitudinally staggered. The shape of the spreader dipoles is of the same H-type as the arc dipoles. To limit the sagitta of the beam and therefore the aperture dimensions, the magnets are rather short. In most of the locations in the spreader, three magnets are needed to achieve the necessary $\int B\mathrm{d}l$.

To achieve an aperture comparable to the high-energy arc dipoles, the coils have to be built compact and consequently have a higher current density. More than one cooling circuit per coil is needed.

Three different types of magnet are necessary in the spreader region, one being considered as 'standard' type (MBSS). A second type (MBSC) is the first common dipole with large vertical aperture and a third narrower type (MBSN) has to be used in one position for the extracted beam.

Figure 72 shows the field line distribution in the standard spreader dipoles (MBSS) obtained from a 2D finite element calculation. Only one quarter of the magnet is modelled; the symmetry is accounted for by appropriate boundary conditions. The relative transverse field homogeneity is better than 1×10^{-3}.

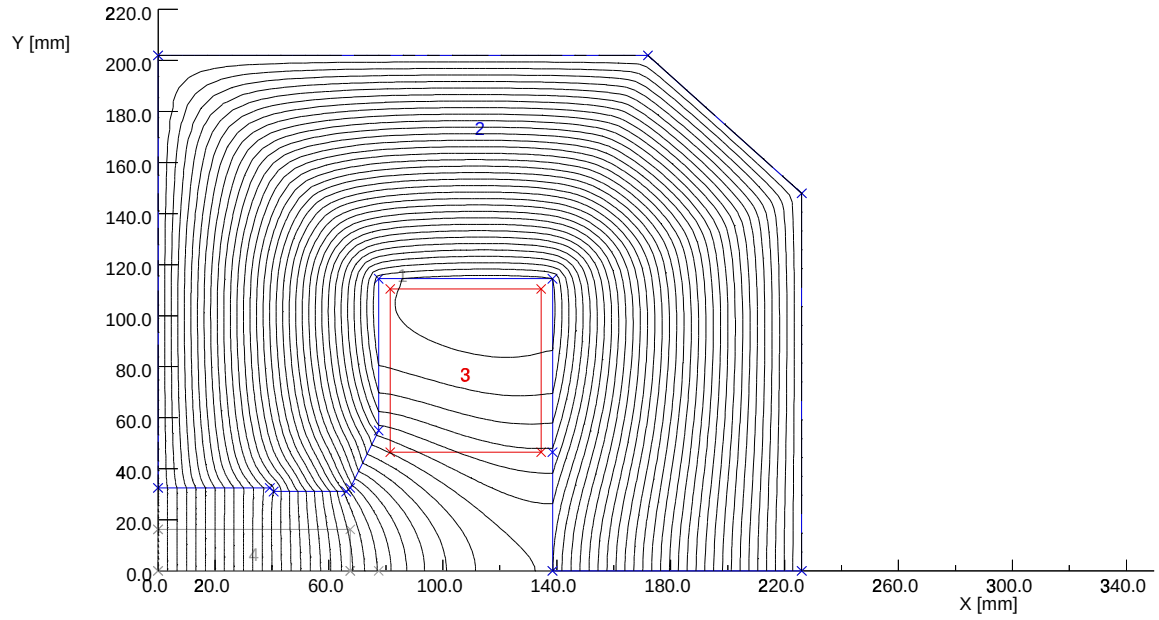

Fig. 72: Field lines in the MBSS dipoles.

14.6 Spreader quadrupoles

The spreader quadrupoles for all passes (MQS) are built using the same yokes as the high-energy arc quadrupoles (MQAH). Contrary to the arc quadrupoles, each spreader quadrupole is powered individually. To obtain a higher resistance and thereby a reasonable voltage/current

ratio for the power supplies, the spreader quadrupole coils have a higher number of turns and a smaller conductor cross-section.

14.7 Linac quadrupoles

The required gradients for the linac quadrupoles are rather low. In order to make use of existing equipment wherever possible and sensible, it is proposed to re-use the LEP MQ quadrupoles. They are designed for significantly higher field levels, but can be operated air-cooled at the required low current. Remanence effects due to the low pole-tip field can probably be controlled by a dedicated cycling before ramping to the operating current.

14.8 Linac corrector dipoles

The LEP MCVA corrector dipoles can be re-used for this purpose.

14.9 Return-line quadrupoles

The $\int G\mathrm{d}l$ needed for the return-line quadrupoles at a given energy is about one quarter of the corresponding value of the arc quadrupoles. The magnets are built with the same pole profile and yoke cross-section as the arc quadrupoles, but have only half their length and operate at lower currents.

The quadrupoles in the low-energy return lines (MQRL) have the same cross-section as the MQAL magnets, but half their length. Similarly the quadrupoles in the high-energy return lines (MQRH) have the same cross-section as the MQAH magnets and half their length.

The quadrupoles in the adaptor region (MQM), where the arcs are matched to the return lines, are identical to the spreader quadrupoles (MQS).

14.10 Summary tables

The magnet characteristics are summarized in Table 28.

Table 28: Magnet characteristics.

Parameter	MBAL	MBAH	MBSS	MBSN	MBSC	
B	0.65	1.23	1.46	1.43	1.54	T
∫Bdl	2.5	4.8	1.6	1.5	4.9	Tm
Aperture height	25	65	65	65	65	mm
Iron length	3800	3800	1000	1000	3100	mm
Effective length	3833	3885	1085	1085	3185	mm
Total length	4100	4300	1200	1160	3650	mm
Total width	390	760	450	400	1850	mm
Total height	240	440	400	370	1050	mm
Weight	2400	8500	1300	1000	46000	kg
I_{max}	708	1458	1450	1450	1375	A
R at 20 °C	0.015	0.020	0.027	0.053	0.024	Ω
Conductor height	15	22	10	8	22	mm
Conducor width	15	22	10	8	22	mm
Cooling hole	6	12	4	5	12	mm
Layers	2	3	6	6	4	
Turns/Layer	5	8	5	5	8	
Cooling flow	5.7	21.6	35.4	64.8	56.7	l/min
Δp	6.0	6.0	6.0	6.0	6.0	bar
ΔT	19	29	24	26	12	°C

Parameter	MSAL	MSAH	
S	66	140	T/m^2
∫Sdl	14	30	Tm/m^2
Aperture diameter	37	65	mm
Iron length	200	200	mm
Effective length	209	216	mm
Total length	300	300	mm
Total width	140	260	mm
Total height	140	260	mm
Weight	25	90	kg
I_{max}	7.6	8.8	A
R at 20 °C	0.074	0.742	Ω
Conductor height	2	2	mm
Conducor width	4	4	mm
Cooling hole	-	-	mm
Turns	8	80	
Cooling flow	-	-	l/min
Δp	-	-	bar
ΔT	6	16	°C

Parameter	MQAL	MQAH	MQS	MQM	MQRL	MQRH	
G	20.8	19.4	20.9	13.9	8.1	7.9	T/m
∫Gdl	6.6	12.2	13.1	8.7	1.4	2.6	Tm/m
Aperture diameter	37	65	65	65	37	65	mm
Iron length	300	600	600	600	150	300	mm
Effective length	317	629	629	629	167	329	mm
Total length	400	780	780	780	250	480	mm
Total width	230	410	410	410	230	410	mm
Total height	230	410	410	410	230	410	mm
Weight	100	600	600	600	50	320	kg
I_{max}	241	482	224	224	135	204	A
R at 20 °C	0.026	0.024	0.197	0.197	0.013	0.016	Ω
Conductor height	6	10	6.5	6.5	6	10	mm
Conducor width	6	10	6.5	6.5	6	10	mm
Cooling hole	3	4	4.5	4.5	3	4	mm
Turns	12	18	43	43	9	18	
Cooling flow	1.8	6.6	5.5	5.5	0.9	1.0	l/min
Δp	6.0	6.0	6.0	6.0	6.0	6.0	bar
ΔT	12	13	27	27	4	10	°C

15 Vacuum

The ELFE vacuum system presents four main parts with completely different vacuum requirements. Owing to the short time the electrons spend in the accelerator, a beam lifetime of 10^{-3} s is sufficient to avoid any significant energy loss. Hence the pressure requirements given by lifetime considerations are not stringent. On the contrary, the presence in the linac of superconducting cavities necessitates producing a clean and dust-free vacuum having all the characteristics of the ultra-high vacuum. The linac vacuum system is described in Section 15.1. At the other extreme, the six return lines do not show any peculiarities or intense source of degassing. A short description of these lines is given in Section 15.3.2. In the arcs, there is no sensitive equipment but the bending of a high-energy electron beam generates the production of synchrotron light which is a known source of possibly intense degassing. This problem will be addressed in Section 15.2. The use of recovered LEP equipment allows substantial cost saving, especially in the linac sections; however the cost of reconditioning the equipment must also be taken into account. Moreover the decision concerning the recovery of this equipment must be taken soon enough to avoid both the extra cost of storing unnecessary equipment and the destruction of equipment such as vacuum chambers which could be used in some parts of ELFE.

15.1 The linac vacuum system

The linac vacuum system must ensure the clean and dust-free pumping of the delicate superconducting (SC) cavities. It is a copy of the actual LEP straight sections where the cavities are operating. The vacuum system is designed to minimize detrimental gas condensation inside the helium-cooled cavities. The procedures to operate it are defined to avoid the propagation of dust particles during the roughing or the venting of these cavities. They also use ultra-high vacuum standards in order to avoid any hydrocarbon contamination of the cavitiy surfaces.

The warm vacuum system is a bakeable stainless-steel system using mainly items recovered from LEP. Strong pumping stations are needed to trap the molecules that outgas in the warm parts, thus preventing condensation in the cold modules. This is achieved with 400 l/s ion and titanium sublimation pumps. Inverted magnetron gauges are used in the vicinity of the cold parts to avoid excessive heat loads to the cold system. All-metal roughing valves allow connection of the roughing stations to the vacuum system. Each module is isolated by all-metal gate valves to avoid any contact with the dusty environment of the accelerator tunnel during its installation and transport. At the extremities of the linac system a baked matching section will be used to provide a strong differential pumping of the gas desorbed in the spreader/recombiner section and prevent its adsorption in cavities.

15.2 The arcs vacuum system

In this part of ELFE there is a strong desorption due to the intense synchrotron light generated in the bending magnets. This synchrotron-radiation-induced desorption is the main source of gas in these sections (arcs and spreader/recombiner) and must be carefully studied to determine the adequate size of the pumping system. In particular the important reduction in desorption observed during the initial part of the operation of electron accelerators must be taken into account in order to avoid an oversizing of the pumping system.

15.2.1 The synchrotron-radiation spectrum

The moderate energy of ELFE rings and their large circumference could lead, when comparing with LEP for example, to the false conclusion that the synchrotron-light radiated power is insignificant in ELFE. This is not the case because in ELFE only part of the circumference is occupied by magnets to preserve the beam properties. Hence the bending radius of the beam in

these magnets is relatively small and the radiated power accordingly high. The main characteristics of the synchrotron radiation emitted by the ELFE dipoles are shown in Table 29. In the high-energy ring, the critical energy reaches 400 keV and the radiated power 880 W/m/mA, i.e. 88 W/m for the nominal beam intensity of 0.1 mA.

Table 29: Main characteristics of the synchrotron radiation in ELFE.

ELFE ring	6	5	4	3	2	1
Energy (GeV)	21.8	18.3	14.8	11.3	7.8	4.3
Radiated power (W/m/mA)	884	440	190	65	60	5
Critical energy (keV)	383	230	120	55	35	6
LEP equivalent energy E_{eq} (GeV)	82	71	60	48	37	26

15.2.2 Consequences on the vacuum system design

Cooling and shielding

Calculations [62] show that with this power dissipation an uncooled stainless-steel chamber would reach 230°C. Hence a moderate water cooling (6 l/min) of the high-energy-ring vacuum chambers is needed. With the high critical energy (400 keV), the screening by the stainless steel is not sufficient to protect the magnet coils. A simple lead ribbon, approximately 1 cm thick, strapped on the chamber where the synchrotron light impinges could produce an adequate shielding. More calculation is needed to estimate the exact dose to the magnet coils and the importance of Compton-scattered photons for a complete design of the shielding.

Outgassing

In this study, stainless steel will be considered as the chamber material as it constitutes an obvious possibility to build the ELFE vacuum system. A more refined analysis for the choice of the vacuum chamber material is left to the detailed study. Measurements [63] have shown that an unbaked stainless-steel chamber exhibits a desorption induced by photons equivalent to the desorption of a baked aluminium chamber, i.e. the case of LEP.

To estimate the desorption stimulated in the ELFE rings by the impact of the synchrotron radiation, the extensive studies made to design the LEP vacuum system and the measurements carried out during its operation are very useful. Nevertheless most of the measurements were made at an energy corresponding to the operation of LEP at 45 GeV. Hence the scaling between the two machines require some attention. This scaling is necessary to take into account:

- the different energy distribution of the photons in LEP at 45 GeV and in ELFE;
- the difference in the radiated power for the same critical energy and the same circulating current in ELFE and LEP due to the different bending radii.

The procedure used to estimate the evolution of the degassing in ELFE with the beam dose is the following. The cleaning curve for LEP giving the evolution of the pressure increase with the beam dose is given in Ref. [64]. Measurements carried out in LEP [65] give the evolution of the residual gas composition as a function of the beam dose. Taking into account the pumping speed in the LEP vacuum chamber, it is possible to estimate the evolution of the partial pressure for the main components of the residual gas as a function of the beam dose in LEP operating at 45 GeV. The results are shown in Fig. 73.

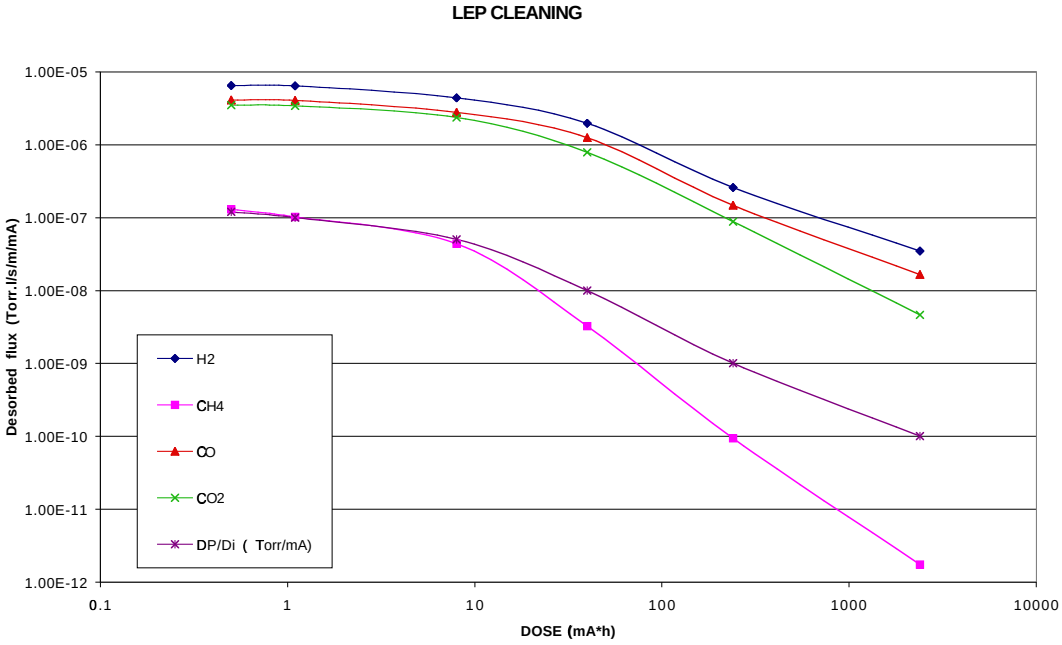

Fig. 73: The variation with the beam dose of the desorbed flux in LEP at 45 GeV.

The LEP equivalent energy (LEP E_{eq}) is defined as the beam energy in LEP giving the same critical energy for the synchrotron radiation as the beam energy E in ELFE, i.e. the same relative energy distribution for the photons. LEP E_{eq} is plotted as function of the ELFE energy in Fig. 74. The photon spectrum radiated in the ELFE high-energy ring corresponds to the spectrum radiated in LEP operating at 82 GeV. The low-energy ring corresponds to LEP at 26 GeV.

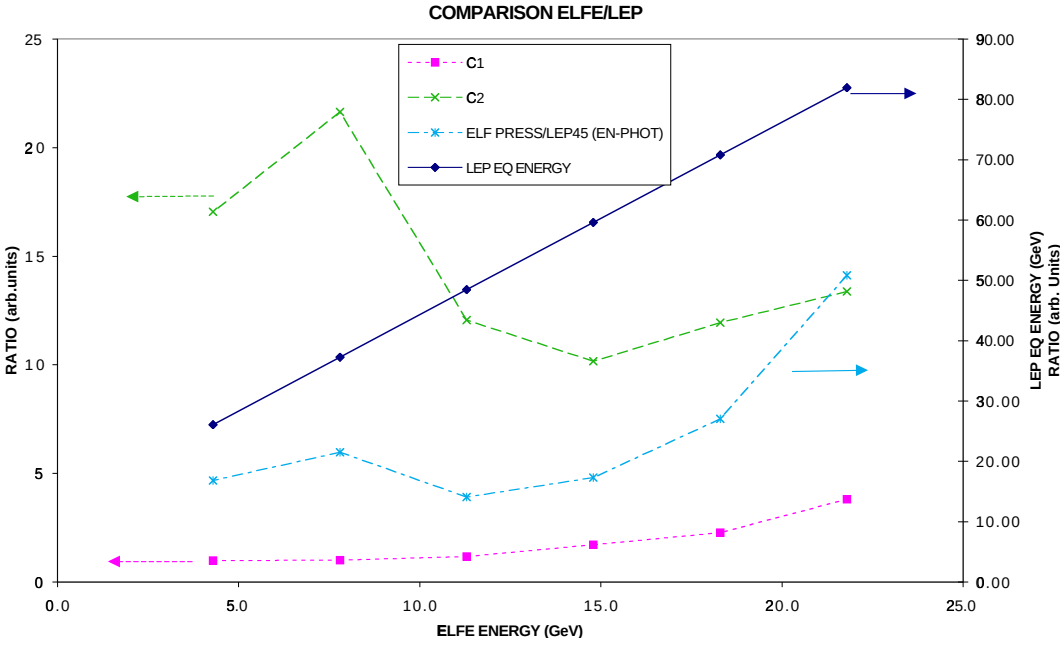

Fig. 74: Scaling coefficients between LEP and ELFE.

The LEP degassing rate measured at 45 GeV must be multiplied by a coefficient C_1,

$$C_1 E_{\mathrm{eq}} = \frac{\Delta P_{\mathrm{LEP}}(E_{\mathrm{eq}})}{\Delta P_{\mathrm{LEP}}(45)} \ ,$$

as given in Fig. 74 (curve C_1) to obtain the degassing in LEP at the energy E. This coefficient can be measured by recording for the same current the variation of the desorption in LEP with the beam energy [65].

In LEP at LEP E_{eq} and in ELFE at E beam energies, the power radiated per mA of circulating beam current [respectively $P_{1\mathrm{LEP}}(E_{\mathrm{eq}})$ and $P_{1\mathrm{ELFE}}(E)$] is different. As the outgassing scales with the radiated power for beam energies above 50 GeV (LEP E_{eq}) and with the number of photons below this energy, another coefficient C_2 plotted on Fig. 74 must be introduced. This coefficient takes into account the difference in the power (from the number of photons) radiated by a 1 mA beam in ELFE at the energy E and in LEP at the energy LEP E_{eq}, i.e. both machines running with the same critical energy.

$$C_{2(E>50)} = \frac{P_{1\mathrm{LEP}}(E_{\mathrm{eq}})}{P_{1\mathrm{ELFE}}(E)}$$

$$C_{2(E<50)} = \frac{N_{1\mathrm{LEP}}(E_{\mathrm{eq}})}{N_{1\mathrm{ELFE}}(E)}$$

where $P_{1\mathrm{ELFE}}(E)$ is the radiated power per mA of beam current in ELFE at energy E and $P_{1\mathrm{LEP}}(E_{\mathrm{eq}})$ the radiated power per mA of beam current in LEP at equivalent energy E_{eq}. $N_{1\mathrm{ELFE}}(E)$ is the number of photons emitted per mA of beam current in ELFE at energy E and $N_{1\mathrm{LEP}}(E_{\mathrm{eq}})$ the number of photons emitted per mA of beam current in LEP at the equivalent energy E_{eq}.

Finally, for the same reason, the beam dose expressed in mA·h must also be scaled using the coefficient C_2.

To convert the LEP cleaning curve measured at 45 GeV to an ELFE cleaning curve at energy E (LEP equivalent energy E_{eq}) the ordinates have to be multiplied by $C_1(E_{\mathrm{eq}}) * C_2(E)$ (given in Fig. 74) and the abscissa divided by $C_2(E)$. The evolution with the beam dose of the desorbed flux in ELFE allows the pumping system to be defined and the evolution of the beam lifetime to be predicted. This evolution is given in Fig. 75 for the high-energy ring of ELFE.

15.3 Vacuum system layout

For the first estimate of a vacuum system for ELFE, a stainless-steel chamber of rectangular profile has been considered. It consists of a rectangular stainless-steel tube, 1.5 mm thick, equipped, at least for the high-energy rings, with a brazed copper cooling pipe and a 1 cm thick lead shield strapped on the vacuum chamber. A section of the tube is shown in Fig. 76. Given the conductance of this chamber and the desorbed flux calculated in the preceding section, it is possible to define the size and position of the pumps.

The ion pumps mounted in the arcs of LEP have a pumping speed of 40 l/s and are available in large number. For ELFE it is proposed to reuse these pumps according to the scheme proposed in Fig. 77.

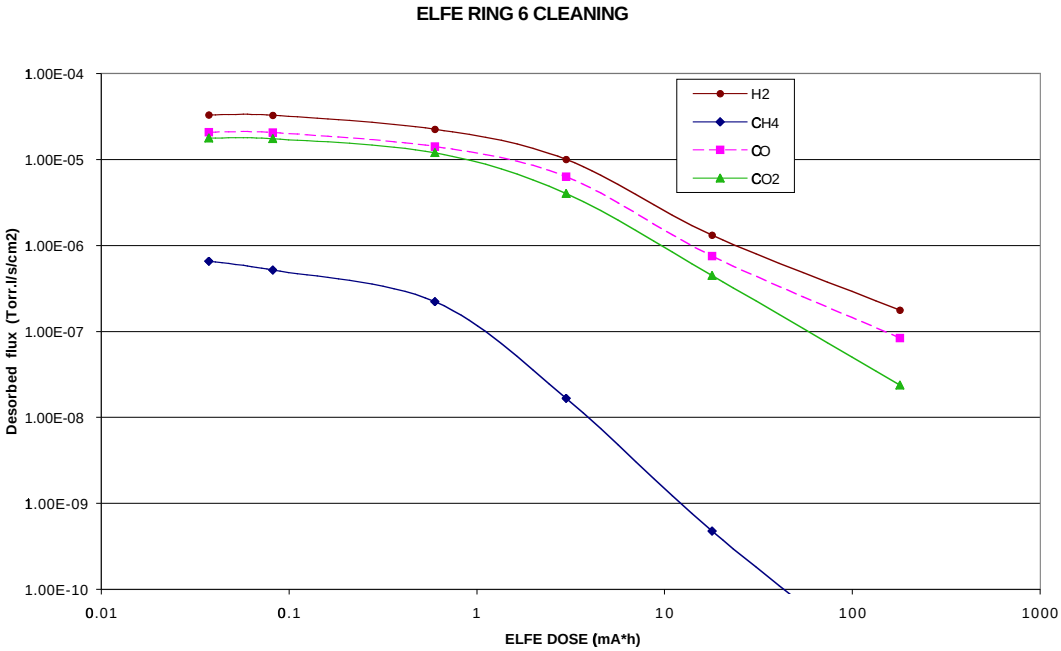

Fig. 75: ELFE ring 6 cleaning curve.

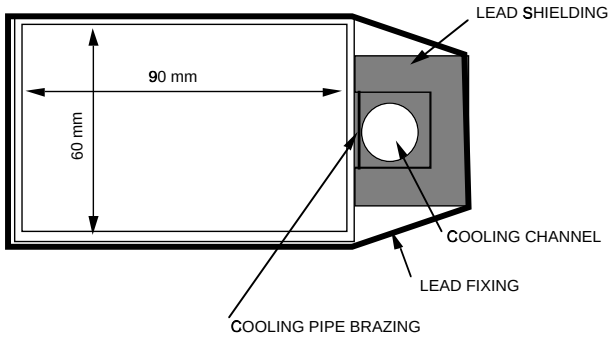

Fig. 76: ELFE's arc vacuum chamber cross-section.

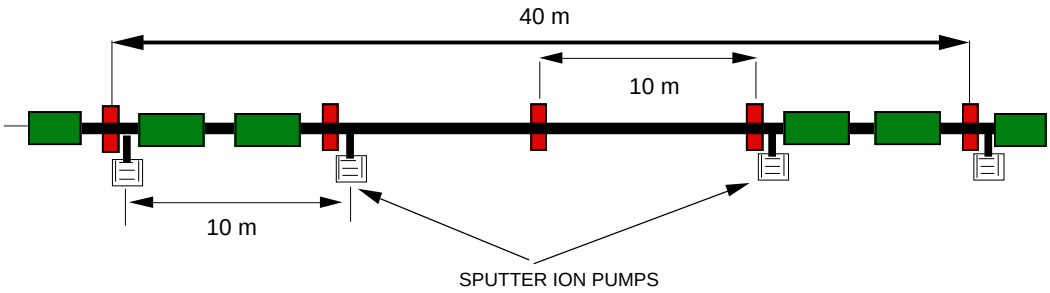

Fig. 77: Layout of the pumping in the ELFE arcs.

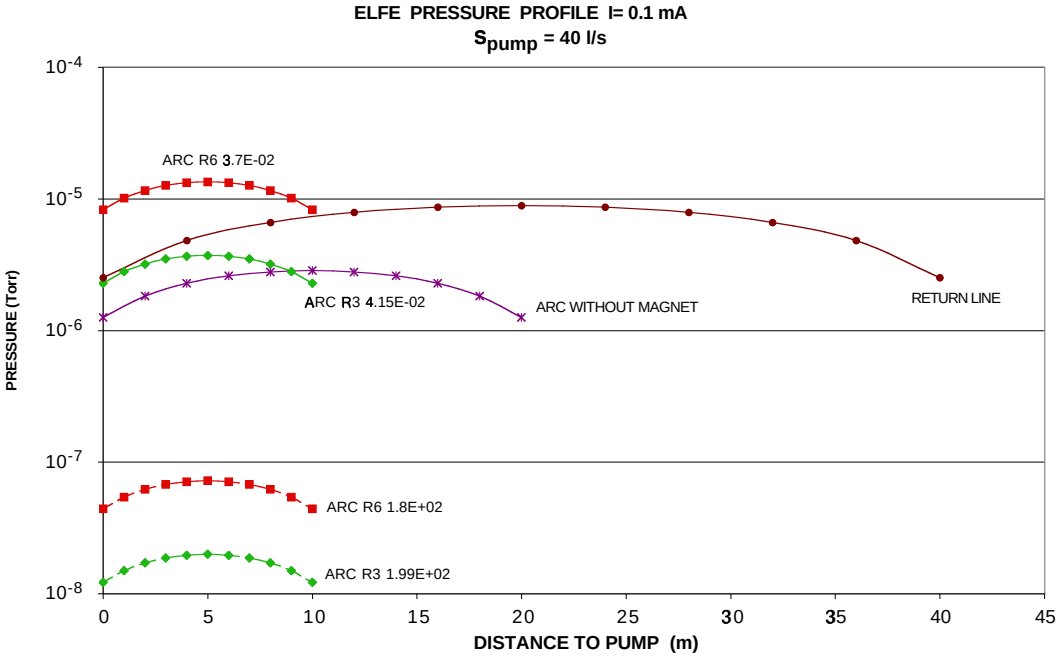

Fig. 78: Pressure profile in various sections of ELFE.

Figure 78 presents the pressure profile obtained with this pumping configuration and its variation with the accumulated beam dose (4×10^{-2} and $2 \times 10^{+2}$ mA·h) for ring 6 and ring 3. The same graph also shows the pressure distribution in the part of the arc not equipped with magnet and in the straight return lines. The high initial pressure drops by a factor 100 after an accumulation of 200 mA·h. The mean pressure in the arcs will be high at the start of ELFE as shown in Fig. 79 displaying the evolution of the gas composition and the corresponding lifetime change. This could limit the maximum circulating current during the first part of the operation (accumulation of a beam dose greater than 10 mA· h).

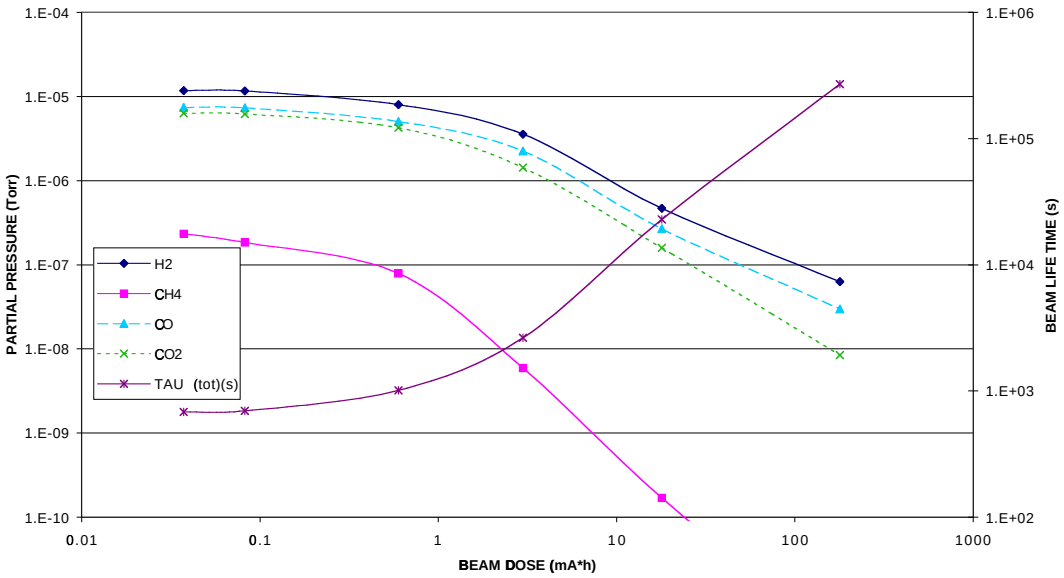

Fig. 79: Evolution of the mean gas composition in the ELFE ring for $I = 0.1$ mA.

The same ion pumps will be used in all parts of the machine, their spacing being adjusted to fit the variation of the gas load. In the parts of the arcs without magnet, the spacing between pumps is raised to 20 m; in the return lines it reaches 40 m.

In the combiner section a large pumping station using 400 l/s ion pumps will cope with the high gas load produced by the combiner magnet and avoid its diffusion to the region of the SC cavities.

15.3.1 Sectorization and vacuum valves

ELFE will be divided in vacuum sectors not longer than 500 m and corresponding to the various regions of the machine. Because of the six parallel beam lines in most of the machine, a large number of sector valves are necessary, which could be recovered from LEP. The total number of sector valves is 182. Each sector will be evacuated by a mobile turbomolecular pumping station connected to roughing valves 100 m apart. These roughing valves could also be recovered from LEP. A scheme of the sectorization is given in Fig. 80.

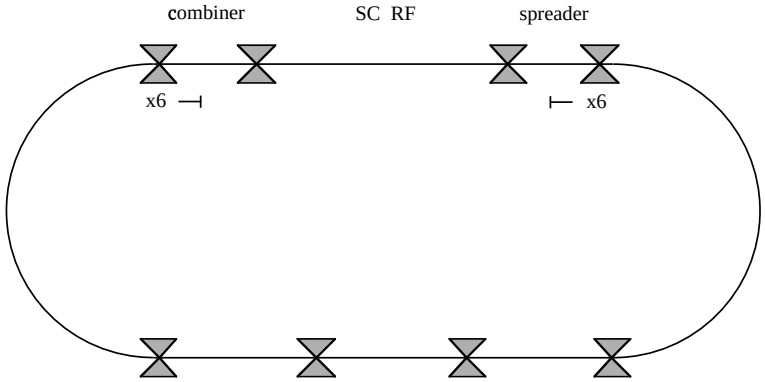

Fig. 80: Separation in vacuum sectors proposed for ELFE.

15.3.2 The vacuum monitoring equipment

A proper measurement of the vacuum is of great importance during operation to allow the early detection of possible leaks. The ion-pump current will be used to this effect using a scheme similar to that of LEP, with individual current measurements for each pump. Gauge heads will be mounted in each sector and used during leak detection. They will not be permanently connected to the main control system.

For the SC cavities, a more elaborate monitoring system is mandatory. All the existing equipment will be recovered from LEP with the exception of the gauge controllers which could be used in LHC.

15.4 Conclusion

In ELFE a non-negligible heat and radiation load is generated by the synchrotron light emitted in the bending magnets. This very preliminary study has given some basic information concerning the gas loads to be handled by the vacuum system and their evolution with the beam dose. As a basic solution an unbaked stainless-steel vacuum system evacuated by lumped sputter ion pump which could be recovered from LEP has been studied for the arcs and return lines. Many other components from LEP (e.g. valves, gauges) could also be reused if available. Alternative solutions could also be considered in a more detailed study based on pumping using

non-evaporable getters. The possibility of reusing part of the LEP aluminium chambers should also be questioned. For this preliminary study numerous results obtained during the operation of LEP have been used. For the operation of ELFE, the experience of the teams trained in LEP to deal with these very delicate components would certainly help to obtain, within a short period, the best results from this unique accelerator.

16 Beam diagnostics

16.1 Operation modes

A first evaluation of the beam instrumentation for ELFE has been made for the following two modes of operation:

- d.c. mode: continuous electron beam.
- Pulsed mode for set-up and commissioning. The main purpose of this mode is to reduce the total beam power by pulse-width modulation, whilst maintaining the intensity per bunch within a factor of two equal to the intensity in d.c. mode. As many instruments (CCD cameras for example) work synchronous to the 50 Hz mains supply, a pulse cycle length of 20 ms is assumed. A pulse 'on' time of one revolution (13.2 μs) would yield an acceptable duty cycle of about 1/1500.

16.2 Reuse of LEP equipment

In general one can say that all electronics of the LEP instrumentation has been designed for 11 kHz repetition rate and a bunch spacing of 22.4 μs. In addition, after 10 years of operation most electronics has lasted more than 50% of its expected lifetime. Hence no reuse of electronic components is considered. On the contrary the reuse of mechanical detector components, such as collimators, vacuum vessels, and electromagnetic couplers, seems to be possible and economic.

16.3 Beam-position monitoring system

A first survey of the requirements in terms of number of position monitors has been done and is summarized in Table 30.

Table 30: Survey of the number of pickups in various sections of ELFE.

Number	Section	Comment
288	arcs	24 pickups/arc, there are 12 arcs
36	linac	one pickup per cell
108	return lines	assumed half of linac · 6 lines
8	matching linac	4 quads, 2 matching sections
104	spreader/recombiner	8 quads, 6+7=13 passes
52	matching arc	4 quads, 6+7=13 passes
596	ELFE	number of pickups per plane (1192 total)

For the numbers in the table at least three pickups per betatron phase were assumed, and preferentially one pickup next to each quadrupole, which is quite conservative.

For the following evaluation a total of 1000 monitors with one measurement plane is assumed. The basic question is the choice of the electromagnetic sensors.

16.3.1 Button monitors

From LEP about 1750 button-type monitors with 34 mm diameter will be available, which approximately fits the number of monitors required above. These monitors have a transfer impedance of about 1.1 Ω above 370 MHz for a 43/86 mm elliptic vacuum chamber. With the beam specifications of ELFE this yields a signal amplitude of about −83 dBm or about 70 μV for a centred beam. These numbers have to be compared with the noise figures of modern high-frequency electronics. A typical number of 2 nV/$\sqrt{\text{Hz}}$ gives for 1 MHz bandwidth a signal-to-noise ratio of about 31 dB or a factor 30.

This performance is acceptable in orbit mode, where precision can be gained statistically by averaging over many measurements. However, a signal-to-noise ratio of 30:1 is very marginal in trajectory or multi-turn mode, both modes being very useful for injection studies and measurements of optics parameters.

In addition the above calculations assume no losses in signal cables, hence the electronics has to be located very close to the signal source and for this case the radiation effects would have to be studied.

16.3.2 Electromagnetic couplers

Electromagnetic stripline couplers could be constructed with about 10 times the signal strength compared to the LEP button monitors. This would give in every operation mode sufficient signal-to-noise ratio and even allow the front-end electronics to be installed after a cable length of about 80 m outside the machine tunnel.

16.3.3 Front-end electronics

As the beam has very little bunch-to-bunch amplitude dynamics and in the frequency domain the beam has only one dominant spectral line at 354 MHz, a signal treatment by Δ/Σ hybrids and 354 MHz homodyne receivers (SPS experience) seems the best choice.

16.4 Beam-current monitors

A device for the measurement of the total d.c. current to 10 ppm resolution and about 1% absolute calibration is commercially available and can be installed at any place in the machine. In order to measure the bunch structure a fast current transformer toroid with rise times in the nanosecond domain could be used, in which case one would measure the relative bunch amplitude at 354 MHz with 8-bit ADCs.

16.5 Bunch length

In the return arcs at higher energies, enough synchrotron light should be available to use a streak camera for bunch-length measurements. From experience at LEP it should be recalled that a streak camera is a very delicate device, which offers an enormous diagnostics potential, but which is very labour intensive for maintenance.

At much lower cost a high-bandwidth electromagnetic coupler could be used and the bunch length could be measured from the bunch spectrum. This type of monitor is very cheap and needs almost no maintenance. One can measure bunch length down to several millimetres (corresponding to several GHz bandwidth used in the monitor), but it should be retained that this monitor is very difficult to calibrate, as the overall transfer impedance of the monitor and the signal cable is not known exactly.

16.6 Emittance measurements

- About 10 wire scanners are available from LEP. Their scan speed would have to be adapted to the slow 20 ms repetition rate in pulsed mode. Wire scaners are considered to be precision instruments which can measure beam sizes down to 5% error. On the other hand, by nature the devices provide single-shot measurements, which do not allow real-time displays of the time evolution of the beam sizes.
- Optical transition radiation (OTR) screens could be used in LEP mechanics. The screens could deliver continuous real-time images of the beam size in pulsed mode. Further studies are needed to see if an OTR screen could stand the heat load of the d.c. beam.

- The two synchrotron-light telescopes from LEP (called BEUV in LEP) could be used, one in each arc. It should be noted that the proposal to vary the beam energy by a factor 3 will result in big design problems for emittance measurement devices based on synchrotron light.

16.7 Collimators

Many of the LEP collimators are available for reuse. In any case one has to rebuild the collimation jaws and possibly also the vacuum chamber.

16.8 Polarimeter

Using Compton backscattering of polarized laser light does not seem feasible with the very low bunch intensity and the high bunch repetition rate.

On the other hand, Moeller scattering by using as target a wire scanner or a foil could be envisaged. A detailed study would be needed.

16.9 Beam-loss monitors

The average beam power is considerable. At top energy and for the design current we have $P = 2.5\,\mathrm{GV} \cdot 0.1\,\mathrm{mA} = 2.5\,\mathrm{MW}$. There is a potential risk of severe damage to equipment in case of a continuous, localized beam loss and an almost full longitudinal coverage with a beam-loss monitoring system is required. A possible choice is ionization chambers in the form of long, flexible and air-filled cables. About 200 such detectors and readout channels would be needed. The time resolution can be made easily 1 ms, which should be adequate to prevent major damage and which also gives sufficient diagnostics potential.

17 Power converters

The power converters can be listed in two families: the klystron power converters and the magnet power converters (the power converters of the vacuum system are considered as part of the vacuum system).

17.1 RF power converters

- The ELFE project will need nine power converters (100 kV – 40 A) which will feed all the klystrons in the RF system. The power converters will be installed in individual buildings with their associated RF system.
- Each converter consists of three oil-immersed units (one step-down transformer, one step-up transformer and one high-voltage rectifier/filtering tank) installed outside on a transformer pit. The output power is controlled via an a.c. line controller installed inside the building.
- These nine power converters will be recuperated from LEP and reinstalled in ELFE without modification to the power part. Electronic crates will have to be replaced because of the new remote-control system.

17.2 Magnet power converters

- The ELFE project will need 940 power converters to feed the magnets. Bipolar power converters will feed the 596 corrector magnets, all the other magnets will be fed by unipolar power converters.
- The output power ratings of the power converters lie between 10 W and 2.2 MW (see Table 31 for further details). A large range of current ratings is required owing to the different energies in the return lines.
- Up to 0.5 MVA the power converters will be supplied by the 400 V network, above they will be directly supplied by the 18 kV network (eight units).
- The magnet power converters will be installed in two converter buildings.
- Up to medium power ($\cong$ 50 kW) switch-mode topology will be used. For higher power, we will use thyristor line-commutated topology.
- At the moment we do not envisage to reuse LEP power converters for ELFE magnets because the electrical characteristics (current and voltage) are very different and remote-control systems incompatible. Nevertheless, at a later stage, it may be possible to envisage reusing some power parts of LEP power converters. A precise cost study will have to be done at that time to determine whether this is economical.

Table 31: Power converters for ELFE.

Location	Energy [GeV]	Magnet Type	Number of magnets in series	I [A]	R [Ohm]		Voltage drop estimation [V]	Power converter Voltage [V]	Power converter Power [kW]	Number of Power Converters
					Magnet	Family				
Arc (2π)	4.3	MBAL	48	262	0.015	0.720	34	223	58.3	2
	7.8	MBAL	48	475	0.015	0.720	37	379	180.0	2
	11.3	MBAL	48	688	0.015	0.720	43	538	370.4	2
	14.8	MBAH	48	991	0.021	1.008	39	1038	1028.6	2
	18.3	MBAH	48	1225	0.021	1.008	48	1283	1571.4	2
	21.8	MBAH	48	1460	0.021	1.008	46	1518	2215.8	2
Total arc dipoles:										12
Arc (2π)	4.3	MQAL	12	119	0.027	0.324	39	78	9.2	6
			6	119	0.027	0.162	39	58	6.9	4
	7.8	MQAL	12	174	0.027	0.324	36	92	16.1	6
			6	174	0.027	0.162	36	64	11.2	4
	11.3	MQAL	12	248	0.027	0.324	33	113	28.1	6
			6	248	0.027	0.162	33	73	18.1	4
	14.8	MQAH	12	331	0.025	0.300	43	142	47.1	6
			6	331	0.025	0.150	43	93	30.7	4
	18.3	MQAH	12	406	0.025	0.300	42	164	66.5	6
			6	406	0.025	0.150	42	103	41.8	4
	21.8	MQAH	12	476	0.025	0.300	50	193	91.8	6
			6	476	0.025	0.150	50	121	57.8	4
Total arc quadrupoles:										60
Arc (2π)	4.3	MSAL	12	2.2	0.076	0.912	12	14	0.0	4
	7.8	MSAL	12	4.8	0.076	0.912	25	29	0.1	4
	11.3	MSAL	12	6.9	0.076	0.912	36	42	0.3	4
	14.8	MSAH	12	5.0	0.791	9.492	26	73	0.4	4
	18.3	MSAH	12	6.4	0.791	9.492	33	94	0.6	4
	21.8	MSAH	12	7.9	0.791	9.492	42	117	0.9	4
Total arc sextupoles										24
Spreader 1	All	MBSC	1	1376	0.025	0.025	11	45	62.5	2
Spreader 2	4.3...21.8	MBSS	18	1413	0.028	0.504	11	723	1021.8	2
	25.3	MBSN	3	1383	0.055	0.165	11	239	330.8	1
Spreader 3,4	4.3	MBSS	2	706	0.028	0.056	11	51	35.7	2
	7.8	MBSS	2	1280	0.028	0.056	10	82	104.6	2
	11.3	MBSS	4	926	0.028	0.112	12	116	107.1	2
	14.8	MBSS	4	1213	0.028	0.112	12	148	179.3	2
	18.3	MBSS	6	1000	0.028	0.168	10	178	178.0	2
	21.8	MBSS	6	1191	0.028	0.168	12	212	252.6	2
	25.3	MBSS	6	1383	0.028	0.168	11	243	336.5	1
Total Spreader dipoles:										18
Spreader	4.3	MQS	1	40	0.207	0.207	9	17	0.7	16
	7.8	MQS	1	73	0.207	0.207	12	27	2.0	16
	11.3	MQS	1	104	0.207	0.207	12	34	3.5	16
	14.8	MQS	1	114	0.207	0.207	10	34	3.8	16
	18.3	MQS	1	127	0.207	0.207	11	37	4.7	16
	21.8	MQS	1	204	0.207	0.207	11	53	10.9	16
	25.3	MQS	1	196	0.207	0.207	11	52	10.1	8
Total Spreader quadrupoles:										104
Return lines	4.3	MQRL	32	47	0.013	0.416	119	139	6.5	1
	7.8	MQRL	32	85	0.013	0.416	108	143	12.2	1
	11.3	MQRL	32	123	0.013	0.416	115	166	20.4	1
	14.8	MQRH	32	126	0.016	0.512	118	183	23.0	1
	18.3	MQRH	32	155	0.016	0.512	92	171	26.6	1
	21.8	MQRH	32	185	0.016	0.512	110	205	37.9	1
Total return line quadrupoles:										6
Matching	4.3	MQM	1	26	0.207	0.207	26	31	0.8	8
adaptors	7.8	MQM	1	41	0.207	0.207	42	50	2.1	8
	11.3	MQM	1	67	0.207	0.207	47	61	4.1	8
	14.8	MQM	1	90	0.207	0.207	45	64	5.7	8
	18.3	MQM	1	113	0.207	0.207	42	65	7.4	8
	21.8	MQM	1	136	0.207	0.207	50	78	10.6	8
Total Adaptor quadrupoles:										48
Linac		LEP MQ	1	11.76	0.066	0.066	29	30	0.4	72
Correctors		MCVA	1	2.5	12	12.000	30	60	0.2	44
Correctors		MCBA	1	3	7.3	7.300	30	52	0.2	552
Total correctors										596
Grand total:										940

Notes:
1.) Safety margin on current: 5%
2.) Assuming 1 spreader, 1 recombiner
3.) Arcs powered separately
4.) Spreader/Recobiner powered seperately

18 Power distribution

The ELFE accelerator, its injector, experimental halls and service buildings are estimated to require approximately 60 MVA. The CERN power-distribution infrastructure is in its present state not able to provide this amount of power beyond the needs of the LHC, the SPS and the other installations of the laboratory. The accommodation of the ELFE power requirements will thus require substantial extensions to the high-voltage installations of CERN, i.e. both the 400 kV substation and the 66 kV substation at Prévessin. The energy transport to ELFE and the power distribution within the ELFE area will be integrated into the CERN power grid at the high-voltage level: a direct 66 kV cable link from the main substation, for the ELFE machine systems (magnets, klystrons, etc.), and insertion of the ELFE general-service supply into the so-called 18 kV stable loop of the north area.

The different elements of the ELFE power distribution will be designed to respect the technical and safety conventions maintained since the construction of LEP.

18.1 Load

The ELFE accelerator resembles LEP, seen from the power distribution point of view. The main load elements for the machine systems will be power converters for klystrons and magnets. The presence of an important number of nonlinear load elements will most likely require a harmonics filter, to obtain the required main quality with respect to THD. Depending on the demands for voltage stability it may be necessary to install a reactive power compensator. The compensator will also reduce the load on the 66 kV supply transformer and the 66 kV cable link, as the reactive component of the connect will be annihilated locally.

The layout of the ELFE accelerator complex comprises nine small surface buildings for klystron supplies, interspersed by a distance of approximately 100 m along the linac. Each of these will be supplied by an 18 kV cable, laid in a duct or gallery, along the linac. The 18 kV distribution will be in the main ELFE substation. It is anticipated that the magnet supplies will be concentrated in two service buildings, one at either end of the linac. Each of these will be given an adjacent 18 kV substation, housing the necessary 18 kV switchgear for the magnet power supplies.

The general-service load will comprise the surface buildings needed for the different systems, as well as the two experimental halls. The general-service load in the 4 km long ELFE tunnel will be supplied from two tunnel substations, limiting the maximum low-voltage supply distance to 500 m.

The ELFE accelerating cavities will be the SC cavities from LEP. ELFE will thus require a major cryogenic installation. From the power distribution point of view a 3.3 kV substation, of a design identical to that to be used for LHC, is proposed. The substation will be housed with the major cryogenic installations.

18.2 The ELFE power network

The power requirements of ELFE are such that an additional 400 kV power transformer is required. It is, however, not straightforward to install it in the 400 kV substation, as this, in its present layout, offers only five bays, all already occupied. To create a sixth bay within the existing substation, for the most advantageous solution from the installation point of view, the 400 kV incomer from Bois Tollot will have to be moved from its present position to a position over the future third compensator.

The extensions to the 66 kV compound can be done in the same way as those for LEP200, BE9 and SEH1. The 66 kV system still has place for one incomer and one feeder. The 66 kV power cable link to the ELFE area will be laid in a cross-country trench to avoid cohabitation

with different links in the Prévessin galleries. The routing still has to be determined. The 66 kV station in the ELFE area will be of the same design as the 66 kV substations in LEP/LHC.

The high-voltage distribution of the ELFE area will be concentrated around an 18 kV substation of the same design as is known from the even points of LEP/LHC, i.e. a primary busbar for the machine systems fed from the 66/18 kV transformer and another primary busbar, fed from the north-area non-puked loop. The 'machine' busbar will feed three secondary switchboards, which supply the klystrons and the two 18 kV switchboards, one in either of the magnet supply substations. These substations will be similar to those of an odd point of LEP/LHC. Any high-voltage harmonics filters and compensator will be connected to the machine switchboard.

The general-service loop of the ELFE tunnel will originate from the general-service switchboard. The design of the electrical system of the tunnel substations will be based on that of the LEP/LHC stub-tunnels.

18.3 Reactive power compensation and harmonics filters

The installations will be similar to those already installed for LEP. The reactive power compensation will be based on a static solution, using most likely thyristors or IGBTs as switches. The filters will be LC series circuits with appropriate damping and capacitor discharge transformers. The filter circuits will be tuned to the characteristic harmonic frequencies of the load, as well as the main noncharacteristic frequencies between 50 Hz and the lowest characteristic one. The required space on the general layout covers the necessary space for these installations.

18.4 Safe power

A certain number of ELFE installations will undoubtedly require back-up supplies. The situation of ELFE, far away from other CERN installations, is similar to that of most of the LEP/LHC access points. A basic proposal would be to equip the ELFE compound (area grouping all service buildings) with a diesel generator set, providing assured and secured power to the same extent as is known in LEP. Each of the four tunnel substations would be equipped with an uninterruptable power supply (UPS), if necessary, covering either with or without redundancy, two 500 m sectors of the tunnel.

18.5 Installations in the tunnel

The ELFE magnets, and other machine elements, will require a cabling as known from LEP. It must thus be expected that a considerable number of cable ladders will have to be installed in the most densely populated sectors of the tunnel. The electrical service will further require a cable ladder for the general services in the tunnel, as well as a so-called safety ducting for emergency-light cabling, emergency-stop cables, etc. The tunnel lighting will be fixed to the general-service cable ladder and should thus be adequately positioned.

18.6 Summary of main parameters

The main supply of ELFE will be from the EDF 400 kV network. It is proposed to install a 110 MVA, 400/66 kV transformer, identical to the two units installed for LEP and LEP200. The two units already installed are still relatively new, installed in 1986 and 1992, respectively; but in 2006 the oldest will be 2/3 into its prospective lifetime of 30 years. For the time beyond LHC commissioning, it would be sound engineering to possess a third unit. The 400 kV bay protecting the transformer will be of a standard design. The 66 kV switchgear to be installed will have the same ratings as the switchgear so far used. For the ELFE machine systems a 70 MVA, 66/18 kV transformer will be installed. It will be of a design as close as possible to the units installed in the Meyrin–Prévessin connections. The 66 kV cable unit to ELFE would be

a 520 mm^2 or possibly a 630 mm^2 aluminium cable, rated voltage 72.5 kV, with solid extruded XLPE insulation.

18.7 Low-voltage distribution, 400/230 V

The power distribution at the 400/230 V level will use standard industrial equipment, supplied under blanket order contracts in force during the construction. The low-voltage distribution will be made available as normal supply, i.e. no back-up in case of fault; assured supply, i.e. supply backed up by the proposed diesel generator set in case of fault; and finally secured supply, i.e. back-up as an assured supply, but in addition not cut on emergency stop. The low-voltage supplies will exist as general-service supply, for lighting, socket boxes and other general-purpose use, and as dedicated supplies for large consumers, such as the cooling and ventilation, the cryogenics and the power converters. The lighting of the premises, as well as general distribution, will follow the same design as used elsewhere at CERN. The installation contractor at the time of construction will be given the task of design and execution of the works.

18.8 Safety systems

The safety systems will follow the safety instructions in force, in particular safety instruction number 5, concerning the emergency stop, and safety instruction number 37, concerning the transmission of level-3 alarms. Another safety aspect, the safety lighting, will be developed to the same extent as described in the LEP safety manual. All buildings and metallic structures will be earthed according to the standards. All relevant low-voltage installations will be protected by differential protection.

19 Civil Engineering

This chapter summarizes the conclusions of the preliminary design of the civil-engineering aspects of the ELFE project.

The main guidelines taken into consideration for the design were that, as far as possible,

- the whole project should stay within CERN allotted land,
- the selected options should minimize the civil-engineering costs,
- the selected options should minimize the environmental impact,
- the selected options should leave the possibility for future extensions.

The main objectives of the design were to assess the technical feasibility of the civil-engineering part of the project as well as to give a sound basis for cost estimation. It takes into account the assumptions agreed upon in the working group, and thus should be considered as indicative of what could be carried out efficiently under these assumptions. Refinements or improvements are, of course, still possible at a later stage.

The project is approached in this section from two viewpoints:

- a description of the various parts, with the main geometrical parameters;
- an account of the working methods.

19.1 Description of the project

19.1.1 General

The civil-engineering project has been divided into four parts:

- machine tunnels and injector
- surface buildings and structures
- experimental areas
- accesses, fences and landscaping.

Two alternatives have been considered from the very beginning and are presented in this section.

- Alternative 1, with only one new experimental hall, housing high-luminosity experiments. In this case, low-luminosity experiments could take place in the existing ECN3 hall. See Fig. 81.
- Alternative 2, with two new experimental halls, for high- and low-luminosity experiments. See Fig. 82.

In view of the guidelines mentioned above, a certain number of options for civil-engineering techniques have been selected. Tunnel works are carried out by the 'cut and cover' method, optimizing the depth by reference to foreseen costs and environmental impact. The balance of the respective volumes of excavated and refill materials has also been carefully looked at. A close eye will be kept on all shielding needs, in order to make the land reusable for agriculture and the public to the largest extent possible, once the construction is finished. All dimensions given hereafter are to be considered as internal.

19.1.2 Machine tunnel and injector cavern

The overall length of the machine tunnel is 3924 m. It comprises four main section types:

- The linac tunnel, length 1081 m, cross dimensions 4 m in width by 4.80 m in height.
- The spreader and combiner tunnels at both ends of the linac, total length including their matching sections twice 205 m, cross dimensions 4 m in width by 6.30 m in height.

- The return-lines tunnel, length 1491 m, cross dimensions being exactly the same as for the linac tunnel, and the spreader and combiner tunnels. Hence, from one arc to the opposite one, the tunnel characteristics are identical on both sides, making it possible to double the linac, spreader and combiner at a later stage.
- The two arcs, total length twice 471 m, cross dimensions 4 m in width by 4.80 m in height. The injector cavern floor is at the same level as the tunnel. Its dimensions are 32 m in length by 17 m in width by 4.80 m in height.

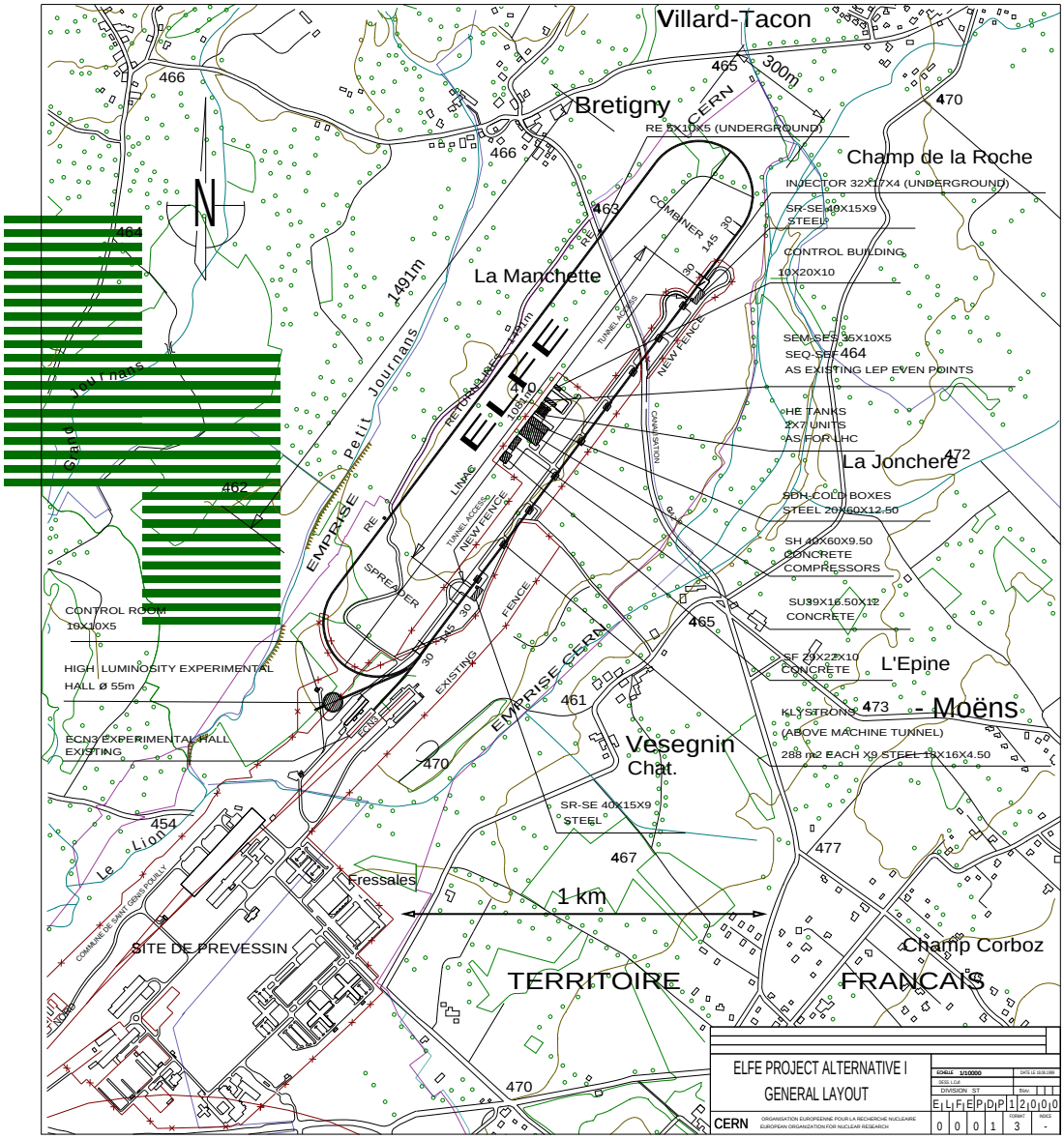

Fig. 81: General layout, Alternative 1.

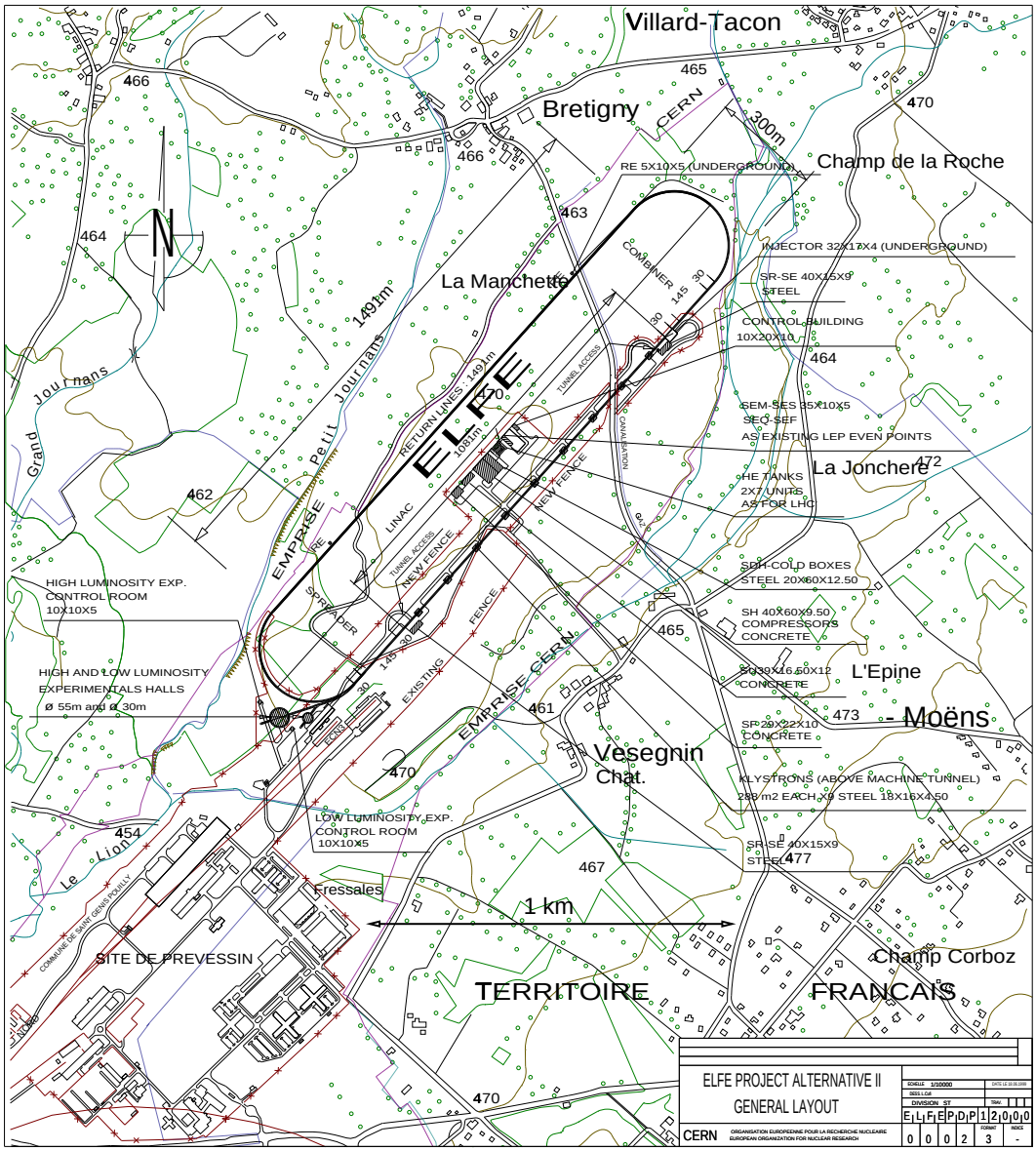

Fig. 82: General layout, Alternative 2.

In order to optimize the design and cost of the project, the whole machine tunnel and injector cavern floors are in the same slightly inclined plane, with a slope of 0.17%. All underground structures are made of concrete with thicknesses in the order of 40 cm for the walls, 60–70 cm for floors and covering slabs, to be determined more precisely at later design stages.

Two curved access ramps are located at each end of the linac tunnel for installation of the equipment in the main tunnel. Their slope is 10%. There is one dedicated ramp for the injector cavern.

Shielding doors have been placed in each case at the lowest end of these ramps to close the entrance of the related facility during operating periods. Four accesses to tunnel level for personnel are foreseen:

- two on the linac side, grouped with vehicles accesses,
- two on the return-lines side, symmetrical to those on the linac side.

They use narrow pits next to the tunnel itself, with a staircase and access to/from the surface through a small shielded building.

Refill of earth will be placed on top of the tunnel section where the depth of the inner face of the covering slab is less than 8 m when situated in an area open to the public, 6 m if this is not the case (fenced areas).

Figures 83 and 84 show a longitudinal and transverse cut of the main ELFE tunnels.

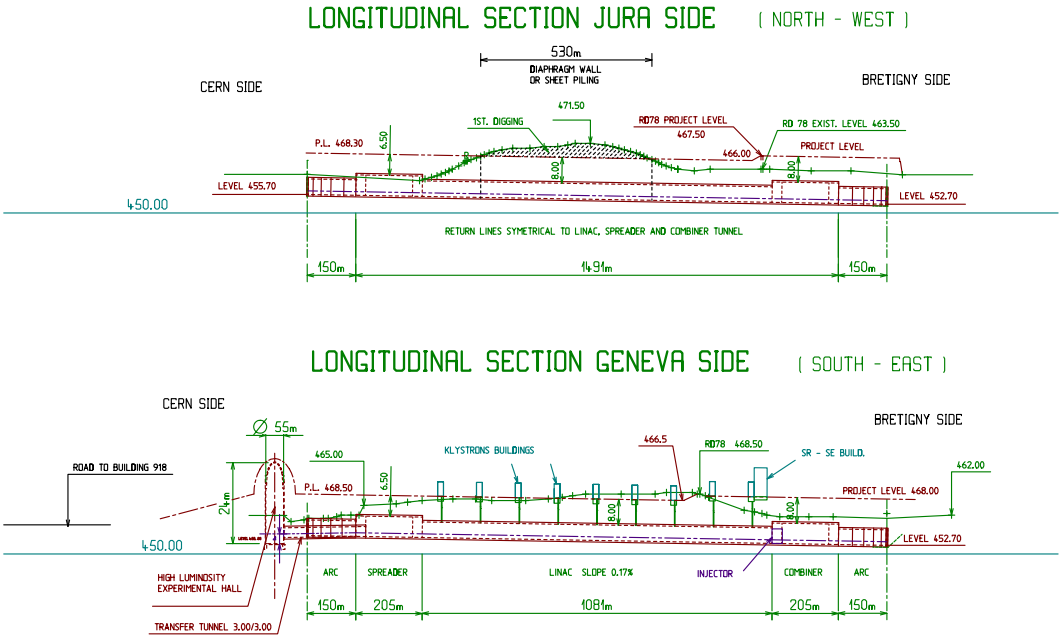

Fig. 83: Tunnels, linac and return lines, longitudinal cut.

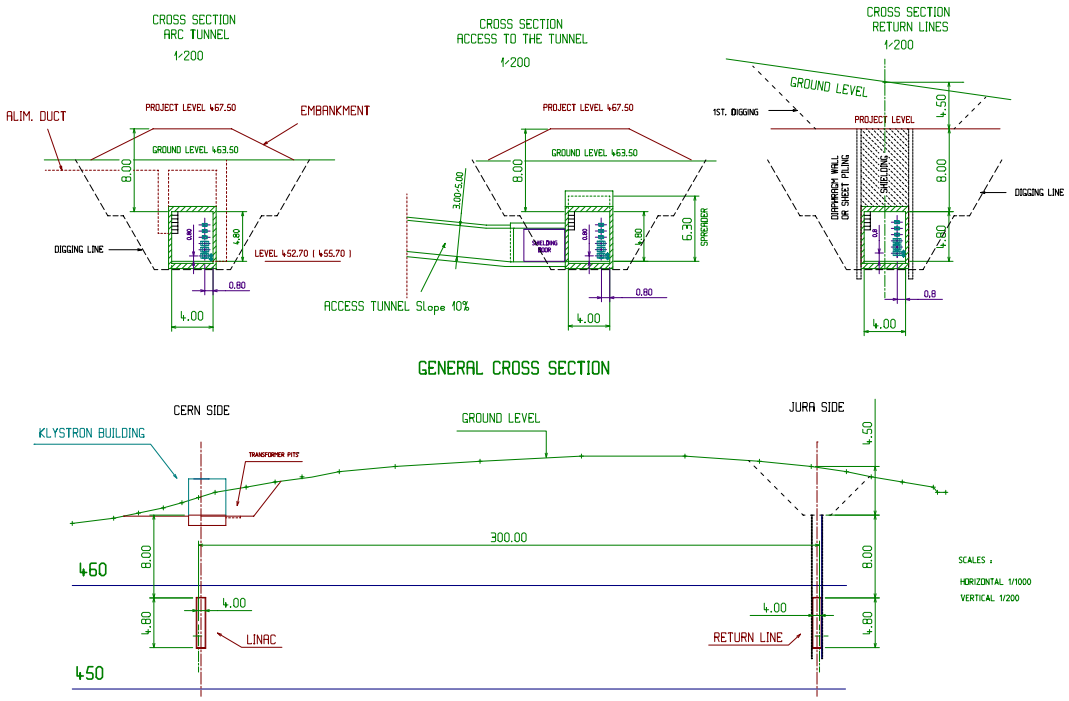

Fig. 84: Tunnels, transverse cut, cross-section.

19.1.3 Machine surface buildings and related structures

The surface buildings and related ancillary structures that are directly linked to the running of the machine are described in Table 32.

Table 32: Surface buildings.

Name	Purpose	Number	Dimensions (m) length × width × height	Materials Base-Superstructures	Particularities
SK	Klystrons	9	18 × 16 × 4.50	Concrete-steel	False floor under racks, two transformer pits outside
SR-SE	Power converters	2	40 × 15 × 9	Concrete-steel	False floor whole surface, one transformer pit outside
SCX	Control room	1	20 × 10 × 10	Concrete-steel-glass	
SEM-SES	Electrical supply (Building)	1	35 × 10 × 5	Concrete-steel Concrete elements	False floor whole surface, one transformer pit outside
SE	Electrical supply (zone)	1		Concrete slab	One transformer pit
SDH	Cold boxes	1	60 × 20 × 12.50	Concrete-steel	
SH	Helium compressors	1	60 × 40 × 9.50	Concrete-concrete	
SU	Cooling-heating-ventilation	1	39 × 16.50 × 12	Concrete-concrete	
SF	Cooling towers	1	29 × 22 × 15	Concrete-concrete	

The total area of machine surface buildings is of the order of 9300 m^2. Some of these buildings are situated directly on top of the linac tunnel or close to it, for example, the SK and SR-SE buildings, see Fig. 85.

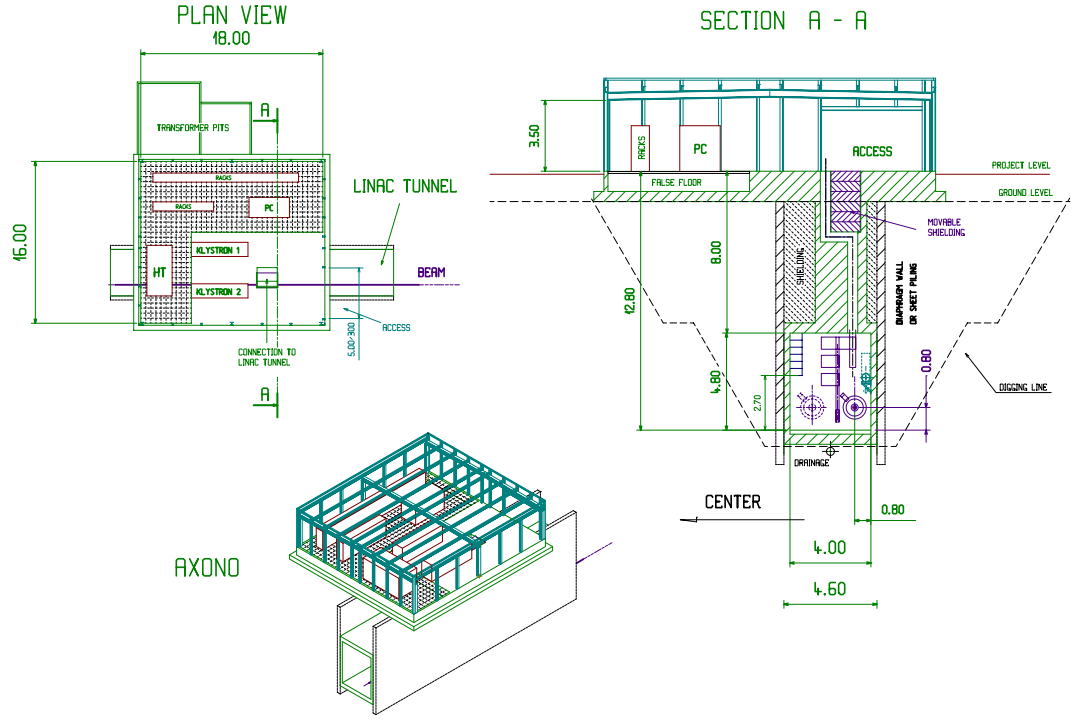

Fig. 85: Klystron buildings, linac tunnel, plan view, cut, axonometric.

The others are grouped at the geometrical centre of the machine in order to ease their access and connections to various services. For the latter, the orientations and positions will easily allow for an extension to the north-west, should the installation of a second linac be decided later in the return-lines tunnel. All these buildings are linked by a technical gallery of 2 m in width by 2.5 m in height. It is itself linked to the linac tunnel at its centre by a second technical gallery of the same cross-section perpendicular to the first one. The floor of the SK building housing the klystrons is connected to the machine tunnel through a concrete duct to allow high-frequency connections. The concrete shielding around the duct is partially removable to allow for installation and maintenance of the connections.

19.1.4 Experimental areas

As mentioned before two options are presented:

- In the case of option one, only one new experimental hall for high-luminosity experiments will be built. It has a cylindric shape, with an internal diameter of 55 m and a height of 24 m. It will be equipped with a 40 ton overhead travelling crane with a span of 55 m. The crane will be of the polar twin-girder type with walkways, having variable-speed hoisting, travelling and traversing motions from 0.1 to 10 m/min and a 10 m range of lift. The crane will be radio-controlled with infra-red beam starting and a back-up push-button control box. The power supply will be via separate circular conductors. The precision required on the three motions is +1 mm and the side approach 2 m. The hall is made entirely of concrete, including its dome-shaped cover.
  For shielding purposes, the floor level of the hall is situated approximately 6 m below ground level and it will be buried under a refill of earth of 1.5 m on top of its dome, down to ground level around it with a gentle slope. It receives the connection tunnel to the machine tunnel on one side, and a beam-dump facility, with 2 m thick concrete around, on the opposite side.
  An access road, with a slope of 10%, will allow equipment to be brought in through a movable shielding door. The access has a curved layout to improve its tightness to radiations.
  In option one, the low-luminosity experiments are housed in the existing ECN3 hall, under the assumption that it will become available at the time of the commissioning of the project.
  Whether the ECN3 hall will need modification to cope with the requirements of low-luminosity experiments remains to be checked.
- In the case of option two, the high-luminosity experimental hall will remain identical, whereas a new low-luminosity one has been foreseen in case the ECN3 hall could not be made available for that purpose.
  This new hall will be as the one described in option one above, but with a diameter of only 30 m. It will be equipped with a 20 ton overhead travelling crane with a span of 30 m of the same type as the crane for the large hall.

The experimental halls are shown in Fig. 86. In all cases, beams are transferred from the end of the spreader section to the experimental halls through connection tunnels with internal dimensions of 3 m by 3 m. Two 4 m wide, 4 m high and 2 m thick shielded motorized doors running on rails will be fitted at each tunnel entrance and provide radiation protection.

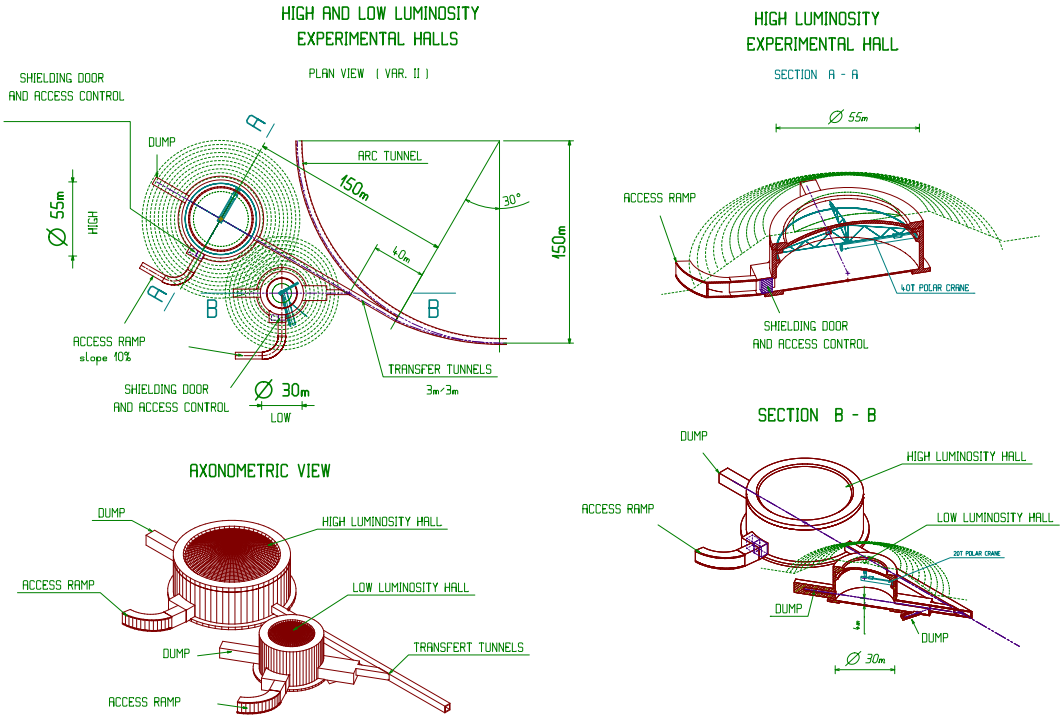

Fig. 86: Alternative 2: high- and low-luminosity experimental halls, plan view, cut, axonometric.

19.1.5 Roads, fences and landscaping

A road network is to be created to provide access to all surface buildings, experimental halls, and the underground machine facilities.

It is connected through gates:

- to the existing CERN network,
- to the Vesegnin–Bretigny road,
- to the existing agricultural tracks.

Car parks and areas for handling of equipment are foreseen around the buildings according to their use. The Vesegnin to Bretigny road will stay in its present location, any deviation to its present layout being too costly to implement. However, its level will be adjusted to 8 m from the inner face of the tunnel-covering slab, to allow public use without restrictions. As the condition is already fulfilled above the linac thanks to the level of the project, it applies only to the return-lines side, where 3–4 m of shielding height need to be secured with additional earth.

Standard CERN fences are foreseen around all building areas, which will permit a reduced shielding height in those areas of 6 m only. This will apply also to the area on the CERN site, whereas the other area will be refilled with earth in order to reach a 8 m thick shielding.

In this way, the major part of the project area will be rendered to the public and agriculture once the works are complete. Trees will be planted wherever they are required to compensate for those which had to be cut down because of their location and the project layout.

With the help of a landscape designer, as for most of the LHC areas, particular care will be given to the final landscaping of the area including planting in order to recover as far as possible the natural aspects of that beautiful part of the Pays de Gex.

19.2 Working Methods

19.2.1 General organization

The working methods, material resources and sequencing of works to be adopted to implement the civil-engineering part of the project depend on several factors, including:

- the starting date, milestones and deadlines;
- the options taken by the selected consultants and contractors, as a consequence of their own personnel and material resources;
- the need to reduce as far as possible the environmental impact of the works.

As was the case recently for other big projects such as the LHC, the major part of the civil-engineering works will be contracted out to

- consultants (likely joint ventures);
- contractors (likely joint ventures);
- architects;
- experts in various fields, like safety and geotechnics.

All these external contributors to the project will be selected according to CERN procedures, i.e. by way of market surveys and calls for tender. For consultants, architects and experts these will be prepared by the CE group, but the main consultant will prepare those for the works. This consultant would be in charge of all design phases except preliminary ones left to CERN, as well as all work-supervision tasks.

In order to be on the safe side if problems with a given consultant or contractor arise during implementation, it is proposed to split the whole project into two packages.

Package 1 would comprise:

- Linac, spreader and combiner tunnelling works.
- All surface buildings and ancillary structures such as technical galleries.
- All roads, car parks, fences except those for the experimental areas.
- All landscaping work in the area of the package.

Package 2 would comprise:

- Return lines and areas tunnelling works.
- Experimental hall(s), transfer tunnel(s).
- Control buildings, roads and car parks for the experimental hall(s).
- All landscaping work in the area of the package.

Of course, precautions will be taken at the tender stage to ensure that the same consultants/contractors are not awarded contracts for both packages.

In parallel to the performance of the design phases, an impact study report will be made. It should start as soon as the project is approved, in order to secure the French 'Déclaration d'Utilité Publique' (DUP) in time for the start of the works. As soon as the DUP is obtained, a building permit application will be prepared with the help of the selected architect and sent to the Commune de Prévessin for approval.

As far as the works area is concerned, it is anticipated to separate it from the Prévessin site of CERN, and make it a French work site, which will ease access and formalities while the works are being carried out.

19.2.2 Work procedures and planning

As mentioned above, all tunnelling works will be carried out according to a 'cut and cover' method, which is the cheapest one for works situated at shallow depths.

When the base of the tunnel is positioned deeper than 8 m or in forest areas, diaphragm walls or sheet-piling techniques will be used to minimize the impact and cost of excavation works. However, preference will be given to sheet piling which does not leave buried concrete walls close to the surface once the works are complete. In all other cases, underground works will be carried out in open trenches with standard slopes on both sides.

Tunnels will be made of normal reinforced cast concrete, which could be partially prefabricated if the selected contractor so wishes.

The experimental hall(s) will also be made of reinforced concrete, and possibly prestressed concrete, using techniques usually adopted for water-tank construction. Given the relatively poor bearing capacities of local moraines, their foundations will lie on a number of 'cast in the ground' concrete piles, to be determined at the design stage.

All other building will use traditional techniques:

- whole concrete structure for buildings housing noisy equipment;
- concrete foundation and steel structure, steel roof and wall cladding with intermediate insulation material for other buildings.

Starting from the initial 'green light', the total duration of the civil-engineering design and work implementation has been estimated at 6.5 years. Of this period, half will be dedicated to design, call for tender, and contract-awarding phases. This has been assessed taking into account our past and present experience with CERN purchasing procedures.

Construction times for alternatives 1 and 2 are estimated to be similar. The time needed to adapt the existing ECN3 hall will be comparable to the time needed to construct a new low-luminosity hall. In both cases, the work can be done partially in parallel to the work on the high-luminosity hall.

20 Cooling

20.1 Demineralized-water and chilled-water production and distribution plant - SU

The general layout of the cooling facilities is shown in Fig. 87, where the primary cooling (SF building) and the demineralized water plants (SU building) can be seen. This plant comprises the production of chilled water for the air-conditioning facilities and the main demineralized water plant. This plant covers the cooling needs of the machine proper and the klystron buildings. The surface needed to accommodate the equipment described below (and its auxiliaries) is 34.5 m × 16.5 m × 10 m (see Fig. 88). A false floor (with grille boards) some 2 m below the ground level and a travelling crane (10 tons) will be needed (see Fig. 89).

A very important parameter is the distance from the primary cooling station (SF building) to the machine itself and to the SU, SH, and klystron buildings. In view of the important investment cost needed both for primary, demineralized, and chilled water, it is recommended to foresee a cluster of buildings, which will minimize the length of service galleries and piping.

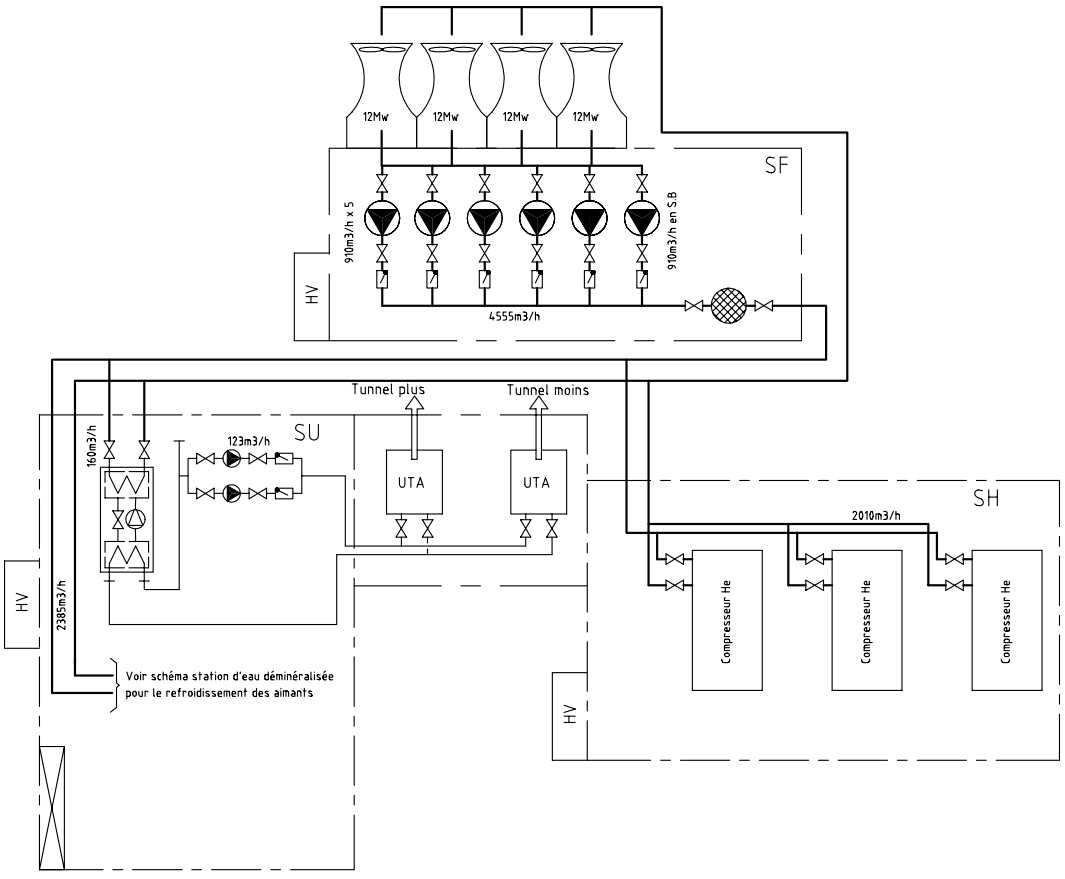

Fig. 87: General layout of the cooling facilities.

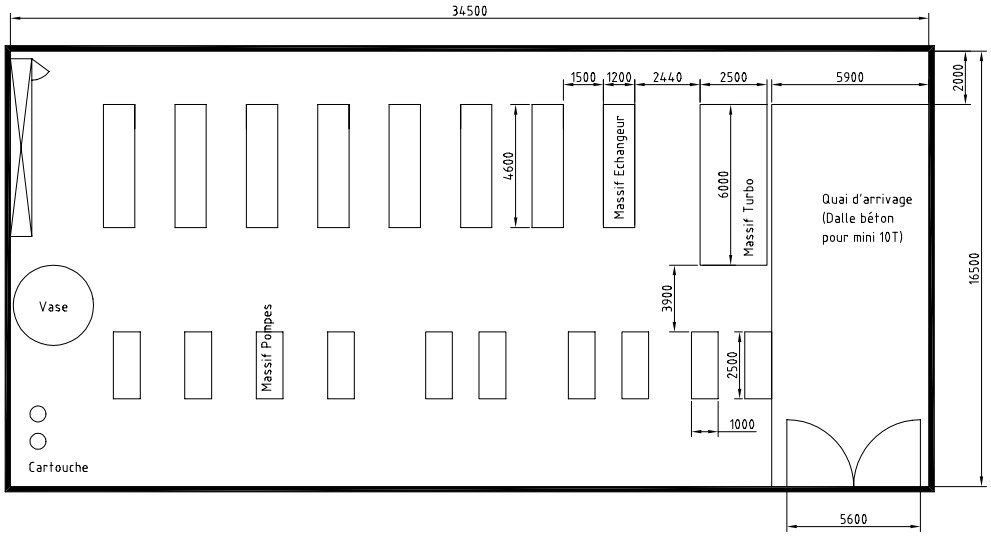

Fig. 88: Top view of the SU building.

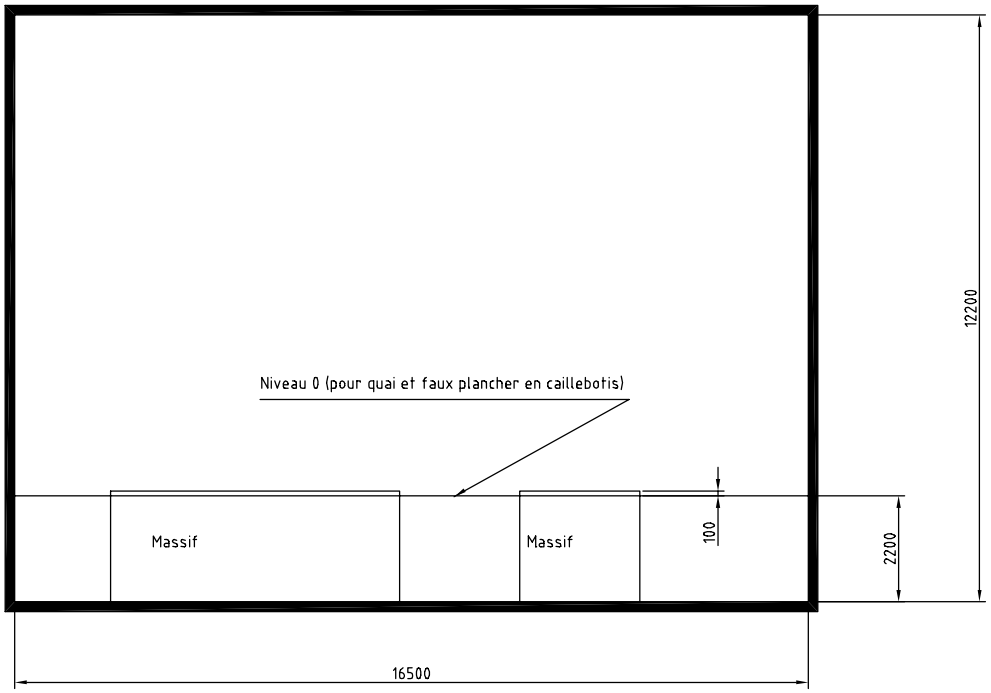

Fig. 89: Side view of the SU building.

20.1.1 Chilled-water plant

Capacity of the station:

- The different systems described in the heating, ventilation and air-conditioning systems description amount to a cooling capacity of 860 kW, for which one screw-compressor chiller has been considered.
- The electric motor of the unit will require 220 kW.
- The chilled-water (6–12 °C) flow rate is 123 m^3/h.

20.1.2 Magnets demineralized-water plant

This plant houses the cooling circuits necessary for the cooling of the machine magnets and the klystron buildings, from a centralized station (see Fig. 90). Owing to the large amount of heat dissipated, a series of sub-circuits are necessary.

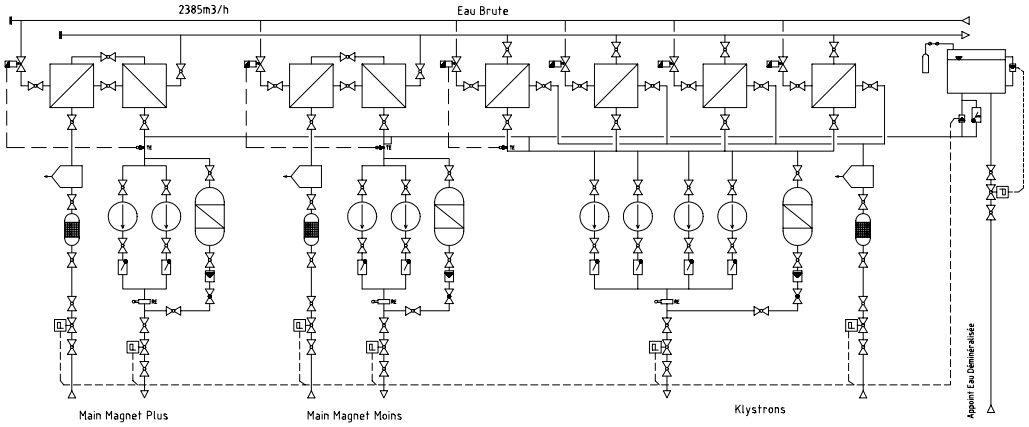

Fig. 90: Schematic view of the hydraulic system in the SU building for the demineralized water plant for the magnets.

Capacity of the station:

- The total capacity required is some 18 MW, with a total flow rate of around 890 m^3/h.
- Two separate sub-circuits have been considered, each having half the total capacity. The distribution will be done within the tunnel itself, along the linac gallery and up to the machine tunnel technical alcoves (RE) at the far end of the arcs. No water cooling is foreseen for the return line, where the few dissipating items will be air-cooled.
- The demineralized water supply temperature is 26 °C.
- A number of discharge pumps for the infiltration water and drains will be needed.

At the moment the details necessary for the sizing of the cooling facilities for the transfer tunnels and experimental areas are not well known. It is, however, very likely that the requirements will be only a fraction of those of the main ring's and their cost estimate a corresponding percentage.

20.1.3 Klystrons demineralized-water plant

Capacity of the station:

- The total capacity required is 13.5 MW, with a total flow rate of around 1454 m^3/h.
- Three separate sub-circuits have been considered, each supplying three buildings. The distribution will be done along the linac gallery (see Figs. 91 and 92).
- The demineralized water supply temperature is 26 °C.

20.2 Primary cooling station in SF building

Cooling towers and a primary pumping station will be needed for the cooling of the cryogenic and refrigeration compressors (see Figs. 93 and 94).

Cooling towers provide primary water at a temperature which is limited by the local dew-point temperature. In practical terms, for the region of Geneva the primary cooling tower water temperature is 24 °C.

Caractéristiques

Désignations	ΔT en K	P en Kw	Q en l/mn	ΔP en Bars
Klystrons	8	447	800	8
Corps	8	28	50	8
Isolateur	8	56	100	8
Charge	8	223,5	400	8
Charge Tunnel	8	28	50	8

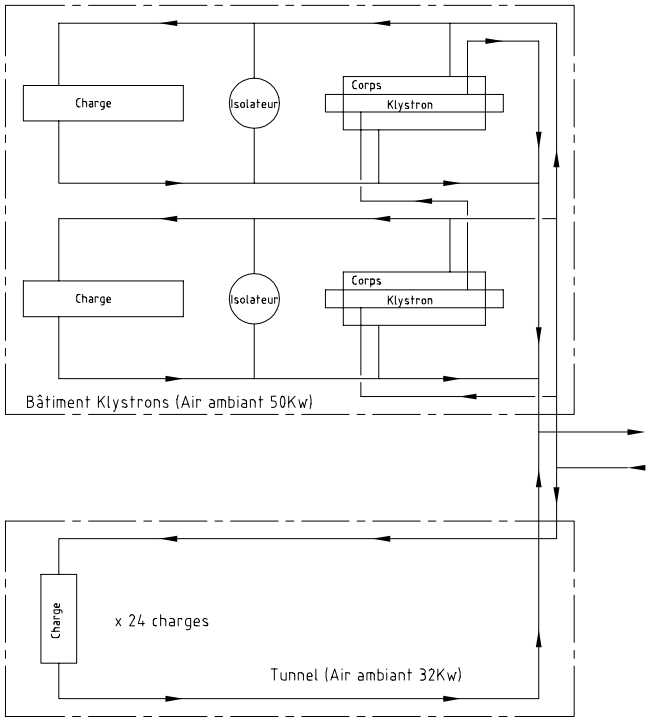

Fig. 91: Schematic view of the cooling for the klystron buildings.

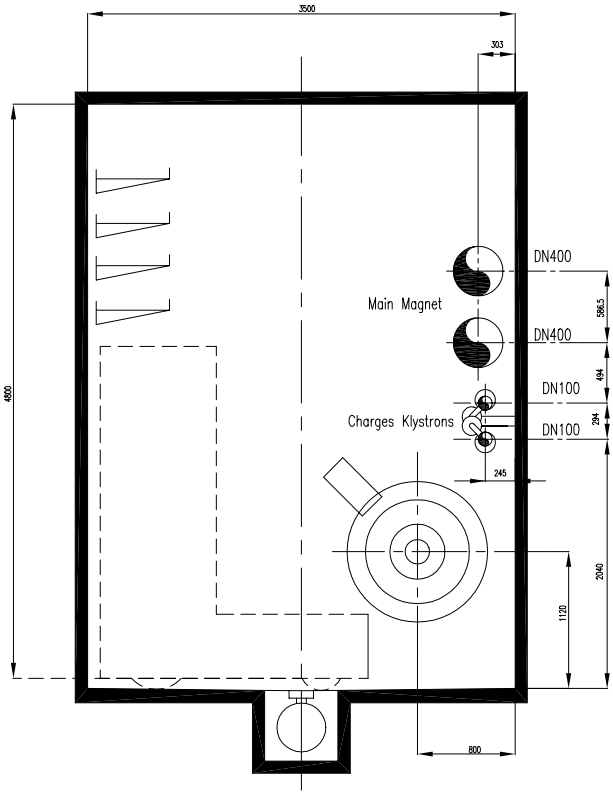

Fig. 92: Linac tunnel layout.

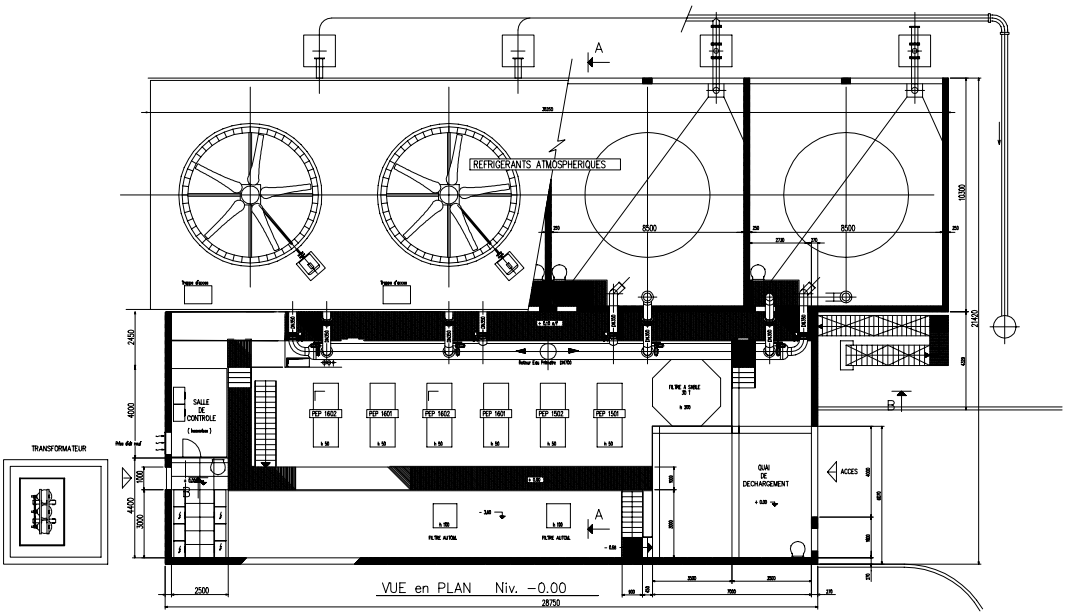

Fig. 93: Top view of the cooling tower and primary pumping station complex (SF building).

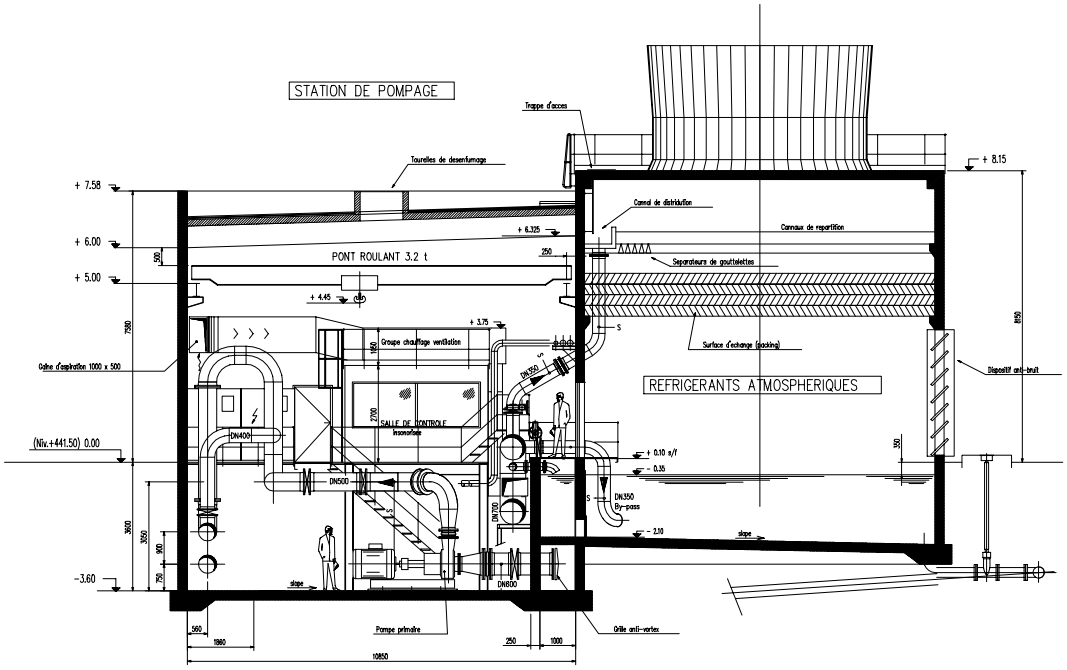

Fig. 94: Side view of the cooling tower and primary pumping station complex (SF building).

The total cooling capacity required is as follows:

Primary cooling of warm magnets	18 MW
Cryo compressors	14 MW
Klystrons	13.5 MW
Refrigeration compressors	1.1 MW
Total	47 MW

This will be achieved by installing four cooling towers of 12 MW capacity each plus one back-up unit.

Primary flow rates:

Both the cryogenic and the refrigeration compressors typically accept a ΔT of 5–6 K, which dictates the primary flow rate necessary. For conventional warm magnets the temperature rise will be somewhat higher, around 17 K according to the data available. The klystron circuit's ΔT is some 8 K.

Primary cooling of warm magnets	900 m^3/h
Cryo compressors	2010 m^3/h
Klystrons	1485 m^3/h
Refrigeration compressors	160 m^3/h
Total	4555 m^3/h

These primary cooling flow-rates in turn dictate the diameter of the piping needed, calculated on the basis of a mean velocity of around 1 m/s.

In view of the total flow rate of the station it is necessary to install a number of pumps in parallel, discharging in a common manifold. This will reduce the number of back-up pumps to just one.

21 Heating, Ventilation and Air Conditioning (HVAC)

The following is a preliminary calculation based on the internal loads, as announced by the user(s), and on a series of assumptions, which will be listed below. A detailed calculation of the building's air-conditioning system will be performed when the layout and structural design studies have been advanced to the point of knowing the precise location and orientation of the building, the surface, materials and thickness of the components of walls, doors, windows, the level of internal lighting, etc. The present paper is based both on the prices and technologies, which are to be applied for the LHC surface buildings.

For the missing data some general assumptions are made concerning the civil engineering and ventilation:

- outside dimensions of the building, if not given, will be estimated according to the functions housed in the building;
- concrete buildings, heavy construction (noise constraints), assumed thickness of walls $\sim 30\,\mathrm{cm}$, thermal insulation required;
- steel buildings, 20 cm of mineral wool insulation, high density;
- apparent surface density of walls $> 200\,\mathrm{kg/m^2}$;
- minimum fresh-air rate of $4\,\mathrm{m^3/h/m^2}$ (requirement for industrial buildings: $2\,\mathrm{m^3/h/m^2}$);
- summer and winter modes of operation are considered;
- the outside design conditions in Geneva in summer are: dry bulb temperature T = 32 °C, relative humidity (RH) 40%;
- the winter design conditions are dry bulb temperature T = – 12 °C, 80% RH.

21.1 Heating and ventilation of the SH building

The SH cryogenics building houses the helium compressors. The motors, although liquid-cooled, are known from previous experience to dissipate some 5% of the installed power to the air.

- Summer indoor conditions: $T_{max} = 40\,°C$ up to the height of 2 m from the floor.
- Winter indoor conditions: T = 19 °C, no control of humidity.

21.1.1 Description of the equipment and mode of operation

A number of classical air handling units (AHUs) will be needed in view of the required duty. These will be housed in technical rooms adjacent to the SH building and will have the same noise constraints necessary for the SH building itself. The distribution of supply air is foreseen by means of displacement terminals, such as those which will be used in the future LHC SH buildings.

On a general basis all systems (SH, SU and SF) will run on make-up air during the summer season. The maximum temperatures expected within the SH building in summer may go as high as +50 °C. Recirculated air grilles will be foreseen for the recovery of warm air during the winter season, when the flow rates needed will be below the maximum summer values.

In view of the very high flow rate involved in the case of the SH building, it is recommended to use at least three units (54 000 $\mathrm{m^3/h}$, 100 kW heating capacity each) housed in separate technical rooms around the building. To give an idea of the size of these units, a SPS AHU delivers some 45 000 $\mathrm{m^3/h}$ for a cooling power of some 450 kW. A room of 6 m × 10 m × 10 m should be foreseen for each unit. Ducts placed under the travelling-crane supports will carry out the distribution of cooling air in the summer. The ducts will have a diameter close to 1500 mm.

The power-supply boards and the control and supervision units will be like those foreseen for the LHC (ST-CV standard).

Hot air in the summer will be extracted from the buildings via a series of roof-mounted static heat vents (eight to ten for the SH, two for the SU and three for the SF) which also have a smoke venting functionality. For that purpose a 'standardized fire-brigade control cubicle' will be installed outside the building.

21.2 Heating and ventilation of the SU building

The SU building houses the chilled-water plants necessary for the air conditioning (i.e. the chilled-water production plant and its distribution pumping station). The outside dimensions of the building are 34.5 m × 16.5 m × 10 m.

The sizing of the chiller needed in this building is based on the needs of the air-conditioning units only. This estimate (capacity of the station, cost and size of the building itself) will need to be revised when the requirements for chilled and mixed water for the experimental areas and control rooms are precisely known.

- Summer indoor conditions: T = 32 °C, no control of humidity.
- Winter indoor conditions: T = 19 °C, no control of humidity.

21.2.1 Description of the equipment and mode of operation

A standard heating and ventilation unit will be provided for the SU building. Being of small size, this unit can be wall mounted by means of brackets. The distribution of supply air is foreseen by means of displacement terminals. The air-exhaust is carried out by two roof-top type heat and smoke ventilation fans.

21.3 Heating and ventilation of the SF building

The SF building houses the primary cooling facilities, in this case the cooling towers and the primary water distribution plant. The outside dimensions of the pumping station are 29 m × 11 m × 10 m.

- Summer indoor conditions: T = 35 °C, no control of humidity.
- Winter indoor conditions: T = 19 °C, no control of humidity.

21.3.1 Description of the equipment and mode of operation

Being a unit of medium size, it will only need a light support structure within the SF building. The distribution of supply air is foreseen by means of displacement terminals and the distribution of exhaust-air with four roof ventilators.

21.4 Heating and ventilation of the big experimental hall (d = 55 m) and attached control building

The experimental equipment in the building is not known. All human actions are concentrated in the control building. The hall has dimensions of 2375 m^2 and 47 500 m^3. The control building is estimated to have dimensions of 30 m × 10 m × 4 m and it houses, in addition to the control room, some offices and administrative areas. A technical room (15 m × 15 m × 10 m) for the air-handling units and the water chiller will be constructed close to the hall, for instance along the access tunnel. A 6 m × 3 m concrete duct divided in two lengthways carrying the fresh and exhaust air will be built from the surface to the AHUs.

21.4.1 Hall

- Summer indoor conditions: T = 26 °C, $T_{dewpoint}$ = 14 °C.
- Winter indoor conditions: T = 19 °C.

21.4.2 Control building

- Summer indoor conditions: T = 25 °C.
- Winter indoor conditions: T = 22 °C.

21.4.3 Description of the equipment and mode of operation

For the experimental hall, one classical AHU will be needed in view of the required capacity. This unit will be housed in a machine room adjacent to the hall. The distribution of supply air is foreseen so that the supply air ducts run along the walls at a height of about 3 m around the whole hall and supply the air through the grilles. An exhaust (recirculation) ducting is placed in the upper part of the hall. Systems for smoke extraction and emergency ventilation in case of a gas leak are foreseen. The smoke extraction will be done using the same AHUs as for air conditioning. For that purpose a 'standardized fire-brigade control cubicle' will be installed outside the building.

During the operation of the experiment (hall non-accessible), the AHU will operate 100% on recirculation and with a maximum air flow. During the shutdown (hall accessible) the unit will run entirely on fresh air and with half of the maximum air flow.

No special heating system will be needed for the hall. When the experiment is running the heat loads will be more than the heat losses. If the shutdown is during the winter months, the ventilation will provide enough heating.

The power supply boards and the control and supervision units will be like those foreseen for the LHC (ST-CV standard).

For the control building, one AHU with cooling and heating coil will be needed. This unit can be located on the roof of the building. The air conditioning will operate mostly on recirculated air, but always supplying the minimum of fresh air. A system for smoke extraction can be incorporated in the air-conditioning system. During winter, rooms will be heated with electric radiators.

A water chiller located in the technical room close to the hall will provide cooling for the AHUs. This unit will also serve the smaller (d = 30 m) experimental hall and its control building. The chiller will be air-cooled.

21.5 Heating and ventilation of the small experimental hall (d = 30 m) and attached control building

The experimental building equipment in the building is not known. All human actions are concentrated in the control building.

The dimensions of the hall are 710 m^2 and 9940 m^3. The control building is estimated to have dimensions of 30 m × 10 m × 4 m and it houses, in addition to the control room, some offices and administrative areas.

A machine room for the AHU will be constructed attached to the hall (for example entrance from access tunnel), dimensions 10 m × 10 m × 10 m. A concrete shaft will be built up to ground level for the fresh air intake and to exhaust the used air.

21.5.1 Hall

- Summer indoor conditions: T = 26 °C, $T_{dewpoint}$ = 14 °C.
- Winter indoor conditions: T = 19 °C.

21.5.2 Control building

- Summer indoor conditions: T = 25 °C.
- Winter indoor conditions: T = 22 °C.

21.5.3 Description of the equipment and mode of operation

For the experimental hall, one classical AHU will be needed in view of the required capacity. This unit will be housed in a machine room adjacent to the hall. The distribution of supply air is foreseen so that the supply air ducts run along the walls at a height of about 3 m around the whole hall and supply the air through the grilles. An exhaust (recirculation) ducting is placed in the upper part of the hall. Systems for smoke extraction and emergency ventilation in case of a gas leak are foreseen. The smoke extraction will be done using the same AHUs as for air conditioning. For that purpose a 'standardized fire-brigade control cubicle' will be installed outside the building.

During the operation of the experiment (hall non-accessible), the AHU will operate 100% on recirculation and with a maximum air flow. During the shutdown (hall accessible), the unit will run entirely on fresh air and with half of the maximum air flow.

No special heating system will be needed for the hall. When the experiment is running the heat loads will be more than the heat losses. If the shutdown is during the winter months, the ventilation will provide enough heating.

The power supply boards and the control and supervision units will be like those foreseen for the LHC (ST-CV standard).

For the control building, one AHU with cooling and heating coil will be needed. This unit can be located on the roof of the building. The air conditioning will operate mostly on recirculated air, but always supplying the minimum of fresh air. A system for smoke extraction can be incorporated in the air-conditioning system. During winter, rooms will be heated with electric radiators.

The cooling for the AHUs will be supplied by a water chiller located in the machine room of the bigger experimental hall. From there the cooling pipes will be brought to these units.

21.6 Ventilation of the RE spaces

The RE space houses the low-voltage electrical equipment. There are four separate spaces along the ring. Each of them is 50 m^2 in area. Since the space is enclosed and not accessible, a 100% redundancy system is needed for ventilation.

- Indoor conditions: T = max. 28 °C, T = min. 19 °C, no control of humidity.

21.6.1 Description of the equipment and mode of operation

Cabinet-type air-conditioning units (2) will be provided for the RE areas. Each unit will comprise a direct expansion cooling coil with a water-cooled condenser. The supply of air will be from underneath through a perforated floor. Exhaust will be at the top of the room. The unit will operate in recirculation mode, with some fresh air when the space is accessible.

A heat exchanger will be installed for the condenser cooling; on the primary side the demineralized water circulates and on the secondary side, the condenser cooling water. This type of solution is used in the alcoves in the LEP tunnel.

21.7 Ventilation of the machine tunnel

The tunnel holds the accelerator machine itself. The tunnel is approximately 3900 m long and 4.5 m × 3.5 m in cross-section. Two buildings (spaces) have to be provided for supply and exhaust units, dimensions 10 m × 10 m × 5 m.

- Indoor conditions: T = max. 25 °C, control of humidity $T_{dewpoint}$ = 14 °C,

21.7.1 Description of the equipment and mode of operation

The ventilation of the tunnel will be operated from two points. One point is for supplying the fresh air to the tunnel and the other is for exhaust. Two AHUs will be installed for the supply of air to the tunnel. For the exhaust, two units of the same air flow will be installed and also two exhaust units for smoke extraction. The ventilation will always operate on fresh air. When the space is accessible, the air flow will be reduced to half.

The cooling water will be delivered from the SU building.

21.8 Ventilation of the klystron buildings

There are nine buildings that house the klystron equipment. Each of them is 100 m^2 in area. They are situated on top of the machine tunnel.

- Indoor conditions: T = max. 38 °C, T = min. 19 °C, no control of humidity.

21.8.1 Description of the equipment and mode of operation

For the klystron building, one AHU with cooling and heating coil will be needed. This unit can be located on the roof of the building. The air conditioning will operate mostly on recirculated air, but always supplying the minimum of fresh air. A system for smoke extraction can be incorporated in the air-conditioning system. For the ventilation cooling, direct expansion units will be used.

21.9 Ventilation of the SR buildings

The SR buildings house high-voltage electrical equipment. There are two identical buildings along the ring. They are concrete buildings with dimensions 50 m × 20 m × 10 m.

- Indoor conditions: T = max. 30 °C, T = min. 19 °C, no control of humidity.

21.9.1 Description of the equipment and mode of operation

Two classical AHUs will be needed in view of the required capacity. These will be housed inside the SR building. The distribution of supply air is foreseen by means of displacement terminals and return air from the roof through grilles.

The system will run mostly on recirculated air; however, a minimum amount of fresh air is supplied.

In view of the high flow rate involved in the case of the SR building, it is recommended to use two units (45 000 m^3/h 275 kW cooling capacity 75 kW heating capacity) in each building. The cooling of the air handling units is foreseen to be done by an air-cooled water chiller which will be placed in the technical room. A technical room of of 10 m × 10 m × 6 m should be foreseen for each building. The ducts will have a diameter close to 1500 mm.

The power supply boards and the control and supervision units will be like those foreseen for the LHC (ST-CV standard).

Eight roof-mounted static heat vents for smoke venting will be installed. For that purpose a 'standardized fire-brigade control cubicle' will be installed outside the building.

21.10 Summary tables

The internal loads of the buildings and the dimensioning values for the HVAC installations are given in Table 33 and Table 34, respectively. The power consumption of the heating, ventilation, air conditioning and cooling installations are summarized in Table 35 and the space requirements in Table 36.

Table 33: Internal loads of the buildings (the loads are given per building).

Building	Heat loads (kW)	Heat losses (kW)
SH building	980	100
SU building	110	30
SF building	75	70
Experimental hall (d = 55 m)	100	50
Experimental hall (d = 30 m)	60	20
Two control buildings	60	10
RE spaces	30	5
Machine tunnel	290	150
Klystrons	55	5
SR buildings	480	75

Table 34: Dimensioning values for the HVAC installations (given per building).

Building	Heating (kW)	Cooling (kW)	Air flow (m^3/h)
SH building	300	–	162 000
SU building	90	–	25 000
SF building	85	–	19 000
Experimental hall (d = 55 m)	150	100	30 000
Experimental hall (d = 30 m)	90	60	15 000
Two control buildings	20	60	18 000
RE spaces	–	30	9 000
Machine tunnel	880	860	88 000
Klystrons	15	60	7 200
SR buildings	–	550	90 000

Table 35: Total power consumption of HVAC and cooling installations (kW).

SH building	405
SU building	140
SF building	125
Experimental hall (d = 55 m)	310
Experimental hall (d = 30 m)	100
Two control buildings	60
The RE spaces (4)	70
Machine tunnel	960
Klystrons (9)	375
SR buildings (2)	900
Total power for HVAC	3445
Chilled-water plant	275
Machine dem. water plant	330
Klystron dem. water plant	975
SF cooling towers & pumping station	1440
Total power for cooling	3120
Grand total	6565

Table 36: Buildings/space needed for HVAC installations.

Building	Dim. (m)	Area (m^2)	Volume (m^3)
SH building (3 HVAC tech. rooms)	(3×)6 × 10 × 10	60 (180)	600 (1800)
SU building (HVAC unit inside)	6 × 3	18	–
SF building (HVAC unit inside)	10 × 4	40	–
HVAC experimental hall (d = 55m)	15 × 15 × 10	225	2250
HVAC experimental hall (d = 30m)	10 × 10 × 10	100	1000
Control buildings (HVAC units on roof)	–	–	–
Four RE (HVAC units inside)	(4×)4 × 2	8 (32)	-
Machine tunnel HVAC tech. room	(2×)10 × 10 × 5	100 (200)	500 (1000)
Nine klystron buildings (HVAC units inside)	(9×) 4 × 2	8 (72)	
SR buildings (2 HVAC techn. rooms)	(2×) 10 × 10 × 6	100(200)	600 (1200)
SF cooling towers and pumping station	29 × 21.4 × 10		
SU demineralized water station	34.5 × 16.5 × 10		
Cooling station for experimental areas	(2×) 15 × 10 × 10		

22 Access Control and Machine Interlock Systems

22.1 Introduction

The realization of the ELFE project implies the implementation of safety systems ensuring personnel and equipment protection. The purpose of this chapter is to give a general overview of the access-control and machine-interlock safety systems applied to the ELFE project. The different layers of the safety systems and the access operation principles will be described.

22.2 Safety considerations

At CERN the areas under radiation control are divided in two types:

- primary beam areas,
- secondary beam areas.

These areas are submitted to the following safety rules:

- Access to the areas under radiation control must be forbidden and nobody should be present in these areas during beam exploitation.
- The beam should be absent, the machine should be off and the level of resident radiation must be acceptable in order to access such areas.

In order to cope with these rules, an access control system and a machine-interlock system are to be provided for each type of beam area.

Access-Control-System (ACS). The ACS controls the equipment (doors, separating grids, shielding walls, etc.) enclosing and dividing up a primary beam area. All these items of equipment are called (following the INB regulations) Important Safety Components of the access (ISC-access).

Machine-Interlock System (MIS). The MIS manages the equipment (beam stoppers, magnets power supply, RF cavities, etc.) in charge of beam circulation. All these items of equipment are called (following the INB Regulations) Important Safety Components of the machine (ISC-machine).

The safety concept is based on the interlock of these two systems:

- Under the MIS exploitation all the ISC-access should be bolted in a 'SAFE' position and a 'VETO' signal inhibits and prevents any access procedure. In case of emergency, by opening a door the ISC-machine are immediately stopped.
- In the same way, under the ACS exploitation, all the ISC-machine should be stopped ('SAFE' position) and a 'VETO' signal inhibits and prevents the engaging of the power supply.

22.3 Safety systems of the ELFE project

The following ELFE infrastructure will be considered as primary beam area: the injector, the transfer tunnels, the main ring, the extraction lines and the high-/low-intensity experimental zones.

22.3.1 Safety-systems layers

The architecture of an industrial network can be divided in the following layers: the equipment layer, the control/safety layer, and the supervision layer. Below are the layers foreseen for ELFE's safety systems.

The equipment layer is made up of the following items (see Fig. 95 for the schematic layout).

- Six primary-beam-area access points equipped with

  - one door (material transport - if any),
  - one turnstile or equivalent (personnel traffic),
  - a film-badge reader,
  - key distributors,
  - one monitor (assistance to the users),
  - a panel signalling the access mode.
- Eleven separating grids dividing up the different areas: Each transfer line (injection and the two extraction tunnels) will be divided up by two separating grids. The main ring will be subdivided into five sectors for test facilities and patrol procedures.
- Additional interlocked emergency exits from the experimental areas.
- Eight pieces of hardware equipment dedicated to the patrol procedure (search boxes or equivalent).
- Cabling/hardware interfaces related to the acquisition of the safety signals (access and machine equipment).
- Switches, contacts dedicated to the generation of the ISC-access/-machine safety signals.

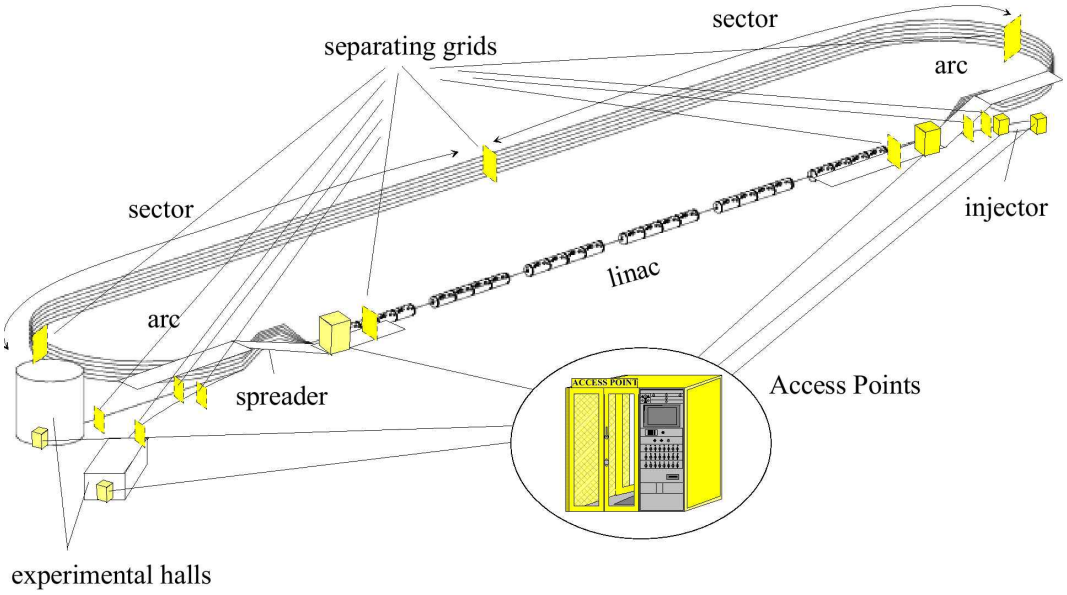

Fig. 95: Schematic layout of the Access Control equipment location.

The control/safety layer is made up of the following items.

- A hardware fail-safe industrial network based on nine Programmable Logic Controllers (PLCs) (NB: if ELFE is treated as an INB installation, the number of PLCs will be increased).
- Its Profibus-based communication network.
- A central interlock safety system.

The supervision layer is made up of the following items.

- An Ethernet TCP/IP-based communication network.
- One workstation running the access application program.
- Two X-Terminals dedicated to the access procedures.

In order to exploit the access system, video and audio equipment/networks are needed.

22.3.2 Access exploitation principle

During machine exploitation (ISC-machine ON), the access points are bolted and prevent any access to the machine areas (CLOSED MODE). As soon as the ISC-machine are off, the operator of the control room sets the access points to a SUPERVISED MODE, thus granting access to the machine. The users are identified by the system (by insertion of their film-badge in the film-badge reader) and, if they are authorized, the operator releases an access key and enables the turnstile in order to let them cross the access point (everything is supervised using the audio and video networks).

In SUPERVISED MODE the doors should be opened using the access key. An additional FREE/CONTROLLED MODE will be implemented in order to allow people to enter the areas during the long shutdown periods of the accelerator without supervision from the control room. During access exploitation (ISC-machine OFF), machine equipment tests are allowed under specific conditions. Obviously the test area will be emptied and the separating grids concerned will be in a CLOSED mode. Any activation of the emergency passage equipment will immediately stop the tests.

22.4 Remarks

- Owing to the obsolescence of the LEP hardware and software equipment, its reutilization for ELFE is impossible. Thus the safety systems foreseen for ELFE will be entirely new.
- Further investigations need to be made in order to describe more precisely the safety systems for ELFE.
- The INB aspect of this project should be checked.

23 Safety and Radiation

The following is based on policy stated in the CERN Radiation Safety Manual [66]. The hazard to man from occupational exposure to ionizing radiation is measured in sieverts (Sv). The annual exposure limit for a person who is exposed to radiation as a result of his/her professional activities in CERN, as in most European nations, is 20 millisievert (mSv). At CERN, with the aim of keeping exposures as low as reasonably achievable, a reference dose of 15 mSv/y has been introduced. Exposures above this level (and below the limit of 20 mSv) can be authorized only in exceptional circumstances. Persons who could be exposed to these levels are expected to carry personal dosimeters in order to record their exposure.

The dose limit for all other persons working at CERN is 1 mSv, the internationally agreed limit to 'public' exposure.

CERN policy is to make sure that, outside the fenced areas, the dose at any point must not exceed 1.5 mSv per year and the dose actually received by a person must not exceed 0.3 mSv per year. This limit includes both external exposure and the dose resulting from the intake of any radioactive releases from CERN.

In order to ensure that these limits are respected, certain parts of the fenced land belonging to CERN are considered to be Designated Areas. Outside these areas, the dose must be kept below the limit of public exposure. The result is that persons who spend their entire working time outside Designated Areas cannot be regarded as being occupationally exposed.

Designated Areas are either considered as Supervised or Controlled areas. The former are areas in which working conditions are constantly kept under review but no special procedures are required. Those employed there are unlikely to receive doses above 1 mSv in the course of their normal work, taking account of their working hours. In Controlled Areas normal working conditions will require persons to follow well-established procedures and to have been given specific information concerning radiation exposures. In the normal course of their work, such persons are liable to receive a dose of over 1 mSv per year, i.e. greater than the limit for persons who are not individually monitored.

In order of increasing severity of control, Controlled Radiation Areas are classified as:

- **Simple controlled areas**, where persons who work in the area must carry personal monitors (film-badges), but where all necessary precautions are taken to ensure that normal work over a year will not give rise to an absorbed dose greater than that permitted for persons designated by their employers as being exposed to radiation in the course of their profession.
- **Limited-stay areas**, where persons who work in the area must carry personal monitors (film-badges) and it is not possible to authorize any permanent residence in the area. An Operational Dosimetry System (pen dosimeters, electronic dosimeters, etc.) is necessary to control the rate of accumulation of dose during work in such areas.
- **High radiation areas**, where dose rates may reach levels (2 mSv/h) such that the annual dose could be received in less than ten hours' work in localized zones inside the area. Thus no visitors can be allowed and strict access control must be maintained.
- **Prohibited areas**, where dose rates may reach levels (100 mSv/h) such that the annual dose could be received in less than ten minutes' work in localized zones inside the area. Access can only be authorized under very special circumstances.

The classification of the preceding areas is a function of the dose rate and the permitted occupancy times. There is one other type of area classification, that of an Exclusion Area where, because of the risk of high levels of radiation during circumstances such as beam operation, access is excluded by an integral perimeter fence and an interlock system.

One design constraint for all accelerator installations is that the dose rate in an accessible area from a continuous loss under the worst credible circumstances should never exceed $100\,\mathrm{mSv\,h^{-1}}$. Above this limit, access must not be possible because the area becomes a Prohibited Radiation Area.

Experience has shown that annual doses remain well below the annual dose limits if one takes as a design constraint that the dose rate in a Simple Controlled Area, averaged over 24 hours for normal, expected loss situations, should be lower than $10\,\mu\mathrm{Sv\,h^{-1}}$. The design constraints for other classes of areas where people are likely to work permanently are summarized in Table 37. It should be noted that these dose-rate constraints are supplemented by installing radiation monitoring systems to warn operators if levels exceed three times the design level during actual operation. If levels exceed ten times the design constraints the offending operation must be stopped. This allows the shielding to be improved or the area classification made more restrictive.

Table 37: Design dose-rates outside shielding.

Area Classification	Dose rate μSv/h
Normal loss	
Simple Controlled	< 10
Supervised	< 1
Non-designated	< 0.1
Maximum loss rate	
Any area	$< 100\,\mathrm{mSv/h}$

One then has to reach a balance between these different constraints. For example, if in a Simple Controlled Area such as the klystron galleries of ELFE, the shielding attenuation provided meets the constraint for a full loss, it will automatically meet the normal dose-rate constraint of $10\,\mu\mathrm{Sv/h}$ if the loss is less than 0.01% of the full beam over a distance in the beam line of several metres.

In the initial stages of shield design, a simple model can be used to estmate the lateral shielding required around targets and dumps at electron accelerators. The first assumption is that the source has to be approximated by a point source, i.e. it must be localized in a geometrical region which is small in size compared with the other dimensions of the shielding situation in order for the inverse-square law of geometrical dilution to hold. The second is that the dose in pure cylindrical geometry, H, as a function of position can be described in terms of the relative co-ordinates of the point source, S, and the point of interest, P (see Fig. 96), and that there are no contributions from any other secondary sources. If the point S is assumed to be at the origin of the co-ordinate system then the dose equivalent per lost particle, $H(r,z)$, at the point P which is at a distance r off-axis and at a longitudinal depth z can be described:

$$H(r,z) \;=\; H(\zeta,\theta) \;=\; kZ(\zeta,\theta)\,\Theta(\theta)/R^2 \;,$$

where $R = \sqrt{r^2+z^2}$ is the distance from S to P, ζ is the line-of-sight distance in the shield of the vector joining S to P, and $\theta = \arctan(r/z)$ is the polar angle of this vector.

The function H can be separated into two other functions: $Z(\zeta,\theta)$ which is a build-up/attenuation function and $k\ \Theta(\theta)$ which is the particle source term as a function of polar angle. The function $Z(\zeta,\theta)$ need not have *a priori* any particular functional form and could have a build-up as well as an attenuation component.

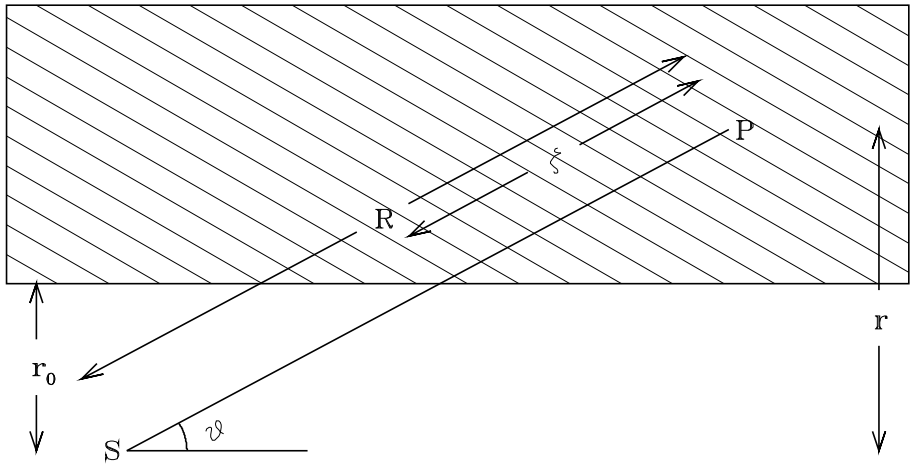

Fig. 96: Sketch of the cylindrical geometry situation.

In its simplest form, and the most appropriate since the model is basically only applicable to angles θ close to 90°, for lateral shielding the above equation reduces to

$$H \;=\; H_0 E_{\rm e} \frac{\exp(-(r-r_0)/\lambda)}{r^2} \;,$$

where $E_{\rm e}$ is the electron energy in GeV.

Each of the three components of the radiation field needs to be considered separately, but in each case there is a linear dependence of H on primary electron energy. The parameters in the above formula which were used for the design of LEP are listed in Table 38 [67].

Table 38: Parameters for use with the simple formula for shielding electron accelerators.

Radiation component	H_0 (Sv.m^2/GeV)	$\lambda_{\rm concrete}$ (g/cm^2)	$\lambda_{\rm iron}$ (g/cm^2)
High-energy hadrons	2.0×10^{-17}	100	164
Resonance neutrons	1.1×10^{-15}	42	130
Bremsstrahlung	2.0×10^{-15}	46	50

Thus, to meet the design requirement for the klystron galleries, approximately 3 m thickness of concrete shielding will be required. For the operation of the machine to be essentially undetectable at the shield surface, even in the case of a full beam-loss at maximum energy, about 8 m of concrete would be required. It would thus be prudent, and ease the defence of the installation to any environmentalists, to ensure that the machine passed this depth below any public areas such as main roads. Final shield thicknesses can be optimized during the actual design phase of the ELFE machine, taking account of the self-shielding provided by the accelerator components themselves and using Monte Carlo simulations of the cascades produced by the lost electrons rather than simple empirical models.

24 Cost Estimate, Alternatives

24.1 Capital expenditure

The capital expenditure for ELFE hardware is given in Table 39. The prices are in MCHF (1999) and include development, material and installation, no salaries.

Table 39: Capital investment for ELFE (MCHF).

Polarized electron source	0.4
Microtron pre-accelerator	20.0
Cryogenics	63.0
Electrical power distribution	29.0
Cooling / ventilation	25.8
Beam diagnostics	9.4
Power converters	11.2
RF equipment	10.9
Civil engineering	109.7
Vacuum	19.4
Magnets	55.2
Control system	10.0
Access control / fire detection	2.1
Sum accelerator	**366.1**

Two experimental areas are foreseen, one for a high-intensity spectrometer, the other one for a detector with 4π geometry. For the latter an existing hall at CERN might be used. Table 40 gives the cost for the experimental areas for both options.

Table 40: Cost of experimental areas (MCHF).

Only high-intensity hall has to be built	26.7
Second experimental hall (low intensity)	4.5

24.2 Manpower

For a construction time of about six years the required manpower has been estimated to be 756 man-years, all categories together. Industrial support is included in the capital expenditure estimate.

24.3 Option

The reference design is based on a linac with all accelerating cavities on one side of the race track only, and a simple return line on the opposite side. An alternative could be to split the linac between the two straight sections. This would lead to a reduced tunnel length of about 500 m in total. The consequences of this layout have not been studied in detail; however, the main points are:

a) The beam energy is 1.75 GeV lower, because it seems unrealistic to add a seventh recirculation channel to one of the arcs.

b) The energy spread of the beam is larger, because of the higher energy in the last arc.

c) An additional set of spreader and recombiner assemblies are required.

The cost saving is estimated to be about 17.9 MCHF.

24.4 Operating cost

The cost for operating ELFE has been estimated to be 18.6 MCHF per year. Eight months of accelerator operation has been assumed. The operation of the cryogenics plant is subcontracted to industry, following the example of LEP. The major items are given in Table 41, the rest is required for general repair and maintenance.

Table 41: Major operating cost contributions (MCHF).

Electrical power	8.6
Cryogenics	3.5
RF equipment	2.0
Injector complex	0.6

24.5 Manpower for operation

For the operation and maintenance of the ELFE accelerator about 63 full-time-equivalent staff are required. This includes 15 operators assuring 24-hour operation.

References

[1] *The ELFE Project: an Electron Laboratory for Europe, Proc. of Mainz Workshop* (Oct. 92), edited by J. Arvieux and E. De Sanctis, (Editrice Compositori, Bologna, 1993).

[2] *Prospects of Hadron and Quark Physics with Electromagnetic Probes, Proc. of Saint-Malo Workshop* (Sept. 96), edited by N. D'Hose et al., Nucl. Phys. **A622** (1997) 1c–389c.

[3] *Electron Laboratory for Europe, Accelerator Technical Proposal, 'Blue Book'*, J.-M. De Conto (Ed.), Institut des Sciences Nucléaires de Grenoble, RME02, (October 1993).

[4] R. Brinkmann et al., *The Machine Project for ELFE at DESY*, Nucl. Phys. **A622** (1997) 187c–224c.

[5] G. Geschonke and E. Keil, *A recirculating electron accelerator (ELFE) using the LEP superconducting RF cavities*, CERN-SL-98-060-RF.

[6] H. Herminghaus et al., *The design of a cascaded 800 MeV normal conducting C.W. race track microtron*, Nucl. Instrum. Methods **138** (1976) 1.

[7] H. Herminghaus et al., *First operation of the 855 MeV CW electron accelerator 'MAMI', Proc. LINAC Conf. 1990*, Albuquerque, N.M., p. 362.

[8] X. Ji., J. Phys. **G24** (1998) 1181; Phys. Rev. Lett. **78** (1997) 610.

[9] A. V. Radyushkin, *Scaling limit of deeply virtual Compton scattering*, Phys. Lett. **B380** (1996) 417–425, `hep-ph/9604317`.

[10] P. A. M. Guichon and M. Vanderhaeghen, *Virtual Compton scattering off the nucleon*, Prog. Part. Nucl. Phys. **41** (1998) 125–190, `hep-ph/9806305`.

[11] G. Sterman and P. Stoler, Ann. Rev. Nucl. Part. Sci. **47** (1997) 193.

[12] A. E. M. Anselmino and E. Leader, Phys. Rep. **261** (1995) 1.

[13] J. Collins, *Fragmentation of transversely polarized quarks probed in transverse momentum distributions*, Nucl. Phys. **B396** (1993) 161–182, `hep-ph/9208213`.

[14] P. Jain, B. Pire and J. Ralston, Phys. Rep. **271** (1996) 67.

[15] R. Jaffe, X. Jin and J. Tang, Phys. Rev. Lett. **80** (1998) 1166.

[16] A. Kotzinian and P. J. Mulders, Phys. Rev. **D54** (1996) 1229.

[17] T. Maruyama et al., *Observation of strain enhanced electron spin polarization in photoemission from InGaAs*, Phys. Rev. Lett. **66** (1991) 2376–2379.

[18] A. Subashev *in* C.W. de Jager et al., (Eds.), *Proc. Spin96*, (World Scientific, Singapore, 1997), p. 749.

[19] V. Shvedunov et al., *Proc. EPAC 96*, Sitges/Barcelona, 1996, p. 1556.

[20] C. Nachtigall, PhD thesis, Institut für Kernphysik, Universität Mainz, (1996).

[21] P. Drescher et al., Appl. Phys. **A63** (1996) 203.

[22] K. Aulenbacher, PhD thesis, Institut für Kernphysik,Universität Mainz, (1994).

[23] R. Alley et al., *The Stanford Linear Accelerator polarized electron source*, Nucl. Instrum. Meth. **A365** (1995) 1–27.

[24] K. Aulenbacher et al., Nucl. Instrum. Meth. **A391** (1997) 498.

[25] M. Poelker *in* Y. Mamaev et al. (Eds.) *Proc. LE98*, SPES-Lab publishing, St. Petersburg, (1998), p. 105.

[26] C. Benvenuti, *Proc. EPAC 98*, Stockholm (1998), p. 200.

[27] M. Poelker, Appl. Phys. Lett. **67** (1995) 2762.

[28] K. Aulenbacher et al., *Proc. EPAC 98*, Stockholm (1998), p. 1388.

[29] M. Steigerwald et al., *Proc. EPAC 98*, Stockholm (1998), p. 1430.

[30] H. Babic and M. Sedlacek, Nucl. Instrum. Methods **56** (1967) 170.

[31] U. Ludwig, Diplomarbeit (1979), Institut für Kernphysik der Johannes Gutenberg Universität, Mainz, Germany.

[32] J. Martin, *The use of a field gradient in microtron end magnets for improved focusing properties*, Int. Rep. MAMI 1/82, Institut für Kernphysik der Johannes Gutenberg Universität, Mainz.

[33] S. Schriber, *Proc. 1976 Proton Lin. Acc. Conf.*, AECL–5677, p. 405.

[34] K. Aulenbacher et al., *Proc. EPAC 98*, Stockholm (1998), p. 523.

[35] H. Euteneuer et al., *Proc. 1992 Lin. Acc. Conf.*, Ottawa, 24–28 Aug. 1992, AECL–10728, p. 356.

[36] M. Pekeler, *Experience with superconducting cavity operation in the TESLA Test Facility, IEEE Particle Accelerator Conference (PAC 99)*, New York, 29 Mar. – 2 Apr. 1999.

[37] D. A. Edwards (Ed.), *TESLA Test Facility Linac: Design report*, Version 1.0, 1 March 1995, DESY-TESLA-95-01, 590 p.

[38] J. Delayen, *Frequency tuning of the CEBAF upgrade cavities, PAC 99*, New York (1999) 928–930.

[39] J. G. Weisend et al., *Operating experience with the first TESLA Test Facility (TTF) cryomodule, 17th International Conference on Cryogenic Engineering (ICEC 17)*, Bournemouth, England, 14–17 Jul. 1998.

[40] M. Bernard et al., *The TESLA test facility linac injector, 4th European Particle Accelerator Conference (EPAC 94)*, London, England, 27 Jun. – 1 Jul. 1994.

[41] R. Bakker et al., *1 GHz modulation of a high-current electron gun*, Nucl. Instrum. Meth. **A307** (1991) 543–552.

[42] R. Chaput et al., *Operation of the CLIO accelerator, 14th FEL Conf.*, (1992), Kobe, Japan.

[43] M. Ciarrocca et al., *2.45-GHz synchronised polarised electron injection at MAMI*, Nucl. Instrum. Meth. **A406** (1998) 351.

[44] C. Sinclair, *Recent advances in polarized electron sources, PAC 99*, New York, pp. 65–69.

[45] H. Heinrichs, U. Klein, G. Muller, H. Piel, D. Proch, W. Weingarten, H. Genz, H.D. Graf, T. Grundey, A. Richter and E. Spamer, *Charlottesville Conf. on Future Possibilities for Electron Accelerators*, 1979, J1–j16 and *Mainz Conf. on Nuclear Physics with Electromagnetic Interactions* 1979, pp.176–181.

[46] A. Nadji et al., *The effect of nonlinear synchrotron motion on the SOLEIL energy acceptance, Proc. 1999 Part. Accel. Conf.*, New York (1999) 1533.

[47] B. Autin, A. Blondel and J. Ellis (Eds.), *Prospective Study of Muon Storage Rings at CERN*, CERN 99–02.

[48] A. Mosnier, Nucl. Instrum. Methods **A257** (1987) 81–90.

[49] K. Brown et al., SLAC–91 (1974).

[50] C. Lyneis et al., Nucl. Instrum. Methods **204** (1983) 269–284.

[51] E. Haebel, (CERN), Private communication.

[52] G. Krafft and J. Bisognano, *PAC 87*, p. 1356.

[53] L. Merminga, (TJNAF), Private communication.

[54] P. Wilson, SLAC-PUB-2884 (1982) 55–56.

[55] D. Boussard, *Performance of the LEP2 SRF system*, CERN SL-97-024-RF, *Proc. PAC'97* Vancouver, 1998, p. 2879.

[56] G. Cavallari, *LEP 2000 Status Report*, CERN SL-98-011 DI (1998).

[57] H. Frischholz, *Proc.1993 IEEE Accel.Conf.*, Washington, pp. 1247–1249.

[58] H. Frischholz and G. Pecheur, *The high voltage interface for the LEP II RF power generation system*, CERN SL/94-38 (RF), *Proc. EPAC 94*, London (1994).

[59] D. Boussard, P. Brown and J.Tückmantel, *Electroacoustic oscillations in the LEP SC cavities* CERN-SL-96-17 RF, *Proc. EPAC 96*, Sitges/Barcelona, (1996), p. 1484.

[60] E. Descharoet and J.P.M. Sladen, Phase compensated fibre-optic links for the LEP reference distribution, US Particle Accelerator Conference, Chicago, 1989.

[61] D. Brandt and S. Myers, '*LEP performance limits re-visited*, CERN–SL–98–074–DI.

[62] B. Jenny, *Calculs thermiques concernant la chambre à vide ELFE*, 22/7/1999.

[63] V. Baglin, O. Gröbner, C. Herbeaux and P. Marin, LURE report RT/97–03, 14/03/1997.

[64] J. Bojon, O. Gröbner, J.-M. Laurent and P. Strubin, *EPAC*, Berlin 24–28 March 1992.

[65] J. Billy et al., *Proceedings of the Workshop on LEP Performance*, Chamonix, January 25–29 1999.

[66] Radiation Protection Group, *Radiation Safety Manual 1996*, CERN (1996).

[67] *Rapport définitif de sûreté du LEP*, CERN (1994).